Ab initio design of efficient zeolite catalysts for methanol and hydrocarbons conversion

Author: Pau Ferri Vicedo

Doctoral Advisor: Dr. Mercedes Boronat

April 2023

UNIVERSITAT POLITÈCNICA DE VALÈNCIA

Ab initio design of efficient zeolite catalysts for methanol and hydrocarbons conversion

Author: Pau Ferri Vicedo

Doctoral Advisor: Dr. Mercedes Boronat

A dissertation submitted in partial fulfilment of the requirements for the degree of Doctor of Philosophy.

EDITORIAL

UNIVERSITAT POLITÈCNICA DE VALÈNCIA

"Els homes van començar a filosofar en quedar-se meravellats davant alguna cosa, en un primer moment davant el que comunament causa estranyesa i, en progressar a poc a poc, sentint-se perplexos també davant coses de major importància, com la lluna, el sol i els astres. Ara bé, el que se sent perplex i meravellat reconeix que no sap. Així doncs, si van filosofar per fugir de la ignorància, és obvi que perseguien el saber per afany de coneixement i no per cap utilitat."

Aristòtil, Metafísica I

Agraïments

La realització d'aquesta tesi doctoral no hagués estat possible sense l'ajut professional i personal d'un conjunt de persones i institucions. Expresso el meu agraïment sincer a tots ells. En primer lloc, a la directora de la tesi doctoral, la Dra. Mercedes Boronat pels seus consells, paciència i suport durant aquests anys que han ajudat a portar a bon terme aquests projectes. Ha sigut un privilegi poder aprendre de tu. També m'agradaria agrair al Prof. Avelino Corma per les lliçons sobre química apreses durant les discussions científiques i els consells a l'hora de com presentar un treball al públic.

També dec reconèixer l'excel·lent treball del Dr. Manuel Moliner i la Dra. Cecilia Paris a la direcció de la part experimental d'aquest treball que tant bé ha compassat amb les prediccions teòriques que hem anat aportant. Particularment, agraeixo al Dr. Chengeng Li i a l'Estefania Bello ja que han dedicat les hores al laboratori per a que la síntesi de zeolites i reacció fora un èxit.

D'altra banda, agraeixo al Dr. Germán Sastre i als companys del "laboratori", la Dra. Estefanía Fernández, la Dra. Alechania Misturini, el Santiago León, el Mario Gallego, l'Omer Faruk, el Pablo Garcia i el Nacho Tirado pel suport mutu, per crear un ambient de treball agradable i per les converses entretingudes i interessants als cafenets del matí. Especialment, al Dr. Reisel Millán qui sempre ha contribuït amb respostes interesants a les meues preguntes sobre química i computació. I sense dubte, pel disseny del "rmol" sense el que aquesta tesi no haguera aplegat al mateix volum de resultats de cap manera.

A part of this investigation was developed in collaboration with the Center for Molecular Modelling (CMM) of Ghent University, where I spent three months doing a research stay. I want to thank Prof. Veronique Van Speybroeck for allowing me to be part of their group and for her good scientific advice. Also, I would like to thank all the staff of the CMM for their warm welcome received and, in particular, to my office colleagues, Dr. Louis Vanduyfhuys, Dr. Peter Cnudde and Elias Van den Broeck for their help during my MD learning.

Quant a institucions, vull agrair al Instituto de Tecnología Química per la concessió d'un contracte predoctoral, a la Red Española de Supercomputación (RES), al Centre de Càlcul de la Universitat de València, al Flemish Supercomputer Center (VSC) de la Ghent University pels recursos computacionals i el suport tècnic, a la Unió Europea i al Gobierno de España pel finançament d'aquest projecte a traves dels programes ERC-AdG-2014-671093 (SynCatMatch) "Severo Ochoa" (SEV-2016-0683, MINECO) i dels projectes MAT2017-82288-C2-1-P i PID2020-112590GB-C21 (AEI/FEDER, UE), i al CSIC pel finançament de la estada al CMM a través del projecte i-Link (LINKA20381).

En una part més personal, m'agradaria agrair a mon pare i a ma mare pel suport durant aquests anys i per haver-me deixat seguir el meu camí sense qüestionar mai les meues decisions. A la resta de la família, perquè, encara que ningú entenga a que em dedique, sempre vos alegreu de les bones noves que van arribant. A les amistats, d'Alfafara, d'Ontinyent i d'altres indrets, per ser una xarxa de complicitat que sempre ha estat present als bons i mals moments. I com no, agrair a Ferran i al inseparable Oscar per les hores i hores passades entre tristors, alegries i sorpreses al llarg de tot aquest temps.

Contents

List of Symbols and abbreviations

8r	Eight Membered Rings
AIMD	Ab-initio Molecular Dynamics
AlPO	Aluminophosphate
CDR	Cage Defining Ring
CP^+	Cyclopentenyl
d6r	Double Six-Membered Ring Units
D	Diameter of the Largest Possible Included Sphere
DEB	Diethylbenzene
DEB^+	Diethylbenzenium Carbenium Ion
DFT	Density Functional Theory
DFT-D	Dispersion-Corrected Density Functional Theory
DMDEA	Dimethyl-diethyl-ammonium
$DPDMP^+$	Diphenyldimehylphosphonium
Ea	Activation Energy
EB	Ethylbenzene
Eint	Interaction Energy
FF	Force Fields
G	Gibbs Free Energy
GGA	Generalized Gradient Approximation
HP	Hydrocarbon Pool
IZA	International Zeolite Association
K_{eq}	Equilibrium Constant
kJ/mol	Kilojoules per mole
MB	Polymethyl-Benzenes
MB^+	Carbenium Polymethyl-Benzenes
MD	Molecular Dynamics
MTEA	Methyl-triethyl-ammonium
MTO	Methanol to Olefins

NBO	Natural Bond Order
NEB	Nudged Elastic Band
OSDA	Organic Structure Directing Agent
OSDB	Organic Structure directing agent DataBase
PAW	Projector Augmented Wave
PBE	Perdew-Burke-Ernzernhof
revPBE	Revised Perdew-Burke-Ernzernhof
SAPO	Silicoaluminophosphate
TEA	Tetraethyl-ammonium
TEB	Triethylebenzene
TS	Transition State
TST	Transition State Theory
VASP	Vienna Ab-initio Simulation Package

Chapter 1
Introduction

The present dissertation covers our research efforts over the catalytic behaviour of zeolites. These are microporous, crystalline aluminosilicate materials that can be synthesized or found in nature. They are mainly composed of silicon, aluminium and oxygen. These materials are able to host metal ions or protons, H^+, inside their pores acquiring distinctive catalytic properties that have gathered scientist's attention becoming a specific field of research on its own throughout the years.

While catalysis was initially a much more empirical trial-and error science, it has evolved during the last decades into a directed interdisciplinary science that strives for fine rational design. As computational chemists, we participate in this goal employing theoretical modelling to simulate a chemical system as much realistically as possible, in order to obtain reliable information regarding its behaviour. Using these research tools, the understanding of catalytic behaviour can be achieved, and suggestions for improvement or predictions for other systems may be derived. Consolidated in the 20th century, both catalysis and computational chemistry are very wide fields of specialization in chemistry nowadays. A summary of the key ideas of catalysis is presented in Chapter 1, whereas the foundations behind the computational approaches employed can be consulted in Chapter 2. Finally, the results and conclusions of our research are presented from Chapter 3 onwards.

1.1 Catalysis.

Catalysis is the process of increasing the rate of a chemical reaction by adding a substance known as a catalyst.[1,2] The name was given in 1836 by Berzelius, the chemist that first noticed this phenomena, but the catalytic process was not fully understood until the 20th century.[3] Unlike reagents, a catalyst is not consumed in the chemical process. It can change during reaction but it eventually recovers its original state. This particular characteristic allows catalysts to undergo chemical reactions more than once, establishing what is called a catalytic cycle. As a consequence, catalysts modify reactions dramatically even when they are barely present at very low concentrations.

Three fundamental features characterize catalysts. Firstly, the activity, which refers to the degree of positive alteration introduced in the reaction by the catalyst. Contrariwise, if a catalyst diminishes the reaction rate, it is then called inhibitor. Secondly, the selectivity, which specifies how much the catalyst changes the distribution of products with respect to the no-catalysed reaction. Finally, the stability of the catalyst accounts for how fast it deactivates over time because of the adsorption of unreactive species that are said to poison it or how fast it decomposes due to the specific reaction conditions. This property is usually measured as the number of catalytic cycles that it can undergo before deactivation.

In the specific case of zeolites, deactivation by blockage of their micropores as a consequence of non-reactive species or side products is always a concerning issue. However, catalysts may be recoverable with appropriate post-reaction treatments and, in the case of zeolites, micropores can be cleaned by calcination of the blocking organic species at temperatures where the silicoaluminate structure of the catalyst remains stable ~500 °C.[4]

Catalysts introduce a direct impact into the elementary reaction steps that yield the overall chemical reaction building up the reaction mechanism. The modification that each catalyst causes in these steps defines its activity and selectivity. The Transition State Theory (TST) states that reactants form an unstable intermediate called activated complex or transition state (TS), which refers to the point of maximum free energy along the reaction coordinate, i. e. chemical bond formation, before their decomposition into products. In order to reach the TS, reactants need to obtain a certain amount of energy called activation free energy ΔG_{act}, which is the difference between the absolute free energy of the TS and the absolute free energy of the reactants (Figure 1.1). As a result, each elementary step has an energetic barrier, ΔG_{act} that needs to be overcome. If a specific elementary step has a much higher barrier than the others do, it will limit the velocity of the reaction constituting the rate determining step of that reaction mechanism. This theory was developed by Henry Eyring and independently by M.G. Evans and Michael Polanyi[5,6], and is the fundamental model with which the kinetics of chemical reactions are explained.

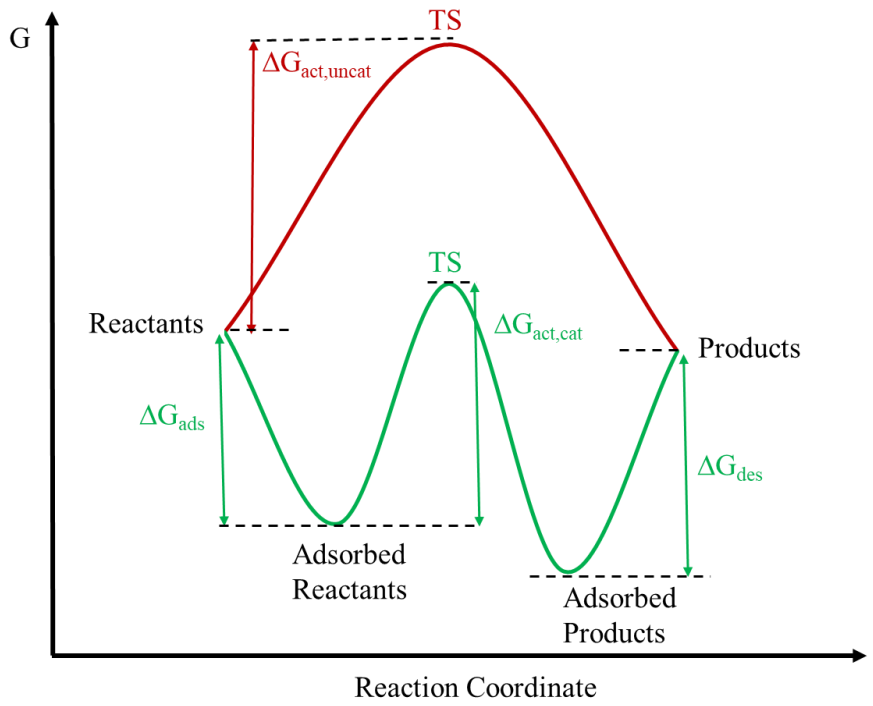

Figure 1.1. Schemes of the free energy profiles for an uncatalysed (red) and catalyzed (green) reaction. ΔG_{act}, ΔG_{ads} and ΔG_{des} stand for activation, adsorption and desorption energies respectively.

Thus, an active catalyst significantly decreases the barrier of the rate determining step of the reaction mechanism (see Figure 1.1 green), leading to an increase in the reaction rate. In practice, a numerical way of measuring catalyst activity has been settled by the so-called Turnover Frequency (TOF), which is calculated as the number of molecules that react per amount of catalyst and hour. The larger the TOF, the more active the catalyst. Regarding to selectivity, it implies modifying the reaction rate of two or more competing steps or pathways leading to different products, in order to favour one over the other. Therefore, the catalyst should be selective towards the desired step or pathway mechanism while being an inhibitor for those that lead to undesired products.

Decreasing activation energies for chemical reactions also implies that these processes are usually carried out under more efficient thermodynamic conditions, at significantly lower temperatures and pressures. This reduces costs and time compared with the non-catalyzed counterparts turning catalysts

a very appealing tool for all kind of industries.[7,8] Nowadays, catalysts are present in 85-90% of chemical processes in industry[9] such as the catalytic cracking of crude oil with zeolites[10,11], the chemoselective reduction of nitroarenes with noble and non-noble metal based catalysts[12], the synthesis of ammonia[9], and the selective oxidation of hydrocarbons.[13,14]

It is important to note that catalysis is not only present in industry crafting processes, it also occurs naturally in our own bodies. The proteins that are responsible for the regulation of our metabolism, millions of daily life-sustaining reactions, are called enzymes and they are the most efficient catalysts known until this day.[15,16]

As it is a very wide discipline, catalysis is commonly divided into homogeneous, where all the chemical species including the catalyst are in the same phase, either solid, liquid or gas. Heterogeneous, where the catalyst is present as a different phase from that of the reactant molecules, and biocatalysis, that deals with reactions catalyzed by enzymes. An example of biocatalysis is the breakdown of larger complex molecules into smaller molecules, such as glucose, in the digestive system allowing the body to use them as fuel.

1.2 Heterogeneous catalysis.

In heterogeneous catalysis the solid phase acts as the catalyst and interacts with the liquid or gas phase reactant molecules through adsorption, reaction and desorption of the products establishing a complete catalytic cycle (see Figure 1.1).

Within the heterogeneous catalytic cycle, adsorption is a crucial part for catalysis success. It can take place by two different manners. On the one hand, when this event occurs by weak intermolecular interactions of the adsorbate with the catalyst and no chemical bond is formed, it is called physisorption. On the other hand, the adsorption where chemical bonds are formed is called chemisorption. When chemisorption takes place, internal bonds of the reactant molecules are weakened because of their interaction with the catalyst, this phenomenon is called activation. The term “active sites” was coined by Hugh Stott Taylor to refer to the specific groups of atoms of the catalyst responsible for the enhancement of chemical reactions.[17] They could be atoms of a metal surface or Brønsted and Lewis centers in zeolites caused by Al introduction or metals such as Sn, Ti, Zr, in the silica framework respectively.

When looking for an optimal catalyst, one has to take into account the interaction strength between adsorbates and catalyst active sites. It must be strong enough to activate the reactant molecules, but a too strong interaction might hinder the reaction or the posterior product desorption. Therefore, there is an optimum interaction energy that maximizes the reaction rate as described by the Sabatier principle with its volcano-shaped representation of the dependence of the reaction rate on the adsorption energy of adsorbates.[18] After desorption at the end of the specific heterogeneous catalytic cycle, the active sites become again available to start another cycle.

There are two general mechanisms that explain how heterogeneous reactions proceed, the Langmuir-Hinshelwood mechanism assumes that species A and B are chemisorbed before any kind of reaction between them.[19] The general scheme for the Langmuir-Hinshelwood mechanism can be outlined with this simple description where * represents the empty active site, and A*, B* and AB* represent the chemisorbed state of species A, B and AB:

Chemisorption $A + * \rightleftarrows A*$

Chemisorption $B + * \rightleftarrows B*$

Reaction $A* + B* \rightleftarrows AB* + *$

Desorption $AB* \rightleftarrows * + AB$

Differently, the Eley-Rideal mechanism states that one chemisorbed species can react with another species that is not adsorbed and comes directly from the gas or liquid phase.[20] In this case, the general scheme for this mechanism can be outlined as follows:

Chemisorption $A + * \rightleftarrows A*$

Reaction and Desorption $A* + B \rightleftarrows AB + *$

The Eley-Rideal mechanism possess the advantage for the reaction taking place without the need of free active sites for one of the reactants. However, when reaction takes place directly from the gas phase, it comes paired with a significant loss of entropy, hence a higher ΔG_{act}, than the reaction of the same two species after being both adsorbed. Therefore, Eley-Rideal kinetics is rarely observed.[21]

1.3 Solid catalysts.

Pure metal surfaces, alloys, acid and basic metal oxides, silicoalumiantes and silicoaluminophosphates are common materials used as solid catalysts. Thus, one could think that there is no limitation in the nature of solid catalysts and any type of material could be a catalyst. Nonetheless, there are certain properties that all relevant solid catalyst shall present. They should be stable against sintering and structural change at working temperatures. They should have a far-reaching surface area because the larger the surface area the greater the number of active sites available for the reactant molecules. Besides, they should be stable against deactivation or at least, easy to regenerate if deactivation is bound to happen fast. In the following sections, some comments are devoted to the structure of common solid catalysts.

1.3.1 Crystal lattices.

Solid catalysts are usually crystalline materials, they have a highly defined and periodically repeatable arrangement of atoms. This class of arrangement can be summarized into a unit cell, which is the smallest repeating unit that contains the full symmetry of the crystal structure. Unit cells are specified by vectors a, b, and c and angles α, β and γ when working on the three-dimensional space (see Figure 1.2a). By using discrete translation operations along the unit cell vectors according to $\vec{T} = n_1 a + n_2 b + n_3 c$ where n_1, n_2, n_3 are integers, and a, b and c are the unit cell vectors it is possible to generate any point in the three-dimensional space.

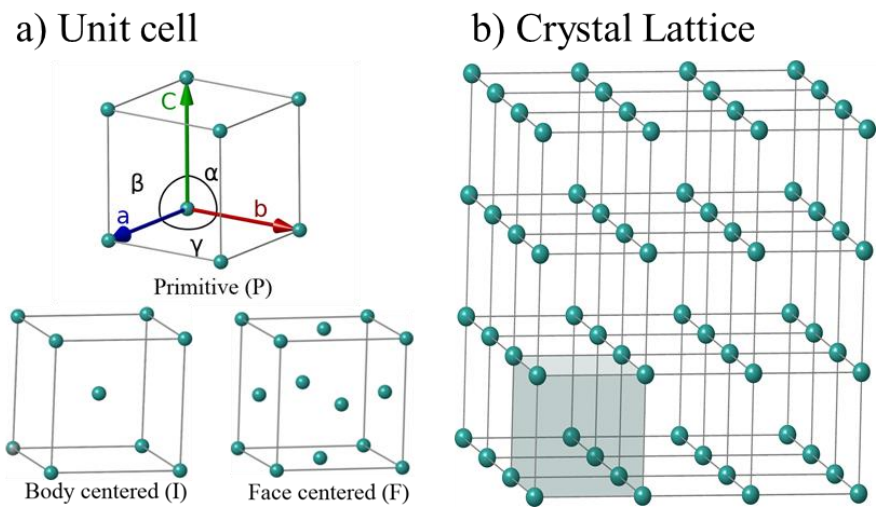

Figure 1.2. Representation of a) unit cell parameters a, b, c, α, β and γ and different kinds of unit cells b) crystal lattice generated by repetition of the unit cell.

For any three-dimensional lattice, the conventional unit cells are parallelepipeds, which in special cases may have orthogonal angles, equal lengths or both. Seven lattice systems can be defined by taking different combinations of unit cell vectors and angles, namely, cubic, hexagonal, rhombohedral, tetragonal, orthorhombic, monoclinic and triclinic (see Table 1.1). Aside from unit cell vectors and angles, different arrangements of particles inside unit cells give rise to different possible centering: primitive (P), face-centered (A, B and C), all-face-centered (F), body-centered (I), and rhombohedral (R). Combining the seven lattice systems with the lattice centering yields the so-called 14 Bravais lattices (see Table 1.1).

Table 1.1. Definition of the seven lattice systems, each of which can have different centering.

Name	**Vectors**	**Angles**	**Lattice Centering**
Cubic	$a = b = c$	$\alpha = \beta = \gamma = 90°$	P, F, I
Hexagonal	$a = b$	$\alpha = \beta = 90°, \gamma = 120°$	P
Rhombohedral	$a = b = c$	$\alpha = \beta = \gamma \neq 90°$	R
Tetragonal	$a = b \neq c$	$\alpha = \beta = \gamma = 90°$	P, I
Orthorhombic	$a \neq b \neq c$	$\alpha = \beta = \gamma = 90°$	P, C, F, I
Monoclinic	$a \neq c$	$\alpha = \gamma = 90°, \beta \neq 90°$	P, C
Triclinic	$a \neq b \neq c$	$\alpha \neq \beta \neq \gamma \neq 90°$	P

1.3.2 Zeolites.

Zeolites are crystalline micro-porous materials composed of corner-sharing tetrahedra, TO_4.[22] They can be found as silicates when $T=Si^{+4}$ or as aluminophosphates (AlPOs) when $T=Al^{+3}$ and $T=P^{+5}$ stitching a neutral charge framework created by the alternation of AlO_4^- and PO_4^+ units, Al-O-P-O-Al-O-P.[23] The periodic sequence of TO_4 builds up three-dimensional networks that present cavities and channels of different molecular dimensions, ~3-12 Å (Figure 1.3).

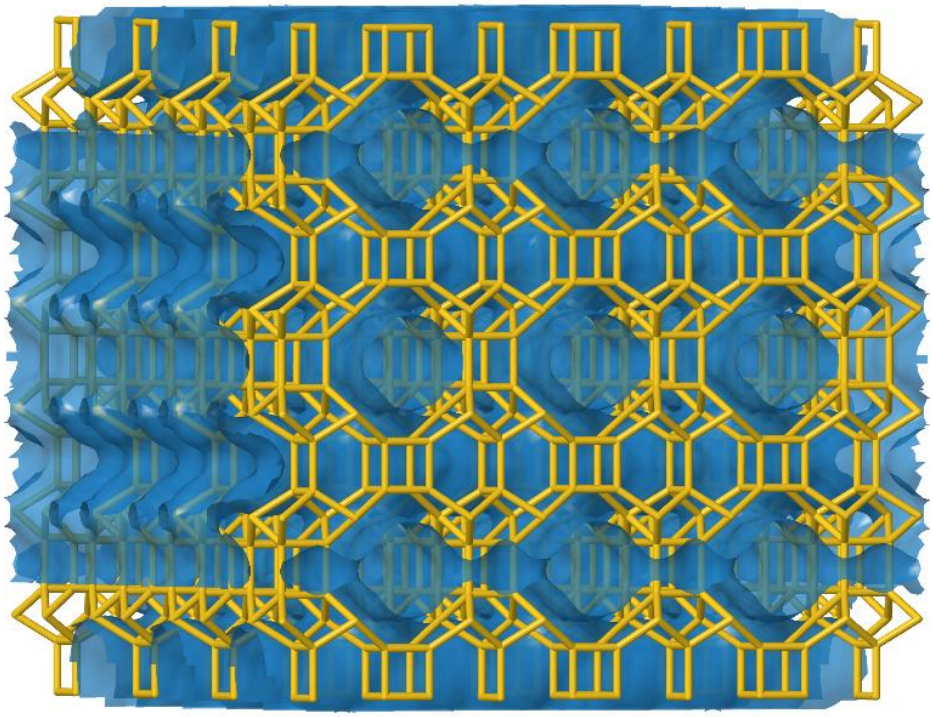

Figure 1.3. Schematic representation of the channel systems of the BEC framework extracted from IZA database.[24]

The TO_4 units are commonly referred as the primary building units (PBUs) because they are the first level of structural complexity in zeolites. The connection between these tetrahedra forms the secondary building units (SBUs) that display a variety of geometric arrangements (see Figure 1.4) with which the whole three-dimensional framework of the different zeolites can be generated.

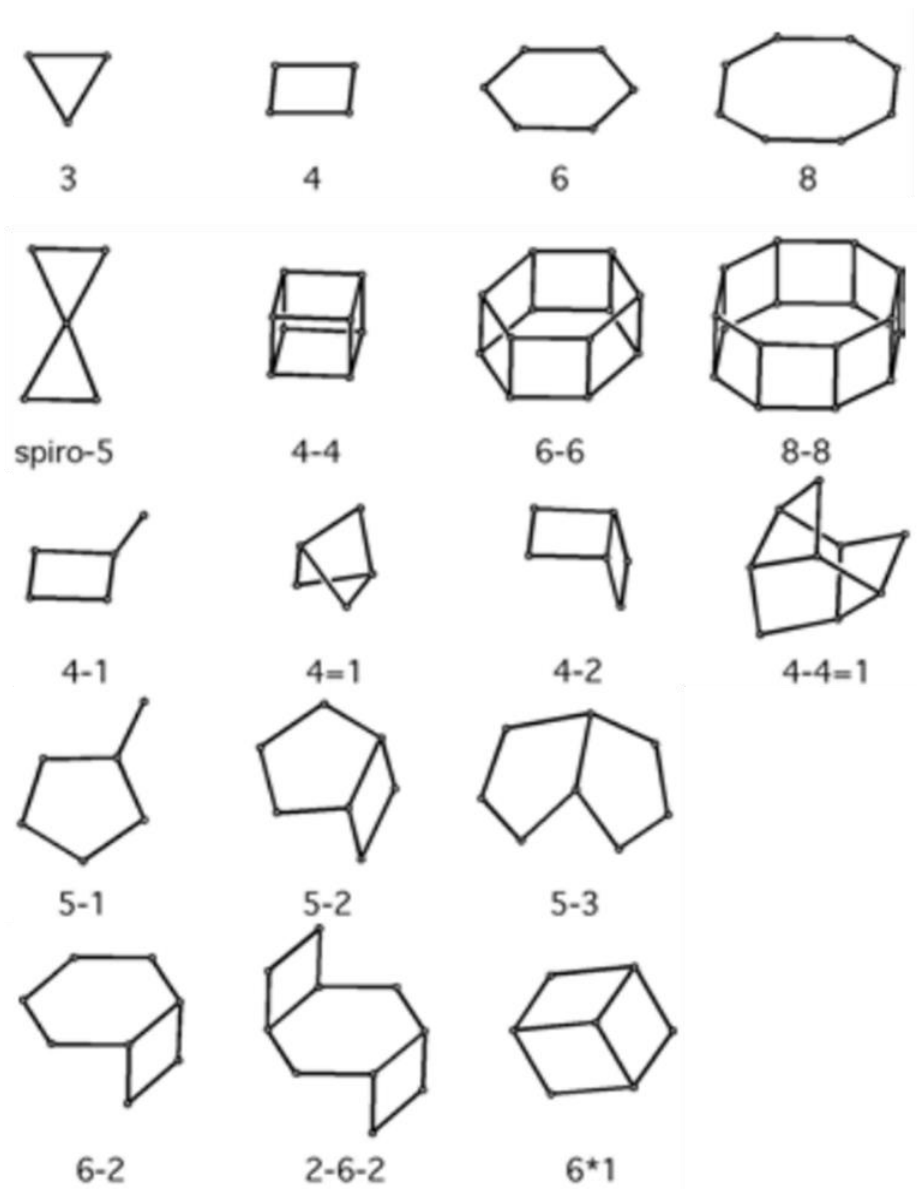

Figure 1.4. Schematic representation of some SBUs extracted from the Atlas of Zeolite Framework types.[25]

Rings size is the most important characteristic of zeolites because it controls the size of its pores, hence the reactions that can occur inside them. In addition, the conventional criteria to classify them in small-, medium- and large-pore zeolites is also determined by ring size. Rings are named by specifying the number *n* of TO_4 units they are made up with. Small-pore zeolites, such as LEV or RTH, contain rings of up to eight members (8r) with an approximate diameter of 3.4 - 4.5 Å. Medium-pore zeolites possess rings of 9-11 members

with diameters of ~5 - 5.5 Å. Similarly, large and extra-large pore frameworks contain rings, such as MOR and ITT, with 12 and 18 members respectively (see Figure 1.5). Another criterion to classify zeolites is dimensionality. Depending on the number of channels that exist in the framework, one, two or three, they can be one-, two- or three-dimensional respectively (1D, 2D, 3D). These channels can be independent or connected, either directly or indirectly through cavities. Zeolites particular channel systems and cavities grants them the capacity to act as molecular sieves in refining and petrochemistry catalytic processes, isomerization, alkylation and transalkylation of aromatic compounds increasing the selectivity towards specific products because of their shape selectivity.[26–29]

Each unique silicoaluminate or aluminophosphate topology that is discovered and characterized gets assigned a three-letters code by the Structure Commission of the International Zeolite Association (IZA), and included in the IZA database which hosts more than 200 of these frameworks.[24] Some frameworks have been synthesized with aluminosilicate and aluminophosphate chemical composition meanwhile others have only been achieved with one of both compositions. In this work, we have studied zeolites corresponding to the AEI, AFX, BEA, BEC, BOG, CHA, CON, DDR, ERI, FAU, ITE, ITT, IWR, IWV, KFI, LEV, LTA, MOR, RHO, RTH, SEW, UFI, USI, UTL frameworks with different chemical compositions that will be detailed from Chapter 3 onwards.

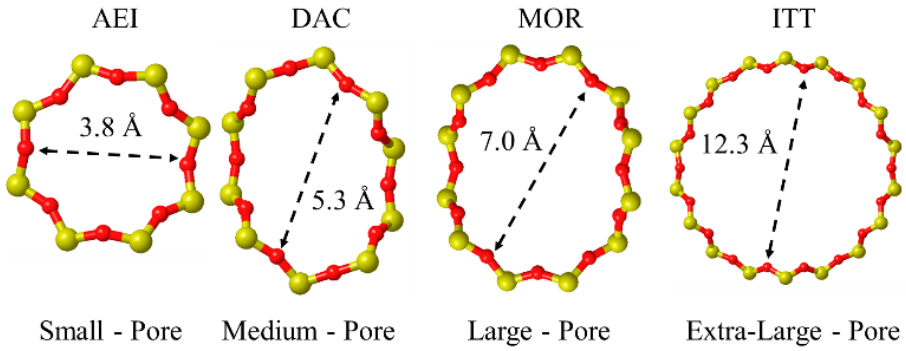

Figure 1.5. Pore diameter of several zeolite frameworks, measures taken from IZA database.[24]

Zeolites can also be considered structures in which a fraction of the tetravalent T atoms has been substituted by the trivalent Al in silicates, or the pentavalent P by the tetravalent Si in AlPOs. For silicates, this substitution produces a negative charge on the AlO_4^- unit that must be compensated with a cation. For AlPOs, substitution of a P^{5+} ion with a Si^{4+} also leaves an AlO_4^- unit uncompensated and generates a negative charge that requires to be

compensated, yielding the so-called silicoaluminophosphates (SAPOs). If the compensating cation is a proton, H^+, a Brønsted acid site (Figure 1.6 a and b) is generated. Likewise, if the compensating cation is a metal it produces Lewis acid sites. According to Lowestein's rule, there cannot exist Al-O-Al bonds in any chemical composition of zeolite frameworks, nor silicates, nor AlPOs, because of their instability caused by an increase in kinetic electron energy.[30,31] This fact implies that the Si/Al ratio ranges from 1 to infinity. For silicates, the incorporated Al atoms must be stabilized by the existence of Si-O-Al-O-Si moieties that avoid the repulsive interaction of adjacent AlO_4^- units. Meanwhile for AlPOs they are alternated with PO_4^+ units that compensate the charge (Figure 1.6 b and d).

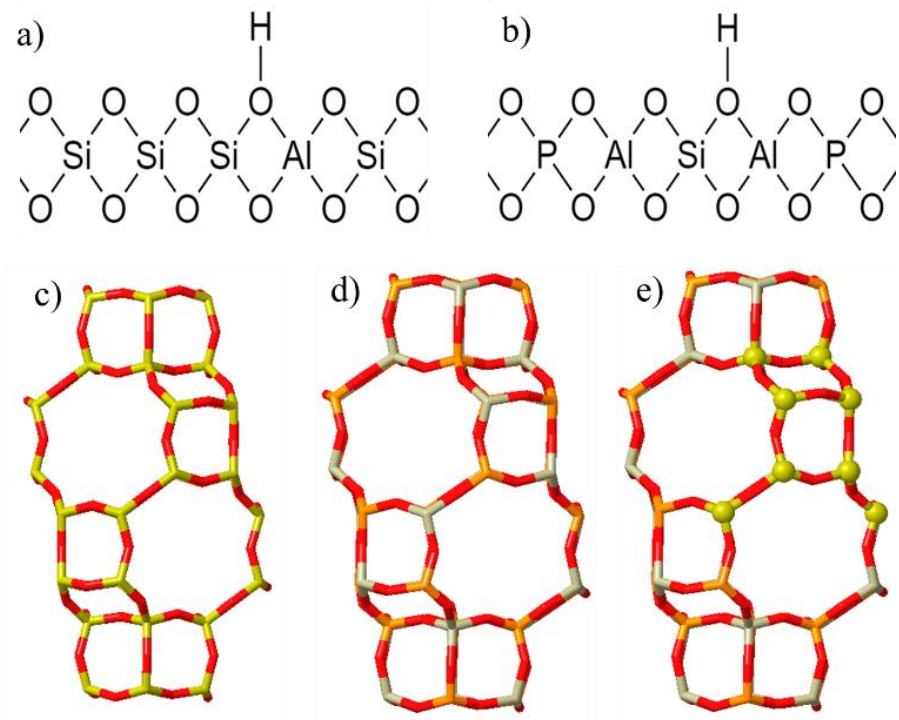

Figure 1.6. Illustration of Brønsted acid site in a) silicate and b) SAPO. Same framework with different chemical composition c) silicate d) AlPO e) AlPO with silicon island. Si atoms are depicted with yellow color, P orange, Al grey, O red.

When Si^{4+} is introduced in AlPOs to create SAPOs by substituting a P^{5+} atom, there may appear regions in the framework where silicon aggregates because of the stability of Si-O-Si bonds forming silicon islands.[32] The arrangement of these regions neglects the presence of acid sites, either Brønsted or Lewis, because of the framework distribution in two neutral charge stable parts, one AlPO part and one silica part (see Figure 1.6d). The crucial point to avoid the formation of silicon isles has been found in zeolite synthesis. The synthesis of zeolites is usually carried out in the presence of organic structure directing agents (OSDAs) or templates which have a significant influence on the size and shape of pores and channel systems.[33–38] During crystallization, they remain trapped inside the cavities stabilizing the zeolite framework mainly through van der Waals interactions. Commonly used OSDAs such as tetraethylammonium, tetraethylphosphonium or pyridine include a positive charge that is set to compensate the negatively charged fragments of the framework, AlO_4^-. Additionally, OSDAs are used to direct these fragments towards specific crystallographic positions and particularly in SAPO synthesis, their main goal is to disperse the Si^{4+} around the entire framework impeding the formation of silicon islands. After synthesis, the OSDA is usually removed by calcination, and a proton compensates the negative charge left in the calcined material. Zeolite synthesis and OSDA behavior are studied in depth at Chapter 6.

Finally, frameworks that can be synthesized with both compositions, silica and AlPO, may not present the same catalytic activity or selectivity towards the same chemical reaction. They differ in the three important aspects that modulate their fundamental catalytic properties, activity, selectivity and deactivation. The acid strength of the Brønsted acid sites is higher for silicates, therefore the activity will vary when framework composition changes.[39,40] Besides, Al-O-P bonds are more flexible than Si-O-Si bonds conferring a higher flexibility to AlPOs that may translate into a better adaptation to the catalytic substrate and a better diffusion of products altering the selectivity[41,42] or an easier adaptation to bulky non-reactive sub-products that end up blocking the catalyst having an impact on catalyst deactivation.[29,43] These differences are covered with further detail in Chapter 3.

1.4 Motivation.

To design an efficient zeolite catalyst is not an easy task, it needs of a complete understanding of the reaction mechanism to catalyze and this is not always achievable. As catalysts performance is determined by the microscopic molecular processes occurring at its active sites, to set up a direct relation with the macroscopic properties observed linking zeolite structure and product selectivity is usually an arduous task. Moreover, spectator species and secondary products that do not participate actively in the main reaction are many times present in considerable amounts including a further complication to the process. Because of the multitude of problems that are encountered during the research process, heterogeneous catalysis has become a multidisciplinary field in which the combination of several predictive techniques, synthesis, characterization and reaction is mandatory. Spectroscopic techniques are commonly applied in characterization of solid catalysts, but interpreting the results is not always straightforward. That is why zeolites require special *in situ* and *operando*[44] conditions to be properly characterized. Consequently, several specific catalytic cells have been developed to allow IR, Raman and NMR experiments under relevant conditions.[45–48] However, the short lifetime of reaction intermediates makes their detection very difficult.[49] That is why computational chemistry has aroused as a relevant tool for the study of catalytic processes because it operates at the molecular level making possible to study the elementary steps and identify the rate determining ones for a specific reaction, especially after the development and implementation of density functional theory (DFT). Since 1990s more accurate functionals, methods, and efficient computer codes have been developed increasing its popularity among chemists. DFT is extensively explained in Chapter 2.

Our research has been focused on chemical reactions of industrial relevance that are driven by zeolites as their heterogeneous catalysts. We devoted our efforts to perform computational studies of their mechanisms looking for an optimization in their catalytic performance.

The first process investigated is the methanol to olefins reaction presented in Chapter 3. Short chain olefins, $C_2^=$, $C_3^=$ and $C_4^=$, are highly demanded products in petrochemical and pharmaceutical industries because they serve as building blocks for more complex value-added molecules such as ethylbenzene and other alkylated molecules. As short olefin manufacturing is essentially dependent on fossil resources, their production is limited and expected to become unaffordable as reserves extinguish. Moreover, environmental concerns about working with fossil resources have to be added on top of the need of looking for an alternative source for the production of short chain

olefins. Biomass has emerged as an alternative feedstock of methanol that can be converted into olefins through an environmentally friendly process catalyzed by zeolites that does not carry any CO_2 production associated. We focused on studying by DFT methods how the different zeolite cavities that are able to catalyze this process influence reaction selectivity towards each short chain olefin, $C_2^=$, $C_3^=$ or $C_4^=$.

In Chapter 4, we present the study the diethylbenzene transalkylation with benzene reaction. Production of alkylaromatics is a crucial process in the modern chemical industry which is catalyzed by zeolites. They are well-established precursors for many important intermediates widely used in chemical and pharmaceutical industries. Ethylbenzene is one of the industrial alkylaromatics with a higher production capacity worldwide that is mostly consumed in the manufacture of polystyrene, styrene-acrylonitrile resin, and other products. Benzene alkylation with light olefins and alcohols catalyzed by acid zeolites has been stablished as the main way of industrial production for alkylaromatics. The industrial alkylation process inevitably produces undesired polyalkylated byproducts with lower added value. From the non-desired mixture of secondary products, diethylbenzene is the most common one, also a considerable amount of ethene is observed depending on the zeolite catalyst employed. To improve ethylbenzene selectivity, the current industrial production combines two reaction processes: alkylation of benzene with ethene then followed by ethylbenzene separation and transalkylation of the polyethylated byproducts with benzene to increase the global yield of ethylbenzene by recycling the side products already obtained. In this case, our computational efforts were focused on finding the optimal catalyst that increases ethylbenzene selectivity hindering the production of any other chemical.

Finally, in chapter 5, we present two different studies about zeolite synthesis with OSDAs. The first one focuses on the templating effect of different OSDAs that determines the synthesis success for the specific CHA framework and rationalizes the Si/Al ratio obtained for different experimental samples. The second one presents a theoretical study about Al positioning in AEI cavities by OSDAs with different shape using a combination of static DFT calculations and "Ab Initio Molecular Dynamics" simulations.

1.5 References

1. Wilkinson, A. D. M. and A. *IUPAC. Compendium of Chemical Terminology, 2nd ed. (the 'Gold Book')*. (1997). doi:10.1351/goldbook.C00876.

2. Masel, R. I. *Chemical Kinetics and Catalysis*. (2001).

3. Lindström, B. & Pettersson, L. J. A brief history of catalysis. *Cattech* **7**, 130–138 (2003).

4. Martínez-Franco, R., Li, Z., Martínez-Triguero, J., Moliner, M. & Corma, A. Improving the catalytic performance of SAPO-18 for the methanol-to-olefins (MTO) reaction by controlling the Si distribution and crystal size. *Catal. Sci. Technol.* **6**, 2796–2806 (2016).

5. Eyring, H. The activated complex in chemical reactions. *J. Chem. Phys.* **3**, 63–71 (1935).

6. Laidler, K. J. & King, M. C. The development of transition-state theory. *J. Phys. Chem.* **87**, 2657–2664 (1983).

7. Iwamoto, M. Air pollution abatement through heterogeneous catalysis. *Stud. Surf. Sci. Catal.* **130 A**, 23–47 (2000).

8. Armor, J. N. Environmental Catalysis. *Appl. Catal. B Env.* **1**, 221–256 (1992).

9. Introduction to Catalysis. *Concepts Mod. Catal. Kinet. John Wiley Sons* 1–21 (2005).

10. Amghizar, I., Vandewalle, L. A., Van Geem, K. M. & Marin, G. B. New Trends in Olefin Production. *Engineering* **3**, 171–178 (2017).

11. Ren, T., Daniëls, B., Patel, M. K. & Blok, K. Petrochemicals from oil, natural gas, coal and biomass: Production costs in 2030-2050. *Resour. Conserv. Recycl.* **53**, 653–663 (2009).

12. Blaser, H. U., Steiner, H. & Studer, M. Selective catalytic hydrogenation of functionalized nitroarenes: An update. *ChemCatChem* **1**, 210–221 (2009).

13. Tolman, C. A. & Herron, N. The selective catalytic oxidation of hydrocarbons in zeolites under mild conditions. *Catal. Today* **3**, 235–243 (1988).

14. Liu, C. C., Ramu, R., Chan, S. I., Mou, C. Y. & Yu, S. S. F. Chemistry in confined space: A strategy for selective oxidation of hydrocarbons with high catalytic efficiencies and conversion yields under ambient conditions. *Catal. Sci. Technol.* **6**, 7623–7630 (2016).

15. Radzicka, A. & Wolfenden, R. A proficient enzyme. *Science (80-.).* **267**, 90–93 (1995).

16. Shevelev, I. V. & Hübscher, U. The 3′-5′ exonucleases. *Nat. Rev. Mol. Cell Biol.* **3**, 364–375 (2002).

17. Taylor, H. S.; Armstrong, E. F. A Theory of the Catalytic Surface. *Proc. R. Soc. Lond. Ser. Contain. Pap. Math. Phys. Character* **108**, 105–111 (1925).

18. Ichikawa, S. Volcano-shaped curves in heterogeneous catalysis. *Chem. Eng. Sci.* **45**, 529–535 (1990).

19. P. W. Atkins. *Physical Chemistry*. (1990).

20. Ertl, G. Reactions at well-defined surfaces. *Surf. Sci.* **299**–**300**, 742–754 (1994).

21. Baxter, R. J. & Hu, P. Insight into why the Langmuir-Hinshelwood mechanism is generally preferred. *J. Chem. Phys.* **116**, 4379–4381 (2002).

22. McCusker, L. B., Liebau, F. & Englehardt, G. Nomenclature of structural and compositional characteristics of ordered microporous and mesoporous materials with inorganic hosts (IUPAC recommendations 2001): Physical chemistry Division commision on colloid and surface chemistry including catalysis. *Microporous Mesoporous Mater.* **58**, 3–13 (2003).

23. Wilson, S. T., Lok, B. M., Messina, C. A., Cannan, T. R. & Flanigen, E. M. Aluminophosphate Molecular Sieves : A New Class of. *J. Am. Chem. Soc.* **104**, 1146–1147 (1982).

24. Baerlocher, C.; McCusker, L. B. Database of Zeolite Structures.

25. Katzer, J. R. Atlas of zeolite structure types. W. M. Meier, and D. H. Olson, 2nd rev. ed., Butterworth, 1987. *AIChE J.* **35**, 875–875 (1989).

26. Degnan, T. F. The implications of the fundamentals of shape selectivity for the development of catalysts for the petroleum and petrochemical industries. *J. Catal.* **216**, 32–46 (2003).

27. Marcilly, C. R. Where and how shape selectivity of molecular sieves operates in refining and petrochemistry catalytic processes. *Top. Catal.* **13**, 357–366 (2000).

28. Gao, S. *et al.* Cavity-controlled diffusion in 8-membered ring molecular sieve catalysts for shape selective strategy. *J. Catal.* **377**, 51–62 (2019).

29. Ghysels, A. *et al.* Shape-Selective Diffusion of Olefins in 8-Ring Solid Acid Microporous Zeolites. *J. Phys. Chem. C* **119**, 23721–23734

(2015).

30. Larin, A. V. The Loewenstein rule: The increase in electron kinetic energy as the reason for instability of Al-O-Al linkage in aluminosilicate zeolites. *Phys. Chem. Miner.* **40**, 771–780 (2013).

31. Loewenstein, W. The Distribution of Aluminum in the Tetrahedra of Silicates and Aluminates. *Am. Miner.* **39**, 92–96 (1954).

32. Martínez-Franco, R., Moliner, M. & Corma, A. Direct synthesis design of Cu-SAPO-18, a very efficient catalyst for the SCR of NOx. *J. Catal.* **319**, 36–43 (2014).

33. Cundy, C. S. & Cox, P. A. The hydrothermal synthesis of zeolites: Precursors, intermediates and reaction mechanism. *Microporous Mesoporous Mater.* **82**, 1–78 (2005).

34. Cundy, C. S. & Cox, P. A. The hydrothermal synthesis of zeolites: History and development from the earliest days to the present time. *Chem. Rev.* **103**, 663–701 (2003).

35. Davis, M. E. & Lobo, R. F. Zeolite and Molecular Sieve Synthesis. *Chem. Mater.* **4**, 756–768 (1992).

36. Martens, J. A. *et al.* Simple synthesis recipes of porous materials. *Microporous Mesoporous Mater.* **140**, 2–8 (2011).

37. Rimer, J. D.; Fedeyko, J. M.; Vlachos, D. G.; Lobo, R. F. Silica Self-Assembly and Synthesis of Microporous and Mesoporous Silicates. *Chem. – Eur. J.* **12**, 2926–2934 (2006).

38. Martínez, C. & Corma, A. Inorganic molecular sieves: Preparation, modification and industrial application in catalytic processes. *Coord. Chem. Rev.* **255**, 1558–1580 (2011).

39. Wang, C.-M., Wang, Y.-D., Du, Y.-J., Yang, G. & Xie, Z.-K. Similarities and differences between aromatic-based and olefin-based cycles in H-SAPO-34 and H-SSZ-13 for methanol-to-olefins conversion: insights from energetic span model. *Catal. Sci. Technol.* **5**, 4354–4364 (2015).

40. Bleken, F. *et al.* The Effect of Acid Strength on the Conversion of Methanol to Olefins Over Acidic Microporous Catalysts with the CHA Topology. *Top. Catal.* **52**, 218–228 (2009).

41. Kang, J. H. *et al.* Further Studies on How the Nature of Zeolite Cavities That Are Bounded by Small Pores Influences the Conversion of Methanol to Light Olefins. *ChemPhysChem* **19**, 412–419 (2018).

42. Kang, J. H., Alshafei, F. H., Zones, S. I. & Davis, M. E. Cage-Defining

Ring: A Molecular Sieve Structural Indicator for Light Olefin Product Distribution from the Methanol-to-Olefins Reaction. *ACS Catal.* **9**, 6012–6019 (2019).

43. Cnudde, P. *et al.* Light Olefin Diffusion during the MTO Process on H-SAPO-34: A Complex Interplay of Molecular Factors. *J. Am. Chem. Soc.* **142**, 6007–6017 (2020).

44. Bañares, M. A. Operando methodology: Combination of in situ spectroscopy and simultaneous activity measurements under catalytic reaction conditions. *Catal. Today* **100**, 71–77 (2005).

45. Bordiga, S., Lamberti, C., Bonino, F., Travert, A. & Thibault-Starzyk, F. Probing zeolites by vibrational spectroscopies. *Chem. Soc. Rev.* **44**, 7262–7341 (2015).

46. Ryczkowski, J. IR spectroscopy in catalysis. *Catal. Today* **68**, 263–381 (2001).

47. Chua, Y. T., Stair, P. C., Nicholas, J. B., Song, W. & Haw, J. F. UV Raman spectrum of 1,3-dimethylcyclopentenyl cation adsorbed in zeolite H-MFI. *J. Am. Chem. Soc.* **125**, 866–867 (2003).

48. Sánchez-Sánchez, M. & Blasco, T. Investigation on the nature of the adsorption sites of pyrrole in alkali-exchanged zeolite Y by nuclear magnetic resonance in combination with infrared spectroscopy. *J. Am. Chem. Soc.* **124**, 3443–3456 (2002).

49. Xu, S. *et al.* Direct Observation of Cyclic Carbenium Ions and Their Role in the Catalytic Cycle of the Methanol-to-Olefin Reaction over Chabazite Zeolites. *Angew. Chemie Int. Ed.* **52**, 11564–11568 (2013).

Chapter 2

Methods and Models

2.1 Electronic Structure Methods.

During the course of this Chapter, we describe the theoretical basis of each calculation method that has been used for this work, with special concern for the description of the fundamental principles that allow us to describe the motion of electrons using the Quantum Mechanics principles. In the last section of the Chapter, all kind of models studied are depicted and detailed.

2.1.1 Introduction to the Basics.

In quantum physics, the mathematical description of the quantum state of an isolated quantum system is given by the wave function Ψ, which is a complex-valued probability amplitude, and the probabilities for the possible results of measurements made on the system can be derived from it. Then, it is necessary to start by the fundamental time-independent, non-relativistic Schrodinger equation:

$$\hat{H}|\Psi\rangle = \mathrm{E}|\Psi\rangle \quad (2.1)$$

Where the Hamiltonian operator $\hat{H}$ corresponds to the total energy of a system, accounting for both kinetic and potential energy. When solving this equation, the motion of the electrons can be decoupled from the nuclei using the Born-Oppenheimer approximation. Because of the greater mass of nuclei they move very slowly, thus, when compared with the fast motion of electrons, they can be seen as fixed points and their kinetic energy can be set to zero meanwhile the repulsion term is set to a constant. Then, we end up with the electronic Hamiltonian:

$$\hat{H}_{elect} = -\frac{1}{2}\sum_{i=1}^{N}\nabla_i^2 - \sum_{i=1}^{N}\sum_{A=1}^{N}\frac{Z_A}{r_{iA}} + \sum_{i=1}^{N}\sum_{j>i}^{N}\frac{1}{r_{ij}} = \hat{T} + \hat{V}_{Ne} + \hat{V}_{ee} \quad (2.2)$$

where $\hat{T}$ is the kinetic energy operator, $\hat{V}_{Ne}$ is the attractive potential between the nuclei and electrons set to a constant and $\hat{V}_{ee}$ is the electron-electron interaction term.

With Born-Oppenheimer approximation we end up with a simpler Hamiltonian, however, the Schrödinger equation cannot be solved for multi-electron systems. The general approach to solve this problem consists of starting with a guess of the wave function Ψ and systematically approximate it to the ground state wave function using the electronic Hamiltonian. This approach is based on the variational principle, which states that the energy calculated with equation 2.3 is an upper bound to the true energy of the system ground state. Thus, the objective is to minimize the functional $E[\Psi]$:

$$E = \frac{\langle \Psi | \hat{H} | \Psi \rangle}{\langle \Psi | \Psi \rangle} \quad (2.3)$$

The first accurate approach to solve this problem was the Hartree-Fock method. In this method, the wave function of an *N*-electron system is approximated as an antisymmetrized product of *N* one-electron wave functions χ_i called spin-orbitals that can be arranged in a Slater determinant:

$$\Phi_{SD} = \frac{1}{\sqrt{N!}} \begin{vmatrix} \chi_1(x_1) & \chi_1(x_1) & \cdots & \chi_N(x_1) \\ \chi_1(x_1) & \chi_1(x_1) & \cdots & \chi_N(x_1) \\ \vdots & \vdots & & \vdots \\ \chi_1(x_1) & \chi_1(x_1) & \cdots & \chi_N(x_1) \end{vmatrix} \quad (2.4)$$

The arrangement of wave functions into a determinant is very convenient because determinants are antisymmetric with respect to exchange of rows and columns, therefore they fulfil Pauli's exclusion principle. Minimizing equation 2.3 with respect to the spin-orbitals defined in equation 2.4 and respecting the constraint that these spin-orbitals remain orthonormal, the Hartree-Fock equation 2.5 is obtained:

$$\hat{f}_i \chi_i = \epsilon_i \chi_i \quad (2.5)$$

where $\hat{f}_i$ is the one electron Fock operator:

$$\hat{f}_i = -\frac{1}{2}\nabla_i^2 - \sum_{A=1}^{M} \frac{Z_A}{r_{iA}} + V^{HF}(i) \quad (2.6)$$

V^{HF} refers to Hartree-Fock potential which represents the average potential on the electron *i* caused by the presence of the remaining *N-1* electrons in the system. The Hartree-Fock potential v^{HF} (equation 2.7) includes the coulomb operator $\hat{J}_j$ which represents the Coulombic potential experienced by an electron at position x_1 due to the average distribution of another electron in spin-orbital *j* (equation 2.8) and the second operator, $\hat{K}_j$, with no classical interpretation, which accounts for the effect of exchanging two electrons of parallel spin and it is called the exchange contribution to the Hartree energy,

that arises from the antisymmetric nature of the Slater determinant used to expand the wave function (equation 2.9):

$$(2.7)\quad v^{HF}(x_1) = \sum_{j}^{N} \left(\hat{J}_j(x_1) - \hat{K}_j(x_1) \right)$$

where,

$$(2.8)\quad \hat{J}_j(x_1) = \int \left| x_j(x_2) \right|^2 \frac{1}{r_{12}} dx_2$$

and

$$(2.9)\quad \hat{K}_j(x_1)\chi_i(x_1) = \int x_j^*(x_2) \frac{1}{r_{12}} \chi_i(x_2) dx_2 \chi_j(x_1)$$

As can be seen from equations 2.8 and 2.9 both operators depend on the spin-orbitals. Thus, the Hartree-Fock equation has to be solved by the self-consistent field (SCF) method. It consists on starting with a first guess of the spin-orbitals to construct the initial coulomb, $\hat{J}_j$, and exchange, $\hat{K}_j$, operators to solve the eigenvalue equations obtaining a new set of spin-orbitals. The new set of spin-orbitals is used again to construct the operators and solve again the Hartree Fock equations. This procedure is repeated iteratively until the input and output orbitals differ by less than a threshold previously defined.

However, the Hartree-Fock method does not succeed in describing all the possible interactions that an electron presents during its motion. That is why the energy of the Hartree-Fock ground state, E^{HF}, is always higher than the energy of the real ground state of the system E_0. The difference between the Hartree-Fock energy and the energy of the ground state of the system is called correlation energy E_c^{HF}.

$$(2.10)\quad E_c^{HF} = E_0 - E_{HF}$$

The correlation energy can be divided into two components. First, the static correlation energy that arises because the Slater determinant is just an approximation to the exact wave function. It describes the exchange effect but it omits the Coulomb correlation. Second, the dynamic correlation energy, related to the instantaneous repulsion of electrons, which is not included in the Hartree-Fock formalism because the studied electron only feels the average repulsion caused by the rest *N-1* electrons from the system.

The Hartree-Fock method described accurately a very important part of the physics. However, nowadays it is barely used in real application because it lacks an accurate description of the electron correlation that wards it off from providing chemical accuracy.

Nonetheless, we have committed a couple pages to this method because it constitutes the basis of most quantum mechanical wave function based methods. In these days, modern methods such as Configuration Interactions, Coupled Cluster and Møller Plesset Perturbation theory are focused on finding better corrections to the electron correlation energy. Post-Hartree-Fock methods will not be discussed in this work but meticulous discussions can be found in the literature[1,2].

2.1.2 Density Functional Theory.

In the previous section we proved that the wave function enables us to obtain all the information about the state of the system using Quantum Mechanics. However, it presents different problems such as the exponential wall[3] caused by the dependence of the wave function on *4N* variables, three spatial and one spin for each electron. In addition, a wave function cannot be measured meanwhile other properties of the system such as the electron density are observables that can be measured by X-ray diffraction.

Because of these problems, electron density began to be considered as a fundamental quantity that enabled the access to the information of a quantum system in the work of Thomas and Fermi.[4–7] They defined an imaginary uniform electron gas model and treated the nuclear-electron and electron-electron interactions in a classical manner deriving equation 2.11 for the energy as a function of the electron density $\rho(\vec{r})$:

$$(2.11)\quad E[\rho(r)] = \frac{3}{10}(3\pi^2)^{2/3}\int \rho^{5/3}(r)dr - Z\int \frac{\rho(r)}{r} + \frac{1}{2}\iint \frac{\rho(r_1)\rho(r_2)}{r_{12}}dr_1 dr_2$$

The electron density is defined as the measure of the probability of an electron being present at an infinitesimal element of space surrounding any given point. This means that this system property used to calculate the energy is at the same time a function of the wave function.

$$(2.12)\quad \rho(r) = N\int |\Psi(r\sigma, x_2, \dots, x_N)|^2\, d\sigma dx_2, \dots, dx_N$$

Thus, this method turns the calculated energy to a functional of the electronic density. In mathematics, a function of a function is called a functional and hence the name "Density Functional Theory".

The starting method presented several limitations[4] until a useful Density Functional Theory formalism was set by Hohenberg and Kohn with the two theorems published in a paper entitled "Inhomogeneous Electron Gas" in 1964.[8] The Hohenberg-Kohn theorems relate to any system consisting of electrons moving under the influence of an external potential $V_{ext}(r)$.

The first theorem can be stated as, "the external potential $V_{ext}(r)$, and hence the total energy, is a unique functional of the electron density $\rho(r)$". Therefore, the energy functional $E[\rho(r)]$ can be written in terms of the external potential $V_{ext}(r)$ in the following way,

$$E[\rho(r)] = \int \rho(r) v_{ext}(r) dr + F[\rho(r)] \quad (2.13)$$

where $F[\rho(r)]$ is an unknown, but otherwise universal functional of the electron density $\rho(r)$ only. Correspondingly, a Hamiltonian for the system can be written such that the electron wave function Ψ that minimizes the expectation value gives the ground state energy,

$$E[\rho(r)] = \langle \Psi | \hat{H} | \Psi \rangle \quad (2.14)$$

The Hamiltonian can be written using two terms as in equation 2.15,

$$\hat{H} = \hat{F} + \hat{V}_{ext} \quad (2.15)$$

where $\hat{F}$ is the universal electronic Hamiltonian that is valid for any system with any number of electrons and consists of a kinetic energy operator $\hat{T}$ and an interaction operator $\hat{V}_{ee}$,

$$F[\rho] = T[\rho_0] + E_{ee}[\rho_0] \quad (2.16)$$

The electron operator $\hat{F}$ is the same for all N-electron systems, therefore $\hat{H}$ is completely defined by the number of electrons N and the external potential $V_{ext}(r)$.

Summarising, the first Hohenberg-Kohn theorem is the formal proof that the electron density can be used to determine the properties of a particular quantum state and two different external potentials cannot produce the same ground state electron density.

The second theorem can be stated as follows, "the groundstate energy can be obtained variationally: the density that minimizes the total energy is the exact groundstate density". The proof of the second theorem is also straightforward. As just shown, $\rho(r)$ determines $V_{ext}(r)$. Then, N and $V_{ext}(r)$ determine $\hat{H}$, therefore determining the wave function Ψ. This ultimately means that Ψ is a functional of $\rho(r)$, and so the expectation value of $\hat{F}$ is also a functional of $\rho(r)$.

$$F[\rho(r)] = \langle \Psi | \hat{F} | \Psi \rangle \quad (2.17)$$

A density that is the ground state of some external potential is known as v-representable. Following from this, a v-representable energy functional $E_v\ [\rho(r)]$ can be defined in which the external potential $V_{ext}(r)$ is unrelated to another density $\rho'(r)$ different from the ground state one.

$$E[\rho'(r)] = \int \rho'(r) v_{ext}(r) dr + F[\rho'(r)] \quad (2.18)$$

By applying the variational principle to this trial electron density $\rho'(r)$, an energy value that is an upper bound to the true energy of the ground state will be obtained.

$$E_v[\rho'(r)] > E_v[\rho(r)] \quad (2.19)$$

Thus, the energy can be thought of as consisting of two parts: one dependent and one independent of the system:

$$E[\rho_0] = \int \rho_0(r) V_{Ne} dr + F[\rho] \quad (2.20)$$

where the first term of the right hand is system-dependent. The functional form of the second term, $F[\rho]$, is not known and the main goal of modern density functional theory is to find better approximations to this quantity.

2.1.3 The Kohn-Sham Approach.

The two Kohn-Sham theorems stated in the previous section constructed the basis for the development of the modern DFT. Despite their novelty, none of them provided any clue on how to find the ground state density of a system. This section describes how Kohn and Sham approached this problem.

The Kohn-Sham approach centres on mapping the full interacting system with the real potential onto a fictitious non-interacting system where the electrons move within an effective "Kohn-Sham" single-particle potential $V_{KS}(r)$. The Kohn-Sham method is still exact since it yields the same ground state density as the real system, but greatly facilitates the calculation.

The idea of Kohn and Sham was to set up a system where the kinetic energy could be determined exactly, since this was a major problem in Thomas-Fermi theory. This was achieved by invoking a non-interacting system of electrons confined in an effective potential V_s. The corresponding ground state wave function Ψ_{KS} for this type of system is given exactly by a Slater determinant of single-particle orbitals $\varphi_i(r_i)$,

$$\Psi_{KS} = \frac{1}{\sqrt{N!}} det[\psi_1(r_1)\psi_2(r_2) \dots \psi_N(r_N)] \quad (2.21)$$

This was observed by Kohn and Sham who proposed the idea of using the following Hamiltonian for a non-interacting reference system:

$$\widehat{H} = -\frac{1}{2}\sum_{i}^{N}\nabla_i^2 + \sum_{i}^{N} V_s(r_i) \quad (2.22)$$

Notice that this Hamiltonian does not contain any electron-electron interaction term, and so, it is the true Hamiltonian of the non-interacting system. Thus, the spin orbitals can be obtained in a similar manner to the HF method as:

$$\left(-\frac{1}{2}\nabla^2 + V_s(r)\right)\phi_i = \epsilon_i\phi_i \quad (2.23)$$

where

$$\hat{f}^{ks} = -\frac{1}{2}\nabla^2 + V_s(r) \quad (2.24)$$

is the Kohn-Sham one-electron operator. The kinetic energy of the real system is not the same as that of the fictitious system,

$$T_s[\rho(r)]\sum\left\langle\Psi\left|-\frac{1}{2}\nabla^2\right|\Psi\right\rangle \quad (2.25)$$

but the underlying idea is to split up the energy into all that can be calculated exactly and dump the rest into one term, that is, approximate the unknown contributions. So the universal functional $F[\rho(r)]$ was decomposed in three different terms. The first two are known exactly and correspond to the kinetic energy of an electron in a non-interacting system and the Coulomb interaction, both constituting the majority of the energy, and the third is a small unknown quantity E_{xc} called the exchange-correlation energy:

$$F[\rho(r)] = T_s[\rho(r)] + J[\rho(r)] + E_{xc}[\rho(r)] \quad (2.26)$$

This term contains the non-classical contributions from the self-interaction corrections, exchange and correlation, and the difference of the kinetic energy between the real and the fictitious system. Minimization of the former expression under the constraint that the Kohn-Sham spin-orbitals remain orthogonal results in the Kohn-Sham equations which are solved self-consistently very similar to Hartree-Fock method:

$$\left|-\frac{1}{2}\nabla^2 + \int\frac{\rho(r')}{|r-r'|}dr' + V_{xc}(r) - \sum\frac{Z_A}{|r-R_A|}\right|\phi_i(r) = \epsilon_i\phi_i \quad (2.27)$$

The Kohn-Sham formulation succeeds in transforming the *N*-body problem into *N* single-body problems, each coupled via the Kohn-Sham effective potential. It is worth noting that formally there is no physical interpretation of these single-particle Kohn-Sham eigenvalues and orbitals: they are merely

mathematical artefacts that facilitate the determination of the true ground state density. The exception is the highest occupied state, for which it can be shown that the eigenvalue corresponding to the highest occupied state yields the ionisation energy of the system.[9]

2.1.4 Approximations to the Exchange-Correlation Functional.

With the Kohn-Sham approach, a fully interacting system is mapped onto an auxiliary non-interacting system that yields the same ground state density. But the exchange correlation energy term, E_{xc}, remains unknown.

As mentioned earlier, the Kohn-Sham kinetic energy is not the true kinetic energy. This can be used to define formally the exchange-correlation energy as:

$$E_{xc}[\rho(r)] = T[\rho(r)] - T_s[\rho(r)] + E_{ee}[\rho(r)] - E_H[\rho(r)] \quad (2.28)$$

where $T_s[\rho(r)]$ and $E_{ee}[\rho(r)]$ are the exact kinetic and electron-electron interaction energies respectively. Physically, this term can be interpreted as containing the contributions of correlation and exchange to the system energy.

The definition above ensures that the Kohn-Sham formulation is exact. However, the actual form of E_{xc} is not known and approximate functionals based upon the electron density must be introduced to describe this term.

There are two common approximations. The local density approximation (LDA) is the simplest approximation and was introduced in 1965 by Kohn and Sham in the paper "Self-Consistent Equations Including Exchange and Correlation Effects".[10] This approximation is based on the homogeneous electron gas model because it is the only system for which the exchange and correlation functionals are known and it assumes that E_{xc} at a point r is simply equal to the E_{xc} of a uniform electron gas that has the same density at the point r.

It consists of expressing the exchange energy E_x as follows:

$$E_x^{LDA}[\rho(r)] = -\frac{3}{4}\left(\frac{3}{\pi}\right)^{1/3} \int \rho(r)^{4/3} dr \quad (2.29)$$

The most common parametrization in use for *Ex* is that of Perdew and Zunger[11], which is based upon the Ceperley and Alder quantum Monte Carlo calculations[12] on homogeneous electron gases at various densities. An example of these functionals is the VWN functional developed by Vosko, Wilk and Nusair in 1980.[13]

LDA ignores corrections to E_{xc} due to non-homogeneities in the electron density about r. Despite being a relentless approximation, LDA has proven to be successful because it respects the sum rule for the exchange-correlation hole[14], that refers to the fact that probability of finding an electron at a certain position (r_1) given that there is an electron at another position (r_2) decreases

when the distance between the two electrons diminishes. The sum rule ensures that exactly one electron is excluded from the immediate vicinity of a given electron at point r. However, the LDA is known to overbind, particularly in molecules.

In order to describe the non-homogeneity of the true electron density the next step towards a more robust functional was to include the gradient of the electron density $\nabla\rho(r)$. This improvement was introduced by Becke, Perdew, Langreth, and Parr in the 1980s and is called generalized gradient approximation (GGA).[15,16]

In GGA, the exchange-correlation term E_{xc} is also split into the exchange E_x and correlation E_c contributions. The exchange term is expressed as:

$$(2.30)\quad E_x^{GGA}[x,\rho] = \int \rho^{4/3} F(x)\, dr$$

where the argument x of the function $F(x)$ is the reduced density gradient defined as:

$$(2.31)\quad x = \frac{|\nabla\rho(r)|}{\rho^{4/3}(r)}$$

The correlation part is much more complicated and is usually derived with Monte Carlo techniques. As GGA functionals offer an acceptable compromise between accuracy and computational cost for the solid periodic systems used in this work with Vienna ab-initio simulation package (VASP) software, we have used the Perdew-Burke-Ernzernhof (PBE) functional for which the exchange contribution is given by,

$$(2.32)\quad E_x^{PBE} = -\int \rho(r)^{4/3}\left[\frac{3}{4}\left(\frac{3}{\pi}\right)^{1/3} + \frac{\mu x^2}{1+\mu x^2/k}\right] dr$$

and also for dynamic calculations with CP2K software we used its revised version, the revPBE functional.[17]

The last two clear advances in DFT are probably the inclusion of the kinetic energy density, which resulted in the so-called meta-GGA functionals and the inclusion of a fraction of the Hartree-Fock exact exchange energy to generate the family of hybrid functionals. In this work we have used the M062X hybrid functional with a 54% Hartree-Fock exchange part.[18]

The step by step improvement of DFT accuracy was called the Jacob's ladder of approximations to the exact exchange-correlation functional by Perdew and Schmidt.[19] This analogy symbolizes the idea of ascending from the roughest approximations towards the "heaven" of chemical accuracy, ~1 kcal/mol, where exact exchange and exact partial correlation are known.

2.1.5 Dispersion Corrections.

The next step on the advance towards chemical accuracy for DFT came during the first decade of the 21st century. The problem presented by density functionals that did not properly capture the long range dispersion interactions, which is a correlation phenomenon, such as van der Waals forces because of their asymptotic $1/R^6$ behaviour was addressed by Grimme et al.[20–22] that allowed to include these terms a posteriori. It turned to be a cheap and pragmatic solution that incorporates potentials of the form $-C_6/R^6$ where the C_6 coefficients are pairwise atomic parameters. This approach is known as dispersion-corrected DFT (DFT-D).

The oldest of these approaches is DFT-D2[21] in which the empirical dispersion potential has the form, pairwise atomic C_6/R^6 terms:

$$E^{disp} = -s_6 \sum_{i=1}^{N-1} \sum_{j=i+1}^{N} \left[\frac{C_6^{ij}}{R_{ij}^6}\right] f^{damp}(R_{ij}) \quad (2.33)$$

where C_6 is an empirical parameter, E^{disp} is damped at short range where R_{ij}^6 diverges with a damping function fdamp that varies from 0 to 1 defined as:

$$f^{damp}(R) = \frac{1}{1 - e^{-\alpha(R/R_0 - 1)}} \quad (2.34)$$

which also helps to avoid double-counting of electron correlation effects, since short- to medium-range correlation is included via the density functional.

Grimme's more recent DFT-D3 method presents an improvement with respect to his D2 approach extending the above definition by including higher dispersion orders and novel modifications to the old damping function:

$$E^{disp} = \sum_{AB} \sum_{n=6,8,10} s_n \frac{C_n^{AB}}{r_n^{AB}} f_{d,n}(r_{AB}) \quad (2.35)$$

$$f_{d,n}(r_{AB}) = \frac{1}{1 + 6\left(r_{AB}/\left(s_{r,n} R_0^{AB}\right)\right)^{-\alpha_n}} \quad (2.36)$$

where n are averaged nth-order dispersion coefficient for n = 6, 8, 10 … for the atom pairs AB with inter-nuclear distance r_{AB}. This approach is less empirical than D2 as the coefficients C_6^{AB} are no longer fixed but geometry dependent. Recently, Becke and Johnson presented a new version for the damping function that is designed to be finite, but non-zero, as $R_{AB} \rightarrow 0$. This version of DFT-D was called DFT-D3(BJ). The damping function used in DFT-D3(BJ) is:

$$(2.37)\quad f_{d,n}(r_{AB}) = \frac{s_n r_{AB}^n}{r_{AB}^n + (a_1 R_0^{AB} + a_2)^n}$$

where a_1 and a_2 are adjustable parameters fit for each density functional. DFT-D3 (BJ) generally outperforms the original DFT-D3 version.

In this work, we have used DFT-D3 for calculations carried out with CP2K and DFT-D3(BJ) for calculations carried with VASP unless otherwise specified. In all cases, we have used the default parameters of the above definitions.

2.1.6 Basis Sets.

In quantum chemistry methods, the wave function of the system is mathematically expressed as a linear combination of certain basis functions, which constitute the basis set. Using a complete basis set, any mathematical function can be exactly represented with an infinite number of basis functions. However, this kind of representation is computationally unfeasible because of its enormous amount of variables. Therefore, a finite basis is used as an approximation whose type and size determine the accuracy of the calculation. For calculations on finite systems, basis sets are usually built using atom-centred Gaussian functions. However, for periodic systems wave functions are mathematically described as plane waves in order to preserve the periodicity of the model.

This section covers the atom-centred Gaussian functions used in this work with the software Gaussian 09[23] for gas phase calculations and next section focuses on solid state theory for periodic models and the plane wave formalism used for calculations with VASP software.[24]

Two of the first and simplest basis sets were proposed in 1930 by Slater, giving its own name to the basis set of Slater Type Orbitals (STO)[25] and in 1950 Samuel Francis Boys introduced Gaussian Type Orbitals (GTO)[26], which were later combined to constitute the so-called STO-NG basis, the most common of minimal basis sets[27]:

$$(2.38)\quad \phi_{STO-NG} = \sum_i a_i \varphi_{i,GTO}$$

$\varphi_{i,GTO}$ is a primitive Gaussian function meanwhile the ϕ_{STO-NG} is a contracted one.

In a minimal basis set, the amount of functions used is the minimum to describe the core and valence orbitals of the atoms with no description of any virtual orbitals. As a consequence, a minimal basis set does not describe properly the atoms in a molecular environment and the results obtained are unpolished.

Since valence electrons are the ones that usually participate in chemical bonds, split valence basis sets describe the valence atomic orbitals with more than one

basis function. If the split is composed of two basis functions, the basis set is called double zeta (DZ) and this terminology scales to triple zeta (TZ), quadruple zeta (QZ) and so on depending on the number of basis functions used. The coefficients of each of these functions can be varied causing a change in the size of the orbital and allowing the adjustment to a particular molecular environment. The most common basis sets of this type are Pople and Watchers-Hay basis sets which are expressed with a notation that comprehends type and composition.[28–30] For instance, in this work we have employed the standard 6-31g(d,p)[31,32], in which each core atomic orbital is described by a function with 6 Gaussian primitive functions. Then, as two digits are indicated, the valence atomic orbitals are split in two, each of which is described by two functions. For heavy atoms and hydrogen atoms, a diffuse *d* and a polarization *p* function are included, and *g* stands for Gaussian. The polarization and diffuse functions are employed to provide additional mathematical flexibility for the correct description of the system. Polarization functions are orbitals with higher angular momentum than the ones an atom presents in its ground state and provide the atom with new directions that can accommodate the electron density in cases where it is deformed such as in polarization processes. Diffuse functions are needed when the atomic orbitals reach farther distances from the nuclei due to it having more charge, as in anions, or in the case of weakly bonded systems. They are included generally as an *s* function and a set of *p* functions for each atom of the system, with the exponents obtained variationally for the anion or hydride anion of the corresponding atoms.

2.2 Solid State Calculations.

2.2.1. Reciprocal Space and Bloch's Theorem.

In solid state physics, lattices are described through the "reciprocal space", also called "k-space" which is a useful frame to carry out electronic calculations in solids because not all concepts in material science can be properly represented

in real space. This non-physical definition of space enables the visualization of the results of the Fourier transform of a spatial function whose immediate application is the representation of diffraction phenomena.

The reciprocal space is the Fourier Transform (FT) of the real space and the reciprocal unit cell vectors (a^*, b^*, c^*) are related to the real unit cell vectors (a, b, c) as follows:

$$(2.39)\quad a^* = 2\pi\frac{b \times c}{a(b \times c)},\quad b^* = 2 * \pi\frac{a \times c}{b(a \times c)}, c^* = 2\pi\frac{a \times b}{c(a \times b)}$$

The reciprocal basis vectors present units of inverse of length of the real basis vectors and are orthogonal to them (Figure 2.1). Then, the volume of the reciprocal unit cell defined by this reciprocal basis vectors presents the inverse of the volume of the real unit cell.

The reciprocal space vectors G are given by,

$$(2.40)\quad G = k_1a^* + k_2b^* + k_3c^*$$

where k_i are integers. Figure 2.1 illustrates in a 2-D representation the relations between real space and reciprocal space unit cells and also shows the first Brillouin zone which is normally used in solid state calculations.

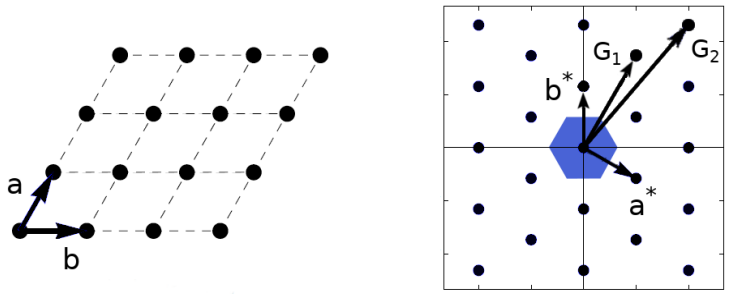

Figure 2.1. Hypothetical 2-dimensional lattice in real space (a) and its corresponding representation in the reciprocal space (b). The first Brillouin zone is delimited in blue.

The first Brillouin zone accounts for the set of points closest to the origin of the reciprocal lattice. It completely accounts for the symmetry of the crystal and therefore its properties can be studied by finding the solutions of the electronic wave functions within the first Brillouin zone.

2.2.2 Plane Waves and Pseudopotentials.

In solid state physics, the best choice to solve the Kohn-Sham equations it to use plane waves which have the following mathematical form:

$$(2.41)\quad \Psi(r) = e^{ikr}$$

where $k = 2\pi/\lambda$ is the wave vector associated with the momentum $p = \hbar k$ and consequently to the energy of the wave, and r is the position vector. Plane waves are a simple way of representing electron wave functions. They offer a complete basis set that is independent of the type of crystal and treats all areas of space equally. This is in contrast to some other basis sets that use localised functions such as Gaussians, which are dependent on the positions of the ions.

When using plane waves we have to take into account Bloch's theorem[33–35] that states that in a periodic solid the one-electron wave functions can be expressed as the product of a plane wave and a lattice periodic part function $u(r)$ with the same periodicity t of the crystal. This division turned out to be fundamental to describe periodic systems.

$$(2.42)\quad \Psi(r) = e^{ikr}\, u(r)$$

$$(2.43)\quad u(r) = u(r + t)$$

Since $u(r)$ has the same periodicity as the direct lattice, it can be expressed in terms of a discrete plane-wave basis set with wavevectors G that are reciprocal lattice vectors of the crystal,

$$(2.44)\quad u(r) = \sum_G c_{i.G} e^{iGr}$$

Where $G \cdot R = 2\pi m$, where m is an integer, R are the crystal lattice vectors and $c_{i,G}$ are the plane-wave coefficients. This shows that the electron wave functions can be expanded in terms of a linear combination of plane-waves,

$$(2.45)\quad \psi_{j,k}(r) = \sum_G c_{j,k+G} e^{i(k+G)r}$$

By virtue of Bloch's theorem, any real-space integral over a periodic system with infinite extent can be replaced by an integral in reciprocal-space over the finite first Brillouin zone. However, as consequence of the infinite number of electrons, it implies calculating periodic functions at an infinite number of k-points in the reciprocal space. This problem is normally solved by the fact that wave functions do not change appreciably over a small distance in k-space, which makes possible to perform integrations as discrete summations over a finite mesh of k-points. Moreover, the size of the basis set can be easily controlled by increasing the kinetic energy cutoff,

$$(2.46)\quad E_{cut} = \frac{\hbar}{2m}|G|^2$$

When studying solid matter, we can find two types of electrons that exhibit different behaviour, the core electrons that are strongly localized in the closed inner atomic shells, and the valence electrons that can be found outside the core. Calculations that use plane-wave basis sets and try to describe all the electrons present in the matter demand a huge computational expense that is simply not practical because a prohibitively large number of wave functions would be required to accurately describe the oscillations in the core regions, which maintain orthogonality between valence and core electrons.

However, by realising that the electronic structure of the core-electrons remains largely unchanged in different chemical environments, and is usually of minimal interest, the problems relating to the core-electrons can be solved by using the pseudopotential approximation.[36–38]

The pseudopotential approximation replaces the strong ionic potential $v_{ion}(r)$ in the core region, by a weaker pseudo-potential $v_{pseudo}(r)$. The corresponding set of pseudo-wave functions $\varphi_{pseudo}(r)$ and the all-electron wave functions $\varphi_{all-electron}(r)$ are identical outside a chosen cutoff radius r_c and so exhibit the same scattering properties, but $\varphi_{pseudo}(r)$ does not possess the nodal structure that causes the oscillations inside r_c, which means they can now be described with a reasonable number of plane-waves (see Figure 2.2).

Nowadays, the most popular pseudopotentials are the ones defined by Martin-Troullier[39], the ultrasoft pseudopotentials[40] and the projector augmented wave (PAW).[41]

The latter is the most accurate, but most demanding, because it allows the reconstruction of the all-electron wave function. The PAW scheme introduces a linear transformation operator τ to map the valence pseudo wave functions onto the corresponding all-electron wave functions as follows:

$$|\Psi\rangle = \tau|\widetilde{\Psi}\rangle \quad (2.47)$$

The transformation operator τ is defined as:

$$\tau = 1 + \sum_{R,n}\left[|\phi_{R,n}\rangle - |\tilde{\phi}_{R,n}\rangle\right]\langle\tilde{p}_{R,n}| \quad (2.48)$$

where $\langle\tilde{p}_{R,n}|$ are a set of projectors, $|\phi_{R,n}\rangle$ are the target all-electron partial waves obtained by applying τ on a set of pseudo partial waves $|\tilde{\phi}_{R,n}\rangle$. The projectors and pseudo partial waves are atom-centered functions with angular momentum quantum number *n*. The most important advantage of the PAW method is that it allows obtaining the expectation values of all-electron operators. In this work, all electronic calculations based on planewave formalism have used this approach.

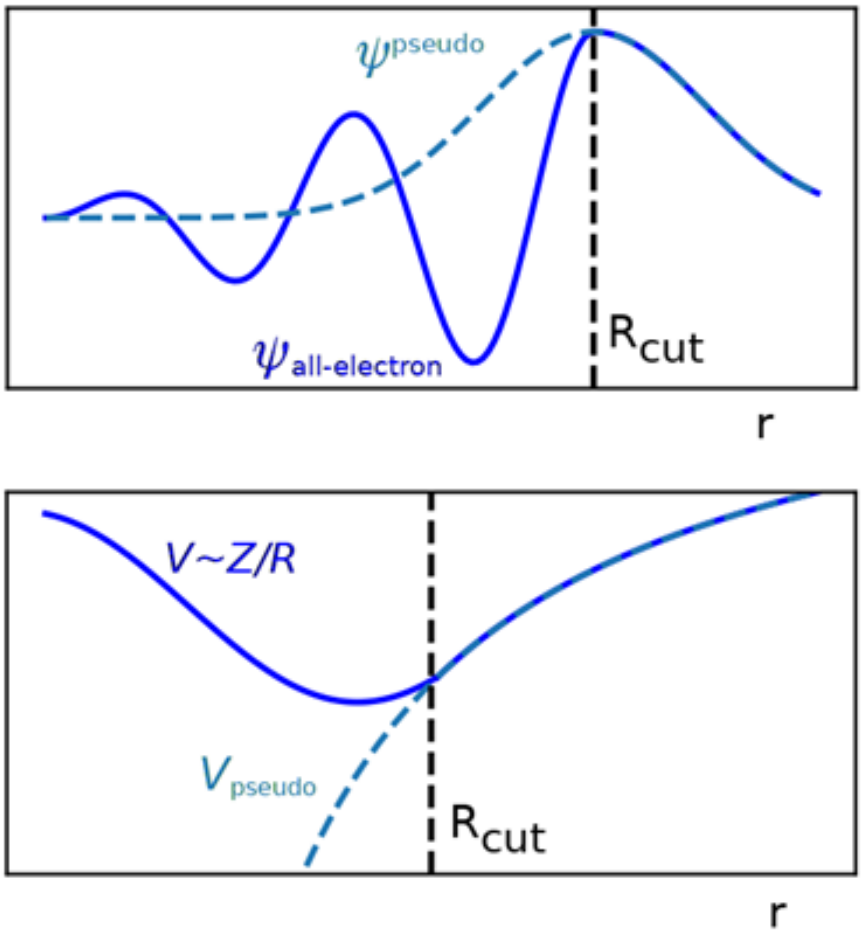

Figure 2.2. Schematic representation of potentials (top panel) and their corresponding wave functions (bottom panel) corresponding to all-electron (solid lines) and the pseudopotential approximations (dashed lines).

$$|\Psi\rangle = \tau|\widetilde{\Psi}\rangle \quad (2.47)$$

$$\tau = 1 + \sum_{R,n} \left[|\phi_{R,n}\rangle - |\tilde{\phi}_{R,n}\rangle\right] \langle \tilde{p}_{R,n}| \quad (2.48)$$

$$\tau = 1 + \sum_{R,n} \left[|\phi_{R,n}\rangle - |\tilde{\phi}_{R,n}\rangle\right] \langle \tilde{p}_{R,n}| \quad (2.48)$$

2.3 Potential Energy Surface.

The methods stated in previous sections allow to compute the energy of a system of particles. Nonetheless, a configuration for the atomic positions needs to be specified as each configuration results in a different energy value. When we calculate the energy for all possible configurations of a set of particles we obtain what is called a potential energy surface (PES). This multidimensional

surface can only be visualized by plotting the energy as a function of only two variables (Figure 2.3). When studying the PES, the more interesting regions because of the information they provide are its local and global minima and its saddle points. Minima represent states of higher stability and are associated with reactants, products, and reaction intermediates. First order saddle points are spots on the surface where the energy reaches a maximum value along one coordinate, called reaction coordinate, and is a minimum along all other coordinates. These points always connect two minima along the reaction coordinate and are associated with transition states (TS). The energy difference between the TS and the minimum corresponding to the reactants is considered the activation energy (Ea) for a step of a reaction.

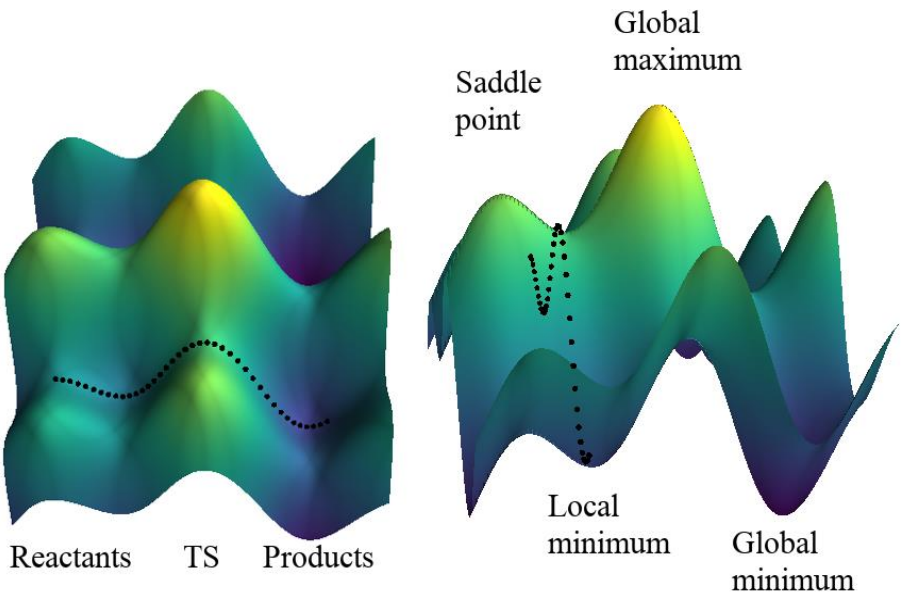

Figure 2.3. Representation of a potential energy surface.

In order to explore the PES, optimization techniques are normally used because the derivative of the energy with respect to atomic positions is zero in minima and saddle points along all coordinates. Minimizing the energy with respect to atomic positions has proven to be a proper way to find structures that can be relevant for a chemical reaction. Nowadays, the most popular techniques for energy minimization are the conjugate gradient (CG), steepest descent (SD) and Limited-memory Broyden-Fletcher-Goldfarb-Shanno (LBFGS) algorithms.[42] In this work we have used the conjugate gradient as implemented in VASP because it stability and guarantee of convergence.

In Gaussian, we always employed the default Berny algorithm.[43] It constructs an approximate Hessian for the system and optimizes the structure using it and the forces on the atoms. Then, the Hessian is subsequently updated from these

forces. Optimizations stop by satisfying four convergence criteria: the maximum remaining force on any atom of the system, the average force on all atoms (root mean square, RMS), the maximum displacement of each coordinate and the average change over all structural parameters in the last two iterations.

TS are much more difficult to find because they present the particularity that the second derivative of the energy with respect to the atomic positions (curvature) is negative along the reaction coordinate and positive along all other coordinates. This fact requires more complex algorithms that are computationally demanding. To find saddle points, we have used two methods implemented in VASP, the nudged elastic band (NEB) and dimer methods.[44–46]

On the one hand, NEB is a method for finding saddle points between known minima of reactants and products. At the start, a series of structures called images are created along the reaction coordinate between both minima, and the optimization of all images runs in parallel. Spring forces between contiguous images are introduced, hence all images are equally spaced from each other resembling an elastic band. Each image finds the lowest energy possible while maintaining equal spacing to neighbouring images, resulting in a complete minimum energy profile for the desired reaction.

On the other hand, the dimer method allows the user to start from an initial guess of the transition state structure and a guess of the reaction coordinate unit vector and search for a nearby saddle point. Dimer is normally used for complex systems whose reaction mechanisms and saddle points are unknown and cannot be described with NEB method because it grants the possibility of starting from a minimum basin and search in random directions for saddle points. Dimer method creates two images equally displaced from the initial guess structure along the reaction coordinate unit vector called dimer axis. These two images are rotated around the dimer axis to maximize the curvature, *C*, along the axis. The curvature is calculated by the approximation defined in equation 2.42 that reduces the computational cost significantly when compared with methods that calculate the Hessian matrix.

$$(2.49)\quad C = \frac{(F_2 - F_1) \cdot \widehat{N}}{2\Delta R} = \frac{E - 2E_0}{\Delta R^2}$$

where F_1 and F_2 are forces acting on image 1 and 2, ΔR is the spacing between both images, E is the sum of both images energy and E_0, the energy of the midpoint of the dimer. After each rotation, the dimer is pushed uphill to the saddle point. The common way to confirm that the structures obtained by energy minimization methods are proper minima or transition states is to perform a vibrational analysis on the optimized geometry. For minimum structures, all calculated frequencies must be positive and for a transition state there must be only one imaginary frequency. Vibrational frequencies are calculated considering that the molecular vibrations can be described as those

of a harmonic oscillator. Then, the energy can be expressed as a Taylor series where the third and higher order terms are neglected:

$$(2.50)\ E(R) = E(R_0) + \frac{dE}{dR}(R - R_0) + \frac{d^2E}{dR^2}(R - R_0)^2 + \frac{1}{6}\frac{d^3E}{dR^3}(R - R_0)^3$$

When structures are minimums or TS, the first order term is zero and we end up with the following harmonic potential:

$$(2.51)\quad E(R) = \frac{1}{2}\frac{d^2E}{dR^2}(R - R_0)^2 = \frac{1}{2}k(R - R_0)^2$$

By solving the Schrödinger equation for this approximation, we get the vibrational energy levels:

$$(2.52)\quad \varepsilon_n = \left(n + \frac{1}{2}\right)h\nu$$

$$(2.53)\quad \nu = \frac{1}{2\pi}\sqrt{\frac{k}{\mu}}$$

$$(2.54)\quad \mu = \frac{m_1 m_2}{m_1 + m_2}$$

where *n* is a quantum number that takes up values from zero to infinity, *h* is the Planck's constant, *ν* is the vibrational frequency, *k* is the force constant and *μ* is the reduced mass. As described in equation 2.52, energy levels are quantized and equally spaced. In addition, anharmonic corrections to the frequencies can be performed including third and higher order terms in the Taylor series of energy expansion (eq. 2.50).

For systems with more than two atoms, the Hessian matrix has to be computed or approximated.

$$(2.55)\quad H = \frac{\partial^2 E}{\partial x_1 \partial x_2}$$

The Hessian matrix H is a $3N\ x\ 3N$ symmetric matrix whose eigenvalues and eigenvectors are the force constants and the normal modes of the $3N$ frequencies. VASP software provides two methods to approximate the Hessian matrix, finite differences and density functional perturbation theory (DFPT).[47]

2.3.1 Free Energy.

Using the methods described in the last section it is possible to explore the PES aiming for minima and saddle points that provide interesting information for chemical reactions and obtaining structures that correspond to the 0 K and low pressure experimental conditions. However, these results are not as accurate as

they should be to describe properly real chemical systems, because these are studied at higher temperatures and pressures. Moreover, these systems are made of an immense number of molecules, ~10^{23}, and this change in N causes that other thermodynamic properties as entropy or free energy gain relevance when predicting reaction spontaneity at constant temperature and pressure of such macroscopic systems. The free energy change between two states is given by the Gibbs equation:

$$\Delta G = \Delta H - T\Delta S \quad (2.56)$$

When enthalpy is approximated to the electronic energy and the change in entropy from reactants to products tends to zero, enthalpy serves as a fairly good approximation to describe the kinetics and thermodynamics of a chemical reaction. This approach has been mainly used through this work to describe different mechanistic steps. Still, entropy is very often a non-negligible property and the activation free energy of a chemical reaction can significantly differ from the electronic energy in certain cases.

The proper way to get an approximate value of the free energy is to resort to statistical mechanics' methods where the macroscopic thermodynamics properties are calculated based on the partition function Z of an ensemble of particles. The partition function is the central quantity of statistical mechanics given as,

$$Z = \sum_i e^{-E_i/K_B T} \quad (2.57)$$

where the summation runs over all microstates i of the ensemble. From the knowledge of the partition function, macroscopic thermodynamic properties can be accessed because the possible microstates depend on the macroscopic constraints of the ensemble such as number of particles, total energy, volume, pressure, etc.

The formulas used in this work to calculate the free energy when static DFT methods were used to study the PES are presented here without any derivation, further details on them can be found in the literature.[48]

The absolute Gibbs free energies were calculated as follows:

$$G = E_{elec} + E_{zpe} + RT + E_{vib} - TS_{vib} \quad (2.58)$$

where E_{elec} is the electronic energy obtained from the DFT calculation, E_{zpe} is the zero point energy correction, E_{vib} is the vibrational thermal energy contribution and S_{vib} is the vibrational entropy. The zero-point energy corrections and the vibrational contributions to the energy and entropy were calculated according to:

$$(2.59)\quad E_{zpe} = \sum_{i=1}^{3N-6} \frac{1}{2} h\upsilon_i$$

$$(2.60)\quad E_{zpe} = R \sum_{i=1}^{3N-6} \frac{h\upsilon_i}{k_b(e^{h\upsilon_i/k_bT} - 1)}$$

$$(2.61)\quad S_{vib} = R \sum_{i=1}^{3N-6} \left[\frac{h\upsilon_i}{k_b(e^{h\upsilon_i/k_bT} - 1)}\right] - \ln(1 - e^{h\upsilon_i/k_bT})$$

using the vibrational frequencies υ obtained from the DFT calculations. For gaseous molecules, the rotation and translational contributions to the entropy and energy were also included in the calculation of the free energy as follows:

$$(2.62)\quad G = E_{elec} + E_{zpe} + E_{vib} + E_{rot} + E_{trans} + RT - T(S_{vib} + S_{rot} + S_{trans})$$

Where

$$(2.63)\quad E_{rot} = E_{trans} = \frac{3}{2}(RT)$$

and the rotational and translational contributions to the entropy are given by:

$$(2.64)\quad S_{rot} = R\left\{\left[\sqrt{\frac{\pi I_a I_b I_c}{\sigma}}\left(\frac{2\pi k_b T}{h^3}\right)^{3/2}\right] + \frac{3}{2}\right\}$$

$$(2.65)\quad S_{trans} = R\left\{ln\left[\left(\frac{2\pi M k_b T}{h^3}\right)^{3/2} V\right] + \frac{3}{2}\right\}$$

Finally, for the most relevant steps of the mechanism, the equilibrium K_{eq} and kinetic rate constants K_r were derived from the calculated reaction and activation Gibbs free energies, as follows:

$$(2.66)\quad K_{eq} = e^{-\Delta G/RT}$$

$$(2.67)\quad K_r = \frac{K_b T}{h} e^{-\Delta G_{act}/RT}$$

2.4 Ab-Initio Molecular Dynamics.

Nowadays, the most popular methods to include entropic contributions to the potential energy surface study are molecular dynamics (MD) and Monte Carlo (MC) simulations.[49,50] In this work, we have used ab initio molecular dynamics

(AIMD) techniques to study the behaviour of different organic structure directing agents inside SSZ-39 cavity.

Molecular dynamics samples the phase space of a system of particles considering atoms as classical particles while their positions are updated by integrating Newton's equations of motion (EOM). The most used algorithm to integrate the EOM is Velocity Verlet because it guarantees that the system will be time reversible.[51,52] This means that the same trajectory is reproduced exactly by iterating forward or backward in time which guarantees the conservation of the energy over long simulation times.

In Velocity Verlet the time is discretized and at each time *t* the velocities and positions of the particles are updated according to the following equations:

$$x(t+\Delta t) = x(t) + v(t) + v(t)\Delta t + \frac{1}{2}a(t)\Delta t^2 \quad (2.68)$$

$$v(t+\Delta t) = v(t) + \frac{1}{2}\big(a(t) + a(t+\Delta t)\big)\Delta t \quad (2.69)$$

The forces acting on the atoms are calculated as the first derivative of the potential energy with respect to the positions of the particles. Then, the acceleration is computed from these forces. In AIMD the forces are derived from electronic structure calculations at each time step which results in significantly expensive simulations. The difference in the way of calculating forces between force field MD simulations and AIMD simulations materializes into the timescales that can be covered by each method. Force field MD covers hundreds of nanoseconds meanwhile AIMD simulations are limited to a few hundreds of picoseconds for systems constituted by some hundreds of atoms with modern supercomputers.

All possible states of a system of particles subject to the same macroscopic constraints constitute an ensemble. The most basic is the microcanonical ensemble (NVE) in which the number of particles, the volume and the total energy of the system are constant. However, the microcanonical ensemble is no realistic because real experiments are carried out at different conditions. Therefore, more realistic ensembles such as the canonical ensemble (NVT) where the number of particles, the volume of the system and the temperature are constant or the isothermal-isobaric ensemble (NPT) where the number of particles, the pressure and the temperature are constant, are normally used.

In regular MD simulations the probability of sampling different states of the system is given by the Boltzman distribution and that is why only low energy states are sampled. As calculations of free energy from MD simulations require abundant sampled states, highly activated transitions cannot be properly studied. This limitation can be overcome using enhanced sampling techniques. Nowadays, the most popular and widely used methods are potential of mean force (PMF), metadynamics (MTD) and umbrella sampling (US).[53–56]

In this work we are not making use of any enhanced sampling technique, further details on their specificities can be found in the cited literature.

2.5 Models.

To study a chemical reaction, we need a description of the physical system, that is, the number, nature and position of the particles. This set of information will be referred to as a model. In this section, the models used for zeolites are described and the complete list of models used in this work can be found in Appendix I.

Describing accurately the real catalytic environment of solids with models grants success in predicting the rate of chemical reactions. For zeolites, the cluster and periodic models are the most used approaches nowadays. Clusters are constructed by cutting the catalytically relevant region out of the framework. The goal of this approach is to reduce the number of atoms, thus shortening computation times and allowing the use of higher levels of theory. A serious drawback of this approach is that the topologic effect of the zeolite framework outside the cluster range, which is a relevant feature for this kind of catalysts, is lost. Besides, confinement effects and long-range interactions are better captured by considering the whole periodic structure. Periodic models consist of the unit cell of zeolite crystals repeated in the three dimensions. The downside is the greater number of atoms included in the zeolite unit cell. Consequently, calculations are usually performed at lower levels of theory but include effects that are not present in cluster models. In this work, we have relied on both kind of models which are shown in the next section and depicted with further detail on Appendix I.

2.5.1 Zeolite Periodic Models.

Periodic models for zeolites and AlPOs studied in this work were designed from their CIF code found at IZA database[62] and their unit cell parameters were later fully relaxed with VASP calculations that minimize forces and the stress tensor allowing freedom to recalculate atomic positions, cell shape and shape volume. These models are detailed with cell parameters and images at Appendix I.

In this work we have studied the following 22 pure silica and AlPO microporous materials for the methanol to olefins (MTO) reaction mechanism in Chapter 3: SSZ-17 and AlPO-35 both with a LEV framework, SSZ-16 and AlPO-17 with an ERI framework, SSZ-13 and SAPO-34 both with a CHA framework, AlPO-56 with a AFX framework, ZSM-58 with a DDR framework, SSZ-39 and AlPO-18 both with a AEI framework, RUB-13 with a RTH framework, ITQ-3 with an ITE framework, STA-7 with a SAV framework, zeolite A and AlPO-42 both with a LTA framework, Rho and DNL-6 both with a RHO framework, ZK-5 and STA-14 both with a KFI framework and UZM-5 with an UFI framework.

For the study of diethylbenzene transalkylation reaction mechanism in Chapter 5 the following 12 pure silica microporous materials were studied. Beta polymorph A with a *BEA framework, FOS-5 with a BEC framework, Boggsite with a BOG framework, CIT-1 with a CON framework, Faujasite with a FAU framework, ITQ-33 with an ITT framework, ITQ-24 with an IWR framework, ITQ-27 with an IWV framework, Mordenite with a MOR framework, SSZ-82 with a SEW framework, IM-6 with a USI framework, IM-15 with a UTL framework. Moreover, with the aim of studying specific parts of the reaction mechanism, zeolite models for IWV and MOR frameworks were designed in which one Si atom was replaced by one Al atom, with its position being selected in terms of intrinsic stability of the system.

2.5.2 Zeolite Cluster Models.

In this work we also used cluster models for CHA, AEI, ITE and RTH frameworks, of composition $Si_{48}O_{78}H_{36}$, $Si_{36}O_{54}H_{36}$, $Si_{40}O_{60}H_{40}$ and $Si_{40}O_{60}H_{40}$ respectively, when starting the study of MTO reaction mechanism to apply a higher level of theory to the confinement interactions between the key hydrocarbon pool intermediates and the zeolite cavity.

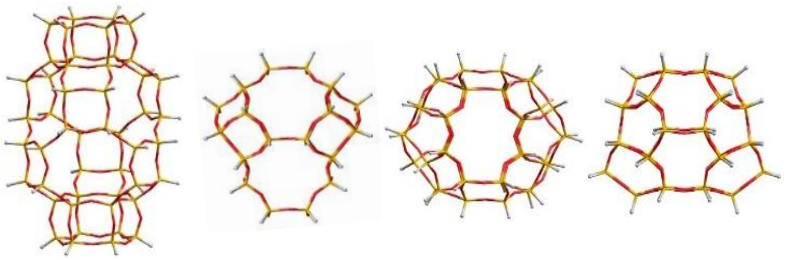

Figure 2.7. From left to right; CHA, AEI, ITE and RTH cluster models used in this work.

2.6 References

1. Szabo, A.; Oslund, N. S. Modern Quantum Chemistry: Introduction to Advanced Electronic Structure Theory; 1989. (1989).

2. P. W. Atkins. Physical Chemistry. (1990).

3. The Nobel Prize in Chemistry 1998 https://www.nobelprize.org/prizes/chemistry/1998/kohn/lecture/.

4. Cohen, A. J., Mori-Sánchez, P. & Yang, W. Challenges for density functional theory. Chem. Rev. 112, 289–320 (2012).

5. Dirac, P. A. M. Note on Exchange Phenomena in the Thomas Atom. Math. Proc. Cambridge Philos. Soc. 26, 376–385 (1930).

6. Slater, J. C. A simplification of the Hartree-Fock method. Phys. Rev. 81, 385–390 (1951).

7. March, N. H. Electron Density Theory of Atoms and Molecules. J. Phys. Chem 86, 2262–2267 (1982).

8. Hohenberg, P.; Kohn, W. Inhomogeneous Electron Gas. Phys. Rev 136, B864–B871 (1964).

9. R. O. Jones and O. Gunnarsson. The density functional formalism, its applications and prospects. Rev. Mod. Phys 61, (1989).

10. Kohn, W.; Sham, L. J. Self-Consistent Equations Including Exchange and Correlation Effects. Phys. Rev 140, A1133–A1138 (1965).

11. Perdew, J. P. & Zunger, A. Self-interaction correction to density-functional approximations for many-electron systems. Phys. Rev. B 23, 5048–5079 (1981).

12. Ceperley, D. M. & Alder, B. J. Ground state of the electron gas by a stochastic method. Phys. Rev. Lett. 45, 566–569 (1980).

13. Vosko, S. H., Wilk, L. & Nusair, M. Accurate spin-dependent electron liquid correlation energies for local spin density calculations: a critical analysis. Can. J. Phys. 58, 1200–1211 (1980).

14. Payne, M. C., Teter, M. P., Allan, D. C., Arias, T. A. & Joannopoulos, J. D. Iterative minimization techniques for ab initio total-energy calculations:

Molecular dynamics and conjugate gradients. Rev. Mod. Phys. 64, 1045–1097 (1992).

15. Langreth, D. C. & Mehl, M. J. Beyond the local-density approximation in calculations of ground-state electronic properties. Phys. Rev. B 28, 1809–1834 (1983).

16. Perdew, J. P., Burke, K. & Ernzerhof, M. Generalized Gradient Approximation Made Simple [Phys. Rev. Lett. 77, 3865 (1996)]. Phys. Rev. Lett. 78, 1396–1396 (1997).

17. Zhang, Y. & Yang, W. Comment on "generalized gradient approximation made simple". Phys. Rev. Lett. 80, 890 (1998).

18. Zhao, Y. & Truhlar, D. G. The M06 suite of density functionals for main group thermochemistry, thermochemical kinetics, noncovalent interactions, excited states, and transition elements: two new functionals and systematic testing of four M06-class functionals and 12 other functionals. Theor. Chem. Acc. 120, 215–241 (2008).

19. Perdew & Schmidt, K. Jacob ' s ladder of density functional approximations for the exchange- correlation energy Jacob ' s Ladder of Density Functional Approximations for the Exchange-Correlation Energy. AIP Conf. Proc. 1, 577 (2011).

20. Grimme, S. Semiempirical GGA-type density functional constructed with a long-range dispersion correction. J. Comput. Chem. 27, 1787–1799 (2006).

21. Grimme, S. Accurate description of van der Waals complexes by density functional theory including empirical corrections. J. Comput. Chem. 25, 1463–1473 (2004).

22. Grimme, S.; Ehrlich, S.; Goerigk, L. Effect of the Damping Function in Dispersion Corrected Density Functional. Theory. J. Comput. Chem. 32, 1456–1465 (2011).

23. Frisch, M. J.; Trucks, G. W.; Schlegel, H. B.; Scuseria, G. E.; Robb, M. A.; Cheeseman, J. R.; Scalmani, G.; Barone, V.; Petersson, G. A.; Nakatsuji, H.; Li, X.; Caricato, M.; Marenich, A.; Bloino, J.; Janesko, B. G.; Gomperts, R.; Mennucci, B.; Hratchian, D. J. Gaussian 09. Gaussian, Inc Wallingfor, (2016).

24. Kresse, G. & Furthmüller, J. Efficient iterative schemes for ab initio total-energy calculations using a plane-wave basis set. Phys. Rev. B 54, 11169–11186 (1996).

25. Slater, J. C. Atomic shielding constants. Phys. Rev. 36, 57–64 (1930).

26. Boys, S. F. & A, P. R. S. L. The integral formulae for the variational solution of the molecular many-electron wave equation in terms of Gaussian functions with direct electronic correlation. Proc. R. Soc. London. Ser. A. Math. Phys. Sci. 258, 402–411 (1960).

27. Hehre, W. J., Stewart, R. F. & Pople, J. A. Self-consistent molecular-orbital methods. I. Use of gaussian expansions of slater-type atomic orbitals. J. Chem. Phys. 51, 2657–2664 (1969).

28. Ditchfield, R., Hehre, W. J. & Pople, J. A. Self-Consistent Molecular-Orbital Methods. IX. An Extended Gaussian-Type Basis for Molecular-Orbital Studies of Organic Molecules. J. Chem. Phys. 54, 724–728 (1971).

29. Hay, P. J. Gaussian basis sets for molecular calculations. The representation of 3d orbitals in transition-metal atoms. J. Chem. Phys. 66, 4377–4384 (1977).

30. Wachtees, A. J. H. Gaussian basis set for molecular wavefunctions containing third-row atoms. J. Chem. Phys. 52, 1033–1036 (1970).

31. Ditchfield, R., Hehre, W. J. & Pople, J. A. Self-consistent molecular-orbital methods. IX. An extended gaussian-type basis for molecular-orbital studies of organic molecules. J. Chem. Phys. 54, 720–723 (1971).

32. Hehre, W. J., Ditchfield, R. & Pople, J. A. Self—Consistent Molecular Orbital Methods. XII. Further Extensions of Gaussian—Type Basis Sets for Use in Molecular Orbital Studies of Organic Molecules. J. Chem. Phys. 56, 2257–2261 (1972).

33. Bloch, F. About the Quantum mechanics of electrons in crystal lattices. Solid State Phys. Proj. 52, 555–600 (1928).

34. Bohm, D. Note on a theorem of bloch concerning possible causes of superconductivity. Phys. Rev. 75, 502–504 (1949).

35. Yamamoto, N. Generalized Bloch theorem and chiral transport phenomena. Phys. Rev. D - Part. Fields, Gravit. Cosmol. 92, 1–9 (2015).

36. Hellmann, H. A new approximation method in the problem of many electrons. J. Chem. Phys. 3, 61 (1935).

37. Gutsev, G. L. Numerical Pseudopotentials within DV-X α Framework. Advances in Quantum Chemistry vol. 29 (Elsevier Masson SAS, 1998).

38. Heine, V. Ehrenreich, H., Seitz, F., Turnbull, D., E. The Pseudopotential Concept. In Solid State Physics. Acad. Press 24, 1–36 (1970).

39. Troullier, N. & Martins, J. L. Efficient pseudopotentials for plane-wave calculations. Phys. Rev. B 43, 1993–2006 (1991).

40. Vanderbilt, D. Soft Self-Consistent Pseudopotentials in a Generalized Eigenvalue Formalism. Phys. Rev. B 41, 7892–7895 (1990).

41. Blöchl, P. E. Projector augmented-wave method. Phys. Rev. B 50, 17953–17979 (1994).

42. Press, W. H. Numerical Recipes : The Art of Scientific Computing; Cambridge [Cambridgeshire]. Cambridge Univ. Press (1986).

43. Schlegel, H. B. Optimization of Equilibrium Geometries and Transition Structures. Adv. Chem. Phys. 67, 249–286 (2007).

44. Henkelman, G., Uberuaga, B. P. & Jónsson, H. Climbing image nudged elastic band method for finding saddle points and minimum energy paths. J. Chem. Phys. 113, 9901–9904 (2000).

45. Henkelman, G. & Jónsson, H. A dimer method for finding saddle points on high dimensional potential surfaces using only first derivatives. J. Chem. Phys. 111, 7010–7022 (1999).

46. Heyden, A., Bell, A. T. & Keil, F. J. Efficient methods for finding transition states in chemical reactions: Comparison of improved dimer method and partitioned rational function optimization method. J. Chem. Phys. 123, (2005).

47. Gonze, X. & Lee, C. Dynamical matrices, Born effective charges, dielectric permittivity tensors, and interatomic force constants from density-functional perturbation theory. Phys. Rev. B - Condens. Matter Mater. Phys. 55, 10355–10368 (1997).

48. Horn, A. H. C. Essentials of Computational Chemistry, Theories and Models By Christopher J. Cramer. Wiley: Chichester, England. 2002. 562 pp.

ISBN 0-471-48551-9 (hardcover). $110. ISBN 0-471-48552-7 (paperback). $45. Journal of Chemical Information and Computer Sciences vol. 43 (2003).

49. van Gunsteren, W. F. & Berendsen, H. J. C. Computer Simulation of Molecular Dynamics: Methodology, Applications, and Perspectives in Chemistry. Angew. Chemie Int. Ed. English 29, 992–1023 (1990).

50. Dubbeldam, D., Torres-Knoop, A. & Walton, K. S. On the inner workings of monte carlo codes. Molecular Simulation vol. 39 1253–1292 (2013).

51. Vekiet, L. Computer 'Experiments' on Classical Fluids. I. Thermodynamical Properties of Lennard-Jones Molecules. Phys. Rev. 159, 98–103 (1967).

52. Frenkel, Daan, B. S. Understanding molecular simulation: from algorithms to applications. Vol. 1. Elsevier. 638 (2001).

53. Hansen, N. & Van Gunsteren, W. F. Practical aspects of free-energy calculations: A review. J. Chem. Theory Comput. 10, 2632–2647 (2014).

54. Christ, C. D., Mark, A. E. & Van Gunsteren, W. F. Basic ingredients of free energy calculations: A review. J. Comput. Chem. 31, 1569–1582 (2010).

55. Abrams, C. & Bussi, G. Enhanced sampling in molecular dynamics using metadynamics, replica-exchange, and temperature-acceleration. Entropy 16, 163–199 (2014).

56. Pietrucci, F. Strategies for the exploration of free energy landscapes: Unity in diversity and challenges ahead. Rev. Phys. 2, 32–45 (2017).

57. Valleau, J. P. & J.M., T. Nonphysical sampling distributions in Monte Carlo free-energy estimation: Umbrella sampling. J. Comput. Phys. 23, 187–199 (1977).

58. Kumar, P. et al. One-dimensional intergrowths in two-dimensional zeolite nanosheets and their effect on ultra-selective transport. Nat. Mater. 19, 443–449 (2020).

59. Souaille, M. & Roux, B. Extension to the weighted histogram analysis method: Combining umbrella sampling with free energy calculations. Comput. Phys. Commun. 135, 40–57 (2001).

60. Laio, A., Rodriguez-Fortea, A., Gervasio, F. L., Ceccarelli, M. & Parrinello, M. Assessing the accuracy of metadynamics. J. Phys. Chem. B 109, 6714–6721 (2005).

61. Barducci, A., Bussi, G. & Parrinello, M. Well-tempered metadynamics: A smoothly converging and tunable free-energy method. Phys. Rev. Lett. 100, 1–4 (2008).

62. Baerlocher, C.; McCusker, L. B. Database of Zeolite Structures.

Chapter 3

Impact of Zeolite Framework, Composition and Flexibility on Methanol to Olefins Selectivity.

3.1 Introduction.

The methanol-to-olefins (MTO) reaction is a relevant process that produces short chain olefins such as ethene ($C_2^=$), propene ($C_3^=$) and butene ($C_4^=$) at industrial scale. [1–3] The commercial demand of these chemical products is nowadays fulfilled by steam cracking or fluidized catalytic cracking of higher hydrocarbons. The MTO reaction provides an alternative path for producing short chain olefins from sources such as coal, natural gas or biomass. In recent years, many MTO plants have emerged, being the coal to-olefin plant built in China in 2010 the first one of its kind.[2] The MTO reaction is catalyzed by acid zeolites (aluminosilicates) and silicoaluminophosphates (SAPO) that can form, within their pores, organic molecules that act as co-catalysts. The true catalytic system comprises both the inorganic framework containing the Brønsted acid sites and the confined organic species, either alkenes or aromatics, that form the so-called "hydrocarbon pool" (HP) and produce light olefins by successive methylation and cracking steps.[4–7] Therefore, the catalyst can be considered a dual system comprising the inorganic zeolite framework and the organic species trapped inside. The topology of the microporous structure determines the nature of the hydrocarbon pool species and, indirectly, the selectivity of the reaction.[8–13] According to the widely accepted dual-cycle mechanism (Scheme 1), channel structured zeolites like H-ZSM-5 favour the formation of propene and higher alkenes by methylation and cracking of alkenes in the 10-membered ring (10r) channels of the bidirectional system, while ethene production requires the participation of aromatic alkylbenzenes, as hydrocarbon pool species, allocated at the wider channels intersections.[5–7]

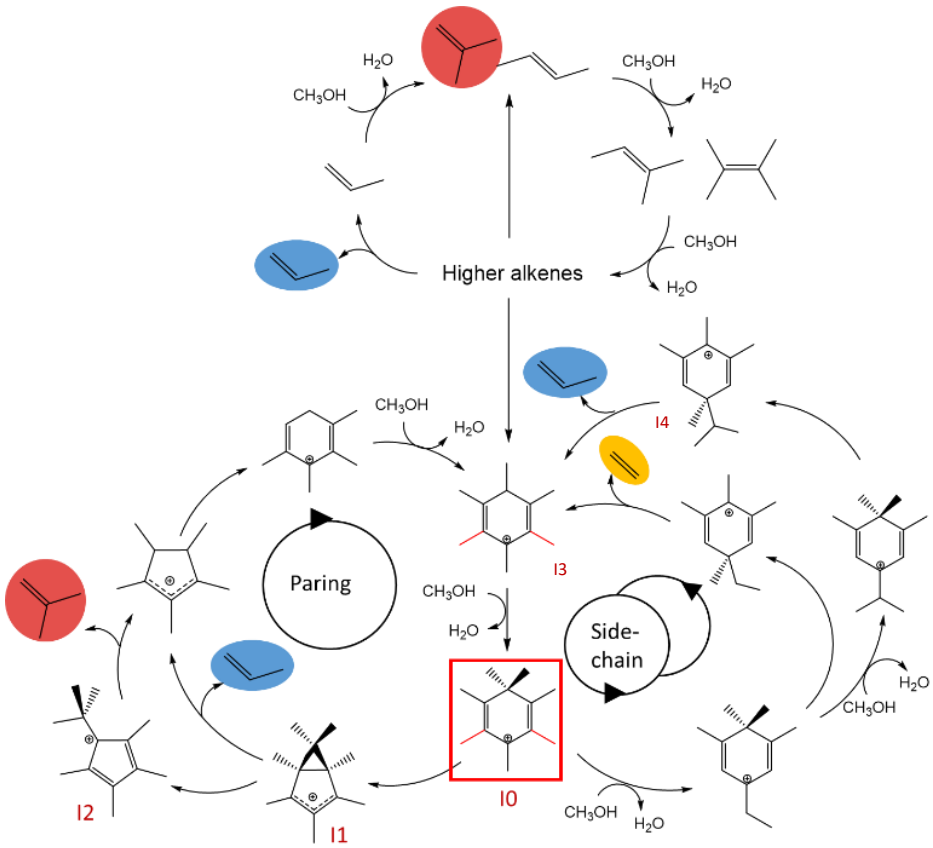

Scheme 3.1. Dual-cycle hydrocarbon pool mechanism proposed for the MTO reaction.

Small-pore zeolites containing large cavities within their structure are particularly suited for conversion of methanol into ethene and propene.[2,3,14] The organic HP species identified in H-SAPO-34 and its aluminosilicate counterpart, H-SSZ-13, both with the CHA structure, are aromatic polymethylbenzenes (MB) and their corresponding carbenium ions (MB^+), which participate in at least two possible competitive reaction pathways: the side-chain and the paring routes (see Scheme 3.1), although some contribution of the alkene-based cycle cannot be ruled out completely.[13,15–17] Both processes share a common intermediate, labelled I0 (red square Scheme 3.1), which is formed by gem-methylation or attack of methanol to a tertiary carbon atom of the aromatic ring. The paring route starts with I0 ring contraction to form a bicycle-hexenyl species I1 that splits off propene or isobutene, generating cyclopentenyl (CP^+) cations, which expand again to yield MB^+ intermediates with a lower degree of methylation. The side-chain pathway involves exomethylation of the I0 intermediate to give I3, followed by some methyl-shift steps and side-chain elimination yielding preferentially ethene and propene.[15,16,18–24]

The two types of carbenium ions, MB^+ and CP^+, have been detected by in situ ^{13}C NMR spectroscopy in small-pore zeolites with the CHA, AEI, RHO, and LEV structures[9,25–27], proving the viability of the two mentioned pathways in these cage-based catalysts. It has also been reported that the contribution of each of the two pathways to the global conversion of methanol, and therefore to the final light olefin product distribution, depends on the topology of the zeolite cage.[5,9,10,17,28] Some authors claim that the final olefin product distribution is determined by differences in the diffusion of ethene and propene through the eight-membered ring (8r) windows of the CHA structure.[29] Others propose, based on density functional theory (DFT) calculations, a non-negligible contribution of an alkene based catalytic cycle analogous to that operating in H-ZSM-5[19,22,30,31] . However, there is not a clear conclusion in the available literature about the role of each factor over the product selectivity yet.

With the aim to establish a relationship between the MTO product distribution and the cavity topology, a large number of small-pore cage-based zeolites and SAPOs were systematically tested as catalysts for the MTO reaction by Davis et al. This study resulted on the definition of a new parameter based on the geometry of the zeolite cavity, the cage-defining ring (CDR) size.[10,28] Fourteen crystallographic zeolite structures with different compositions were classified into four categories according to the relative amount of ethene, propene and butene formed, with the structures containing smaller cavities such as LEV and ERI producing more ethene than propene, and with butene appearing as an important product only in structures containing very large cavities such as SAV, LTA or RHO. However, it was not possible to establish a quantitative linear correlation between product distribution and either the diameter of the largest possible included sphere (D) or CDR size.

In our research group we carried out a study based on a newly developed concept[32]. We used mimics of the key intermediates involved in the MTO reaction as organic structure-directing agents (OSDAs) to synthesize zeolite catalysts that enhanced the contribution of the paring route, and therefore increased the selectivity to propene and butene.[33] One of the findings of the theoretical study included in that work, confirmed by ^{13}C NMR spectroscopy, was the preferential stabilization of penta-MB^+ cations in CHA and hepta-MB^+ species in RTH. Considering that the stability of the bicycle-hexenyl intermediate formed in the first step of the paring route changes with the degree of methylation of the MB^+ precursor, it was proposed that the preferential stabilization of fully methylated species in RTH cages is the origin of the higher selectivity to propene and butene obtained with this material. Previous kinetic and ^{13}C NMR studies already reported that the selectivity to ethene and propene in H-SAPO-34 depends on the number of methyl groups in the MB^+ intermediates.[34] In addition, a recent isotopic tracing study has demonstrated

that the $C_3^=/C_2^=$ ratio increases in an H-SAPO-34 sample entrained with a distribution of methylbenzenes deliberately manipulated toward increasing their degree of methylation.[35] However, this effect is not permanent and after some cycles, the selectivity tends to the values typically obtained with other CHA-type catalysts.

Taking into account the hybrid organic-inorganic nature of the MTO catalysts and the influence of both cage architecture and methylation degree of the aromatic HP species on the selectivity of the process, the first part of this Chapter (section **3.3**) presents a detailed comprehensive study of the most important features of HP mechanisms in gas phase, starting from the first methylation of the benzenium cation and studying all the possible geminal methylations of tetra- penta- and hexamethyl benzene that trigger either paring or side side-chain routes. Then, we analyse in detail the paring route of the reaction mechanism for 1,2,2,3,5-$5MB^+$ (gem-$5MB_a^+$) and $7MB^+$ using pure silica cluster models of SSZ-13, SSZ-39, ITQ-3 and RUB-13 zeolites to identify the key steps in which the specific interactions between a given zeolite framework and the hosted cationic intermediates might control the selectivity of the reaction. To correlate our theoretical data with experimental selectivity, a series of SSZ-13, SSZ-39, ITQ-3 and RUB-13 acid samples were synthesized and tested in the MTO reaction in our group, and a clear linear correlation was found between the relative stability of the key intermediates gem-$5MB_a^+$ and $7MB^+$ in each cage, defined by the $E_{int(7/5)}$ parameter, and the experimental $C_3^=/C_2^=$ ratio obtained.

In a second step, in section **3.4** we move the study towards solid state periodic calculations using VASP software and we apply the $E_{int(7/5)}$ parameter previously found to explain the different light olefin product distribution obtained with isostructural H-SSZ-13 and H-SAPO-34 catalysts, both of them with the CHA structure but different chemical composition. With this aim we analyse separately each one of the possible factors influencing selectivity. On one hand, we study the larger flexibility of the silicoaluminophosphate materials and its effect over cage expansion and stabilization of fully methylated HP intermediates, which can be properly captured by the $E_{int(7/5)}$ parameter. On the other hand, we analyse the effect of acid site strength and position with respect to the HP. In a later step, in section **3.5** we extend the study of the theoretical $E_{int(7/5)}$ parameter to a wider range of zeolites and SAPOs used as MTO catalysts, including the smallest ERI and LEV cages where steric constraints might be present, as well as large cavities such as those of SAV, RHO or LTA structures where the confinement effect might be lost. The final goal is to determine the scope of confinement effects for this process, and set the limits of the $E_{int(7/5)}$ parameter as predictor of product distribution in the MTO reaction.

3.2 Methods and models.

All calculations in section **3.3** are based DFT and were carried out using the M062X functional[36] and the 6-31g(d,p) basis set[37,38], as implemented in the Gaussian 09 software.[39] In the study of the gas-phase reaction mechanism, the positions of all C and H atoms in the cationic intermediates and transition states were fully optimized without restrictions. All stationary points were characterized by means of harmonic frequency calculations, which also provided the thermal corrections to calculate Gibbs free energies under standard state conditions in the gas phase and within the zeolite cages. In a second step, pure silica cluster models of the CHA, AEI, RTH, and ITE cavities, of composition $Si_{48}O_{78}H_{36}$, $Si_{36}O_{54}H_{36}$, $Si_{40}O_{60}H_{40}$, and $Si_{40}O_{60}H_{40}$, respectively, were constructed from the corresponding periodic structures. The cationic intermediates and transition states were then placed inside each of these cluster models and their geometry was fully re-optimized without restrictions while keeping the positions of the Si, O, and terminal H atoms of the clusters fixed. Using this approach, the possibility to obtain small energy differences associated to the relative position of the organic species and the Al centres is discarded, and only the influence of confinement effects associated to the fitting of the organic intermediates within the zeolite cages is evaluated. Equilibrium constants for the different reaction steps K_{eq} were calculated as

$$K_{eq} = e^{-\Delta G_{eq}/RT}$$

where ΔG_{eq} is the change in the Gibbs free energy, calculated as

$$\Delta G_{eq} = G_{products} - G_{reactants}$$

Interaction energies (E_{int}) were calculated as the difference in energy between the global system composed by the organic cation inside the zeolite cage model and the sum of the energies of the isolated cation and cluster model. Net atomic charges were obtained using the natural bond order (NBO) analysis as implemented in Gaussian 09 software.[40]

All calculations in **s**ection **3.4** and section **3.5** are based on periodic DFT and were performed using the Perdew-Burke-Ernzerhof (PBE) exchange-correlation functional within the generalized gradient approach (GGA)[41,42], as implemented in the Vienna Ab-initio Simulation Package (VASP) code.[43] The valence density was expanded in a plane wave basis set with a kinetic energy cutoff of 600 eV, and the effect of the core electrons in the valence density was taken into account by means of the projected augmented wave (PAW) formalism.[44] Integration in the reciprocal space was carried out at the Γ k-point of the Brillouin zone. Dispersion corrections to the energies were evaluated using the DFT-D3 Grimme's method.[45,46] The pure silica and pure

aluminophosphate (AlPO) models of ERI, LEV, AEI, CHA, DDR, AFX, RTH, ITE, SAV, UFI, RHO, KFI, and LTA structures were generated by optimizing the unit cell parameters and atomic positions of the experimental structures reported in the IZA database[47] with the computational setup described above. Images and detailed data of each model can be found in Appendix I. Then, keeping the unit cell parameters fixed, one cationic intermediate was placed in each unit cell and the positions of all atoms in the system were fully optimized without restrictions. The interaction energies E_{int} were calculated as the difference in energy between the global system composed by the cationic intermediate inside the zeolite or zeotype model and the sum of the energies of the empty catalyst and the isolated cation. For VASP calculations the isolated cationic intermediates were optimized inside a 20x20x20 unit cell.

$$E_{int} = [E(Zeo_{I^+}) - E(Zeo) - E(I^+)]$$

The interaction energy ratio parameters $E_{int(7/5)}$ and $E_{int(I2/I1)}$ were calculated as:

$$E_{int(7/5)} = E_{int}(7MB^+)/E_{int}(5MB^+)$$

$$E_{int(I2/I1)} = E_{int}(I2^+)/E_{int}(I1^+)$$

As this thesis is mainly based in theoretical chemistry, experimental details produced by collaborators about the aluminosilicates and SAPOs synthesized and reaction conditions shown in this work can be found at the supporting information of each of the articles published by the author of this thesis.[48–50]

3.3 Chemical and Structural Parameter Connecting Cavity Architecture, Confined Hydrocarbon Pool Species, and MTO Product Selectivity in Small-Pore Cage-Based Zeolites.

In a first step, we investigated theoretically the successive methylation of benzenium cation ($C_6H_7^+$) with methanol, considering only isolated organic species not stabilized within any zeolite model. We found, in agreement with a previous work in literature[51], that successive ring methylation leads to the fully substituted hexa-MB^+ cation through several exothermic steps (see Table 3.1a and Scheme 3.2).

As geminal methylation, that is, attack of methanol to a tertiary carbon atom of the aromatic ring, is only favoured for systems with no less than four methyl groups[15,16], we repeated the same procedure for the gem-methylation of several tetra-, penta-, and hexa-MB^+. Results obtained point out that in all cases gem-methylation is less favourable than ring-methylation and it presents clear preferences about the ring position to gem-methylate (see Table 3.1b).

Considering the ring and geminal methylation of tetra-, penta-, and hexa-MB^+ cations, Figure 3.1 was designed for better comprehension of the reader. It comprises values of the relative stabilities of each group of methylbenze isomers with the same stoichiometry, free energy barriers for all possible interconversions between isomers via methyl shifts and energies already presented at Table 3.1 for ring and gem-methylation of each key isomer. All energies are stated in kJ/mol.

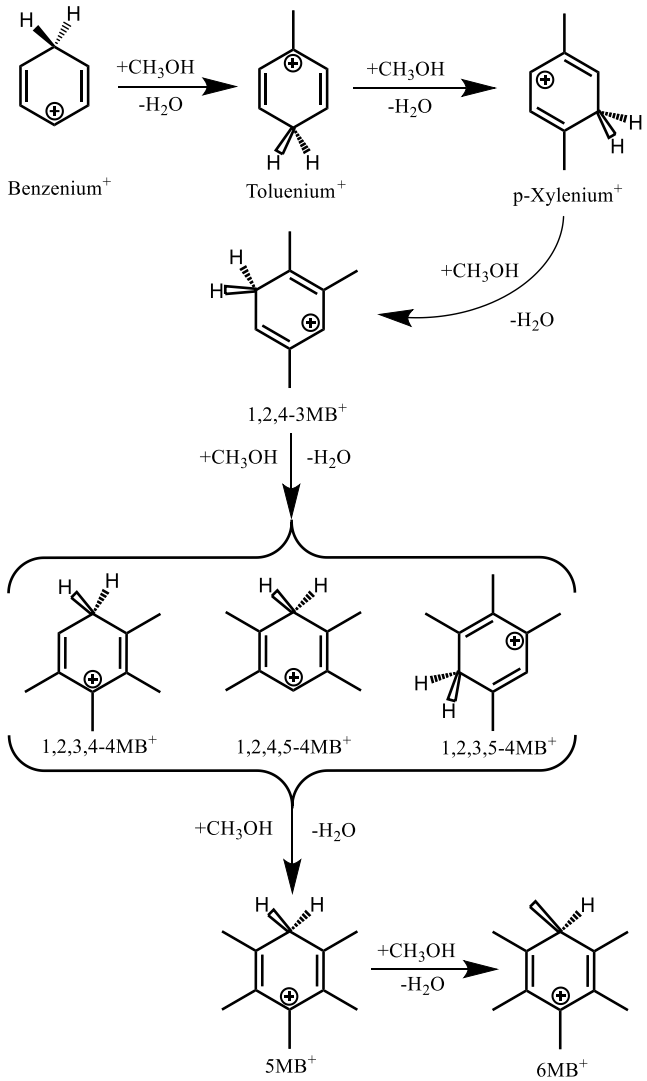

Scheme 3.2. Benzenium cation successive methylations.

Table 3.1. Calculated Gibbs free energies ΔG in kJ/mol and equilibrium constants at 673K for methylation and gem-methylation of polymethylbenzenium cations by methanol according to $R^+ + CH_3OH \rightarrow P^+ + H_2O$.

a) Ring-methylation			
R^+	**P^+**	**$\Delta G_{(ring)}$**	**$K_{eq(ring)}$**
Benzenium$^+$	Toluenium$^+$	-47	4.4×10^3
Toluenium$^+$	p-Xylenium$^+$	-87	5.6×10^6
p-Xylenium$^+$	1,2,4-3MB$^+$ (3MB$^+$)	-57	2.4×10^4
3MB$^+$	1,2,3,5-4MB$^+$ (4MB$_a^+$)	-113	5.2×10^8
3MB$^+$	1,2,4,5-4MB$^+$ (4MB$_b^+$)	-90	9.1×10^6
3MB$^+$	1,2,3,4-4MB$^+$ (4MB$_c^+$)	-86	4.4×10^6
4MB$_a^+$	5MB$^+$	-47	4.4×10^3
4MB$_b^+$	5MB$^+$	-70	2.5×10^5
4MB$_c^+$	5MB$^+$	-74	5.2×10^5
5MB$^+$	6MB$^+$	-33	3.7×10^2
b) Gem-methylation			
R^+	**P^+**	**$\Delta G_{(gem)}$**	**$K_{eq(gem)}$**
4MB$_a^+$	1,2,2,3,5-5MB$^+$ (gem-5MB$_a^+$)	-24	75.5
4MB$_a^+$	1,2,3,5,5-5MB$^+$	0.4	0.91
4MB$_a^+$	1,1,2,3,5-5MB$^+$	8	0.24
4MB$_b^+$	1,1,2,4,5-5MB$^+$ (gem-5MB$_b^+$)	-37	7.7×10^2
4MB$_c^+$	1,1,2,3,4-5MB$^+$ (gem-5MB$_c^+$)	-34	4.1×10^2
4MB$_c^+$	1,2,2,3,4-5MB$^+$	-27	1.3×10^2
5MB$^+$	1,2,2,3,4,5-6MB$^+$ (gem-6MB$_a^+$)	-25	86.4
5MB$^+$	1,1,2,3,4,5-6MB$^+$	4	0.5
5MB$^+$	1,2,3,3,4,5-6MB$^+$	-10	5.9
6MB$^+$	7MB$^+$	-36	6.8×10^2

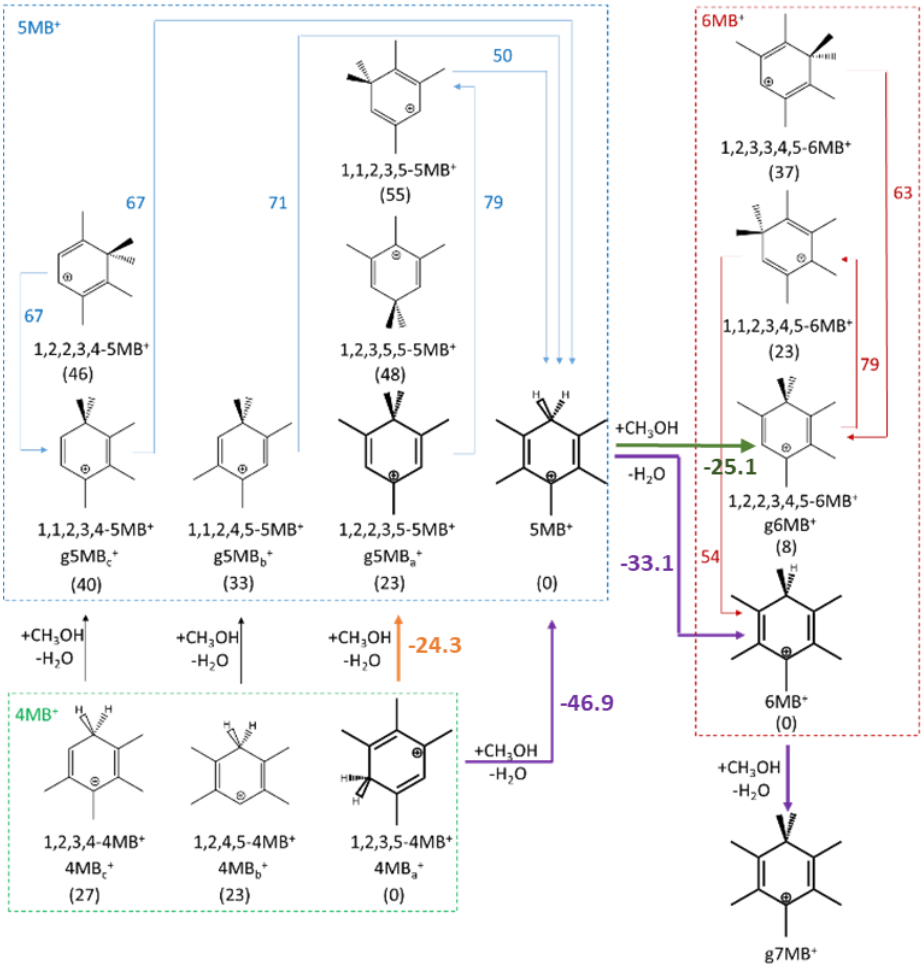

Figure 3.1. Possible pathways for the methylation of isolated MB^+ cations, with the relative stability of isomers with the same stoichiometry ($4MB^+$ in the green box, $5MB^+$ in the blue box, and $6MB^+$ in the red box) given in parenthesis. Activation energies for intramolecular methyl-shifts are shown as coloured numbers alongside the arrows. All values are Gibbs free energies in kJ/mol. Orange and green arrows indicate gem-methylation of species that are more likely to proceed through side-chain route. Purple arrows indicate the preferred methylation steps followed until $g7MB^+$ formation, hence paring route enhancement.

Starting from the most stable isomer of tetra-MB^+ cation ($4MB_a^+$ in Figure 3.1), ring methylation producing $5MB^+$ (-46.9 kJ/mol, purple arrow) is more favourable than gem methylation to form the $g5MB_a^+$ cation (-24.3 kJ/mol, orange arrow), which is considered one of the key intermediates of the MTO mechanism, while other gem-methylated isomers are significantly less stable. Gem-methylation of $4MB_b^+$ and $4MB_c^+$ is also exothermic (Table 1), but the resulting $g5MB_b^+$ and $g5MB_c^+$ species can be directly converted into the most stable $5MB^+$ via one intramolecular methyl shift with activation energies of 70 kJ/mol (values in blue in Figure 3.1). In contrast, the transformation of $g5MB_a^+$ into $5MB^+$ requires two consecutive methyl shifts and the intermediation of the significantly less stable 1,1,2,3,5-$5MB^+$ cation (Figure 3.1 blue box). The thermodynamics of $5MB^+$ ring methylation producing $6MB^+$ (-33.1 kJ/mol, purple arrow) and gem methylation producing $g6MB_a^+$ (-25.1 kJ/mol, green arrow), are not too different, and their interconversion involves two methyl shifts, with the highest activation energy being 79 kJ/mol (red box). Finally, only gem methylation yielding $g7MB^+$ is possible for the fully methylated $6MB^+$ cation. The equilibrium constants calculated at 400 °C, $K_{eq(ring)}$ and $K_{eq(gem)}$, summarized in Table 3.1, indicate that, among the different cationic species studied, $g5MB_a^+$, $g6MB^+$, and $g7MB^+$ can be considered persistent intermediates (I0 in Scheme 3.1) able to react following any of the alternative routes proposed for the MTO reaction, while a much lower contribution of $g5MB_b^+$ and $g5MB_c^+$ should be expected.

Notice that at this point, the zeolite lattice has not yet been taken into account, and therefore, we should be cautious in interpreting the absolute quantitative values. The influence of the zeolite framework will be introduced later for selected frameworks. The side-chain path of the MTO mechanism starts with exomethylation of these I0 gem-PMB^+ cations generating ethyl substituted species (I3 in Scheme 3.1), with calculated Gibbs free energies of reaction that do not change much with the degree of methylation of the I0 intermediates ($\Delta G_{(side)}$ ~40 kJ/mol; see $\Delta G_{(side)}$ Table 3.2). In contrast, the stability of the bicycle hexenyl cation (I1 in Scheme 3.1) formed in the first step of the paring route varies strongly with the substitution pattern in the aromatic ring. Thus, the formation of I1 from $g7MB^+$ cation is endothermic by 14 kJ/mol, but the same process starting from $g5MB_a^+$ is energetically disfavoured by 111 kJ/mol ($\Delta G_{(paring)}$ Table 3.2).

Table 3.2. Calculated Gibbs free energies kJ/mol for the ring- and gem-methylation of MB^+ cations, and for the first step in the side-chain and paring routes of the MTO mechanism in gas phase.

ΔG(ring)	**gas**	**Keq (ring)**
$4MBa^+ \rightarrow 5MB^+$	-47	4.4×10^{3}
$5MB^+ \rightarrow 6MB^+$	-33	3.7×10^{2}
ΔG(gem)	**gas**	**Keq (gem)**
$4MBa^+ \rightarrow g5MBa^+$	-24	7.6×10^{1}
$5MB^+ \rightarrow g6MB^+$	-25	8.6×10^{1}
$6MB^+ \rightarrow g7MB^+$	-36	6.8×10^{2}
ΔG(paring)	**gas**	**Keq (paring)**
$g5MBa^+ \rightarrow I1\text{-}5MBa^+$	113	1.6×10^{-9}
$g6MB^+ \rightarrow I1\text{-}6MB^+$	74	1.8×10^{-6}
$g7MB^+ \rightarrow I1\text{-}7MB^+$	29	6.3×10^{-3}
ΔG(side)	**gas**	**Keq (side)**
$g5MBa^+ \rightarrow I3\text{-}5MBa^+$	-39	1.1×10^{3}
$g6MB^+ \rightarrow I3\text{-}6MB^+$	-40	1.3×10^{3}
$g7MB^+ \rightarrow I3\text{-}7MB^+$	-37	6.9×10^{2}

Such large differences in stability for I1 formation can be understood by analysing the charge distribution, optimized geometry, and molecular orbital composition of the I1 isomers (Figure 3.2). The optimized C-C bond lengths and net atomic charges indicate that the positive charge in the most stable I1-$7MB^+$ isomer is symmetrically distributed between two equivalent carbon atoms of the aromatic ring. Removal of only one methyl group, as in the I1-$6MB^+$ isomer, results in a different electron distribution, with one clear C-C bond and with the positive charge localized on one of the methyl substituted carbon atoms of the ring. The same electron distribution is found in I1-$5MB_b^+$ and I1-$5MB_c^+$, which gives rise to similar stabilities. In I1-$5MB_a^+$, however, the five-membered ring contains two C=C bonds, and the positive charge is localized on the tertiary carbon atom where gem-methylation occurred, leading to rupture of one of the bonds in the three-membered ring and to a significantly less stable species. Although the calculated activation energy barriers for this step are equally high for all isomers considered, in the 140 - 170 kJ/mol range

(see Figure 3.3), the differences in stability of the bicyclic intermediates formed are large enough to determine their concentration in the reaction media, and therefore the probability of the reaction following this route.

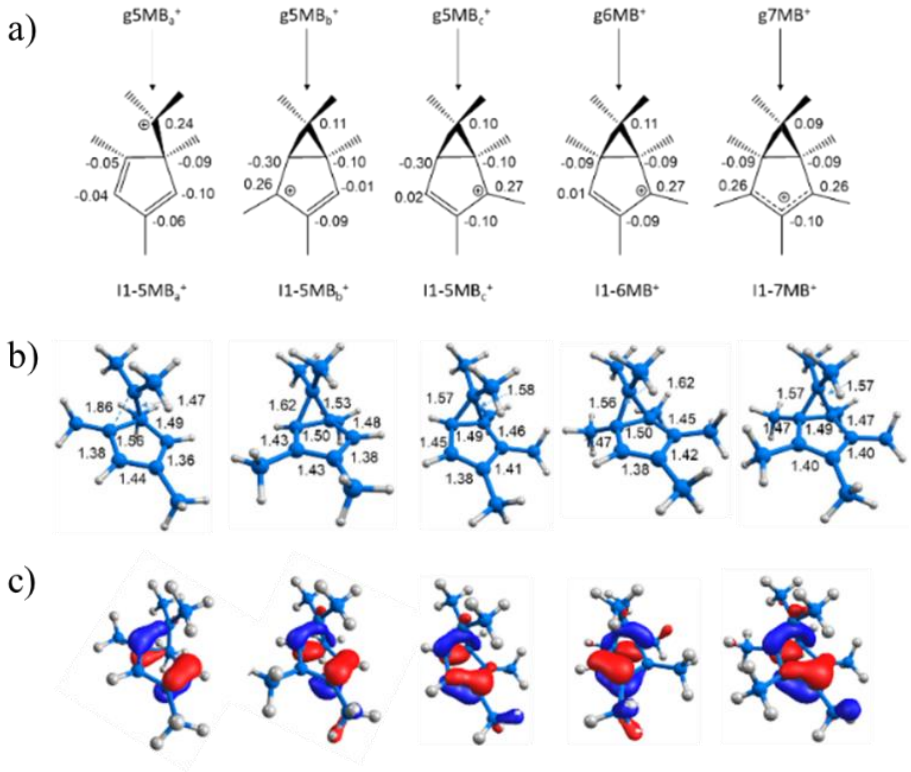

Figure 3.2. I1 intermediates formed in the first step of the paring route from I0 species with different degree of methylation. a) Schematic representation of I1 including net atomic charges on the ring carbon atoms. b) optimized geometries of I1 with calculated C-C bond length values in Å. c) orbital composition of the HOMO of each I1 intermediate. Carbon atoms depicted as blue balls, hydrogen atoms depicted as white balls.

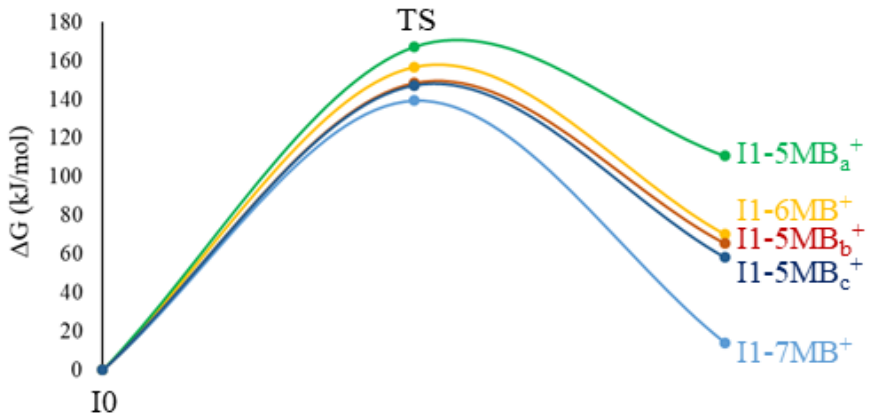

Figure 3.3. Gibbs free energy profile for the first elementary step of the paring route (I0 → I1) calculated at the M062X/6-31G(d,p) level for the five gem-methylated benzenium cation intermediates considered in this work. I0 corresponds to g5MB$_a^+$ (green), g5MB$_b^+$ (red), g5MB$_c^+$ (dark blue), g6MB$^+$ (yellow) and g7MB$^+$ (light blue).

As a conclusion of the gas phase study we use the equilibrium constants calculated at 400 ºC for the first steps in the side-chain and paring pathways summarized in Table 3.2. They indicate that, from the point of view of the intrinsic thermodynamic stability of the key intermediates, the paring route is only affordable for the fully-methylated g7MB$^+$ cation. Therefore, a quantitative parameter trying to describe and predict the olefin distribution in the MTO reaction should include the stability and consequently the concentration of g7MB$^+$.

As a second step of this exhaustive study, the isolated cations, ring- and gem-methylation of MB$^+$ cations, as well as the first steps in the side-chain and paring routes described above, have been re-calculated inside four zeolite cavity models corresponding to CHA, AEI, RTH and ITE structures (Figure 3.4) to evaluate whether the zeolite environment can modify their intrinsic reactivity. The four zeolites contain cages of similar dimensions and different shapes, which are accessible through 8r windows. They also differ in the dimensionality of their pore system, three-directional for CHA and AEI, and two-directional for RTH and ITE. The Brønsted acidic site was not explicitly accounted in these calculations, as we wanted to study particularly the effect of the zeolite cage topology on the stabilization of the key organic intermediates and transition states.

Looking with detail at data on Table 3.3, it points out clearly that the different topology of the four cages plays a key role in the stabilization of the reaction intermediates investigated. The thermodynamic preference for ring- versus gem-methylation of $4MB_a^+$ found in the gas phase is enhanced in RTH and ITE zeolites ($K_{eq(ring)}/K_{eq(gem)}$ ratio ≈ 100), while the CHA and AEI structures have the opposite effect and gem-methylation becomes almost competitive, especially in CHA ($K_{eq(ring)}/K_{eq(gem)}$ ratio = 10). This could be related to the three-fold symmetry of the CHA cage that does not allow all the methyl groups of the higher-methylated planar intermediates to point towards 8r windows to avoid steric repulsions. Due to its smaller size, the $g5MB_a^+$ can rotate and move within the CHA cavity to minimize such repulsions (Figure 3.4).

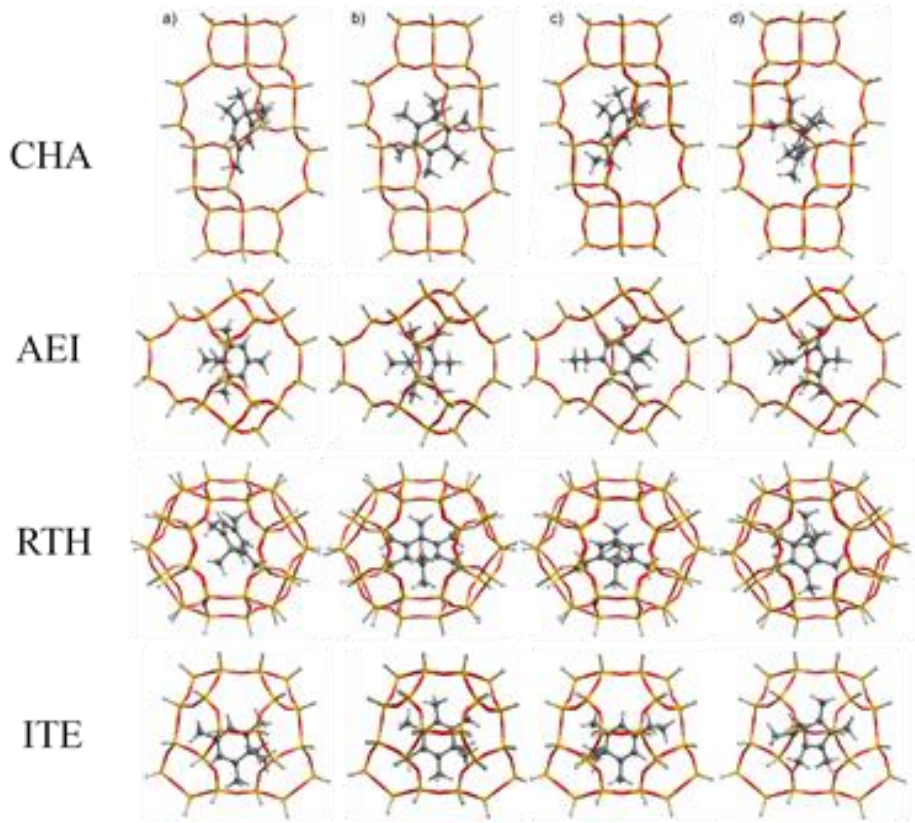

Figure 3.4. Optimized structures of a) gem-$5MB_a^+$, b) $7MB^+$, c) I1-side-$5MB_a^+$ and d) I1-paring-$7MB^+$ cations within the CHA, AEI, RTH and ITE cavity models.

The influence of the cage topology on the gem-methylation of $6MB^+$ cation is also relevant, with the calculated $\Delta G_{(gem)}$ values increasing to -45.6 and -61.1 kJ/mol in ITE and RTH, remaining as in the gas phase in AEI, and becoming endothermic in CHA 3.8 kJ/mol (Table 3.3). Again, this is due to a better fitting of the higher-methylated planar intermediates within the two-fold symmetry of the RTH and ITE cavities, while the particular shape of the AEI cage, also with a 3D pore system, allows a better accommodation of $g7MB^+$ than CHA. These data indicate that the degree of ring-methylation of MB^+ intermediates trapped in CHA will be significantly lower than in the other structures. And, in turn, this has an effect on the probability of the MTO reaction to follow the paring route.

To confirm the trends arising from the relative stability of reaction intermediates, we studied the first steps of the paring mechanism for $g5MB_a^+$ and $g7MB^+$ cations in each of the four different zeolite structures considered, including geometry optimization of both minima and transition states. Previous computational studies report high activation energies, around 100 kJ/mol, for several elementary steps of the side-chain pathway in H-SAPO-34 (exo-methylation, intramolecular methyl-shifts and side-chain ethene elimination),[19–21] which are comparable to the activation energies obtained here for the ring contraction step that starts the paring route. This means that the two proposed pathways are similarly demanding from the kinetics point of view, making more relevant the role of the thermodynamic stability of the key reaction intermediate.

Table 3.3. Calculated Gibbs free energies in kJ/mol and calculated equilibrium constants at 673K for the ring- and gem-methylation of MB^+ cations, and for the first step in the side-chain and paring routes of the MTO mechanism, in gas phase and within different zeolite cavities.

$\Delta G_{(ring)}$	**gas**	**K_{eq}**	**CHA**	**K_{eq}**	**AEI**	**K_{eq}**	**RTH**	**K_{eq}**	**ITE**	**K_{eq}**
$4MB_a^+ \rightarrow 5MB^+$	-47	4.4×10^{3}	-45	3.3×10^{3}	-47	4.2×10^{3}	-57	2.8×10^{4}	-50	7.9×10^{3}
$5MB^+ \rightarrow 6MB^+$	-33	3.7×10^{2}	-38	9.2×10^{2}	-37	7.9×10^{2}	-29	1.9×10^{2}	-36	6.0×10^{2}
$\Delta G_{(gem)}$	**gas**	**K_{eq}**	**CHA**	**K_{eq}**	**AEI**	**K_{eq}**	**RTH**	**K_{eq}**	**ITE**	**K_{eq}**
$4MB_a^+ \rightarrow g5MB_a^+$	-24	7.6×10^{1}	-33	3.3×10^{2}	-31	2.5×10^{2}	-30	2.1×10^{2}	-26	9.3×10^{1}
$5MB^+ \rightarrow g6MB^+$	-25	8.6×10^{1}	-31	2.5×10^{2}	-37	7.4×10^{2}	-24	6.8×10^{1}	-28	1.4×10^{2}
$6MB^+ \rightarrow g7MB^+$	-36	6.8×10^{2}	4	5.2×10^{-1}	-35	5.2×10^{2}	-61	5.4×10^{4}	-46	3.5×10^{3}
$\Delta G_{(paring)}$	**Gas**	**K_{eq}**	**CHA**	**K_{eq}**	**AEI**	**K_{eq}**	**RTH**	**K_{eq}**	**ITE**	**K_{eq}**
$g5MB_a^+ \rightarrow I1\text{-}5MB_a^+$	113	1.6×10^{-9}	98	2.6×10^{-8}	120	5.2×10^{-10}	119	6.0×10^{-10}	114	1.4×10^{-9}
$g6MB^+ \rightarrow I1\text{-}6MB^+$	74	1.8×10^{-6}	71	3.2×10^{-6}	-	-	-	-	74	1.9×10^{-6}
$g7MB^+ \rightarrow I1\text{-}7MB^+$	29	6.3×10^{-3}	-2	1.3	8.4	2.2×10^{-1}	34	2.2×10^{-3}	27	8.6×10^{-3}
$\Delta G_{(side)}$	**gas**	**K_{eq}**	**CHA**	**K_{eq}**	**AEI**	**K_{eq}**	**RTH**	**K_{eq}**	**ITE**	**K_{eq}**
$g5MB_a^+ \rightarrow I3\text{-}5MB_a^+$	-39	1.1×10^{3}	-37	2.6×10^{-8}	-41	1.6×10^{3}	-42	2.0×10^{3}	-33	3.6×10^{2}
$g6MB^+ \rightarrow I3\text{-}6MB^+$	-40	1.3×10^{3}	-70	3.2×10^{-6}	-	-	-	-	-47	4.4×10^{3}
$g7MB^+ \rightarrow I3\text{-}7MB^+$	-37	6.9×10^{2}	-34	1.3	-37	7.9×10^{2}	-44	2.3×10^{3}	-36	5.6×10^{2}
$\Delta G_{(side\text{-}C3)}$	**gas**	**K_{eq}**	**CHA**	**K_{eq}**	**AEI**	**K_{eq}**	**RTH**	**K_{eq}**	**ITE**	**K_{eq}**
$I3\text{-}5MB_a^+ \rightarrow I4\text{-}5MB_a^+$	-37	$7.0\text{x}10^{2}$	-48	$5.3\text{x}10^{3}$	-33	$3.7\text{x}10^{2}$	-8	3.9	-39	$1.0\text{x}10^{3}$
$I3\text{-}7MB^+ \rightarrow I4\text{-}7MB^+$	-16	$1.8\text{x}10^{1}$	-17	$2.2\text{x}10^{1}$	37	$1.3\text{x}10^{-3}$	43	$4.8\text{x}10^{-4}$	23	$1.7\text{x}10^{-2}$

Table 3.4. Relative Gibbs free energies at T = 673 K for the first part of the paring pathway in each zeolite cavity. The origin of energies (G=0) is the sum of the energies of the zeolite cluster model and the corresponding MB^+ cation.

$g5MB_a^+$				
Zeolite	**CHA**	**AEI**	**ITE**	**RTH**
Zeo+ $g5MB_a^+$	0.00	0.00	0.00	0.00
I0	-192.80	-182.45	-198.05	-216.53
TS1	-36.45	-24.61	-29.18	-49.73
I1	-89.31	-72.60	-85.66	-102.44
TS2	-37.97	-28.38	-28.83	-49.94
I2	-58.04	-47.56	-46.19	-66.66
TS3	30.64	44.56	44.23	14.54
I2 + $C_3^=$	-14.40	-15.68	-28.06	-40.73
TS4	41.86	83.62	75.74	28.17
I2 + $C_4^=$	-53.97	-29.68	-56.05	-76.23
$g7MB^+$				
Zeolite	**CHA**	**AEI**	**ITE**	**RTH**
Zeo+ $g7MB^+$	0.00	0.00	0.00	0.00
I0	-122.94	-172.58	-214.98	-240.47
TS1	-36.65	-56.87	-69.91	-90.95
I1	-150.25	-187.17	-200.51	-220.51
TS2	-13.76	-15.12	-60.89	-77.35
I2	-41.31	0.88	-76.37	-82.06
TS3	57.64	45.67	-7.05	-19.71
I2 + $C_3^=$	-80.22	-80.99	-96.19	-112.96
TS4	54.10	30.48	20.88	-24.37
I2 + $C_4^=$	-68.07	-72.63	-95.45	-105.52

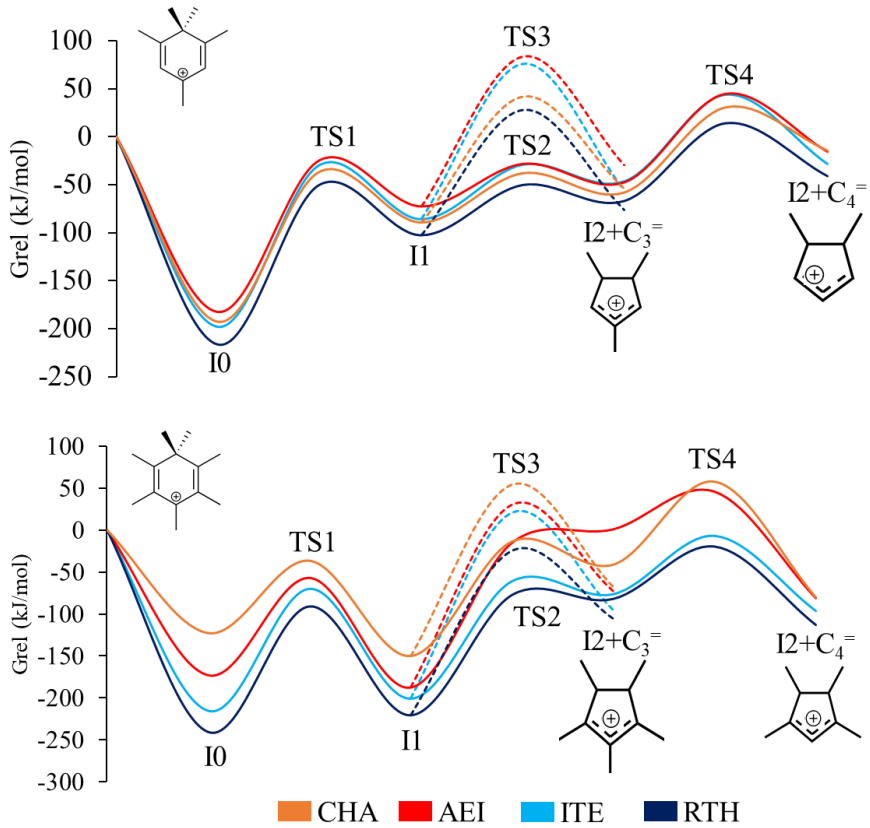

Figure 3.5. Gibbs free energy profile at T = 673 K for the first part of the paring pathway leading to propene (dashed lines) and butene (full lines) for a) g5MBa$^+$ and b) g7MB$^+$ cations within the CHA (yellow) AEI (red) ITE (cyan) and RTH (blue) cavity models. The origin of energies (G=0) is the sum of the energies of the zeolite cluster model and the corresponding MB$^+$ cation. All the corresponding data is shown in Table 3.4.

In Figure 3.5a it is possible to see how the Gibbs free energy profiles obtained for g5MB$_a^+$ cation in different cages are equivalent, suggesting that none of these zeolites would in principle modify the probability of the reaction to start the side-chain pathway. In contrast, the stability of g7MB$^+$ cation depends strongly on the zeolite framework (Figure 3.5b), with the I0 intermediate being up to 117 kJ/mol more stable in RTH than in CHA. As described before, the paring route is energetically affordable only for the fully-methylated g7MB$^+$ cation, whose concentration should be, according to the data in Figure 3.5, much larger in RTH and ITE than in CHA, with AEI being in an intermediate situation. On the other hand, formation of propene through I4 intermediate following the side-chain pathway is energetically disfavored in AEI, RTH and

ITE (Table 3.3 $\Delta G_{(side\text{-}C3)}$) and, despite being feasible in CHA, isotopic labelling studies have shown that propene in CHA is formed via the paring route[34], and some computational studies report higher barriers for propene formation following the side-chain pathway.[17,22]

In summary, this DFT study shows that the relative stability of some reaction intermediates, in particular of the $g7MB^+$ cation necessary to start the paring route, is modified when they are confined in zeolites with different cage topology. In CHA, gem-methylation of $4MB_a^+$ intermediate is competitive, and starts the side-chain pathway that produces ethene. AEI is able to accommodate $g7MB^+$ better than CHA, while full ring-methylation is preferred in RTH and ITE, resulting in a higher concentration of $g7MB^+$ cation and therefore an enhancement of the paring route producing propene and butene.

At this point, we would like to connect the mechanisms proposed theoretically with experimental evidences, including both catalytic tests and advanced characterization techniques. Different cage-based small pore zeolites with the CHA (SSZ-13), AEI (SSZ-39), RTH (RUB-13) and ITE (ITQ-3) frameworks and each of them with different physico-chemical properties were synthesized by our group. Experimental details can be found in Section 3.4 of our published paper and in literature referenced in that section.[52]

These catalysts were first tested for the MTO reaction at 350°C with a WHSV of 0.8 h^{-1}. Under these conditions, their methanol conversion profiles are clearly different, as depicted in Figure 3.6. As a general approximation, larger catalyst lifetimes are observed when the crystal sizes are decreased for a given structure with comparable Si/Al molar ratios (Table 3.4). For instance, CHA-1 and CHA-3 materials, with similar Si/Al ratio but clearly different crystal size, require 260 and 1085 min, respectively, to achieve a methanol conversion drop to 95% (Table 3.4). The same trend is found when comparing CHA-2 and CHA-4, or AEI-1 and AEI-2 although less pronounced in this last case. However, the analysis of their product distributions when the different catalysts are compared at the same conversion level (X~95%) clearly reveals a direct relationship between the products formed and the framework topologies, regardless their crystal size and/or Si/Al ratio. In fact, the $C_3^=/C_2^=$ and $C_4^=/C_2^=$ ratios of the four different CHA catalysts at 95% methanol conversion give analogous values of ~0.8 and ~0.3, respectively (Table 3.4) but, even more interestingly, these ratios remain almost unaltered with TOS during the MTO reaction (Figure 3.6b). The other small pore zeolites AEI, RTH and ITE produce more propene and butene than ethene as compared to CHA. It is worth noting that the overall product selectivity for each zeolite framework mostly remain unaltered when compared at the same conversion level and/or different TOS, even when the physico-chemical properties of the crystals are substantially modified. Interestingly,

there is an experimental correlation between propene and butene selectivity for the different small pore zeolites, where the order found for the $C_3^=/C_2^=$ and $C_4^=/C_2^=$ ratios at 350ºC is ITE > RTH > AEI > CHA. This order is maintained when the different zeolite frameworks are tested at 400ºC (Table 3.4).

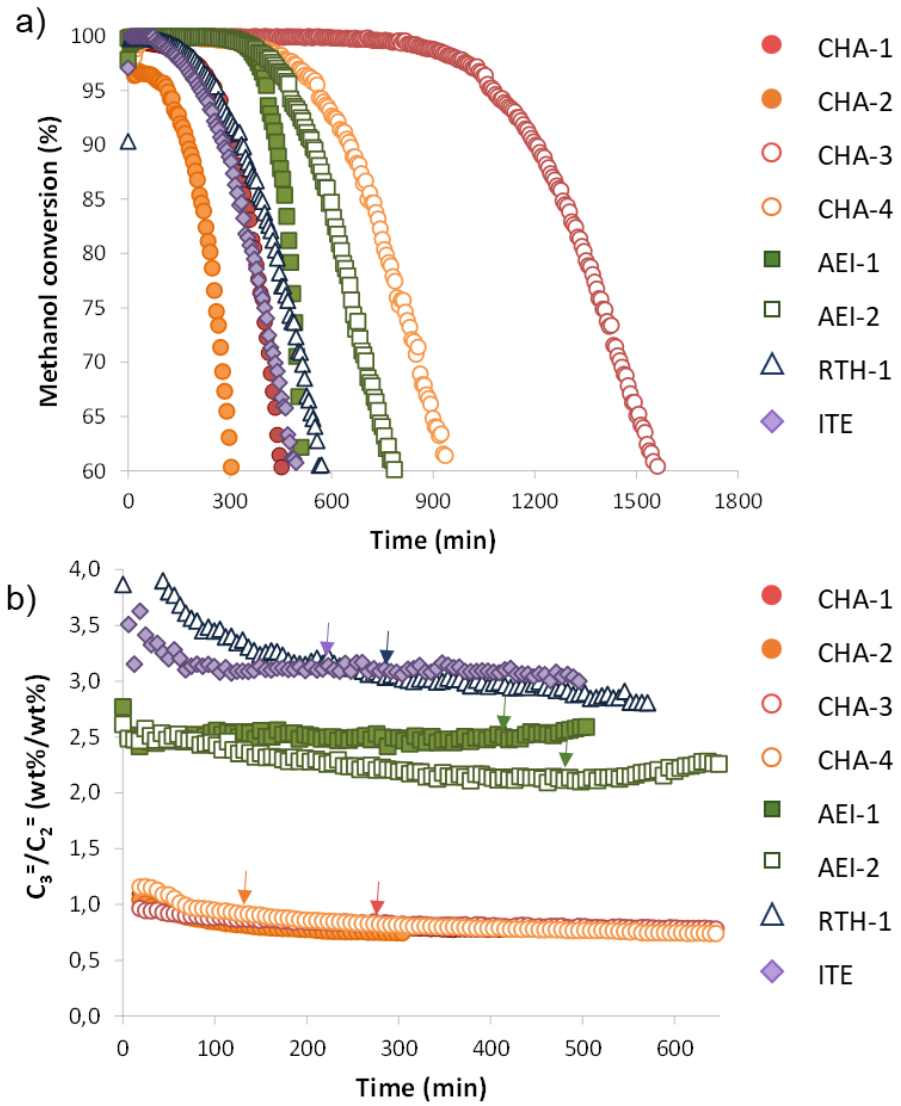

Figure 3.6. Methanol conversion (a) and $C_3^=/C_2^=$ ratio (b) vs time on stream for different small pore zeolites. Reaction conditions: T=350°C, WHSV=0.8 h^{-1}, w_{cat}=50 mg. The arrows indicate the $C_3^=/C_2^=$ ratio at 95% methanol conversion.

Table 3.4. Product selectivity at the same methanol conversion level (X=95%) for the different small pore zeolites with TOS. Reaction conditions: T=350 or 400°C, WHSV=0.8 h^{-1}, w_{cat}=50 mg.

		Lifetime (min)	**Selectivity (%wt)**				
Sample	**T (°C)**	**X_{95}**	**$C_2^=$**	**$C_3^=$**	**$C_4^=$**	**$C_3^=/C_2^=$**	**$C_4^=/C_2^=$**
SSZ-13_1	350	260	45.1	37.0	12.4	0.82	0.27
SSZ-13_2	350	117	44.1	36.6	13.0	0.83	0.29
SSZ-13_3	350	1085	47.1	34.2	12.1	0.73	0.26
SSZ-13_4	350	564	46.8	35.1	12.3	0.75	0.26
SSZ-39_1	350	408	19.6	49.4	21.6	2.50	1.10
SSZ-39_2	350	480	22.6	47.9	22.0	2.20	0.98
RTH-1	350	270	14.7	45.1	24.7	3.07	1.68
ITE	350	217	13.7	42.6	28.2	3.11	2.06
SSZ-13_1	400	670	56.4	30.4	9.2	0.54	0.16
SSZ-39_1	400	446	33.6	44.5	14.2	1.32	0.42
RTH-1	400	236	27.6	44.2	16.8	1.60	0.61
RTH-2	400	105	26.9	42.9	14.8	1.60	0.55
ITE	400	378	24.4	47.8	20.6	1.95	0.84

Although it is not possible to absolutely rule out an influence of diffusion issues through the zeolite windows in this work[31], the trends in selectivity observed for the zeolite structures studied can be mostly associated to the nature of the zeolite cages.[24,25,27] According to molecular dynamics and experimental studies, diffusion of ethene and propene in zeolites with 12r or 10r openings like BEA, FAU or MFI is almost unrestricted, with self-diffusion coefficient ratios of ethene to propene around 2. In contrast, diffusion of propene through the 8r windows of CHA becomes sterically hindered and the self-diffusion coefficient ratio of ethene to propene increases to 20-40 depending on the temperature.[53] Since ethene diffuses much more easily than propene in zeolites containing 8r windows[53], the observation of $C_3^=/C_2^=$ ratios larger than unity in some of the structures indicates that propene is formed in much larger amounts in these materials, in agreement with the DFT results.

In order to evaluate properly the nature of the HP species along the different small-pore zeolites, the MTO reaction was carried out using ^{13}C-labelled methanol at 350 or 400°C, and the used catalysts were characterized by ^{13}C MAS NMR spectroscopy. Two well-differentiated regions appear in the ^{13}C MAS NMR spectra presented in Figure 3.7, one between 155 and 110 ppm assigned to the aromatic carbons present in the HP (C_{arom}), and another between 25 and 10 ppm assigned to alkyl-substituent carbon groups (C_{alk}). From the ^{13}C CP/MAS refocused INADEQUATE spectrum it is possible to differentiate between methylated (C_A) and non-methylated (C_B) aromatic carbons, highlighted in blue and yellow, respectively, in Figure 3.7. The integration of the signals area attributed to these two types of aromatic carbons allows obtaining a quantification of the degree of alkylation of the hydrocarbon pool for the different catalysts (see Table 3.6). Thus, the C_A/C_B ratio at 400ºC is remarkably higher for ITE and RTH (0.6) than for CHA (0.4), confirming the conclusions from the theoretical study.

Table 3.6. C_A/C_B and C_{alk}/C_{arom} ratios estimated from the ^{13}C MAS NMR spectra of the retained organic species in SSZ-13_1, RTH-1 and ITE after performing the MTO reaction with ^{13}C-labelled methanol.

T (ºC)	**time (min)**	**C_A/C_B**			**C_{alk}/C_{arom}**		
		CHA	**RTH**	**ITE**	**CHA**	**RTH**	**ITE**
400	2	0.36	0.61	0.61	0.25	0.38	0.42
400	20	0.42	0.64		0.23	0.39	
350	20	0.56		0.72	0.48		0.59

Table 3.7. E_{int} between the key reaction intermediates and the zeolite cavities.

E_{int}	**CHA**	**AEI**	**RTH**	**ITE**
$g5MB_a^+$	-195	-194	-219	-201
$g7MB^+$	-149	-190	-244	-218
$E_{int(7/5)}$	0.76	0.98	1.11	1.08

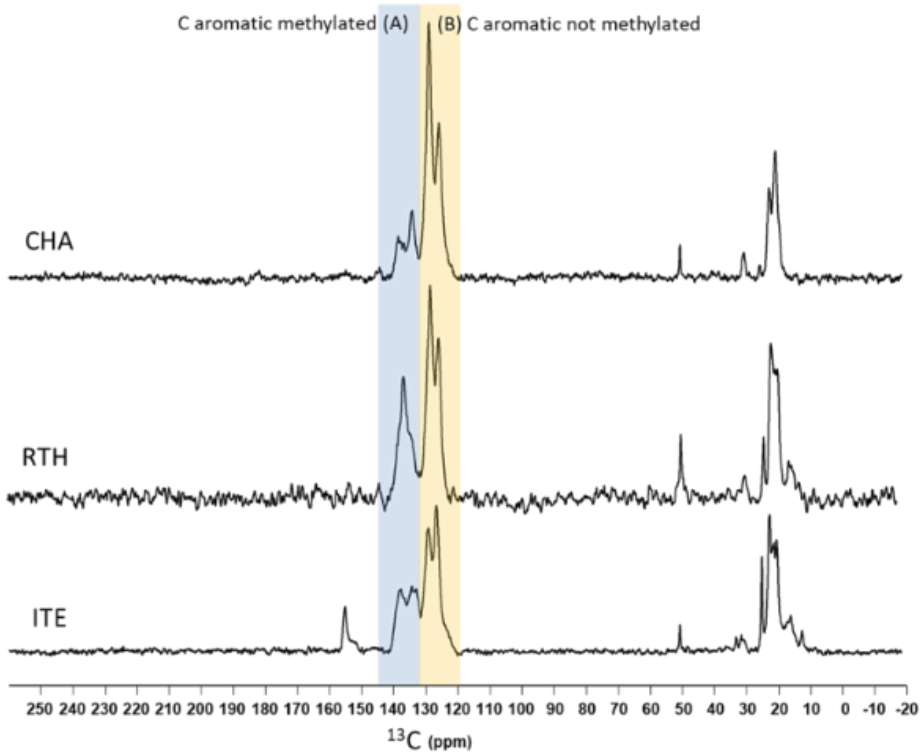

Figure 3.7. ^{13}C MAS NMR spectra of the retained organic species in SSZ-13_1, RTH and ITE after performing the MTO reaction with ^{13}C-labelled methanol at 400°C.

From the mechanistic study shown in this section, it is possible to conclude that the contribution of the paring route is determined by the ability of each cage to host the fully-methylated g7MB$^+$ cation in comparison with the g5MBa$^+$ cation that initiates the side-chain pathway. This ability is quantitatively described by the interaction energy between the cation and the cavity model $E_{int(g5MBa^+)}$ and $E_{int(g7MB^+)}$ in Table 3.7 and therefore we can define an interaction energy ratio $E_{int(7/5)}$ as

$$E_{int(7/5)} = {E_{int(g7MB^+)}}\Big/{E_{int(g5MB_a^+)}}$$

This conclusion is proven by the clear linear relationship found between the measured $C_3^=/C_2^=$ ratios (see Table 3.5) and the $E_{int(7/5)}$ parameter calculated for the four zeolites investigated in this work (Figure 3.8a), and for other reaction conditions and zeolite structures reported in the bibliography (Figure 3.8b).[25,26]

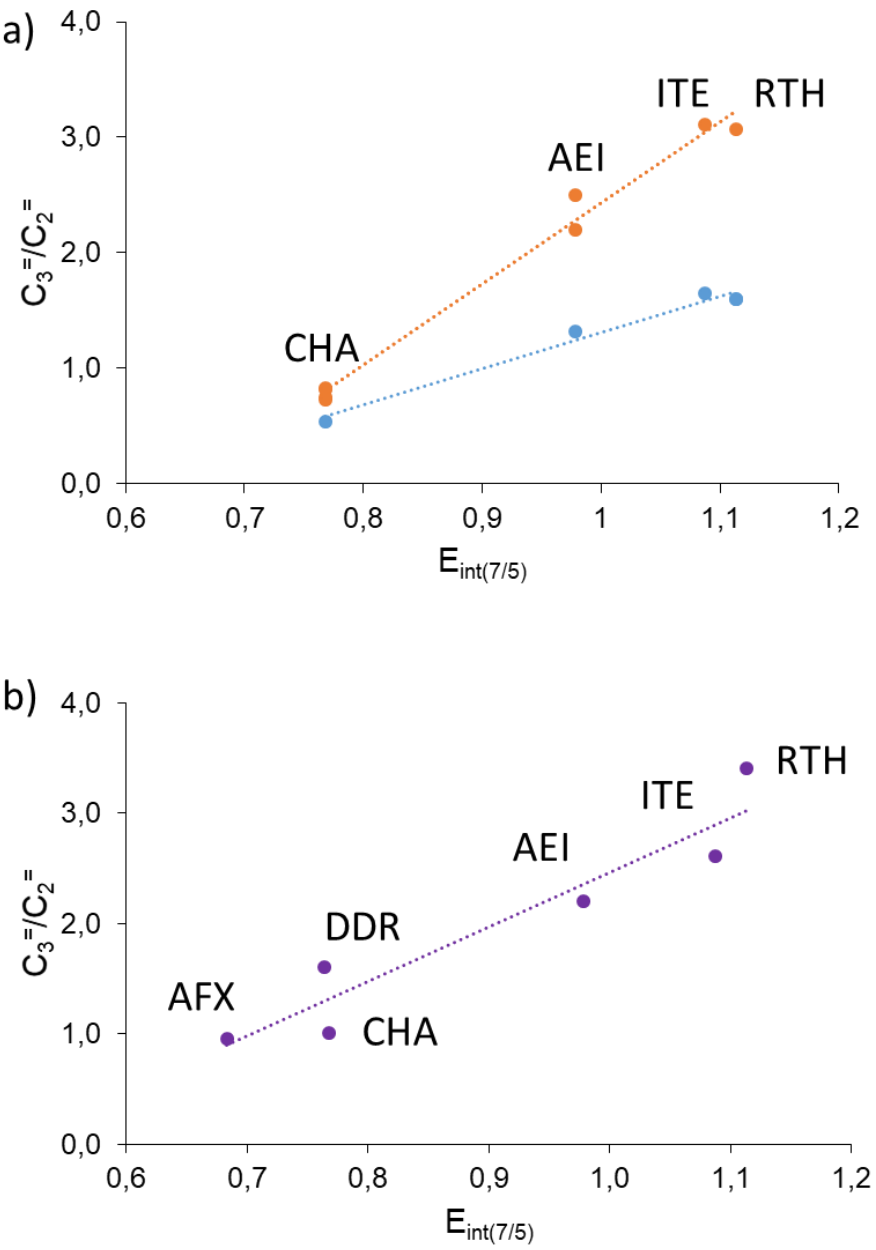

Figure 3.8. Relationship between measured $C_3^=/C_2^=$ ratio and $E_{int(7/5)}$ parameter in different small-pore cage-based zeolites. Reaction conditions: a) WHSV=0.8 h^{-1}, T=400°C (blue) and T=350°C (orange), data from this work, b) WHSV=1.3 h^{-1}, T=400°C, data from Davis et al. work.[28]

3.4 Framework Composition Impact in MTO Product Selectivity.

In the previous section, the study of the MTO mechanism focused on its paring route key intermediates concluded that the ability of each cage to host $7MB^+$ or $5MB^+$ can be quantitatively described by the interaction energies between the cations and pure silica models of different cavities obtained from DFT calculations. Using the calculated interaction energies, an interaction energy ratio or $E_{int(7/5)}$ parameter has been established as descriptor of this relative stabilization. The theoretical parameter presents a linear relationship with the experimental $C_3^=/C_2^=$ ratios measured for different zeolites under different reaction conditions, thus confirming the confinement effect associated to cage topology as the factor governing the MTO product selectivity.[52]

However, the pure silica cluster models used in the study presented in section **3.3** do not take into account the possible effect of acid site concentration or distribution, nor the influence of framework composition on the MTO reactivity. In this section we introduce the effect of framework composition to compare the catalytic behaviour of pairs of zeolites (aluminosilicates) and SAPOs with the same crystallographic structure but different framework composition, H-SSZ-13 and H-SAPO-34 with the CHA structure (Figure 3.9a), or H-SSZ-39 and H-SAPO-18 with the AEI structure (Figure 3.9b). Experimental $C_3^=/C_2^=$ selectivity difference has only been observed between H-SSZ-13 and H-SAPO-34 meanwhile H-SSZ-39 and H-SAPO-18 present similar $C_3^=/C_2^=$ relation.[6,26,28,54–56] The framework composition effect can be divided in different aspects that may have direct incidence over experimental $C_3^=/C_2^=$ selectivity. One factor that could be invoked is the lower acid strength of SAPOs as compared to zeolites, that leads to a lower optimal reaction temperature for the more acidic zeolites and might also have an impact on the reaction mechanism. The different framework flexibility of SAPOs and zeolites could also be claimed as the origin of these observations, since the diffusion of the larger olefins might be enhanced in the more flexible SAPO catalysts.[53–56] In this section, we use periodic DFT to analyse the impact of acid site location and framework flexibility of zeolites and SAPOs on the stabilization of the key MTO reaction intermediates determining the mechanism.

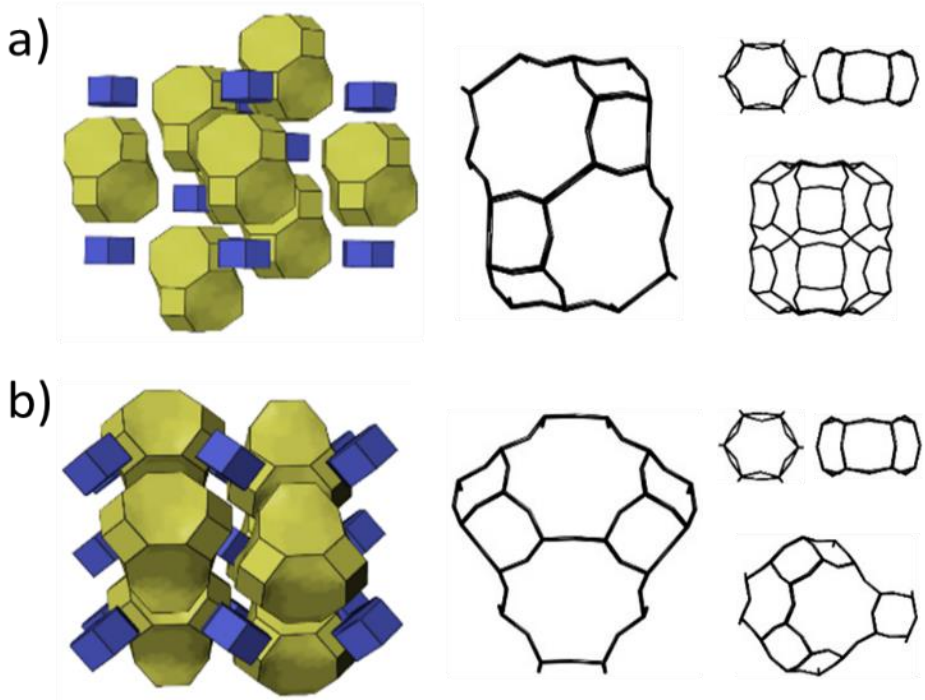

Figure 3.9. Structures of a) CHA and b) AEI frameworks.

The CHA and AEI frameworks are depicted in Figure 3.9. Both crystallographic structures are composed by double six-membered ring units (d6r) that link to form cavities connected by 8r windows with a similar pore opening of 3.8 Å in diameter, but the shape of the resulting cavities is clearly different. The CHA cages are cylindrical whereas AEI presents a basket-like topology with a wider part. This particular shape of the AEI cavity allows a better stabilization of the $7MB^+$ intermediate that leads to a large production of propene when either H-SSZ-39 or H-SAPO-18 catalysts are tested in the MTO reaction. Thus, a product distribution consisting of ~50% propene and similar amounts of ethene and butene, around 20% each, have been reported for the two AEI-based catalysts independently of their framework composition.[10,26,28,54–56] In contrast, CHA-type catalysts tend to produce more ethene and much less propene and butene, but there are differences in product distribution associated to framework composition. H-SSZ-13 always produces more ethene than propene, 45% and 35% respectively, while the opposite relationship is always found for H-SAPO-34.[6,28–30,57]

As a first step of the comparison we started by the global dimensions extracted from IZA database[47] for zeolites SSZ-13 and SSZ-39 (see Table 3.8). Unit cell volumes are similar but their topology is clearly different. From these data and taking into account the accessible volume for each material, (17.27 %) for CHA and (17.31 %) for AEI, and the number of cavities per unit cell, three for CHA and four for AEI, we derived the total volume of the internal cavities that present also similar values and different topology (Table 3.8). According to IZA database, changing the framework composition from silicate to AlPO results in an increase of the unit cell volume of 2.1% for CHA and 1.6% for AEI structures. To confirm the ability of our computational approach to reproduce these trends the unit cell parameters and atomic positions of the SSZ-13, AlPO-34, SSZ-39 and AlPO-18 catalyst models were fully relaxed without restrictions and, in agreement with experiment, the AlPO-34 and AlPO-18 unit cell volumes obtained from the periodic DFT calculations are, respectively, 3.4% and 3.1% larger than the corresponding silica counterparts (Table 3.8).

Table 3.8. Experimental and calculated unit cell volume and cavity volume for SSZ-13, SAPO-34, SSZ-39 and SAPO-18 catalysts.

		Unit Cell V(Å^3)		**Cavity V (Å^3)**	
	Catalyst	**Exp.**	**Calc.**	**Exp.**	**Calc.**
CHA	SSZ-13	2391.6	2416.2	137.8	139.2
CHA	AlPO-34	2441.4	2497.9	140.6	143.9
AEI	SSZ-39	3189.4	3214.1	138.1	139.2
AEI	AlPO-18	3241.9	3312.6	140.4	143.4

The larger unit cell volume of AlPO materials as compared to zeolites could help stabilizing the bulkier $7MB^+$ intermediate, thus favouring the paring route and enhancing the formation of propene and butene, a fact that was experimentally observed in the case of H-SAPO-34. To clarify this point, the interaction energies of $5MB^+$ and $7MB^+$ cationic intermediates with neutral frameworks of SSZ-13, AlPO-34, SSZ-39 and AlPO-18 catalysts were obtained from periodic DFT calculations. In a first set of calculations, the atoms of the zeolite and AlPO lattices were kept fixed to simulate rigid materials, and only the cationic intermediates were fully optimized without restrictions (Table 3.8). In a second step, all the framework atoms were also allowed to relax to simulate flexible materials (Table 3.8).

Table 3.8. Interaction energies in kJ/mol between the key reaction intermediates $5MB^+$ and $7MB^+$ and neutral catalyst models and $E_{int(7/5)}$ parameters calculated with fixed and relaxed frameworks.

	Fixed Framework			Relaxed Framework		
Catalyst	**E_{5MB}**	**E_{7MB}**	**$E_{(7/5)}$**	**E_{5MB}**	**E_{7MB}**	**$E_{(7/5)}$**
SSZ-13	-598	-548	0.91	-607	-569	0.93
AlPO-34	-590	-536	0.91	-598	-565	0.95
SSZ-39	-632	-590	0.93	-649	-640	0.99
AlPO-18	-619	-602	0.97	-623	-619	1.00

In general, the calculated interaction energies are larger in the silicate models than in the aluminophosphates, which could be related to the acid strength difference between zeolites and SAPOs. To have a reference for this difference in acid strength, the interaction of NH_3 with H-SSZ-13, H-SAPO-34, H-SSZ-39 and H-SAPO-18 catalyst models containing one Brønsted acid site per unit cell, as well as the interaction of NH_4^+ cation with the corresponding neutral catalyst frameworks was studied by means of periodic DFT calculations (Table 3.9 and Figure 3.10). NH_3 is spontaneously protonated to form NH_4^+ cation in all acid catalysts considered, and the calculated interaction energies between NH_4^+ and the negatively charged frameworks are systematically larger in zeolites than in SAPOs. The same ordering is found for the interaction of NH_4^+ cation with the neutral frameworks, indicating that even in the absence of active sites the framework composition alters the charge distribution and the oxygen atoms of silicates are intrinsically more basic than those of aluminophosphates.

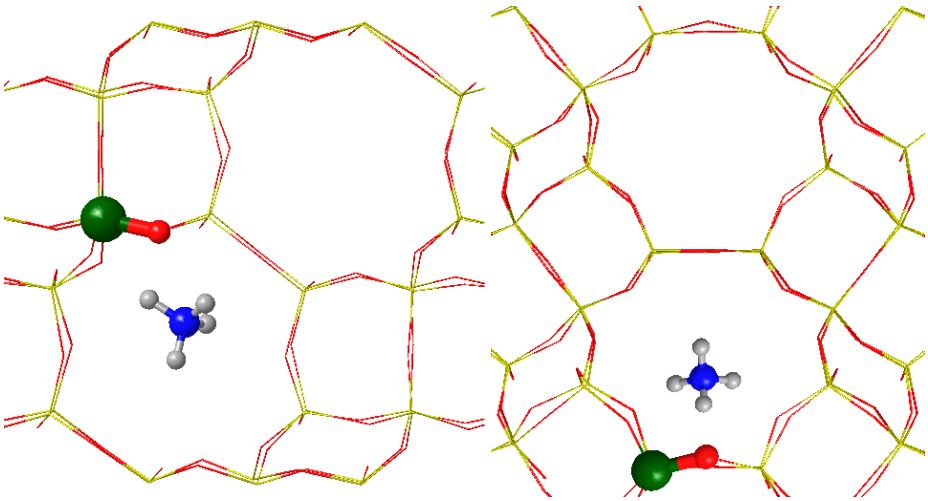

Figure 3.10. a) SSZ-13 cavity with NH_4^+ cation inside b) SSZ-39 cavity with NH_4^+ cation inside.

Table 3.9. Interaction energy in kJ/mol of NH_3 with Brønsted acid sites in zeolites and SAPOs and of NH_4^+ cation with neutral zeolite and AlPO catalyst models.

Catalyst	[a] E_{int} (NH_3)	Catalyst	[b] E_{int} (NH_4^+)
H-SSZ-13	-658	SSZ-13	-626
H-SAPO-34	-652	AlPO-34	-612
H-SSZ-39	-683	SSZ-39	-633
H-SAPO-18	-646	AlPO-18	-615

a) E_{int} (NH_3) = E(H-SSZ-13 + NH_3) – E(H-SSZ-13) – E(NH_3)
b) E_{int} (NH_4^+) = E(SSZ-13 + NH_4^+) – E(SSZ-13) – E(NH_4^+)

Therefore, the fact that the interaction energies of $5MB^+$ and $7MB^+$ are larger in the silicate models than in the aluminophosphates is mostly due to the higher intrinsic acidity of zeolites as compared to SAPOs. However, as $5MB^+$ and $7MB^+$ are similar molecules, this acid strength effect is quite similar for them, so their relative stabilization measured by the $E_{int(7/5)}$ parameter is not too affected by the catalyst composition.

To analyse the influence of framework flexibility we compared the interaction energies calculated keeping the lattice atoms fixed with those obtained from fully relaxed optimizations (see Table 3.9). When materials are considered rigid, $5MB^+$ is always better stabilized than $7MB^+$ because of its smaller size. The $E_{int(7/5)}$ parameters calculated with fixed framework indicate, on one side, that the two AEI catalysts would produce more propene than the two CHA materials and, on the other side, that changing catalyst composition in CHA would have no effect on product distribution, while SAPO-18 would produce more propene than SSZ-39. This result clearly contradicts the experimental observations in literature, and suggests that rigid models are not adequate to describe these systems. When framework flexibility is included in the second set of calculations, interaction energies increase systematically due to a better accommodation of the cations inside the cavities, but the effect is more pronounced for the bulkier $7MB^+$ intermediate. Indeed, while E_{int} values for $5MB^+$ increase from 4 to 17 kJ/mol, the extra stabilization achieved for $7MB^+$ ranges from 17 to 50 kJ/mol, leading to significant differences in the $E_{int(7/5)}$ parameters. The $E_{int(7/5)}$ values obtained with relaxed framework atoms for the two AEI catalysts are similar (see Table 3.9) and larger than those calculated for CHA materials, for which catalyst composition has an influence and the $E_{int(7/5)}$ parameter calculated for AlPO-34 is larger than for SSZ-13.

To understand this effect, the geometry deformations that the entrapped hydrocarbon pool intermediates provoke in the four cavities considered have been analysed in detail. According to Davis[10], the cage-defining ring encircles the centre of the cages in cage-based zeolites, that is, it is the ring enclosing the cationic intermediates of the MTO reaction, and its size can be defined as the number of tetrahedral atoms of the ring, 12 for CHA and 16 for AEI. The cage-defining ring can also be considered as an ellipse whose area can be more accurately estimated from the *a* and *b* distances obtained from the geometry optimizations (see Figure 3.11). Making use of this topologic parameter, we calculated the cage-defining ring for fully relaxed structures of the empty cavities of each catalyst and monitored its changes when $5MB^+$ and $7MB^+$ cations were introduced (see Table 3.10). Empty cavities in AlPO-34 are initially larger than in SSZ-13, and the presence of entrapped $5MB^+$ and $7MB^+$ cations leads to a systematic enlarging of the ellipse area in the flexible aluminophosphate. In contrast, the dimensions of the cages in the more rigid SSZ-13 framework can only increase slightly in the presence of entrapped cations, resulting in a low stabilization of the bulkier $7MB^+$. Notice that the ellipse area in empty AlPO-34 is larger than in SSZ-13 hosting $7MB^+$, which would explain the different stabilization of this intermediate in the two CHA catalysts. The situation is completely different in the catalysts with the AEI structure. The area of the ellipse in the empty SSZ-39 and AlPO-18 cavities is much larger than in the empty cavities of SSZ-13 and AlPO-34, and the presence of entrapped $5MB^+$ and $7MB^+$ cations leads to a contraction of the ring to try to increase the stabilizing interactions between the organic cations and the framework oxygen. Again, the geometry deformation is easier in the more flexible AlPO-18 than in the more rigid zeolite SSZ-39, and the final optimized area of the ellipse containing the cationic intermediates in the less restricted AlPO-34 and AlPO-18 materials are quite similar. The larger cage-defining ring size of AEI (16T atoms) as compared to CHA (12T atoms) could explain the easier deformation of the AEI cavity to stabilize entrapped organic cations, irrespectively of the framework composition.

Table 3.10. Cavity geometry deformation in neutral catalysts due to the presence of entrapped $5MB^+$ and $7MB^+$ cations. The ellipses used to define each cavity are shown in Figure 3.11.

Catalyst	**Area of empty cavity ($Å^2$)**	**Area with $5MB^+$ ($Å^2$)**	**Area with $7MB^+$ ($Å^2$)**
SSZ-13	40.6	41.9	41.8
AlPO-34	41.9	42.1	43.2
SSZ-39	47.9	45.6	45.9
AlPO-18	48.2	42.5	43.9

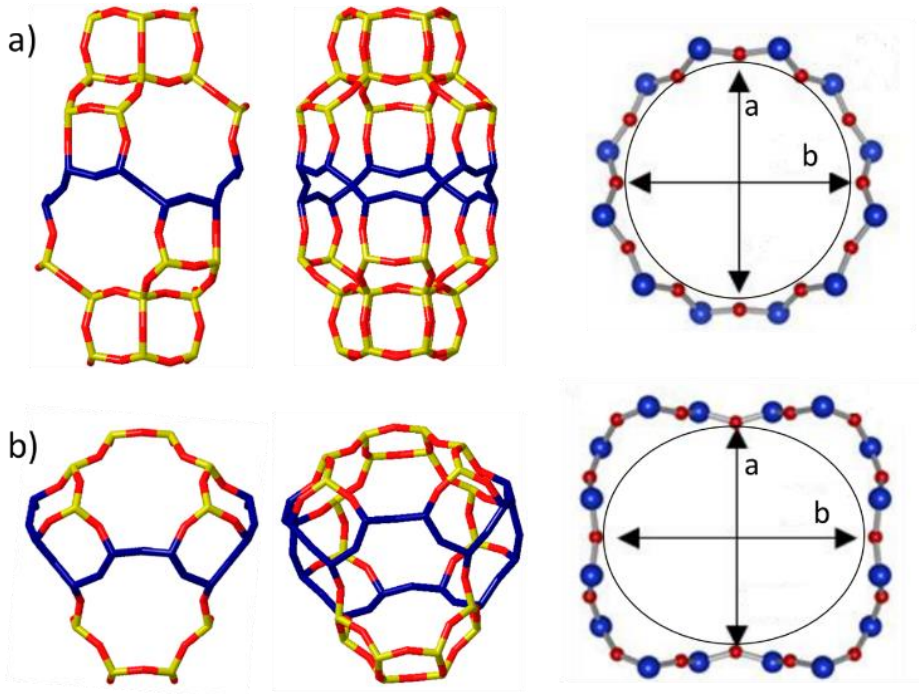

Figure 3.11. Cage defining ring in a) CHA and b) AEI frameworks.

From these data it can be concluded that framework flexibility favours the stabilization of $7MB^+$ in AlPO-34 as compared to SSZ-13, but the effect is less important in catalysts with the AEI structure. The calculated $E_{int(7/5)}$ parameters follow the order SSZ-13 < AlPO-34 < SSZ-39 ≤ AlPO-18, in good agreement with the $C_3^=/C_2^=$ olefin ratio experimentally measured in literature.

The neutral models employed in previous section are able to capture the confinement effect associated to framework architecture or cavity topology, but do not contain the Brønsted acid sites responsible for the catalytic activity of zeolites and SAPOs. Acid sites, Al atoms in zeolites and Si atoms in SAPOs, can occupy different framework positions around the confined intermediates, and the different interactions arising might have an impact or not on product distribution. To clarify this point Brønsted acid sites were created in different positions of CHA and AEI structures by introducing Al and Si in silicates and AlPOs, respectively, thus generating several H-SSZ-13, H-SAPO-34, H-SSZ-39 and H-SAPO-18 models (see Figure 3.12). The interaction of the cationic intermediates with the negatively charged heteroatom-containing catalyst models was evaluated and the results are summarized in Table 3.11.

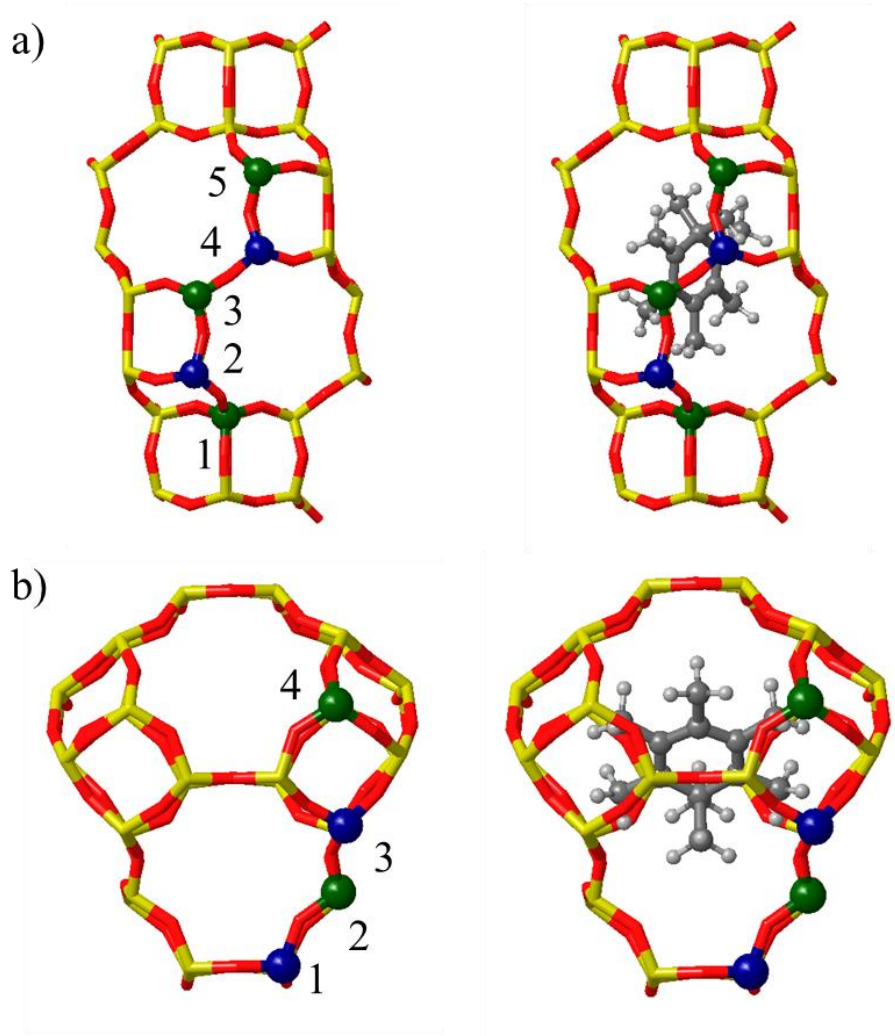

Figure 3.12. Acid site location in a) CHA and b) AEI frameworks. For blue positions Si was substituted by Al, for green positions Si substituted by Al in silicates and P was substituted by Si in AlPO models.

Table 3.11. Interaction energies in kJ/mol between the key reaction intermediates and active-site containing catalyst models and $E_{int(7/5)}$ parameters.

	T	$E_{int}(5MB^+)$	$E_{int}(7MB^+)$	$E_{int(7/5)}$
SSZ-13	1	-561	-515	0.92
	2	-561	-519	0.92
	3	-573	-527	0.92
	4	-577	-527	0.91
	5	-569	-519	0.92
AlPO-34	1	-552	-527	0.96
	3	-552	-536	0.97
	5	-552	-527	0.96
SSZ-39	1	-619	-611	0.99
	2	-628	-619	0.99
	3	-615	-607	0.99
	4	-615	-607	0.99
AlPO-18	2	-594	-594	1.00
	4	-594	-594	1.00

A general trend that can be observed from Table 3.11 is the better stabilization produced by the heteroatom locations closer to the positive charge in the cationic intermediates (see Figure 3.12). But taking into account that the positive charge in $5MB^+$ and $7MB^+$ is highly delocalized and the large number of van der Waals interactions or contacts with framework oxygen atoms contributing to the stabilization by confinement, the differences in stability associated to Al or Si position are relatively small. The differences are less than 16 kJ/mol in the zeolites and almost negligible in the SAPOs because of the milder acid strength explained previously and the lower number of positions to study, as only P framework atoms can be substituted by Si atoms (atoms with green colour at Figure 3.12). Moreover, the order of stability is the same for $5MB^+$ and $7MB^+$, so that the $E_{int(7/5)}$ parameters are almost independent of heteroatom location. Interestingly, the $E_{int(7/5)}$ values obtained using more realistic active-site containing models (0.92 for H-SSZ-13, 0.96 for H-SAPO-34, 0.99 for H-SSZ-39 and 1.00 for H-SAPO-18) are nearly the same as those obtained considering neutral SiO_2 and AlPO frameworks (see Table 3.9), confirming that cavity architecture is the key factor determining the stability of the entrapped carbocationic intermediates.

At this point, we have already studied theoretically the main factors that may have an influence over experimental MTO selectivity with a clear conclusion relating cavity topology and propene production. Therefore, as the theoretical study is concluded, the results can be correlated with experimental data. Then, as we did in section 3.3, we relate the theoretical data presented with in-house experimental data produced in our group. For this part of the study new samples of SSZ-13, SSZ-39, SAPO-34 and SAPO-18 were synthesized. The catalytic performance of these materials in the MTO reaction was tested at 623 K and 673 K, with a WHSV of 0.8 h^{-1} (see Table 3.12 and Figures 3.13). The two H-SSZ-13 catalysts with different Si/Al ratio and crystal size produce preferentially ethene, with ~46% selectivity at 95% methanol conversion, and the $C_3^=/C_2^=$ and $C_4^=/C_2^=$ ratios are similar for both materials, ~0.8 and ~0.3 (see Table 3.12). In contrast, the two H-SSZ-39 catalysts preferentially produce propene, with ~46% selectivity at 95% methanol conversion, and nearly equivalent amounts of ethene and butene, ~20% each, resulting in $C_3^=/C_2^=$ and $C_4^=/C_2^=$ ratios of ~2.2 and ~1.0, respectively (see Table 3.12). Moreover, these product distributions and ratios mostly remain constant during the MTO reaction under the studied conditions (see Figures 3.11), even during catalyst deactivation when methanol conversion values are below 100%. A wider explanation over synthesis and experimental details can be found in our published paper.[49]

Table 3.12. Product selectivity at the same methanol conversion level (X=95%) for the different small pore zeolites and zeotypes and catalyst lifetime. Reaction conditions: T=623 or 673 K, WHSV=0.8 h^{-1}, w_{cat}=50 mg.

	Time (min)	**Selectivity (%wt)**			**Ratios**	
Sample	**X_{95}**	**$C_2^=$**	**$C_3^=$**	**$C_4^=$**	**$C_3^=/C_2^=$**	**$C_4^=/C_2^=$**
SSZ-13_1	260	45	37	12	0.82	0.27
SSZ-13_3	1085	47	34	12	0.73	0.26
SAPO-34	447	34	46	14	1.40	0.41
SSZ-39_1	267	21	44	20	2.12	0.94
SSZ-39_2	480	23	48	22	2.20	0.98
SAPO-18_1	138	23	48	21	2.09	0.92
SAPO-18_2	246	23	48	19	2.12	0.82
SSZ-13_1	670	56	30	9	0.54	0.16
SAPO-34	298	38	42	13	1.10	0.35
SSZ-39_1	446	34	45	14	1.32	0.42
SAPO-18_2	471	35	46	13	1.34	0.38

When catalysts with the same framework topology but different composition are compared, i.e., H-SSZ-13 with H-SAPO-34 and H-SSZ-39 with H-SAPO-18, two different situations appear. For CHA-type catalysts framework composition affects the product distribution, and the relative concentrations of ethene and propene obtained with H-SSZ-13 zeolite are reversed in H-SAPO-34 (see Figures 3.13 and Table 3.12). H-SSZ-13 shows higher selectivity to ethene and less to propene at 623 K (~46 and 35%, respectively, see Table 3.12) with $C_3^=/C_2^=$ and $C_4^=/C_2^=$ ratios of 0.8 and 0.26, whereas, in the case of H-SAPO-34, propene is the most abundant olefin with 46% selectivity at 623 K, resulting in an increase of the $C_3^=/C_2^=$ and $C_4^=/C_2^=$ ratios to 1.4 and 0.4, respectively (see Table 3.12). In contrast, in catalysts with the AEI structure, the composition of the framework does not alter the product distribution and very similar selectivity values and $C_3^=/C_2^=$ and $C_4^=/C_2^=$ ratios are obtained for H-SSZ-39 and H-SAPO-18 samples (see Table 3.12 and Figures 3.13). The $C_3^=/C_2^=$ olefin ratios follow the order SSZ-13 < SAPO-34 < SSZ-39 ~ SAPO-18, and this trend is maintained when the catalysts are tested at 673 K (Table 3.12).

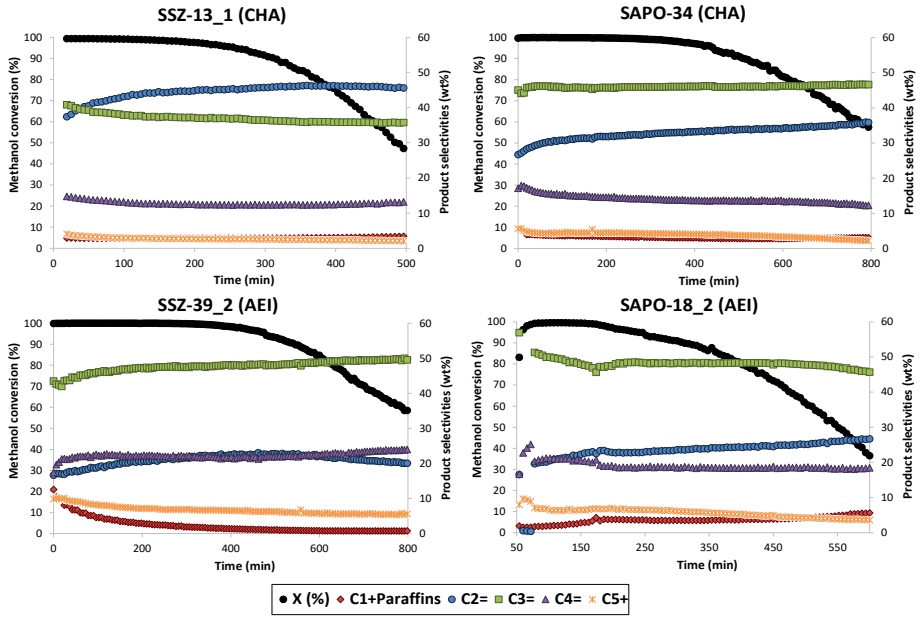

Figure 3.13. Methanol conversion and product selectivities (%wt) with TOS using CHA-type (SSZ-13_1 and SAPO-34) and AEI-type (SSZ-39_2 and SAPO-18_2) catalysts (Reaction conditions: T=623 K, WHSV=0.8 h^{-1}, w_{cat}=50 mg).

When connecting experimental with theoretical data, as it happened in the previous section for cluster models, a linear relationship is found between $C_3^=/C_2^=$ ratios and $E_{int(7/5)}$ parameters for the zeolites and zeotypes considered, either measured in this work (Figure 3.14a) or reported in bibliography using other reaction conditions (Figure 3.14b).[28]

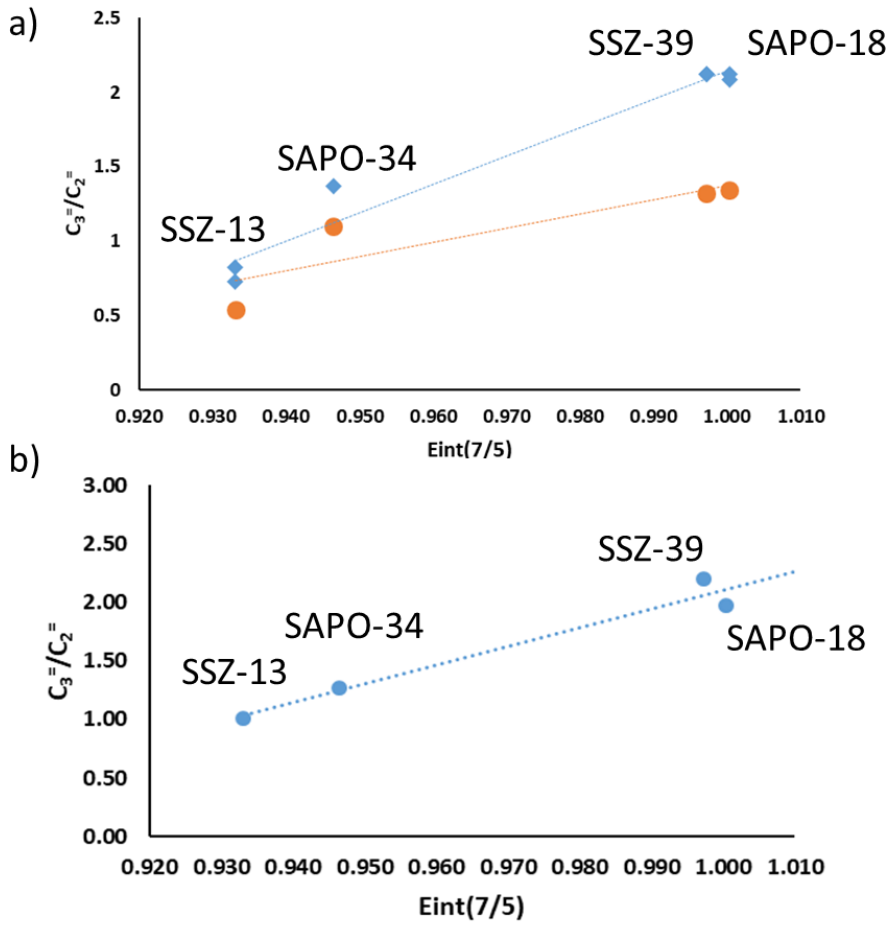

Figure 3.14. Relationship between measured $C_3^=/C_2^=$ ratio and $E_{int(7/5)}$ parameter in small-pore cage-based zeolites and zeotypes. Reaction conditions: a) WHSV=0.8 h^{-1}, T=673 K (orange) and T=623 K (blue), data from this work, b) WHSV=1.3 h^{-1}, T=673 K, data from reference[28].

As a conclusion of the combined analysis with periodic DFT calculations and catalytic activity tests of the main factors that have been proposed to control the olefin product distribution of the MTO reaction catalysed by small-pore cage-based zeolites and zeotypes, we could summarise all the information obtained briefly as follows. First, catalyst samples differing in framework topology (CHA and AEI) and composition (zeolite and SAPO) exhibit different selectivity to ethene, propene and butene. That is because of the cavity topology and its ability to preferentially stabilize the fully methylated $7MB^+$ cations involved in the paring mechanism which is the key factor controlling product distribution, as confirmed by the linear relationship between the experimentally determined $C_3^=/C_2^=$ ratio and the $E_{int(7/5)}$, parameter. Second, the strength, amount and location of the Brønsted acid sites in the catalyst structure has a minor influence, but the larger volume and framework flexibility of SAPOs is key to explain the selectivity differences between SSZ-13 and SAPO-34. The accommodation of the bulky $7MB^+$ cations in the cavities of CHA-type catalysts requires an expansion of the 12T rings enclosing them. This deformation is more energetically demanding in the more rigid zeolite, and consequently the final stabilization of $7MB^+$ and the related $E_{int(7/5)}$ parameter are larger in the more flexible SAPO-34 than in SSZ-13 zeolite.

3.5 Expanding the $E_{int(7/5)}$ parameters towards its limits.

In previous section **3.3** a theoretical study of the paring mechanism for penta- and heptamethylbenzene intermediates in CHA, AEI, RTH and ITE catalyst models showed a preferential stabilization of the fully-methylated species in RTH and ITE cavities, which would result in a higher contribution of the paring route, therefore a larger production of propene, in agreement with the catalytic results. In addition, a new descriptor, the $E_{int(7/5)}$ parameter, was defined from the DFT interaction energy of each cation within the different zeolite cavities to quantitatively describe the ability of a particular cage topology to host the fully methylated intermediates involved in the paring route.[52] A linear relationship was indeed observed between the $C_3^=/C_2^=$ ratios measured for different zeolites and the $E_{int(7/5)}$ parameter corresponding to each catalyst structure, thus confirming that the confinement effect associated to cage topology is probably the factor governing the MTO product selectivity. In section **3.4**, this parameter has been successfully applied to explain the different light olefin product distribution obtained with isostructural H-SSZ-13 and H-SAPO-34 catalysts, both of them with the CHA structure.[49] The larger flexibility of the silicoaluminophosphate material, which is correctly captured by the $E_{int(7/5)}$ parameter, allows the expansion of the cages necessary to accommodate the fully methylated intermediates, leading to an increased production of propene as compared to H-SSZ-13. In this section of the work we extend the study of the theoretical $E_{int(7/5)}$ parameter to a wider range of structures and chemical compositions of catalysts used in the MTO reaction, including the smallest ERI and LEV cages where steric constraints might be present, as well as large cavities such as those of SAV, RHO or LTA structures where the confinement effect might be lost. The final goal is to determine the scope of confinement effects for this process, and set the limits of the $E_{int(7/5)}$ parameter as predictor of product distribution in the MTO reaction. With this aim, the interaction energies of $7MB^+$ and $5MB^+$ intermediates with pure silica and pure AlPO models of ERI, LEV, AEI, CHA, DDR, AFX, RTH, ITE, SAV, UFI, RHO, KFI, and LTA zeolite structures were estimated from periodic DFT calculations (Figure 3.15 and Table 3.13) and used to obtain the $E_{int(7/5)}$ parameters summarized in Table 3.14. For comparison purposes, the diameter of the largest sphere that can be included in each structure (D) according to the IZA database[47] and the CDR according to Davis[28] are also included in Table 3.14.

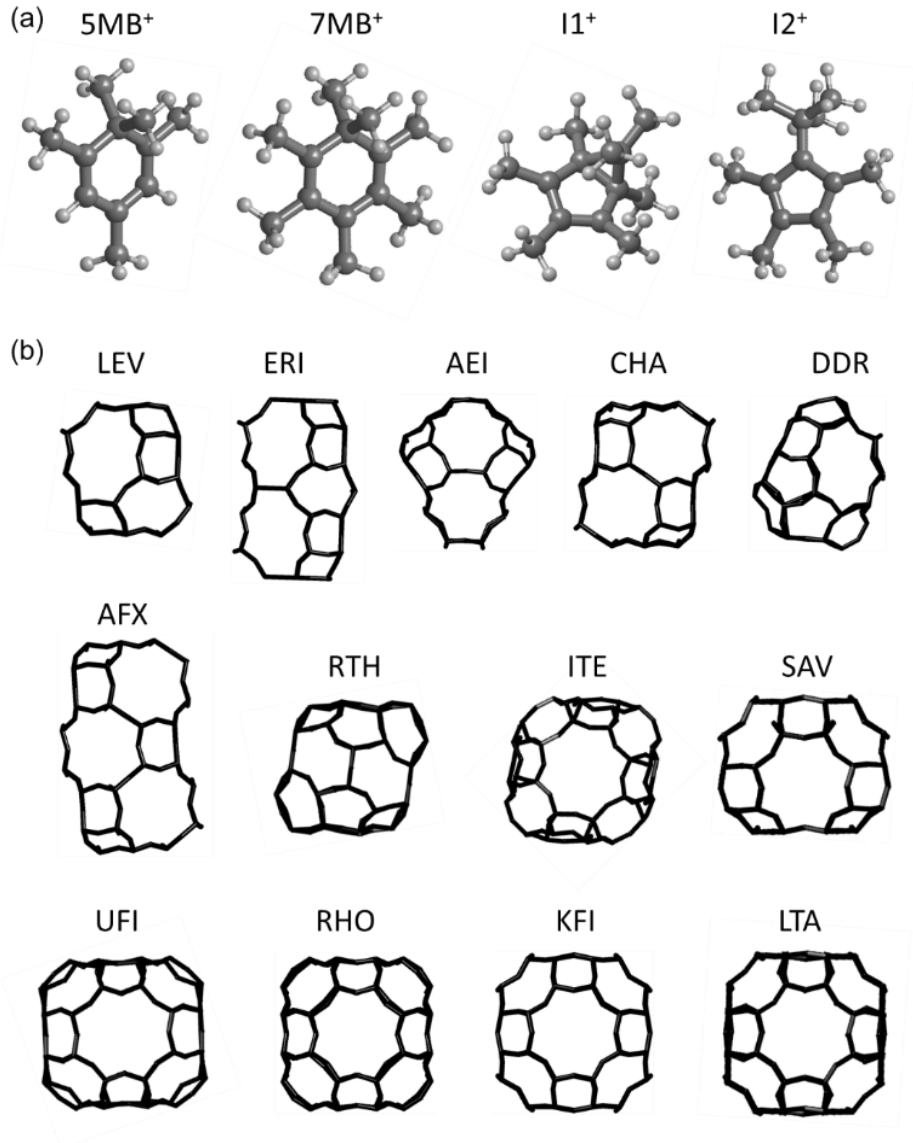

Figure 3.15. Optimized geometries of (a) the key and cationic intermediates in the MTO reaction and (b) the cavities of the ERI, LEV, AEI, CHA, DDR, AFX, RTH, ITE, SAV, UFI, RHO, KFI, and LTA zeolite structures considered in this work.

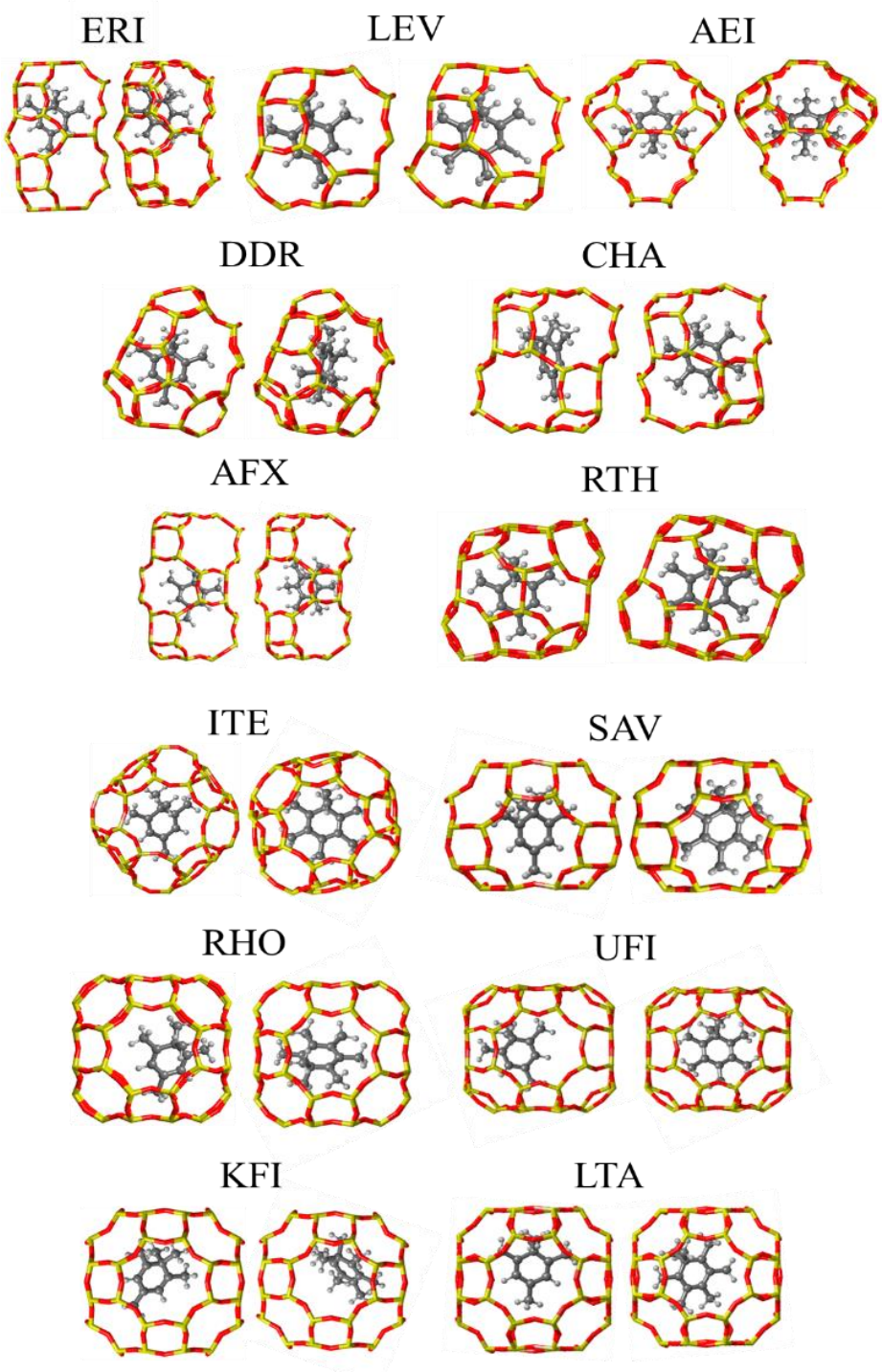

Figure 3.16. Optimized structures of $7MB^+$ and $5MB^+$ confined in pure silica periodic models of small-pore cage-based zeolites.

Table 3.13. Interaction energies (kJ/mol) between selected carbocationic intermediates of the MTO reaction and small-pore cage-based zeolite and AlPO catalyst models.

IZA code	Composition	E_{int} ($5MB^+$)	E_{int} ($7MB^+$)	E_{int} ($I1^+$)	E_{int} ($I2^+$)
ERI	SiO_2	-686	-554	-642	-630
ERI	AlPO	-716	-610	-656	-659
LEV	SiO_2	-621	-510	-598	-545
LEV	AlPO	-626	-560	-619	-543
AEI	SiO_2	-644	-642	-627	-602
AEI	AlPO	-615	-615	-614	-581
CHA	SiO_2	-606	-566	-538	-513
CHA	AlPO	-596	-564	-587	-563
DDR	SiO_2	-707	-676	-690	-653
AFX	SiO_2	-632	-624	-640	-625
AFX	AlPO	-600	-596	-615	-602
RTH	SiO_2	-699	-711	-698	-679
ITE	SiO_2	-676	-684	-709	-690
SAV	SiO_2	-628	-650	-648	-652
SAV	AlPO	-604	-630	-627	-627
UFI	SiO_2	-701	-713	-702	-688
RHO	SiO_2	-606	-616	-613	-611
RHO	AlPO	-583	-589	-591	-597
KFI	SiO_2	-605	-632	-615	-614
KFI	AlPO	-626	-644	-613	-617
LTA	SiO_2	-589	-590	-575	-587
LTA	AlPO	-573	-586	-573	-575

Table 3.14. Structural and energetic parameters used to characterize the cavity topology of small-pore cage-based zeolites used in the MTO reaction.

IZA code	D[a] (Å)	CDR[b] (Å)	$E_{int(7/5)}$		$E_{int(I2/I1)}$	
			SiO_2	AlPO	SiO_2	AlPO
ERI	7.04	6.76	0.81	0.85	0.98	1.02
LEV	7.10	7.15	0.82	0.90	0.91	0.88
AEI	7.33	8.52	1.00	1.00	0.96	0.95
CHA	7.37	7.45	0.93	0.95	0.95	0.96
DDR	7.66	7.07	0.96	-- [c]	0.95	-- [c]
AFX	7.76	7.44	0.99	1.00	0.98	0.98
RTH	8.18	9.00	1.02	-- [c]	0.97	-- [c]
ITE	8.30	9.11	1.01	-- [c]	0.97	-- [c]
SAV	8.82	9.60	1.04	1.04	1.01	1.00
UFI	10.09	10.45	1.02	-- [c]	0.98	-- [c]
RHO	10.43	11.41	1.02	1.01	1.00	1.01
KFI	10.67	10.67	1.05	1.03	1.00	1.01
LTA	11.05	10.44	1.00	1.02	1.00	1.00

[a] IZA Database of Zeolite Structures. [b] Data from ref. [28]. [c] No CIF available.

At first sight, the three parameters used to characterize the cage topology follow the same trend: the smallest spheres are included in the smallest cage-defining rings, for which the smallest $E_{int(7/5)}$ values are obtained. As the diameter of the largest sphere included increases, the cage-defining ring size and $E_{int(7/5)}$ parameter increase too, with the exception of the AEI structure with a very particular cavity shape (see Figure 3.15). A deeper inspection of the values in Table 3.14 and the plot in Figure 16a clearly indicate that while the correlation between CDR and D holds for the whole range of structures considered, in the case of the $E_{int(7/5)}$ parameter this trend is only valid for cavities with diameter D < 9Å, that is, for the zeolite structures from ERI to SAV (see Figure 3.17). In this range of cage dimensions, the composition of the framework (silicate or AlPO) also plays a role in the stabilization of the entrapped carbocations, with the calculated $E_{int(7/5)}$ parameter always being larger for the AlPO materials. As described in the previous section, these results are explained in part by the slightly larger volume cell of the AlPO materials as compared to the isostructural zeolites, (see data in Appendix I), but the most important factor is the increased flexibility of the aluminophosphate framework with respect to that of silicate, which allows a less energy demanding expansion of the cavity that facilitates the accommodation of the bulkier $7MB^+$. This effect is more pronounced for the smaller cavities (ERI, LEV, CHA) and diminishes when the architecture of the silicate cage is adequate to host $7MB^+$ without requiring too much distortion, as in AEI, or SAV with $E_{int(7/5)}$ parameters close to 1. For the wider cavities, UFI, RHO, KFI and LTA, the sphere included can be as large as 11,1 Å diameter and the cage-defining ring oscillates between 10.4 and 11.4

Å (Figure 3.17). However, the $E_{int(7/5)}$ parameter does not further increase and takes values slightly larger than unity, between 1.01 and 1.04, similar to those obtained for RTH and ITE and without any clear influence of framework composition (see Table 3.14). The reason is that $E_{int(7/5)}$ is not just a geometric parameter such as the sphere diameter D or the CDR size, but it is based on the relative stabilization of $7MB^+$ and $5MB^+$ cations by van der Waals interactions with the zeolite framework. Too small cages such as those of ERI and LEV cannot accommodate the bulky $7MB^+$, so that the interaction energies calculated for $5MB^+$ are clearly larger than for $7MB^+$ (see Table 3.13) and the $E_{int(7/5)}$ values are lower than 1. Oppositely, in too large cavities part of the confinement effect is lost because not all the methyl groups of the cationic intermediates can establish good contacts with the framework oxygen atoms. The optimized structures depicted in Figure 3.16 clearly show that the $7MB^+$ and $5MB^+$ cations usually stay in the centre of the cavity in the structures with smaller cages, but tend to move close to the zeolite walls when the cavity dimensions do not fit those of the entrapped organic species. Thus, while $7MB^+$ cation occupies the centre of the UFI cage, which is able to host a sphere of 10.1 Å diameter, the less methylated $5MB^+$ is displaced to one side of the cavity in order to achieve the largest possible number of close contacts with the framework. This displacement aiming to maximize the interactions with the framework is also observed for both $5MB^+$ and $7MB^+$ in the zeolite structures containing the largest cavities, such as RHO, KFI and LTA. In this situation, the bulkier $7MB^+$ is not much better stabilized than the less methylated $5MB^+$ and the calculated $E_{int(7/5)}$ parameter is ~1 regardless the size of the cage. Overall, the results provided are consistent with the idea that the confinement effect associated to cage topology and its influence on the MTO product distribution is diminished in sufficiently large spaces, when the shape and dimensions of the cavity do not fit the hosted species.

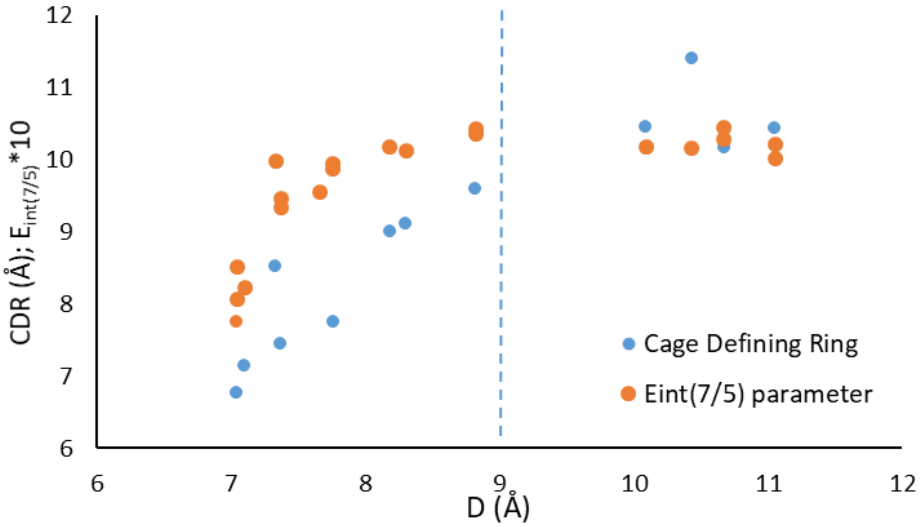

Figure 3.17. Correlation between the diameter (D) of the largest sphere that can be included in small-pore cage-based zeolite structures and the cage-defining ring size (blue) or the Eint(7/5) parameter (orange).

To finish the theoretical study of the paring route for the MTO hydrocarbon pool mechanism we move beyond the HP gem-methylation to rationalize the amount of butene produced by wider cavities, UFI, RHO, KFI and LTA. After the first ring-contraction step in the paring route, the bicycle-hexenyl I1 intermediate formed from I0 can directly decompose yielding propene or convert into a bulkier I2 intermediate precursor of iso-butene. Following the same approach used to quantify the relative contribution of the paring and side-chain routes, a $E_{int(I2/I1)}$ parameter calculated from the interaction energies of the I1 and I2 intermediates with different zeolite structures might provide an estimation of the relative amount of butene and propene that could be expected when using a particular microporous catalyst, assuming that the reaction follows the aromatics-based mechanism. The optimized geometries of the I1 and I2 intermediates allocated in the ERI, LEV, AEI, CHA, DDR, AFX, RTH, ITE, SAV, UFI, RHO, KFI, and LTA zeolite structures are depicted in Figure 3.18, and the calculated parameters $E_{int(I2/I1)}$ are summarized in Table 3.14. Since the two intermediates contain a fully-methylated cyclopentenyl ring and the same number of atoms arranged in a different way, the influence of cavity topology on the $E_{int(I2/I1)}$ values in Table 3.14 is not so evident. Moreover, the values for ERI and LEV are not relevant because in these structures the $7MB^+$ intermediate precursor of I1 and I2 is sterically destabilized and therefore the contribution of the paring route should be low. Altogether, these data suggest that as the $E_{int(7/5)}$ parameter increases and the paring route becomes predominant, the $C_4^=/C_3^=$ relative ratio formed should also increase.

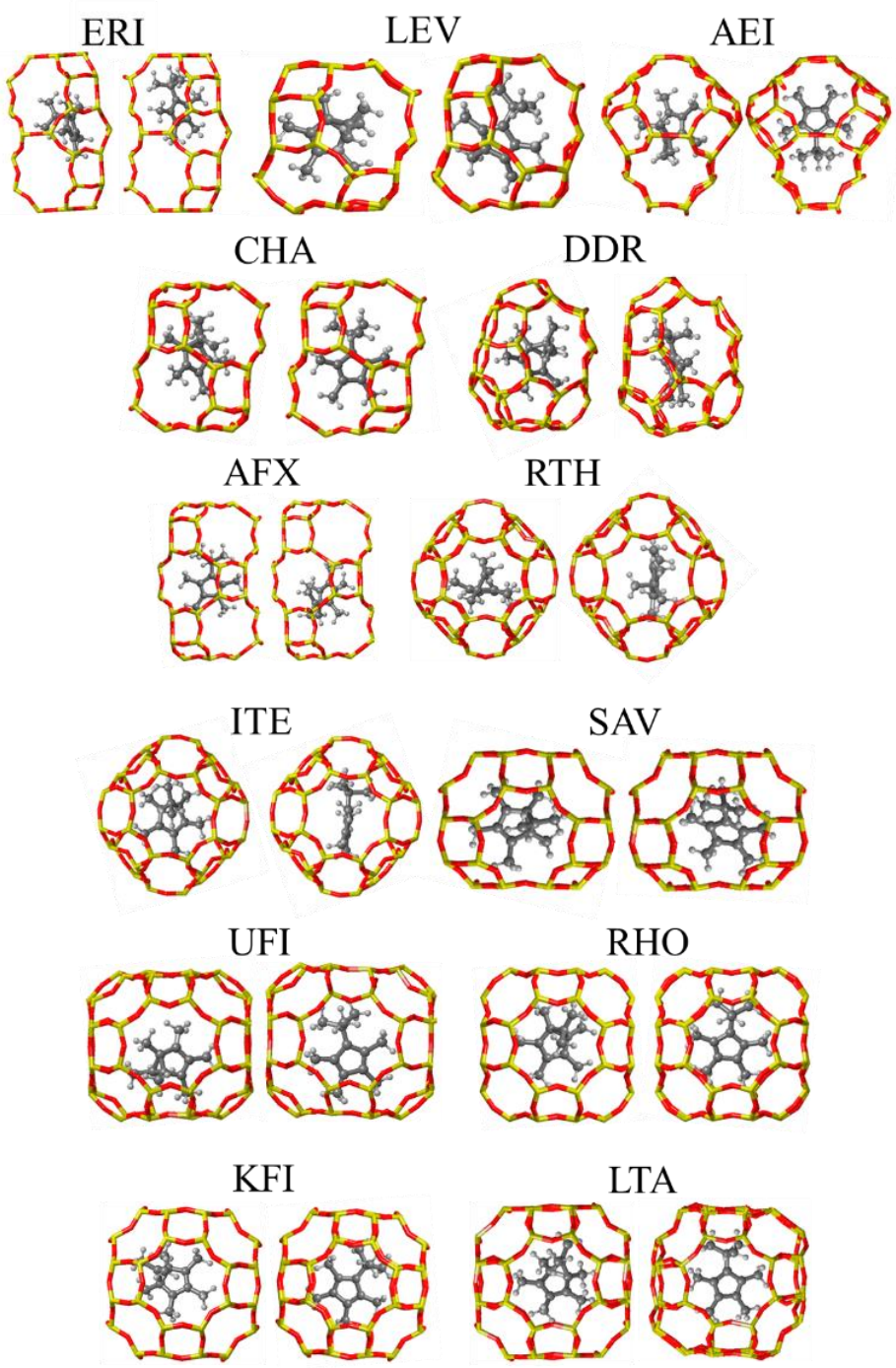

Figure 3.18. Optimized structures of I1 and I2 intermediates (see Figure 3.15) confined in pure silica periodic models of small-pore cage-based zeolites.

To conclude this section and also this Chapter, a systematic evaluation of the catalytic performance of zeolites was done by our group including new LEV and LTA structures that were not present in previous sections. Thus, LEV, CHA, AEI, RTH, ITE and LTA structures with different physicochemical properties, as well as samples of SAPO-34 and SAPO-18 with the CHA and AEI structures were analysed to establish the trends in MTO product distribution expanding the range of cavity topologies studied.

Two samples of zeolite H-SSZ-13 with Si/Al molar ratios of ~15 and crystal sizes of ~1 μm (CHA_1) and ~70 nm (CHA_2), and a sample of isostructural H-SAPO-34 (CHA_3) consisting of crystals of ~1 μm with a (Al+P)/Si molar ratio of ~10 were prepared. For the AEI crystallographic structure, we synthesized two samples of zeolite H-SSZ-39 with Si/Al molar ratios of ~9 and crystal sizes of ~0.7 μm (AEI_1) and ~60 nm (AEI_2), and two samples of H-SAPO-18 with a (Al+P)/Si molar ratio of ~11-13 and crystals of ~150 nm (AEI_3) and ~0.8 μm (AEI_4). Zeolite H-RUB-13 was prepared either as nanocrystallites of ~80 nm with a Si/Al ratio of ~16 (RTH_1) or as micron-sized particles of 1-2 μm and a slightly lower Al content (RTH_2). Zeolite H-SSZ-17 with the LEV structure was synthesized in the form of small crystals of ~70 nm with a Si/Al molar ratio of 9, while ITE and LTA were obtained as intermediate (ITE, 0.5 × 0.2 μm) and large (LTA, 3-4 μm) crystals with Si/Al molar ratios of 13 and 20, respectively. Further experimental details about synthesis and characterization can be found in our published paper.[50] The catalytic performance of all these samples in the MTO reaction was tested at 623 K and 673 K with a WHSV of 0.8 h^{-1}, and the methanol conversion and product distribution results are summarized in Table 3.15 that is an expanded version of Table 3.12 in section **3.4**. In agreement with previous studies, when comparing catalysts with the same crystallographic structure and chemical composition but different physicochemical properties (SSZ-13_1 with SSZ-13_3, SSZ-39_1 with SSZ-39_2, SAPO-18_3 and AEI_4, or RTH_1 with RTH_2), larger catalyst lifetimes are observed for the samples with smaller particle size. However, the light olefin product distribution remains mostly unaltered in these cases, and only varies when the microporous structure of the catalyst is different (see Table 3.15).

As it has been mentioned on each experimental data comparison, it is important to note that the selectivity values and the $C_3^=/C_2^=$ and $(C_4^=+C_3^=)/ C_2^=$ ratios for any given catalyst are not the same at 623 and 673 K because the relative reaction rates change with temperature. However, the trends in selectivity are not modified, and the production of propene and butene via the paring route increases according to LEV < CHA (zeolite) < CHA (SAPO) < LTA ~ AEI (zeolite or SAPO) < RTH ~ ITE (see Table 3.15).

Table 3.15. Product selectivity at the same methanol conversion level (X=95%) for the different small pore zeolites and zeotypes and catalyst lifetime. [a] Reaction conditions: T=623 or 673 K, WHSV=0.8 h^{-1}, wcat=50 mg.

	Life time (min)	**Selectivity (%wt)**					
Sample	**X_{95}**	**$C_2^=$**	**$C_3^=$**	**$C_4^=$**	**$C_3^=/C_2^=$**	**$(C_4^=+C_3^=)/C_2^=$**	**$C_4^=/C_3^=$**
[a]LEV	118	45.7	25.8	9.5	0.56	0.77	0.37
SSZ-13_1	260	45.1	37.0	12.4	0.82	1.10	0.34
SSZ-13_3	1085	47.1	34.2	12.1	0.73	0.98	0.35
SAPO-34	447	33.6	45.9	13.7	1.40	1.77	0.30
SSZ-39_1	267	20.9	44.4	19.6	2.12	3.06	0.44
SSZ-39_2	480	22.6	47.9	22.0	2.20	3.09	0.46
SAPO-18_1	138	22.9	47.8	21.0	2.09	3.00	0.44
SAPO-18_2	246	22.8	48.4	18.7	2.12	2.94	0.39
RTH_1	270	14.7	45.1	24.7	3.07	5.17	0.55
ITE	217	13.7	42.6	28.2	3.11	4.75	0.66
[b]LEV	354	51.9	21.5	9.8	0.41	0.60	0.46
SSZ-13_1	670	56.4	30.4	9.2	0.54	0.70	0.30
SAPO-34	298	37.9	41.8	13.4	1.10	1.46	0.32
SSZ-39_1	446	33.6	44.5	14.2	1.32	1.75	0.32
SAPO-18_2	471	34.5	46.4	13.2	1.34	1.73	0.28
RTH_1	236	27.6	44.2	16.8	1.60	2.80	0.38
RTH_2	105	26.9	42.9	14.8	1.60	2.21	0.34
ITE	378	24.4	47.8	20.6	1.95	2.14	0.43
LTA	-- [c]	28.3	32.2	16.4	1.14	1.72	0.51

[a] 623 K. [b] 673 K. [c] Product selectivity at 75% methanol conversion.

Trying to correlate theory and experiment, we searched for a relationship between the $C_3^=/C_2^=$ and $(C_4^=+C_3^=)/C_2^=$ ratios obtained for zeolites and zeotypes listed in Table 3.15 and the $E_{int(7/5)}$ parameters given in Table 3.14. The plots in Figure 3.19 show that there is indeed a relationship, with the LEV structure with the smallest $E_{int(7/5)}$ value producing more ethene and with the largest $C_3^=/C_2^=$ and $(C_4^=+C_3^=)/C_2^=$ ratios found for the RTH and ITE structures, both of them with a $E_{int(7/5)}$ value larger than 1.01 (Table 3.14). Interestingly, the zeolite structure with the largest cavity, LTA, does not produce the maximum amount of propene and butene among the samples studied. Instead, its catalytic performance regarding olefin product distribution is quite similar to that of AEI, as could be expected from their corresponding $E_{int(7/5)}$ parameters, 1.00 in both cases.

Looking in detail at LEV in Figure 3.19, the relative amount of propene and butene detected in the sample is clearly larger than expected according to its cavity size and its $E_{int(7/5)}$ value, the smallest of all catalysts analysed in both cases. As mentioned before, the cavity in LEV is too small to host the fully-methylated $7MB^+$ intermediate involved in the paring route (see interaction energies in Table 3.13) and the value of the $E_{int(7/5)}$ parameter, 0.822, indicates that $5MB^+$ will be the most abundant aromatic hydrocarbon pool species in LEV, in agreement with previous ^{13}C NMR and GC-MS studies. Therefore, in the absence of $7MB^+$ due to steric constraints, propene and butene in LEV must be formed through the alkene-based cycle of the MTO mechanism while ethene is obtained via the side-chain pathway of the aromatics-based cycle. A deeper inspection of the product distribution shows a larger contribution of pentenes and higher olefins in LEV (~12%) than in any other catalyst (< 6%), further supporting the alkene-based cycle as the main mechanism operating in the smallest cages. On the other hand, the formation of C1 and alkanes is below 5% in all catalysts tested except LTA, where the amount of paraffins is comparable to that of butenes, both of them over 16%. The higher production of alkanes in LTA might be related to the size of the cavity, large enough to accommodate bulky intermediates or transition states participating in hydrogen transfer processes.[58]

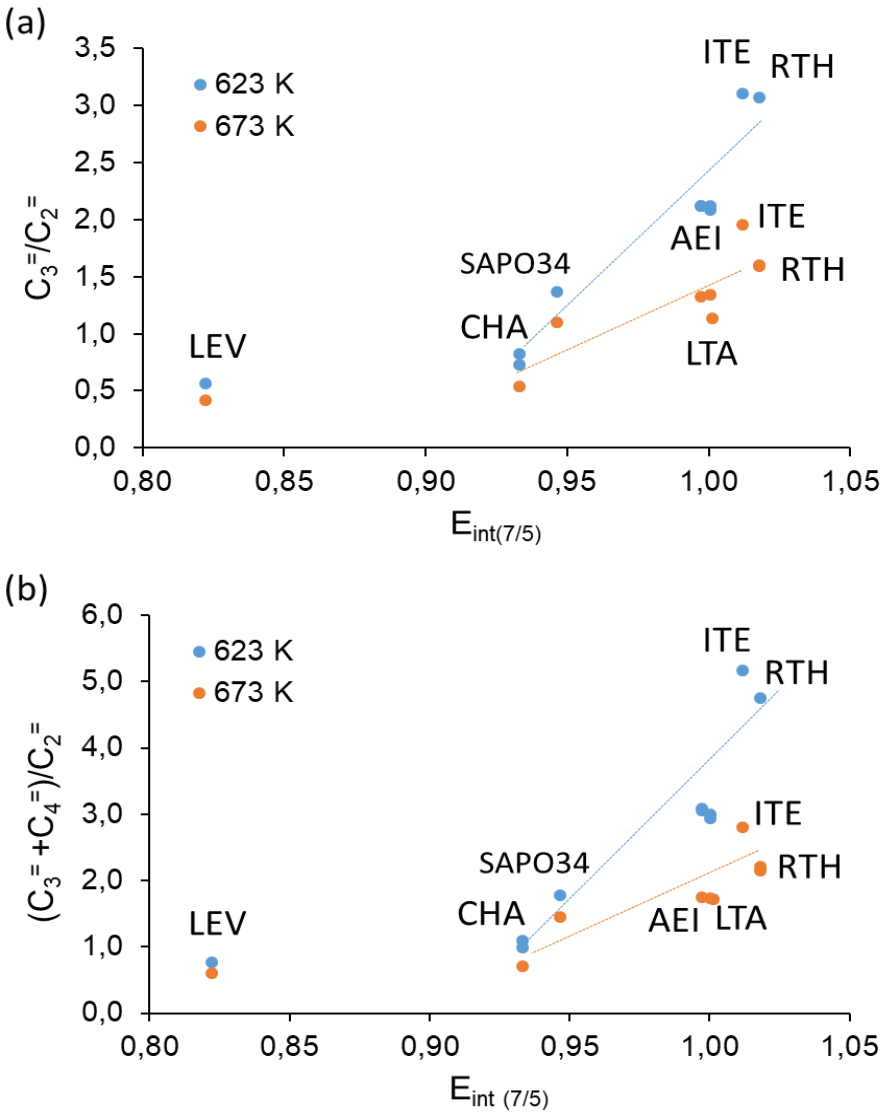

Figure 3.19. Relationships between the measured (a) $C_3^=/C_2^=$ and (b) $(C_4^= + C_3^=)/C2=$ ratios and the $E_{int(7/5)}$ parameter in different small-pore cage-based zeolites and zeotypes. Reaction conditions: T=623 or 673 K, WHSV=0.8 h^{-1}.

Consequently, we excluded LEV from the $E_{int(I2/I1)}$ parameter relation with experimental data. In this case a linear trend was also observed between the measured $C_4^=/C_3^=$ ratios and the calculated $E_{int(I2/I1)}$ parameter (see Figure 3.20). This correlation with a different parameter than $E_{int(7/5)}$ and a different experimental relation than $C_3^=/C_2^=$ proves that the study of the interaction energies of entrapped species is an accurate theoretical method to understand small-pore cage-like zeolite behaviour for certain reactions.

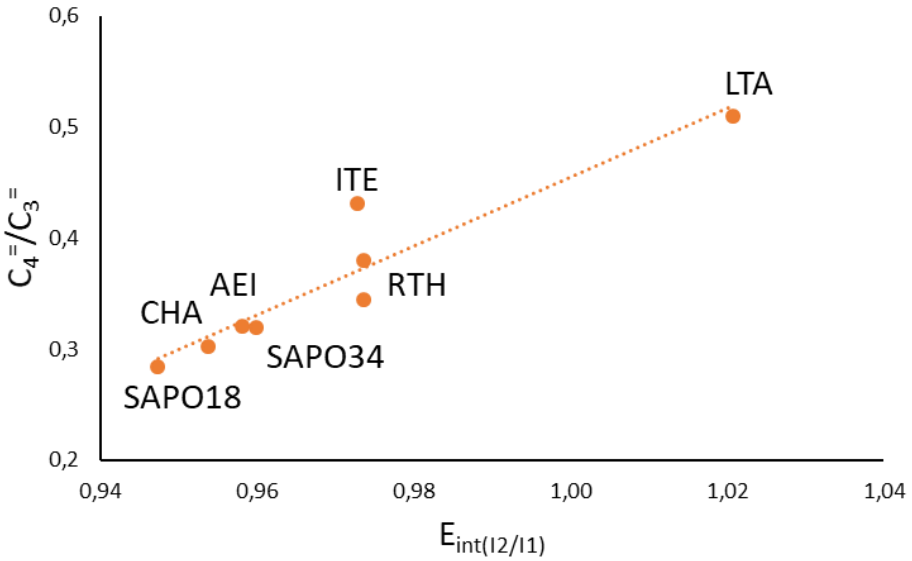

Figure 3.20. Relationships between the measured $C_4^=/C_3^=$ ratio and the $E_{int(I2/I1)}$ parameter in different small-pore cage-based zeolites and zeotypes. Reaction conditions: T= 673 K, WHSV=0.8 h^{-1}.

In a last step, and to further check the validity of the hypothesis behind the $E_{int(7/5)}$ parameter to rationalize the MTO selectivity and to set the limits of its applicability, the larger set of experimental data from ref.[28] were represented against the $E_{int(7/5)}$ parameter in Figure 3.21. Both the $C_3^=/C_2^=$ (in blue) and the $(C_4^=+C_3^=)/C_2^=$ ratios (in orange) follow the trends described for the experimental data presented in this work, and the existence of three types of materials is clearly observed. On the one hand, the group of zeolite structures with diameter of cavity larger than ~7.2 Å and smaller than ~9 Å, with a tight fitting between the cage topology and the entrapped methylbenzenium cations, plotted as squares in Figure 3.21. This group includes AEI, CHA, DDR, AFX, RTH and ITE, with $E_{int(7/5)}$ values between 0.9 and 1.01, and in them the confinement effect determines the relative stability of $7MB^+$ and $5MB^+$ cations and the olefin product distribution. On the other hand, there is a group of cage-based zeolites with larger cavities in their structure (SAV, UFI, RHO, KFI or

LTA, depicted as circles in Figure 3.21) in where the confinement effect is partly lost and other competitive processes start to take place. In this last case, linear correlations with the $E_{int(7/5)}$ parameter are still observed, but the amount of propene and butene detected is lower because of the competing processes leading to alkanes. Finally, the smaller cavities in ERI and LEV form a separate group, depicted as crosses in Figure 3.21, in which propene is probably formed through the alkene-based cycle of the MTO mechanism and the product distribution cannot be predicted from the $E_{int(7/5)}$ parameter.

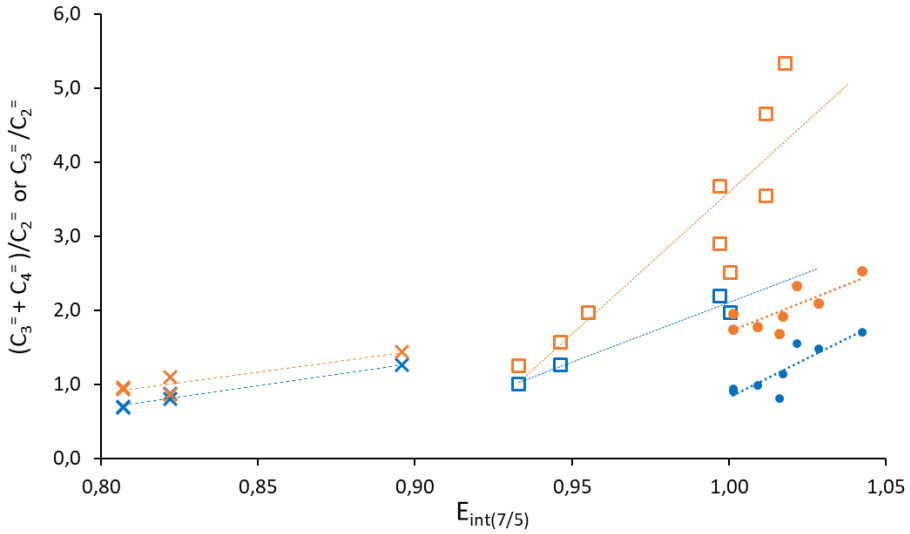

Figure 3.21. Relationships between experimental C3=/C2= (blue) and $(C_4^= + C_3^=)/C_2^=$ (orange) ratios from Davis et al work[28] and the $E_{int(7/5)}$ parameter. Crosses, squares and circles correspond to structures with cavity diameter smaller than ~7.2 Å, between ~7.2 and ~9 Å, and larger than ~9 Å, respectively. Reaction conditions: T = 673 K, WHSV = 1.3 h^{-1}.

3.6 Conclusions.

In this Chapter we have investigated the MTO reaction catalysed by small-pore cage-like zeolites focusing on the paring route of the hydrocarbon pool mechanism.

In first place we performed a gas phase mechanistic study that was later replicated with cluster models of CHA, AEI, RTH and ITE cavities using Gaussian09 software. This study concluded that the paring route contribution is determined by the ability of each cage to host the fully-methylated $g7MB^+$ cation in comparison with the $g5MBa^+$ cation that initiates the side-chain pathway. This ability was quantitatively described by the interaction energy between the cation and the cavity model $E_{int(g5MBa^+)}$ and $E_{int(g7MB^+)}$ that turned into a definition of an interaction energy ratio $E_{int(7/5)}$ as

$$E_{int(7/5)} = {}^{E_{int(g7MB^+)}}\Big/_{E_{int(g5MB_a^+)}}$$

This conclusion was proven by the clear linear relationship found between the measured $C_3^=/C_2^=$ ratios and the $E_{int(7/5)}$ parameter calculated for the four zeolites investigated in that part of the work.

In order to validate the results found with gas phase calculations, we moved the study to periodic DFT calculations using VASP software and studied the main factors that have been proposed to control the olefin product distribution of the MTO reaction catalysed by small-pore cage-based zeolites and zeotypes, focusing on catalyst samples differing in framework topology (CHA and AEI) and composition (zeolite and SAPO) that exhibit different selectivity to ethene, propene and butene. This part of the study concluded that the larger volume and framework flexibility of silicoaluminphosphates is key to explain the selectivity differences between SSZ-13 and SAPO-34 because the accommodation of the bulky $7MB^+$ cations in the cavities of CHA-type catalysts requires an expansion of the 12T rings enclosing them. This deformation is more energetically demanding in the more rigid zeolite, and consequently the final stabilization of $7MB^+$ and the related $E_{int(7/5)}$ parameter are larger in the more flexible SAPO-34 than in SSZ-13 zeolite. The strength, amount and location with respect to the HP intermediates of the Brønsted acid sites in the catalyst structure was also studied and conclusions pointed out that it has a minor influence over HP stabilization when compared to cavity topology.

Finally, by combining the theoretical data and the results from catalytic experiments, the limits of the $E_{int(7/5)}$ parameter as predictor of product distribution in the MTO reaction have been established. Thus, in the small cages of ERI and LEV structures, with $E_{int(7/5)}$ values below 0.9, the bulky $7MB^+$ is

sterically forbidden and propene and higher alkenes are formed through the alkene-based catalytic cycle. In contrast, in zeolite structures with $E_{int(7/5)}$ values larger than 0.9, propene and butene are formed through the paring mechanism, and the relative contribution of the paring and side-chain pathways directly correlates with the $E_{int(7/5)}$ parameter. However, there are clear differences between the structures with a tight fitting between the entrapped methylbenzenium cations and the hosting cavity (CHA, AEI, DDR, RTH and ITE, with $E_{int(7/5)}$ values between 0.9 and 1.01) and those with larger cages in where the confinement effect is lost in part and other competitive processes such as hydrogen transfer start to take place (SAV, UFI, RHO, KFI or LTA, with $E_{int(7/5)}$ values > 1). In this last case, the distribution of the light olefins still correlates with the $E_{int(7/5)}$ parameter, but the formation of alkanes and other products is significant.

3.7 References

1. Olah, G. A. Beyond Oil and Gas: The Methanol Economy. *Angew. Chemie Int. Ed.* **44**, 2636–2639 (2005).

2. Tian, P., Wei, Y., Ye, M. & Liu, Z. Methanol to Olefins (MTO): From Fundamentals to Commercialization. *ACS Catal.* **5**, 1922–1938 (2015).

3. Moliner, M., Martínez, C. & Corma, A. Synthesis Strategies for Preparing Useful Small Pore Zeolites and Zeotypes for Gas Separations and Catalysis. *Chem. Mater.* **26**, 246–258 (2014).

4. Haw, J. F., Song, W., Marcus, D. M. & Nicholas, J. B. The mechanism of methanol to hydrocarbon catalysis. *Acc. Chem. Res.* **36**, 317–326 (2003).

5. Olsbye, U. *et al.* Conversion of Methanol to Hydrocarbons: How Zeolite Cavity and Pore Size Controls Product Selectivity. *Angew. Chemie Int. Ed.* **51**, 5810–5831 (2012).

6. Van Speybroeck, V. *et al.* First principle chemical kinetics in zeolites: The methanol-to-olefin process as a case study. *Chem. Soc. Rev.* **43**, 7326–7357 (2014).

7. Yarulina, I., Chowdhury, A. D., Meirer, F., Weckhuysen, B. M. & Gascon, J. Recent trends and fundamental insights in the methanol-to-hydrocarbons process. *Nat. Catal.* **1**, 398–411 (2018).

8. Wu, X. *et al.* Evolution of C-C Bond Formation in the Methanol-to-Olefins Process: From Direct Coupling to Autocatalysis. *ACS Catal.* **8**, 7356–7361 (2018).

9. Li, J. *et al.* Cavity Controls the Selectivity: Insights of Confinement Effects on MTO Reaction. *ACS Catal.* **5**, 661–665 (2015).

10. Kang, J. H. *et al.* Further Studies on How the Nature of Zeolite Cavities That Are Bounded by Small Pores Influences the Conversion of Methanol to Light Olefins. *ChemPhysChem* **19**, 412–419 (2018).

11. Pinilla-Herrero, I., Olsbye, U., Márquez-Álvarez, C. & Sastre, E. Effect of framework topology of SAPO catalysts on selectivity and deactivation profile in the methanol-to-olefins reaction. *J. Catal.* **352**, 191–207 (2017).

12. Pinilla-Herrero, I., Márquez-Álvarez, C. & Sastre, E. Complex relationship between SAPO framework topology, content and distribution of Si and catalytic behaviour in the MTO reaction. *Catal. Sci. Technol.* **7**, 3892–3901 (2017).

13. Bhawe, Y. *et al.* Effect of Cage Size on the Selective Conversion of

Methanol to Light Olefins. *ACS Catal.* **2**, 2490–2495 (2012).

14. Sun, Q. *et al.* Mesoporogen-Free Synthesis of Hierarchical SAPO-34 with Low Template Consumption and Excellent Methanol-to-Olefin Conversion. *ChemSusChem* **11**, 3812–3820 (2018).

15. Lesthaeghe, D., De Sterck, B., Van Speybroeck, V., Marin, G. B. & Waroquier, M. Zeolite shape-selectivity in the gem-methylation of aromatic hydrocarbons. *Angew. Chemie - Int. Ed.* **46**, 1311–1314 (2007).

16. McCann, D. M. *et al.* A Complete Catalytic Cycle for Supramolecular Methanol-to-Olefins Conversion by Linking Theory with Experiment. *Angew. Chemie Int. Ed.* **47**, 5179–5182 (2008).

17. Zhang, W. *et al.* Methanol to Olefins Reaction over Cavity-type Zeolite: Cavity Controls the Critical Intermediates and Product Selectivity. *ACS Catal.* **8**, 10950–10963 (2018).

18. Lesthaeghe, D., Horré, A., Waroquier, M., Marin, G. B. & Van Speybroeck, V. Theoretical Insights on Methylbenzene Side-Chain Growth in ZSM-5 Zeolites for Methanol-to-Olefin Conversion. *Chem. - A Eur. J.* **15**, 10803–10808 (2009).

19. Wang, C.-M., Wang, Y.-D., Xie, Z.-K. & Liu, Z.-P. Methanol to Olefin Conversion on HSAPO-34 Zeolite from Periodic Density Functional Theory Calculations: A Complete Cycle of Side Chain Hydrocarbon Pool Mechanism. *J. Phys. Chem. C* **113**, 4584–4591 (2009).

20. De Wispelaere, K., Hemelsoet, K., Waroquier, M. & Van Speybroeck, V. Complete low-barrier side-chain route for olefin formation during methanol conversion in H-SAPO-34. *J. Catal.* **305**, 76–80 (2013).

21. Hemelsoet, K., Van der Mynsbrugge, J., De Wispelaere, K., Waroquier, M. & Van Speybroeck, V. Unraveling the Reaction Mechanisms Governing Methanol-to-Olefins Catalysis by Theory and Experiment. *ChemPhysChem* **14**, 1526–1545 (2013).

22. Ilias, S. & Bhan, A. Mechanism of the Catalytic Conversion of Methanol to Hydrocarbons. *ACS Catal.* **3**, 18–31 (2013).

23. Li, X. *et al.* Confinement Effect of Zeolite Cavities on Methanol-to-Olefin Conversion: A Density Functional Theory Study. *J. Phys. Chem. C* **118**, 24935–24940 (2014).

24. Wang, C. M., Wang, Y. D. & Xie, Z. K. Verification of the dual cycle mechanism for methanol-to-olefin conversion in HSAPO-34: A methylbenzene-based cycle from DFT calculations. *Catal. Sci. Technol.* **4**, 2631–2638 (2014).

25. Xu, S. *et al.* Direct Observation of Cyclic Carbenium Ions and Their Role in the Catalytic Cycle of the Methanol-to-Olefin Reaction over Chabazite Zeolites. *Angew. Chemie Int. Ed.* **52**, 11564–11568 (2013).

26. Chen, J. *et al.* Elucidating the olefin formation mechanism in the methanol to olefin reaction over AlPO-18 and SAPO-18. *Catal. Sci. Technol.* **4**, 3268 (2014).

27. Li, J. *et al.* Observation of Heptamethylbenzenium Cation over SAPO-Type Molecular Sieve DNL-6 under Real MTO Conversion Conditions. *J. Am. Chem. Soc.* **134**, 836–839 (2012).

28. Kang, J. H., Alshafei, F. H., Zones, S. I. & Davis, M. E. Cage-Defining Ring: A Molecular Sieve Structural Indicator for Light Olefin Product Distribution from the Methanol-to-Olefins Reaction. *ACS Catal.* **9**, 6012–6019 (2019).

29. Hereijgers, B. P. C. *et al.* Product shape selectivity dominates the Methanol-to-Olefins (MTO) reaction over H-SAPO-34 catalysts. *J. Catal.* **264**, 77–87 (2009).

30. Wang, C.-M., Wang, Y.-D., Du, Y.-J., Yang, G. & Xie, Z.-K. Similarities and differences between aromatic-based and olefin-based cycles in H-SAPO-34 and H-SSZ-13 for methanol-to-olefins conversion: insights from energetic span model. *Catal. Sci. Technol.* **5**, 4354–4364 (2015).

31. Wang, C.-M., Wang, Y.-D., Liu, H.-X., Xie, Z.-K. & Liu, Z.-P. Theoretical insight into the minor role of paring mechanism in the methanol-to-olefins conversion within HSAPO-34 catalyst. *Microporous Mesoporous Mater.* **158**, 264–271 (2012).

32. Gallego, E. M. *et al.* "Ab initio" synthesis of zeolites for preestablished catalytic reactions. *Science (80-.).* **355**, 1051–1054 (2017).

33. Li, C. *et al.* Synthesis of reaction-adapted zeolites as methanol-to-olefins catalysts with mimics of reaction intermediates as organic structure-directing agents. *Nat. Catal.* **1**, 547–554 (2018).

34. Weiguo Song, Hui Fu, and & Haw*, J. F. Supramolecular Origins of Product Selectivity for Methanol-to-Olefin Catalysis on HSAPO-34. (2001) doi:10.1021/JA0041167.

35. Hwang, A., Johnson, B. A. & Bhan, A. Mechanistic study of methylbenzene dealkylation in methanol-to-olefins catalysis on HSAPO-34. *J. Catal.* **369**, 86–94 (2019).

36. Zhao, Y. & Truhlar, D. G. The M06 suite of density functionals for main group thermochemistry, thermochemical kinetics, noncovalent

interactions, excited states, and transition elements: two new functionals and systematic testing of four M06-class functionals and 12 other functionals. *Theor. Chem. Acc.* **120**, 215–241 (2008).

37. Ditchfield, R., Hehre, W. J. & Pople, J. A. Self-Consistent Molecular-Orbital Methods. IX. An Extended Gaussian-Type Basis for Molecular-Orbital Studies of Organic Molecules. *J. Chem. Phys.* **54**, 724–728 (1971).

38. Hehre, W. J., Ditchfield, R. & Pople, J. A. Self—Consistent Molecular Orbital Methods. XII. Further Extensions of Gaussian—Type Basis Sets for Use in Molecular Orbital Studies of Organic Molecules. *J. Chem. Phys.* **56**, 2257–2261 (1972).

39. Frisch, M. J.; Trucks, G. W.; Schlegel, H. B.; Scuseria, G. E.; Robb, M. A.; Cheeseman, J. R.; Scalmani, G.; Barone, V.; Petersson, G. A.; Nakatsuji, H.; Li, X.; Caricato, M.; Marenich, A.; Bloino, J.; Janesko, B. G.; Gomperts, R.; Mennucci, B.; Hratchian, D. J. Gaussian 09. *Gaussian, Inc* **Wallingfor**, (2016).

40. Reed, A. E., Weinstock, R. B. & Weinhold, F. Natural population analysis. *J. Chem. Phys.* **83**, 735–746 (1985).

41. Perdew, J. P., Burke, K. & Ernzerhof, M. Generalized Gradient Approximation Made Simple. *Phys. Rev. Lett.* **77**, 3865–3868 (1996).

42. Perdew, J. P., Burke, K. & Ernzerhof, M. Generalized Gradient Approximation Made Simple [Phys. Rev. Lett. 77, 3865 (1996)]. *Phys. Rev. Lett.* **78**, 1396–1396 (1997).

43. Kresse, G. & Furthmüller, J. Efficient iterative schemes for *ab initio* total-energy calculations using a plane-wave basis set. *Phys. Rev. B* **54**, 11169–11186 (1996).

44. Blöchl, P. E. Projector augmented-wave method. *Phys. Rev. B* **50**, 17953–17979 (1994).

45. Grimme, S. Accurate description of van der Waals complexes by density functional theory including empirical corrections. *J. Comput. Chem.* **25**, 1463–1473 (2004).

46. Grimme, S. Semiempirical GGA-type density functional constructed with a long-range dispersion correction. *J. Comput. Chem.* **27**, 1787–1799 (2006).

47. Baerlocher, C.; McCusker, L. B. Database of Zeolite Structures.

48. Ferri, P. *et al.* Chemical and Structural Parameter Connecting Cavity Architecture, Confined Hydrocarbon Pool Species, and MTO Product Selectivity in Small-Pore Cage-Based Zeolites. *ACS Catal.* 11542–

11551 (2019) doi:10.1021/acscatal.9b04588.

49. Ferri, P. *et al.* Impact of Zeolite Framework Composition and Flexibility on Methanol-To-Olefins Selectivity: Confinement or Diffusion? *Angew. Chemie - Int. Ed.* **59**, 19708–19715 (2020).

50. Ferri, P. *et al.* The Limits of the Confinement Effect Associated to Cage Topology on the Control of the MTO Selectivity. *ChemCatChem* **13**, 1578–1586 (2021).

51. Bjørnar Arstad, †, John B. Nicholas, and & Haw*, J. F. Theoretical Study of the Methylbenzene Side-Chain Hydrocarbon Pool Mechanism in Methanol to Olefin Catalysis. (2004) doi:10.1021/JA035923J.

52. Zeolites, S. C. *et al.* Chemical and Structural Parameter Connecting Cavity Architecture , Con fi ned Hydrocarbon Pool Species , and MTO Product Selectivity in. (2019) doi:10.1021/acscatal.9b04588.

53. Wang, C., Li, B., Wang, Y. & Xie, Z. Insight into the topology effect on the diffusion of ethene and propene in zeolites: A molecular dynamics simulation study. *J. Energy Chem.* **22**, 914–918 (2013).

54. Dusselier, M., Deimund, M. A., Schmidt, J. E. & Davis, M. E. Methanol-to-Olefins Catalysis with Hydrothermally Treated Zeolite SSZ-39. *ACS Catal.* **5**, 6078–6085 (2015).

55. Martín, N. *et al.* Nanocrystalline SSZ-39 zeolite as an efficient catalyst for the methanol-to-olefin (MTO) process. *Chem. Commun.* **52**, 6072–6075 (2016).

56. Martínez-Franco, R., Li, Z., Martínez-Triguero, J., Moliner, M. & Corma, A. Improving the catalytic performance of SAPO-18 for the methanol-to-olefins (MTO) reaction by controlling the Si distribution and crystal size. *Catal. Sci. Technol.* **6**, 2796–2806 (2016).

57. Gallego, E. M. *et al.* Making Nanosized CHA Zeolites with Controlled Al Distribution for Optimizing Methanol-to-Olefin Performance. *Chem. - A Eur. J.* **24**, 14631–14635 (2018).

58. Müller, S. *et al.* Hydrogen Transfer Pathways during Zeolite Catalyzed Methanol Conversion to Hydrocarbons. *J. Am. Chem. Soc.* **138**, 15994–16003 (2016).

CHAPTER 4

Design and synthesis of zeolite catalysts for selectively manipulating mechanistic pathways.

4.1 Introduction.

Production of alkylaromatics is a crucial process in the modern chemical industry since they are well-established precursors for many important intermediates and chemicals widely used in chemical and pharmaceutical industries.[1–3] Ethylbenzene (EB) is one of the industrial alkylaromatics with a higher production capacity worldwide, around 50 million tons,[4] which is mostly consumed in the manufacture of polystyrene, acrylonitrile, butadiene, styrene resin, and other products.[5] Benzene alkylation with light olefins and alcohols catalysed by acid zeolites has been stablished as the main way of industrial production for alkylaromatics.[6–8] The industrial alkylation process inevitably produces undesired polyalkylated byproducts with lower added value, with diethylbenzene (DEB) being the most common one.[9] To improve selectivity, the current production of EB combines two reactions: i) alkylation of benzene with ethene followed by EB separation, and ii) transalkylation of the polyethylated byproducts with benzene to increase the global yield of EB while recycling the side products obtained during the initial alkylation process (see Figure 4.1).[10–12]

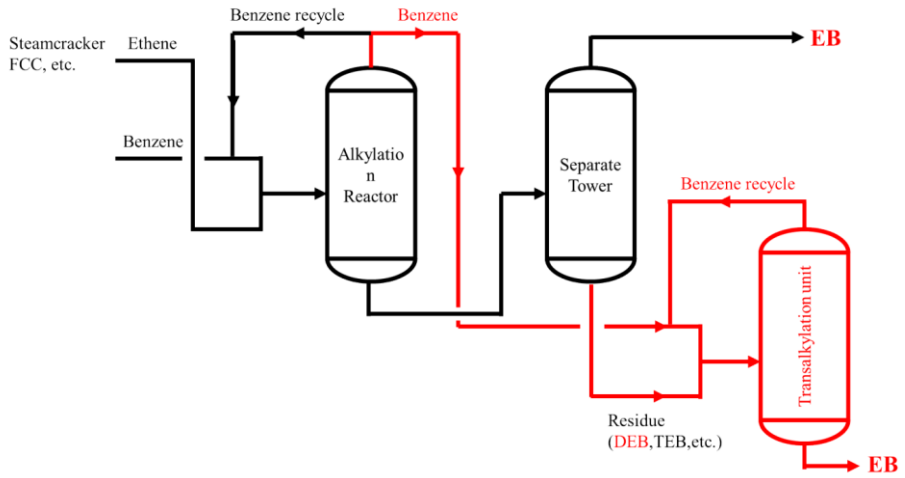

Figure 4.1. A brief scheme of ethylbenzene production industry, the processes in red represent transalkylation between benzene and diethylbenzene.

Some of the catalysts employed in the industrial transalkylation of DEB are large pore zeolites such as faujasite, beta, MCM-22, and mordenite.[10,11] The presence of wide channels, cavities and intersections within these materials topologies allows the stabilization of reaction intermediates and transition states inside the zeolite microporous voids by weak Van der Waals interactions. This effect is very sensitive to the fitting of the adsorbed species with the surrounding environment so that subtle differences in the zeolite structure lead to significant differences observed in catalytic activity, selectivity and catalyst lifetime.

The responsiveness observed for the transalkylation reaction with regard to different zeolite catalysts topologies resembles to enzymatic catalysis. Indeed, attempts to mimic enzymatic behaviour with zeolites by placing the active sites in particular positions or voids have been reported since long.[13–19] However, the structural flexibility that grants enzymes the ability to adopt multiple conformations to control the access of reactants and the release of products from the active site pockets and allows enzymatic active sites to arrange perfectly the biological catalytic residues to give an optimal stabilization for the transition state of the desired reaction, cannot be fully mimicked by solid, and therefore rigid materials as zeolites are.[20,21]

Such specificity relying on conformational changes along the catalytic process cannot be offered by solid catalysts with a very limited flexibility, and therefore an optimum fitting between the target transition state and the almost rigid crystalline structure of the zeolite is initially required. To achieve the desired fitting between catalyst and reactants, the design and synthesis of a proper zeolite for a specific chemical reaction has been proven as the key factor for

success. A novel methodology on zeolite synthesis is based on the use of organic structure directing agent (OSDA) molecules that mimic the geometry and charge distribution of the key transition states of the desired chemical reaction.

The OSDA-mimic approach has been successfully applied to synthesize zeolites exhibiting improved catalytic performance in selected reactions such as toluene disproportionation,[22] ethylbenzene and endo-tricyclodecane isomerizations,[22] Diels-Alder cycloaddition,[23] and the methanol-to-olefins (MTO) reaction where it was possible to control the selectivity to ethene and propene by favouring one out of two competing reaction mechanisms by synthesizing the proper zeolite catalyst for each mechanism as seen in Chapter 3.[24] In this Chapter we apply the OSDA-mimic approach to synthesize an optimum zeolite for DEB-benzene transalkylation.

DEB transalkylation can proceed through two main competing reaction pathways.[25–34] The alkyl transfer mechanism (Scheme 4.1), involves consecutive dealkylation and alkylation steps that proceed through unstable pentacoordinated carbonium ion intermediates generated by the Brønsted acid sites present in zeolite catalysts.[26,35] The first dealkylation of DEB produces an EB molecule and a surface ethoxy group that, in a second step, reacts with benzene and yields EB. However, the ethoxy group can also react with EB or DEB molecules present in the zeolite channels to form undesired over-ethylated byproducts such as DEB and triethylbenzene (TEB) lowering the experimental rate towards the desired product.[36] In addition, the surface ethoxy can decompose into ethene and regenerate the Brønsted acid site, further decreasing the yield of EB.

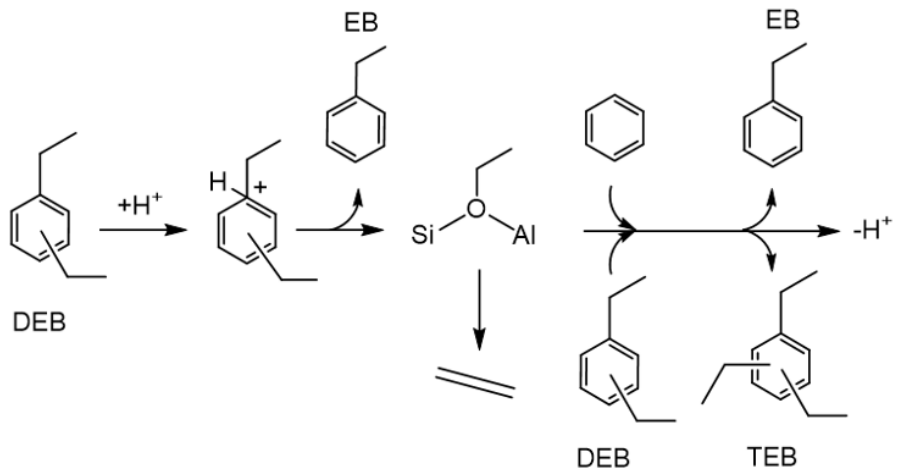

Scheme 4.1. DEB alkyl transfer mechanism.

The second pathway proceeds through cationic diaryl intermediates formed by reaction of benzene with a diethylbenzenium carbenium ion (DEB^+) (Scheme 4.2).[26,37] The nature for the starting step for this mechanism is unknown yet. The initial hydride abstraction step from DEB to form DEB^+ results difficult on Brønsted acid sites, with high activation energy barriers of ~200 kJ/mol reported in literature.[31,34,38] Other hypothesis point towards Lewis acid sites like La^{3+} cations[25,29] or extra-framework Al species[26,39] making this step energetically affordable. Once the first DEB^+ cation is generated, it enters the true catalytic cycle, at the end of which it is regenerated by hydrogen transfer between reactants and products not needing of another high energy hydride abstraction from the zeolite framework anymore.

When the desired diaryl intermediate is formed (see $I1^+$ in Scheme 4.2) a proton must be transferred from one aromatic ring to the other for the transalkylation to take place generating the $I4^+$ intermediate that, by cracking, produces two molecules of EB. The proton transfer converting $I1^+$ into $I4^+$ may proceed through two main ways, intramolecularly through four- or six-membered ring cationic transition states (Scheme 4.2 red and blue) or via consecutive deprotonation and protonation steps with the participation of the zeolite acid sites (Scheme 4.2 green).

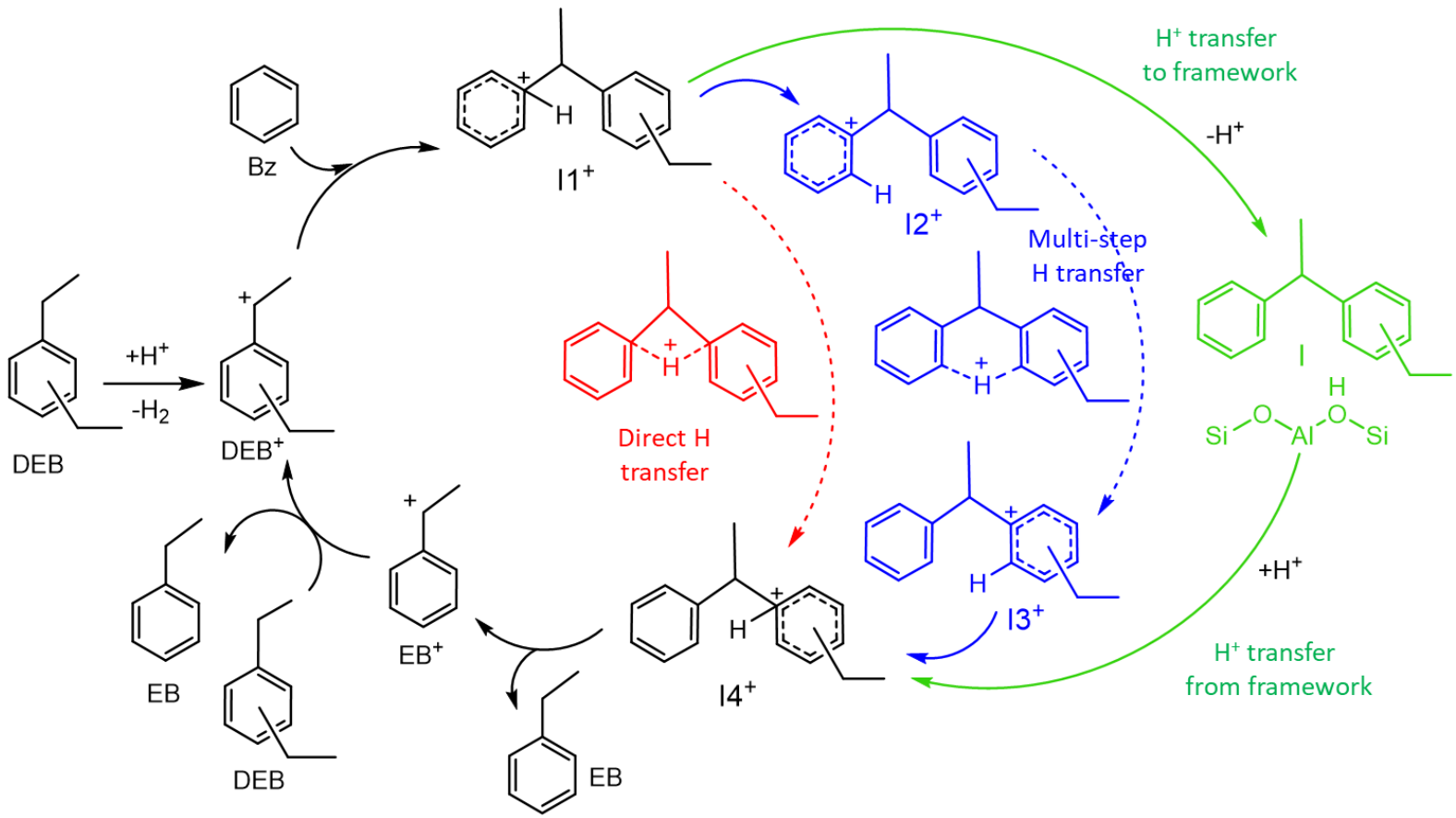

Scheme 4.2. Diaryl Mediated Pathways.

However, another undesired competitive reaction might take place during DEB transalkylation, the disproportionation of two DEB molecules into EB and TEB (Scheme 4.3b).

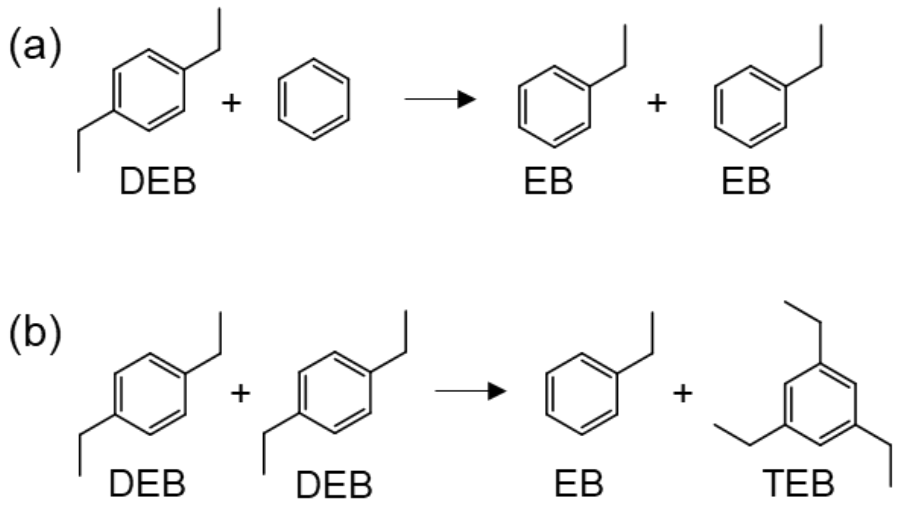

Scheme 4.3. Competitive diethylbenzene reactions: (a) transalkylation with benzene, (b) disproportionation.

From a mechanistic point of view each of the two possible DEB reactions, transalkylation and disproportionation, can proceed through the same two pathways: an alkyl-transfer route involving consecutive dealkylation and alkylation steps (Scheme 4.1) and a diaryl-mediated pathway involving the formation of bulky cationic diaryl intermediates (Scheme 4.2).[26,27,34,37,40] The former route, as mentioned above, produces a mixture of alkylated and poly-alkylated products with the addition of ethene due to the necessary formation of ethoxy intermediates. Therefore, the alkyl-transfer mechanism is a non-selective pathway for the optimal production of EB that has to be minimized in favour of the diaryl-mediated mechanism that proceedswithout the necessity for ethoxy groups and removes the possibility of producing ethene as byproduct. Favouring DEB transalkylation meanwhile disfavoring disproportionation of DEB into TEB can be achieved by selecting a zeolite with the proper topological features to stabilize transalkylation intermediates while impeding the formation of bulkier disproportionation intermediates.

This later paragraph summarizes the challenges and goals that are going to be adressed in this Chapter by a combination of computational and experimental techniques. It starts with a DFT gas phase study of all the possible DEB^+ isomers that can co-exist in reaction and a comparison of transalkylation and disproportionation mechanistic routes in gas phase. After selecting the most stable isomers, hence the ones that will be found in a higher concentration in

experimental enviroments, a high-throughput screening of all zeolite structures potentially well-suited to stabilize these diaryl intermediates performed by the Department of Materials Science an Engineering (DMSE) at the Massachussets Institute of Technology (MIT) is presented. Then, the accuracy of the thermodynamic and kinetic data is improved by means of periodic DFT calculations for the selected ideal candidates to enchance the diaryl-mediated mechanism, ending up with the proposition of a series of large pore zeolites with different microporous structure of channels and cavities. The synthesis, characterization and catalytic test of these materials confirms the theoretical predictions and demonstrates that trivial or subtle changes in pore size and architecture can tune the preferred reaction pathways, leading to a precise control of the host-guest interactions that approaches the specificity of enzymatic catalysts.

4.2 Methods and models.

All calculations in section **4.3** are based on density functional theory (DFT) and were carried out using the M062X functional[41] and the 6-31g(d,p) basis set[42,43], as implemented in the Gaussian 09 software.[44] In the gas-phase study of DEB isomers and of the reaction mechanisms for transalkylation and disproportionation, the positions of all C and H atoms in the cationic intermediates and transition states were fully optimized without restrictions.

High-throughput force fields calculations presented in section **4.4** were carried out by the DMSE at the MIT. As this work has not been done by the author of this thesis and is not published yet, the specific computational details for these calculations are also described in this section. Force field calculations were performed using the General Utility Lattice Program (GULP), version 5.1.1,[45,46] through the GULPy package.[47] Initial zeolite structures were downloaded from the International Zeolite Association (IZA) database[48] and pre-optimized using the Sanders-Leslie-Catlow (SLC) parametrization.[49] SMILES strings for OSDAs were extracted from the literature.[50] Conformers for OSDAs were generated using RDKit[51] with the MMFF94 force field[52,53] after explicit enumeration of all stereoisomers for each molecule.

Generation of OSDA-zeolite and intermediate-zeolite poses was performed using the Voronoi and Monte Carlo docking algorithms as implemented in the VOID package.[54]. At most 5 different conformers for each OSDA and intermediate are used as input guest geometries for VOID. For certain zeolites with lattice parameters smaller than 10 Å in one direction, unit cells and supercells elongated in the direction of the short parameter by factors of 2 and 3 were used as inputs for the docking package. The Voronoi docking algorithm used a threshold of 3 Å for Voronoi node clustering and a threshold fitness function with minimum distance of 1.25 Å. At first, docking is performed with

the batch Voronoi docker parallelized over 20 images. In the case of OSDAs, loading is increased until no more conformers can be added to the pose without clashing, and repeated if the procedure does not yield any poses. In the case of reaction intermediates, a single molecule is placed inside the zeolite using the same docking procedure. In this case, the loading is not increased, but different configurations of the molecule placement inside the framework are explored. The Dreiding force field[55] was used to model interactions between the zeolite and the OSDA. Structural optimizations of poses were performed at constant volume using the conjugate gradient and rational function optimization algorithms, switching to the latter when the norm of the gradient dropped below 0.10 eV/Å. The frozen pose method[56] was then used to compute binding energies. Poses with binding energy larger than zero were considered to have unfavorable host-guest interactions.

In sections **4.4** and **4.5,** all periodic density functional theory (DFT) were performed using the Perdew-Burke-Ernzerhof (PBE) exchange-correlation functional within the generalized gradient approach (GGA)[57,58], as implemented in the Vienna Ab-initio Simulation Package (VASP) code.[59] The valence density was expanded in a plane wave basis set with a kinetic energy cutoff of 600 eV, and the effect of the core electrons in the valence density was taken into account by means of the projected augmented wave (PAW) formalism.[60] Integration in the reciprocal space was carried out at the Γ k-point of the Brillouin zone. Dispersion corrections to the energies were evaluated using the DFT-D3 Grimme's method.[61,62] Electronic energies were converged to 10^{-6} eV and geometries were optimized until forces on atoms were <0.01 eV/A. Transition states were obtained using the DIMER and NEB algorithms.[63–66] All stationary points were characterized by means of harmonic frequency calculations.

The pure silica models of BEA, BEC, BOG, CON, FAU, ITT, IWR, IWV, MOR, SEW, USI and UTL structures were generated by optimizing the unit cell parameters and atomic positions of the experimental structures reported in the IZA database[67] with the computational setup described above. Then, keeping the unit cell parameters fixed, cationic intermediates were placed in each unit cell and the positions of all atoms in the system were fully optimized without restrictions. Images and detailed data of each model can be found in Appendix I. Specific acid models for IWV and MOR frameworks were designed by substitution of one Si atom with one Al, Si/Al ratio equal 37 and 95 respectively. T-site Al location was decided by intrinsic stability criteria furtherly detailed in the corresponding section of this Chapter.

Relative energies and activation barriers (Ea) were calculated by the common procedure and expressed in kJ/mol:

$$E_a = E_{TS} - E_{min}$$

The interaction energies (Eint) were calculated as the difference in energy between the global system composed by the OSDA or intermediate inside the zeolite model and the sum of the energies of the empty catalyst and the isolated molecule.

Regarding to experimental details of aluminosilicates synthesized by collaborators from our group and reaction conditions that are shown in this work, as this thesis is mainly based on theoretical chemistry and the experimental work has not been carried out by the author of this thesis, the corresponding details can be found in Appendix II at the end of this work.

4.3 DFT Gas Phase Mechanism Study.

In order to find the optimum zeolite for the reaction under study, the first step is to evaluate the kinetics of the two competing reactions by means of a DFT study of the reaction mechanism. Taking into account the relative stability of the ortho- meta- and para-isomers of neutral, cationic and diaryl intermediates involving DEB (see Table 4.1), the most stable isomer p-DEB^+ cation was assumed to react with benzene in the transalkylation reaction, and with ortho- meta- and para-DEB in the disproportionation reaction.

Table 4.1. Relative stability of ortho-, meta- and para-isomers of neutral DEB, DEB^+ carbenium ion, and cationic diaryl intermediates involved in transalkylation I_{trans} and disproportionation I_{disp} reactions, in kJ/mol.

Isomers of neutral diethylbenzene (DEB)		
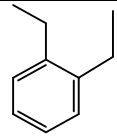	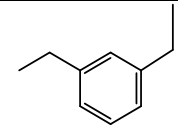	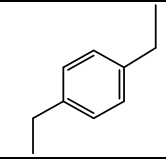
o-DEB E_{rel} = 2	m-DEB E_{rel} = 0	p-DEB E_{rel} = 0.4
Isomers of diethylbenzenium cation (DEB^+)		
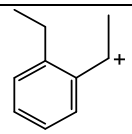	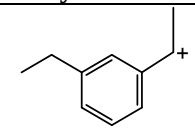	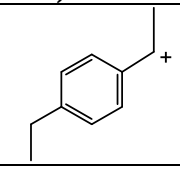
o-DEB^+ E_{rel} = 14	m-DEB^+ E_{rel} = 15	p-DEB^+ E_{rel} = 0
Diaryl intermediates		
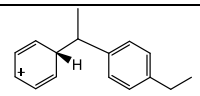	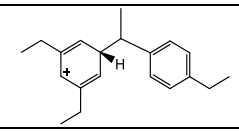	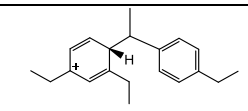
I_{trans}	I_{disp} A E_{rel} = 0	I_{disp} B E_{rel} = 4
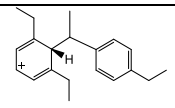	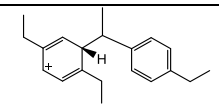	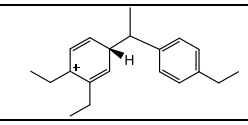
I_{disp} C E_{rel} = 3	I_{disp} D E_{rel} = 4	I_{disp} E E_{rel} = 10

It has been established in previous literature[26,27,34,37] that the proton transfer between the two aromatic rings of the cationic diaryl intermediate $I1^+$ to form

$I4^+$ can follow at least the four different pathways depicted in Scheme 4.4 and Figure 4.1.

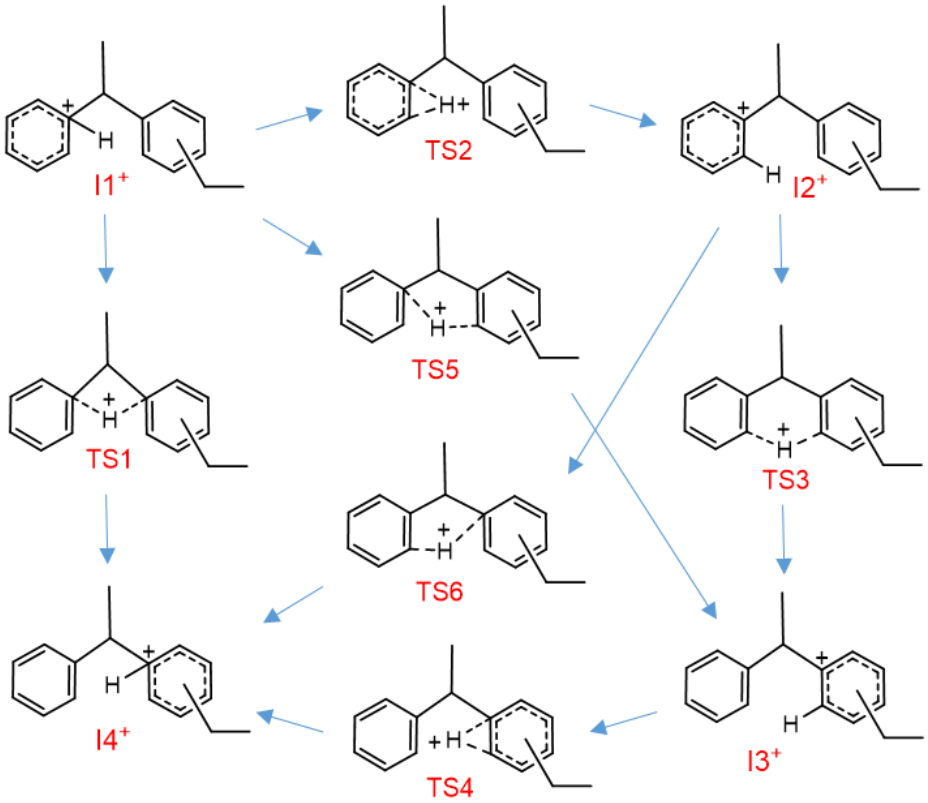

Scheme 4.4. Possible pathways for transformation of the cationic diaryl intermediate $I1^+$ into $I4^+$.

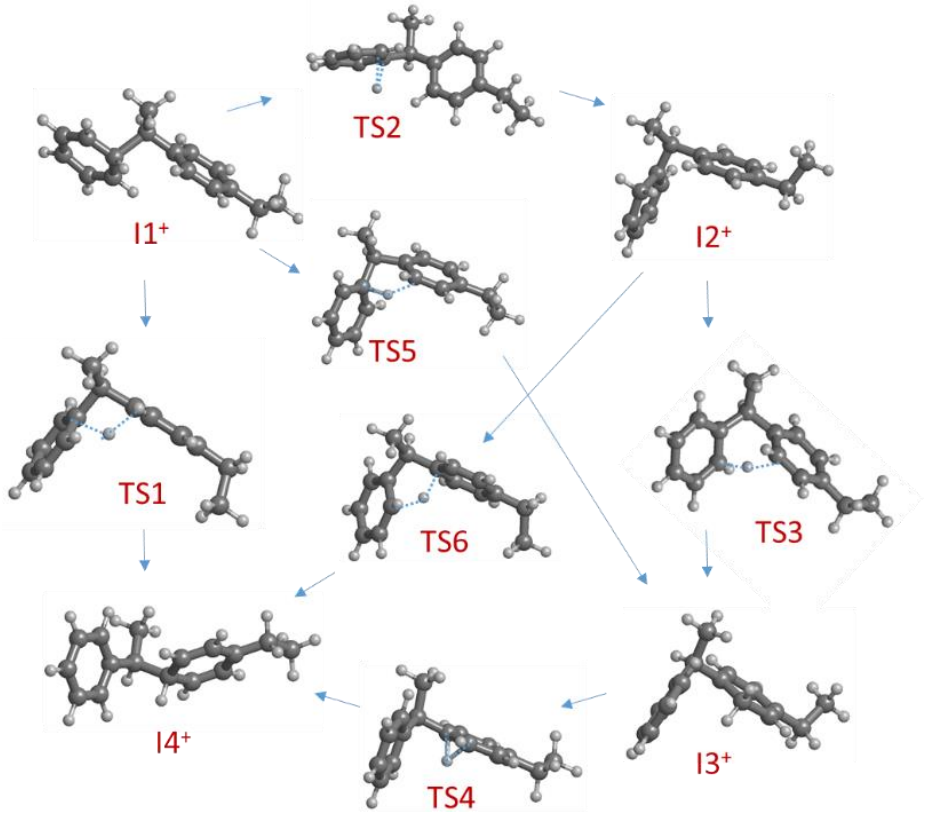

Figure 4.1. Optimized geometries of all minima and transition states involved in the four possible pathways considered for the transalkylation of p-DEB$^+$ with benzene in gas phase.

All calculated energy profiles for the four pathways considered are plotted in Figure 4.2. Numerical values of these graphs can be found at Table 4.2 and Table 4.3.

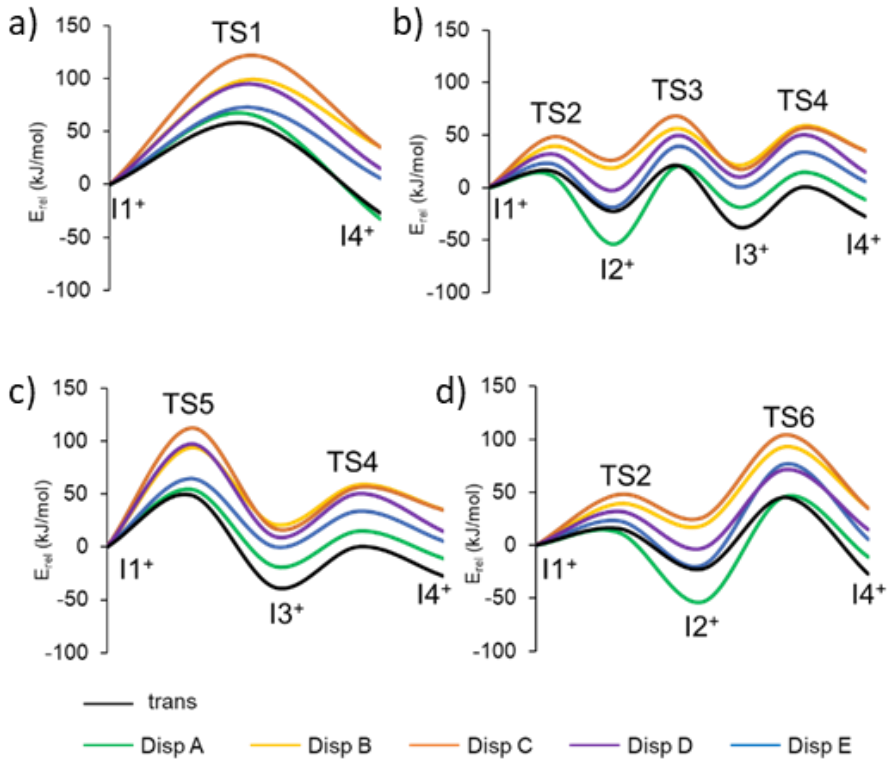

Figure 4.2. Calculated energy profiles for all transalkylation and disproportionation pathways considered in gas phase.

Table 4.2. Relative stability (in kJ/mol) of intermediates and transition states involved in the mechanisms of transalkylation and disproportionation through the different diaryl isomers depicted in Table 4.1 in gas phase.

	Transalkylation	**Disproportionation**				
		A	**B**	**C**	**D**	**E**
$I1^+$	0	0	0	0	0	0
TS1	58	67	99	121	95	73
$I4^+$	-27	-11	35	35	15	6
TS2	16	12	39	48	32	23
$I2^+$	-23	-54	19	26	-3	-20
TS3	21	20	57	68	50	40
$I3^+$	-38	-19	21	17	10	0
TS4	0	15	59	57	51	34
TS5	49	54	94	113	97	65
TS6	45	46	93	105	72	77

Table 4.3. Calculated Ea (in kJ/mol) for all the elementary steps of the mechanisms of transalkylation and disproportionation through the different diaryl isomers depicted in Table 4.1 in gas phase.

	Transalkylation	**Disproportionation**				
		A	**B**	**C**	**D**	**E**
Ea1	58	67	99	121	95	73
Ea2	16	12	44	62	32	23
Ea3	44	74	61	47	53	58
Ea4	38	33	45	52	41	34
Ea5	49	54	94	113	97	65
Ea6	68	100	96	77	75	95

Looking at Figures 4.1 and 4.2 it is possible to see that the proton shifts between carbon atoms belonging to the same aromatic ring occurring through transition states TS2 and TS4 are fast with low activation barriers, and therefore the highest activation energy barrier in each pathway always corresponds to the transfer of the H^+ from one aromatic ring of the cationic diaryl intermediate to the other one. The most favourable route for transalkylation (black lines in Figure 4.2) is the three-step process in which the inter-ring H^+ transfer takes place via a six-membered transition state, TS3 (Figure 4.2b), with an activation energy of 56 kJ/mol. The direct H^+ transfer through a four-membered transition state, TS1 (Figure 4.2a), with an activation barrier of 76 kJ/mol, and the routes via five-membered transition states TS5 and TS6 (Figure 4.2c,d), with calculated barriers of 72 and 91 kJ/mol, respectively, are less favoured. Regarding disproportionation pathways for all the possible isomers, higher activation energies ranging from 80 to 116 kJ/mol are obtained due in part to a better stabilization of the positive charge in more substituted C atoms of the aromatic rings, as for instance in $I2^+$. The schematic charge distribution is depicted in Figure 4.3 where only the lowest energy routes for transalkylation and disproportionation of the para-DEB^+ + meta-DEB isomers are plotted for a clearer comparison.

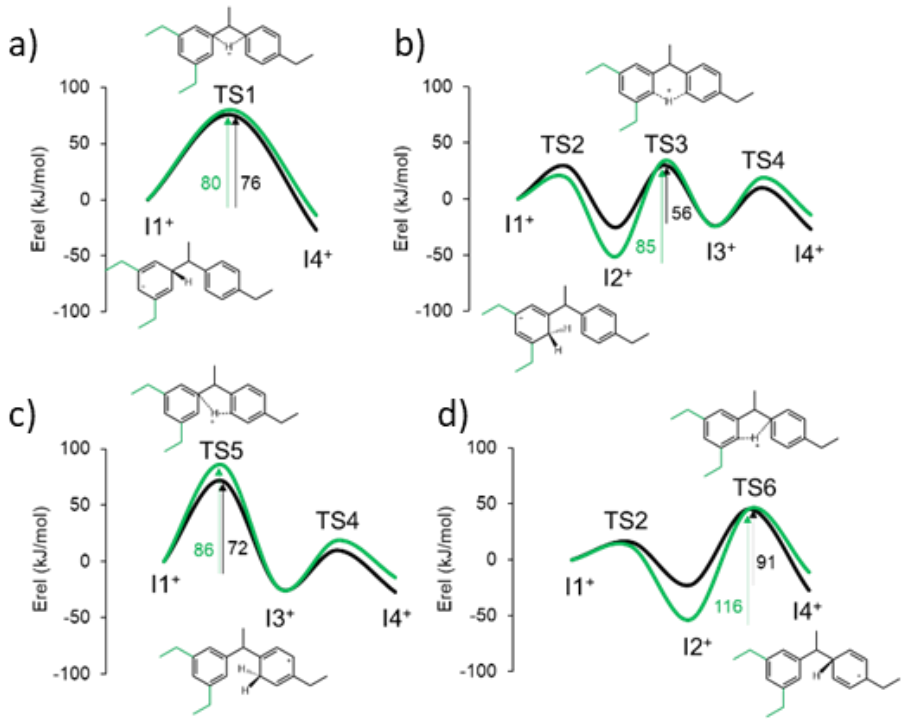

Figure 4.3. Calculated energy profiles for transalkylation (black) and disproportionation (green) pathways in gas phase, and schematic representation of transition states and intermediates. The highest activation energy barrier in each pathway is given beside the arrows (in kJ/mol).

These results indicate that even in the absence of any zeolite confinement effect, disproportionation is intrinsically more energetically demanding than transalkylation. As a conclusion of this part of the study, the para-DEB^+ and the para-DEB^+ + meta-DEB diaryl isomers were selected for the further study of transalkylation and disproportionation reactions respectively inside different zeolite catalysts with the aim of finding an optimal catalyst for the transalkylation.

4.4 Fast computational screening of potentially efficient zeolites.

In this part of the study we collaborated with DMSE at the MIT to make use of their Organic Structure directing agent DataBase (OSDB) (https://zeodb.mit.edu/index). We chose the diphenyldimehylphosphonium ($DPDMP^+$) cation as OSDA because it contains two aromatic rings connected by a positively charged phosphonium center (Scheme 4.5). Its geometry and charge distribution are similar to those of the diaryl intermediates involved in the DEB transalkylation reaction, and therefore it is hypothesized as a proper mimic to be used as OSDA in the synthesis of a zeolite that enhances the diaryl-mediated pathways.[22,40] Then, we selected from OSDB the fifty zeolite structures that better stabilize the neutral mimic of the $DPDMP^+$ OSDA (Scheme 4.5). The interaction energies between the neutral OSDA mimic and each zeolite structure was evaluated using force fields (FF) as described in the Methods and Models section. Only one organic molecule was introduced in each zeolite unit cell with different initial positions, and only the Eint for the most stable location after optimization of each zeolite-OSDA pair is listed in Table 4.4. To evaluate the influence of additional ethyl substituents in the aromatic rings on the stabilization by confinement of diaryl intermediates, the neutral version of the key diaryl intermediates for transalkylation (I_{trans} in Scheme 4.5) and disproportionation (I_{disp} in Scheme 4.5), that only differ in the number of ethyl substituents in one of the aromatic rings, were also included in the study. The Eint of I_{trans} and I_{disp} within each of the fifty zeolite structures investigated, calculated with FF following the same procedure described for the OSDA, are listed in Table 4.4

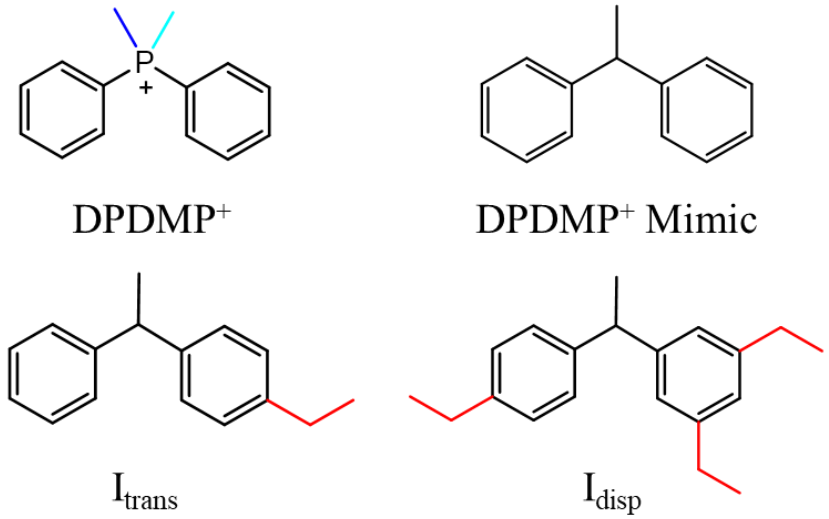

Scheme 4.5. Structures of the $PDPMP^+$ OSDA, its neutral mimic and the diaryl intermediates for transalkylation (I_{trans}) and disproportionation (I_{disp}).

Table 4.4. Eint of neutral OSDA and key intermediates for transalkylation (I_{trans}) and disproportionation (I_{disp}) from FF simulations in kJ/mol.

IZA code	Channels System	BE OSDA	Eint I_{trans}	Eint I_{disp}
AFI	12	-202	-205	-29
AFR	12x8	-203	-179	-194
AFX	8	-203	-210	-226
AVL	8	-197	-200	-
BEA	12x12	-189	-211	-247
BEC	12x12x12	-182	-202	-224
BOG	12x10	-198	-198	-257
CON	12x10x10	-213	-210	-266
CSV	10x8	-207	-205	-244
EEI	8	-199	-239	-204
EON	12x8x8	-190	-239	-204
ERI	8	-209	-133	-6
EUO	10x10	-216	-233	-285
EZT	12	-228	-234	-
FAU	12x12x12	-137	-156	-187
GME	12x8	-180	-200	-179
IFR	12	-211	-193	24
IFW	10x8x8	-194	-208	-248
IFY	8	-238	-218	-163
IHW	8	-197	-226	-158
ISV	12	-181	-203	-265
ITT	18x10x10	-141	-156	-186
IWR	12x10x10	-199	-215	-259
IWV	12x12	-179	-177	-230
KFI	8	-181	-196	-247
LTA	8	-179	-201	-243

MAZ	12x8x8	-192	-179	-104
MEI	12	-192	-198	-255
MEL	10	-203	-196	-253
MFI	10x10	-203	-206	-271
MOR	12x8	-217	-223	-245
MSO	6	-215	-233	-106
MTW	12	-194	-228	-214
MWW	10x10	-181	-178	-241
RHO	8	-180	-192	-244
RTH	8	-188	-204	-164
SAF	12	-206	-211	-61
SEW	12x10	-210	-214	-250
SFG	10	-215	-222	-276
SFO	10x10	-204	-194	-187
SFS	12x8	-198	-212	-263
SFW	8	-194	-207	-215
SOR	8	-212	-203	-170
SOV	12x8	-186	-204	-244
STO	12	-207	-192	-91
TER	10x10	-221	-223	-264
TUN	10x10x10	-204	-206	-265
UFI	8	-186	-203	-244
USI	12x10	-212	-216	-234
UTL	14x12	-183	-188	-225

The fifty candidate zeolites in this set exhibit very diverse internal microporous structures, including closed cavities only accessible through small 8r windows, linear channels of different diameter running parallel along the crystal, and bi-directional (2D) or three-directional (3D) systems of channels that intersect generating wider internal voids. Based on previous knowledge of the reaction, we excluded from this set cage-based small-pore zeolites which do not allow the diffusion of aromatic reactants and products through the 8r windows making impossible the formation of diaryl intermediates (blue points in Figure 4.5a). Also, zeolites with a 1D channel system that tends to be easily blocked by diaryl intermediates leading to fast catalyst deactivation and poor perfomance (orange points in Figure 4.5a). Finally, zeolites containing 2D 10-ring channel systems (yellow points in Figure 4.5a) where the non-desired alkyl-transfer pathway is preferred, and although diaryl intermediates might get formed at the channels intersection they cannot react properly because of too tight space restrictions, again leading to catalyst blocking and deactivation.[68] After applying these criteria, the set of potential zeolite candidates for DEB-benzene transalkylation drops to eleven (red points in Figure 4.5a), summarized in Table 4.5. An important feature to point out from these calculations is that the most selective structures according to Figure 4.5a contain 1D channel systems and therefore are not included in our selected set of candidates due to their expected fast deactivation. Thus, Eint values from the fast screening cannot be taken as a straight solution when looking for optimal catalysts because zeolite catalysis if often governed by multiple factors. However, to confirm or refute the expected behaviour of monodimensional structures and to compare the alkyl transfer mechanism impact inside systems with different dimensionality, MOR, which is a 1D zeolite with 12r channels and has been tested experimentally and used industrially, was included in the dataset.

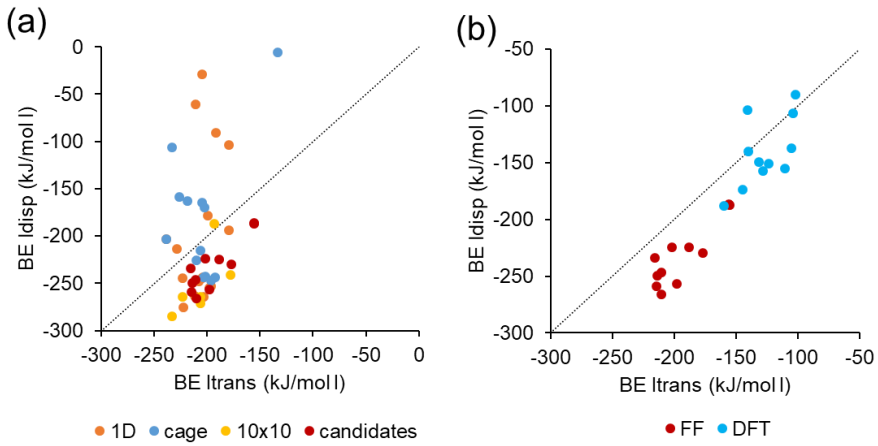

Figure 4.5. Correlations between Eint I_{trans} and Eint I_{disp} for different types of zeolite channels system calculated with force fields (a) and comparison between FF and DFT for the selected candidates (b).

With the aim of improving the accuracy of these data, (I_{trans}) and (I_{disp}) were optimized inside the twelve selected zeolite structures listed in Table 4.5 using periodic DFT calculations. All the corresponding unit cell structures can be found at Appendix I and DFT computational details can be found in section **4.2**. These simulations include multiple interactions other than dispersion and offer the possibility of observing different confinement effects caused by the different channel topologies. For this part of the study, zeolite pores were filled with the maximum number of molecules possible taking the maximum possible as the maximum number of I_{disp} molecules that could fit in, given in column "N" in Table 4.5. The optimized geometries of the I_{trans} intermediates in the twelve zeolites considered are shown in Figure 4.6. Despite the differences in methodology and model, an excellent matching between the FF and DFT results is observed in the plot of Eint I_{disp} versus Eint I_{trans} in Figure 4.5b, thus confirming the trend proposed by the computationally cheaper and faster FF calculations and validating it as a solid method for this kind of calculations.

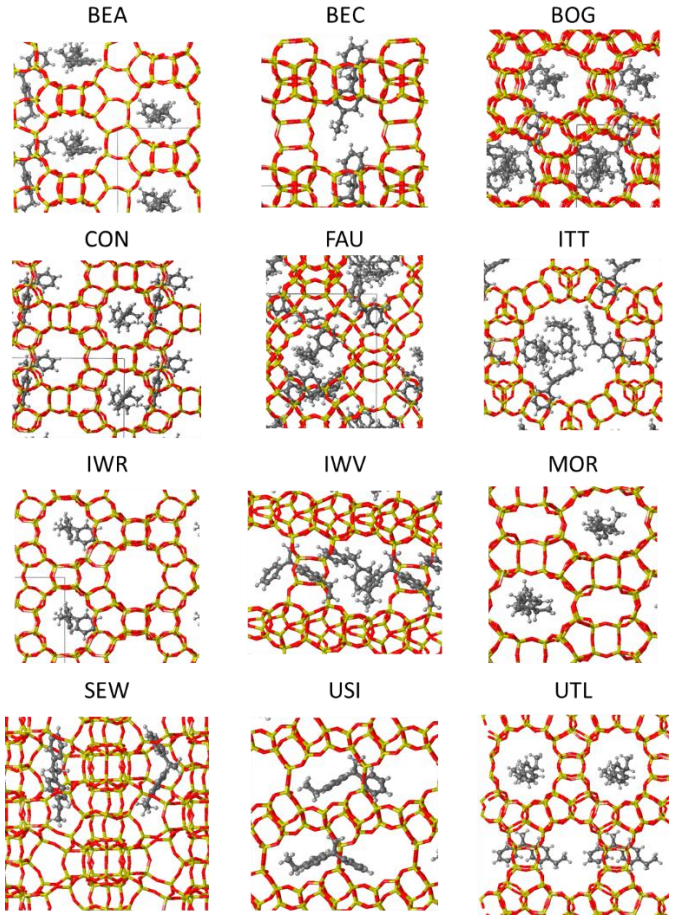

Figure 4.6. Optimized structures of the diaryl intermediate for transalkylation I_{trans} in the twelve zeolites investigated.

Table 4.5. DFT calculated Eint of neutral diaryl intermediates for transalkylation (I_{trans}) and disproportionation (I_{disp}) in zeolites with different microporous structure.

			kJ/mol I		
	Channels system	**N**	$\mathbf{I_{trans}}$	$\mathbf{I_{disp}}$	$\mathbf{I_{disp}/I_{trans}}$
BEA	12x12x12	3	-148	-129	0,87
BEC	12x12x12	1	-123	-151	1,22
BOG	12x10x10	4	-140	-140	1,00
CON	12x10x10	2	-132	-149	1,14
FAU	12x12x12	7	-104	-106	1,02
ITT	18x10x10	4	-110	-155	1,41
IWR	12x10x10	1	-145	-174	1,20
IWV	12x12	2	-102	-90	0,88
MOR	12x8	2	-141	-104	0,74
SEW	12x10	2	-160	-188	1,18
USI	12x10	2	-128	-157	1,22
UTL	14x12	2	-105	-137	1,31

Looking at the data exposed in Table 4.5, it is possible to see that the DFT Eint per mol of diaryl intermediate are in all cases negative and larger than -100 kJ/mol I. This fact indicates that all the zeolite structures selected as optimal candidates from the fast computational screening study are well-suited to stabilize this type of intermediate and therefore should enhance the diaryl-mediated pathway despising the alkyl transfer mechanism. Using the Eint values obtained from DFT calculations, the Eint ratio I_{disp}/I_{trans} was defined as a parameter to provide quantitative information about the potential selectivity of each zeolite structure. For this parameter values larger than 1 indicate a better stabilization of I_{disp} intermediate as compared to I_{trans}, and therefore a larger selectivity to TEB will be given by these catalysts. It is evident from Table 4.5 that zeolites containing large channels like ITT (18x10x10) or UTL (14x12) clearly favour the bulkier I_{disp} stabilization, followed by BEC, USI, IWR and SEW with 2D or 3D channels systems composed by 12r and 10r channels. Meanwhile, IWV with a 2D channel system of 12r and a good stabilization of I_{trans} and BEA with a 3D channel system of 12r and a slightly weaker interaction with I_{trans} should be selective to EB according to data in Table 4.5. These differences between 12r zeolites suggest that not only the size of the channels matters when controlling the diaryl mediated paths selectivity towards DEB or TEB. Zeolites with the same dimensionality but different topology will present different selectivity while promoting our desired mechanism. Thus, in order to distinguish this subtle differences caused by the active site scaffold, a more detailed mechanistic study is necessary.

4.5 Periodic DFT Study of diaryl-mediated transalkylation mechanism.

To start the mechanistic study, the four pathways described in section **4.3** for the transformation of the cationic diaryl intermediate $I1^+$ into $I4^+$ were investigated with pure silica models of the promising BEC, BOG, IWR, IWV and UTL zeolites using periodic DFT calculations to analyse the influence of the zeolite framework on the kinetics of the transalkylation and disproportionation reactions. The selection of these zeolite candidates includes structures with 2D and 3D channels systems containing 10r, 12r, and 14r channels, all of them with good Eint for the neutral transalkylation I_{trans} intermediate. MOR, with a 1D channel system where the diaryl intermediates don't match too well, was included for comparison to prove that the filters applied in section **4.4** to the starting 50 candidates made sense. As UTL presents a 14x12 2D channel system the mechanistic study in UTL was performed in two different locations, in the large 14r channel (UTL(cha)) and at the intersection between the 12r and 14r channels (UTL(int)) to analyse in detail the influence of the channel size and topology on the kinetics of the reaction.

The relative stability found for of all minima and transition states are summarized in Table 4.6, and the corresponding energy profiles are plotted in Figure 4.7.

Table 4.6. Relative stability (in kJ/mol) of cationic intermediates and transition states involved in transalkylation mechanisms in different zeolite structures.

	BEC	**BOG**	**IWR**	**IWV**	**MOR**	**UTL (int)**	**UTL (cha)**
$I1^+$	0	0	0	0	0	0	0
TS1	98	75	71	56	95	59	64
$I4^+$	-32	-17	-19	-25	-25	-27	-30
TS2	35	29	31	21	33	29	28
$I2^+$	-29	-20	-24	-34	-21	-33	-27
TS3	15	45	36	18	57	16	30
$I3^+$	-29	-28	-30	-18	-19	-32	-22
TS4	20	22	14	29	31	17	23
TS5	85	88	91	60	84	82	68
TS6	69	76	66	52	66	72	53

Table 4.7. Calculated activation barriers (in kJ/mol) for all the elementary steps of the transalkylation mechanisms in different zeolite structures.

	Channels system	Ea1	Ea2	Ea3	Ea4	Ea5	Ea6
BEC	12 x 12 x 12	98	35	44	48	85	98
BOG	**12** x 10 x 10	75	29	65	50	88	96
IWR	**12** x 10 x 10	71	31	60	44	91	90
IWV	12 x 12	56	21	52	47	60	86
MOR	**12** x 8	95	33	78	50	84	87
UTL(int)	14 x **12**	59	29	49	49	82	97
UTL(cha)	**14** x 12	64	28	57	45	68	80

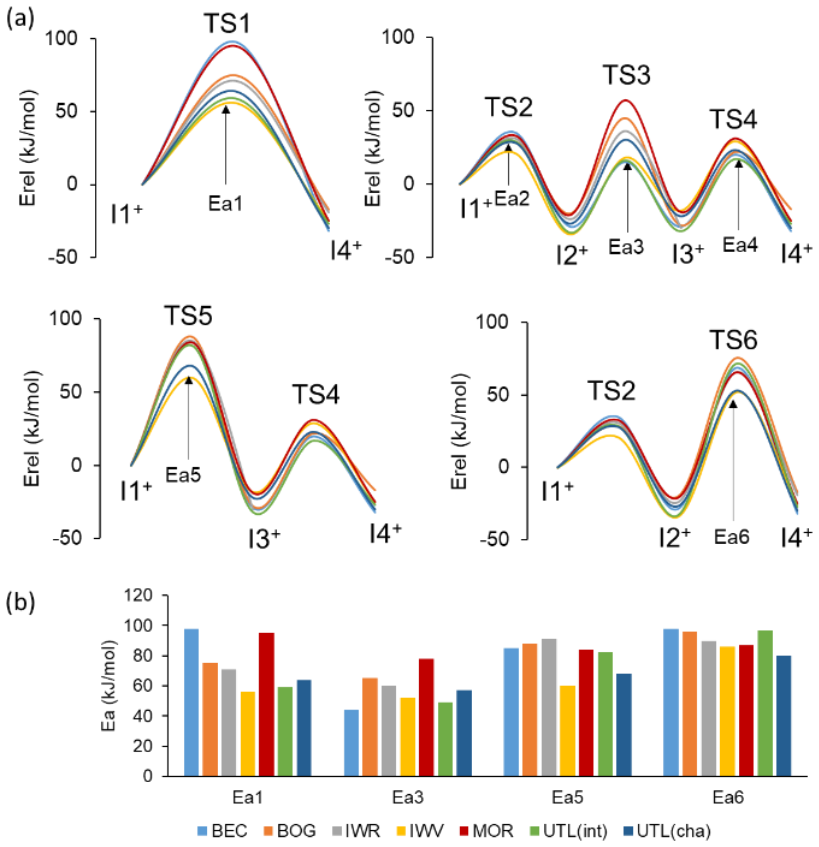

Figure 4.7. Calculated energy profiles (a) and comparison of the activation energy barriers (b) for transalkylation pathways in different zeolite structures.

Comparing Figure 4.7 with Figure 4.2 in section **4.3** it is possible to see that the reaction paths within the zeolite channels are equivalent to those described in gas phase. When analysing Figure 4.7 in detail only small differences in relative energies of intermediates and in activation barriers are found due to the steric restrictions imposed by the different zeolite frameworks. To facilitate the comparison between materials, the activation energies for the six elementary steps investigated are summarized in Table 4.7 and plotted in Figure 4.7b. The barriers for the intra-ring H^+ shifts, Ea2 and Ea4, are between 20 and 50 kJ/mol in all zeolites. These values, like in the gas phase study, are lower than the one found for the H^+ transfer between the two aromatic rings. Thus, this observation confirms that these processes are the rate-determining steps for each possible mechanistic route also in confined spaces. Having one clear rate-determining barrier for each of the four different H^+ transfer processes allows us to apply the energy-span model to compare different zeolite structures and preferred pathways. The values of Ea1, Ea3, Ea5 and Ea6, representative of each route, are plotted together in Figure 4.7b. Comparison of the data obtained indicates that the lowest energy pathway for transalkylation is in all cases the three-step process taking place through TS3, with activation energies Ea3 ranging from 44 kJ/mol in BEC to 78 kJ/mol in MOR. In most zeolite structures considered, the second preferred pathway is the direct H^+ transfer through TS1 with the calculated Ea1 values being ~10 kJ/mol larger than the corresponding Ea3 values (see Table 4.7). Two clear exceptions are BEC and MOR, with activation energies for this step close to 100 kJ/mol. Finally, the activation barriers for the routes involving five-membered transition states, Ea5 and Ea6, are larger than 80 kJ/mol, with the only exception of Ea_5 in IWV (60 kJ/mol) and UTL(cha) (68 kJ/mol).

Studying molecular docking from a geometrical point of view provides high value information about the confinement effects caused by the different zeolite channel topologies. As we have seen, from a geometrical point of view, the most demanding step is the direct H^+ transfer through a four-membered ring, TS1, as depicted in Figure 4.8. In gas phase, that is, in the absence of any steric constraint, the α angle closes from 108º in $I1^+$ to 101º in TS1, which induces a closing of the β angle from 128º to 98º, while the γ and δ angles around 180º reflect the planarity or the two aromatic rings. If zeolite channel systems bother these ideal geometrical changes because of a too tough confinement or because of the lack of channel intersections that host properly the diaryl intermediates, further deformations occur with the associated energy penalty, as exemplified in Figure 4.8 (see all angles in Table 4.8). Comparing all angles measured from optimized structures, the optimized structure of TS1 in IWV is almost the same as in gas phase, and only small variations of ~5º in α and β are observed in IWR. In contrast, inside the unidirectional 12r channels of MOR, the diaryl structure must flatten to fit properly inside its narrower channels, resulting in

an increase of the β angle to 113º getting deformed by 15º from its ideal gas state and a decrease of the γ and δ angles to 170º and 172º, respectively. Surprisingly, a similar deviation from the optimum gas phase geometry of TS1 is forced inside the microporous structure of BEC, which despite being a 3D system of 12r channels it does not form any large void at the channels intersection and its channels are not wide enough to host the intermediates within themselves, thus explaining the significantly higher Ea1 values calculated in these two structures. A different situation is found for TS3, where the six-member ring involved in the H^+ transfer accommodates better the deformations required to fit within the zeolites' voids (see Table 4.8) and it is less sensitive to geometrical deformations than a four-membered transition state. In this case, the largest deviations from the gas phase values of α and β for TS3 are found in MOR (3º and 6º) and BOG (2º and 5º) that correspond to the two zeolites exhibiting the highest Ea3 barriers in Table 4.7.

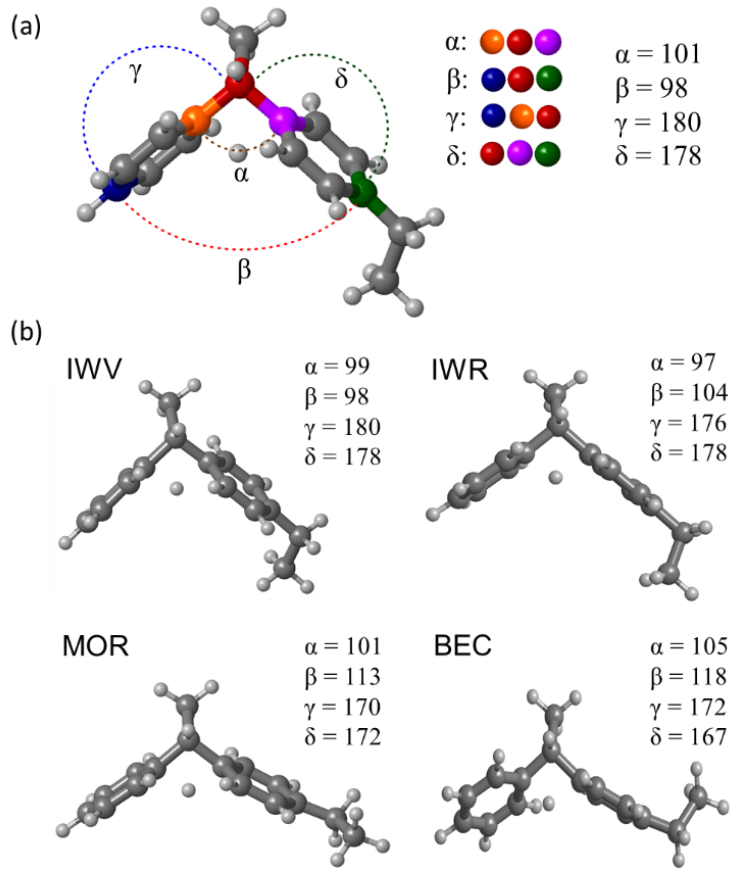

Figure 4.8. (a) Definition of the α, β, γ and δ angles and optimized values corresponding to TS1 in gas phase. (b) Optimized geometries of TS1 in IWV, IWR, MOR and BEC zeolites with the corresponding values of the α, β, γ and δ angles.

Table 4.8. Optimized values of the α, β, γ and δ angles described in Figure 4.5.

		gas	BEC	BOG	IWR	IWV	MOR	UTL(int)	UTL(cha)
I1$^+$	α	108	110	108	108	108	112	109	112
	β	128	130	124	128	121	132	123	126
	γ	118	132	124	123	121	142	133	150
	δ	178	174	178	176	179	171	178	176
TS1	α	101	105	97	97	99	101	100	98
	β	98	118	94	104	98	113	100	97
	γ	180	172	179	176	180	170	178	178
	δ	178	167	175	178	178	172	180	179
I2$^+$	α	104	109	109	103	101	115	112	100
	β	100	113	114	102	97	122	109	94
	γ	175	179	177	177	175	173	176	173
	δ	178	174	175	179	178	173	175	178
TS3	α	106	107	109	107	107	109	107	107
	β	96	97	101	97	97	102	98	96
	γ	171	171	169	171	170	175	173	170
	δ	172	171	177	172	172	171	168	172

$I3^+$	α	110	108	116	104	110	115	109	112
	β	109	106	118	104	106	119	110	111
	γ	179	178	177	179	174	176	177	176
	δ	176	175	176	178	179	173	178	176
$I4^+$	α	109	111	110	109	108	113	111	109
	β	123	124	124	122	118	135	129	125
	γ	179	179	177	179	176	176	177	178
	δ	128	135	135	151	138	129	140	131
TS5	α	103	104	106	105	105	107	101	106
	β	96	104	108	99	97	109	100	106
	γ	175	171	170	179	179	172	166	173
	δ	166	173	173	171	167	159	167	175
TS6	α	110	105	108	100	102	108	104	102
	β	109	111	102	90	94	112	99	95
	γ	179	166	163	163	164	163	166	163
	δ	176	158	175	179	173	165	173	175

To obtain a unique quantitative parameter that permits the characterization of the kinetic behavior of each zeolite structure in the transalkylation reaction, a Boltzmann weighted average of the activation barriers obtained for each of the four inter-ring proton transfer steps studied was calculated. Taking into account that the experimental reaction temperature is 240ºC, only the lowest energy pathway, through TS3 in all cases, contributes substantially to the average activation energy. Thus, defining Ea3 activation energy as predictor of zeolite activity, catalytic performance for the different zeolites can be ordered with the following sequence: BEC > UTL(int) > IWV >> UTL(cha) > IWR > BOG > MOR. Comparing this data with the one obtained for the Eint of the I_{trans} intermediate in section **4.3**, where the order obtained was: IWR > MOR > BOG > BEC > UTL > IWV, arises a discrepancy in the predicted catalytic performance of similar zeolites. These differences suggest that the stability of the main reaction intermediate is a good parameter for the initial screening of optimal catalysts, but it is not accurate enough to describe the outcome of complex reaction networks such as the one under study.

4.6. Periodic DFT study of diaryl-mediated disproportionation mechanism.

To check whether the selectivity to EB and TEB is well described by the stabilization of the corresponding intermediate, I_{trans} and I_{disp}, or also changes appear when considering more in depth mechanistic data, the four pathways for the disproportionation of DEB were calculated in the a priori most selective zeolite towards EB, IWV I_{disp}/I_{trans} = 0.88, and the most selective zeolite towards TEB, UTL I_{disp}/I_{trans} = 1.31. In addition, BEC zeolite with I_{disp}/I_{trans} = 1.22, was also introduced in this part of the study because of its three dimensional 12r channel system.

The trends observed in gas phase at section **4.3** are reproduced inside each one of the zeolite micropores (see Table 4.9 and Figure 4.9). All activation barriers for disproportionation are systematically higher than the ones found for transalkylation.

In an attempt to quantify this effect, the difference between the lowest activation energies for disproportionation and transalkylation were computed for BEC, IWV, UTL(int) and UTL(cha). The calculated values are similar, 12, 15, 20 and 16 kJ/mol, respectively, suggesting that the steric impediments in each zeolite affect similarly all intermediates and transition states. Regarding the specific case of BEC, it is possible to identify that Ea1, Ea5 and Ea6 are among the highest ones found also for disproportionation. However, the three step mechanistic path through Ea2, Ea3 and Ea4 presents low activation energy

values compared with other zeolites for transalkylation and disproportionation (Table 4.9) especially for the inter-ring proton transfer, Ea3, that is the rate determining step for this route. Thus, combining the parameter I_{disp}/I_{trans} = 1.22 with these low barriers, it is possible to conclude that BEC will produce a considerable amount of TEB because it offers a good stabilization to diaryl disproportionation intermediates and also a kinetically affordable pathway for the reaction to proceed. Therefore, the selectivity to TEB will mainly depend on the possibility to form the bulkier I_{disp} intermediate inside the zeolite pores, and will probably be well described by the relative stabilization of the main I_{trans} and I_{disp} intermediates.

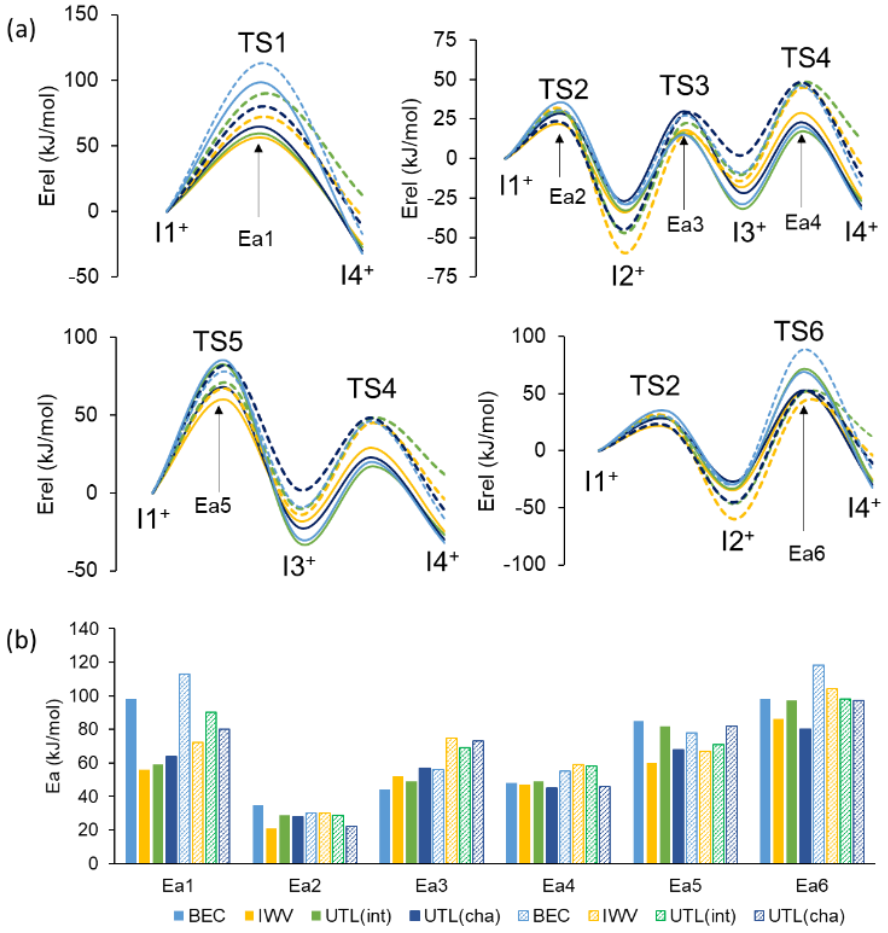

Figure 4.9. Energy profiles (a) and comparison of the activation energy barriers (b) for transalkylation (full lines and columns) and disproportionation (dashed lines and columns) in BEC, IWV and UTL zeolites.

Table 4.9. a) Relative stability and b) calculated activation barriers (in kJ/mol) of intermediates and transition states involved in the mechanisms of disproportionation in different zeolite structures.

a)	**BEC**	**IWV**	**UTL(int)**	**UTL(cha)**
$I1^+$	0	0	0	0
TS1	113	72	90	80
$I4^+$	-17	-4	12	-11
TS2	30	30	29	22
$I2^+$	-29	-60	-47	-45
TS3	27	15	22	28
$I3^+$	-9	-14	-10	2
TS4	46	45	48	48
TS5	78	67	71	82
TS6	89	44	51	52

b)	**Ea1**	**Ea2**	**Ea3**	**Ea4**	**Ea5**	**Ea6**
BEC	113	30	56	55	78	118
IWV	72	30	75	59	67	104
UTL(int)	90	29	69	58	71	98
UTL(cha)	80	22	73	46	82	97

4.7. Explicitly introducing the active site: Periodic DFT study of the alkyl-transfer pathway.

To support the initial assumption that zeolites with 1D channels systems get easily blocked by bulky diaryl intermediates and favor the less selective alkyl-transfer pathway, in this section we investigate in depth the competing mechanism proceeding through ethoxy intermediates. Our goal is to understand the behavior of zeolites with the same channel size (12r) but with different dimensionality of the channels system (MOR, 1D versus IWV, 2D). The reason for the selection of these two materials was the large amount of differences found between them despite their similarity as 12r channel size structures. The most evident difference is their dimensionality, MOR presents a 1D channel system meanwhile IWV's is 2D. This confers IWV a higher maximum diameter of sphere that can be included, 8.54 Å, than MOR, 6.7 Å, and also a much higher accessible volume for the molecules inside IWV channels, 22.28% compared to 12.27% for MOR according to IZA database.[48]

Since the alkyl-transfer mechanism requires the explicit presence of Brønsted acid sites to perform the proton transfer steps and form ethoxy species, we designed three different acid zeolite models, two for IWV framework and one for MOR. When studying proton transfers from zeolite framework to big hydrocarbon molecules, channel dimensions and tortuosity play an important role for the facility of proton abstraction and a proper stabilization of the carbocation formed at the end of the process. That is why we decided to study two different Al position for IWV with the aim of achieving information about the different micro-environments inside its channels, meanwhile the whole MOR behaviour could be explained by studying just one Al position. The T3 and T6 sites in IWV were selected based on their intrinsic stability when one Si atom is substituted by an Al atom and the AlO_4^- unit is uncompensated (see Table 4.10), and T4 site at the 12r channel was selected for MOR (see Figure 4.13).

Table 4.10. Relative stability of Al location in IWV zeolite in kJ/mol

Site	T1	T2	T3	T4	T5	T6	T7
Relative Energy	11	13	0	5	11	1	8

According to Scheme 1, the first step in the alkyl-transfer pathway is the protonation of DEB through transition state TS9 to form a $DEBH^+$ carbonium ion with a pentacoordinated C atom, see IWV optimized geometries in Figures 4.11 and 4.12, and MOR ones in Figure 4.13.

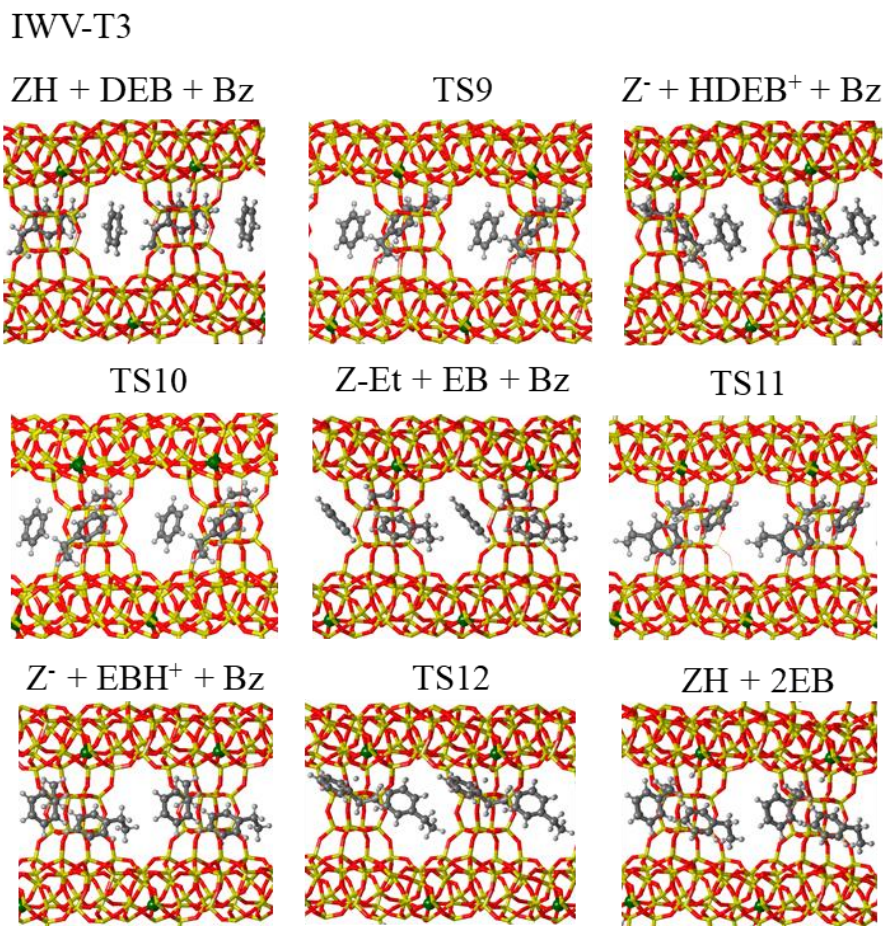

Figure 4.11. Optimized geometries of all structures involved in the alkyl-transfer pathway on IWV-T3 site.

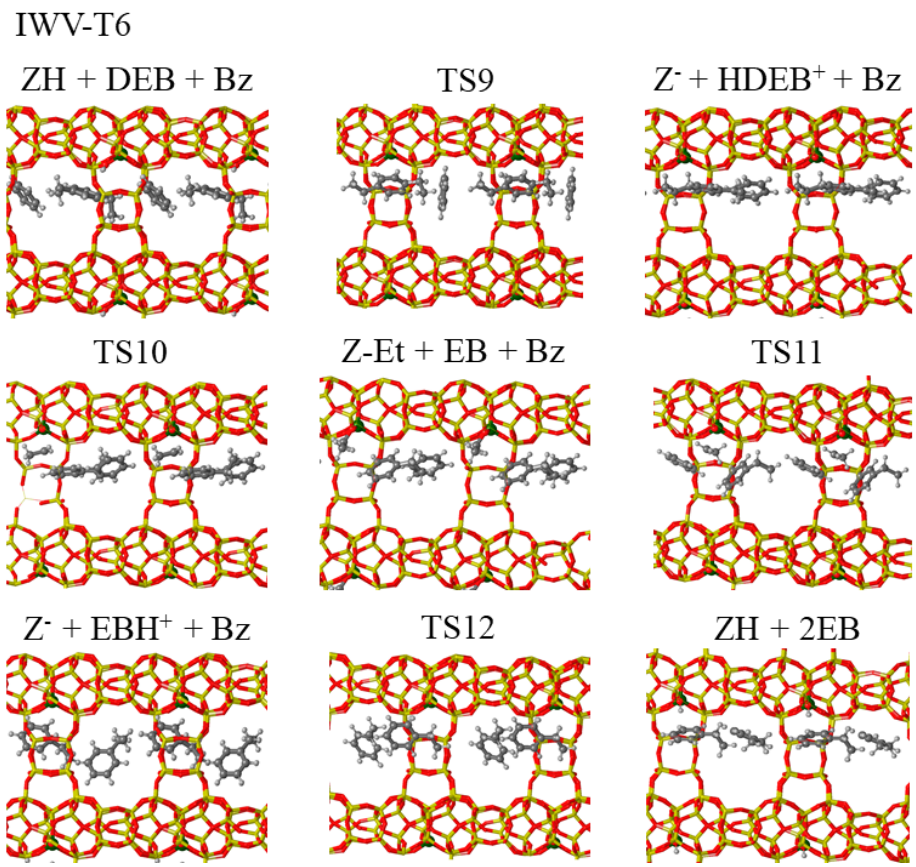

Figure 4.12. Optimized geometries of all structures involved in the alkyl-transfer pathway on IWV-T6 site.

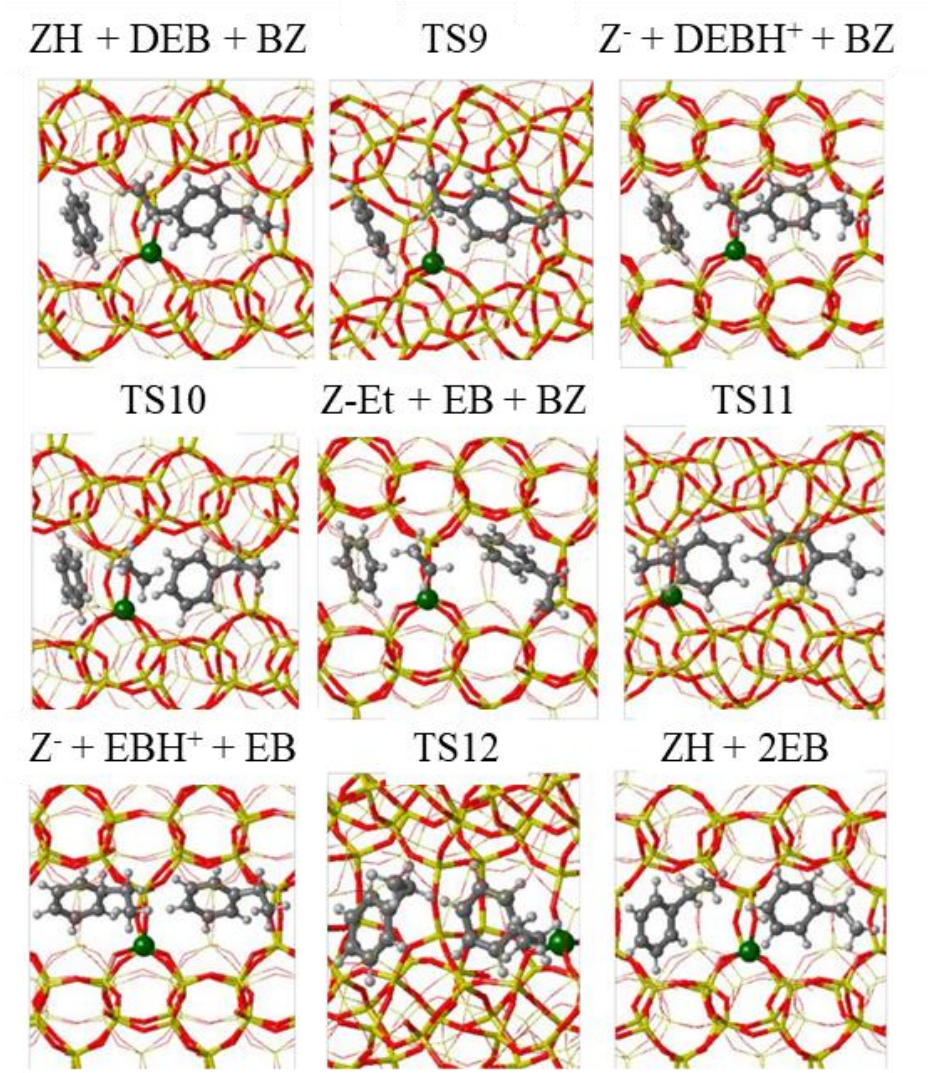

Figure 4.13. Optimized geometries of all structures involved in the alkyl-transfer pathway on MOR-T4 site.

The calculated activation energies for TS9 in IWV are not too high (~ 50 kJ/mol), however, the process is endothermic, and the $DEBH^+$ cations formed are unstable, with the barriers for backward decomposition into DEB reactant being lower than 4 kJ/mol. For the alkyl-transfer mechanism to proceed forward by the alternative ethyl transfer to the zeolite framework through TS10, it requires activation energies between 90 and 100 kJ/mol, which render this pathway highly improbable expecting a low production of ethene for IWV. In MOR-T4, the activation barrier calculated for DEB protonation through TS9 is higher, 84 kJ/mol, but the relative stability against backward decomposition for the $DEBH^+$ carbonium ion formed, with a barrier of 30 kJ/mol, allows some

competitive dealkylation through TS10. The surface ethoxy group generated in this step might react with benzene to form a new EB molecule with an activation energy of 100 kJ/mol or might decompose via transition state TS13, yielding ethene with a similar activation barrier of 97 kJ/mol (see Figure 4.14 and Table 4.11). These results suggest that a considerable amount of ethene should be observed experimentally when working with MOR as DEB transalkylation catalyst.

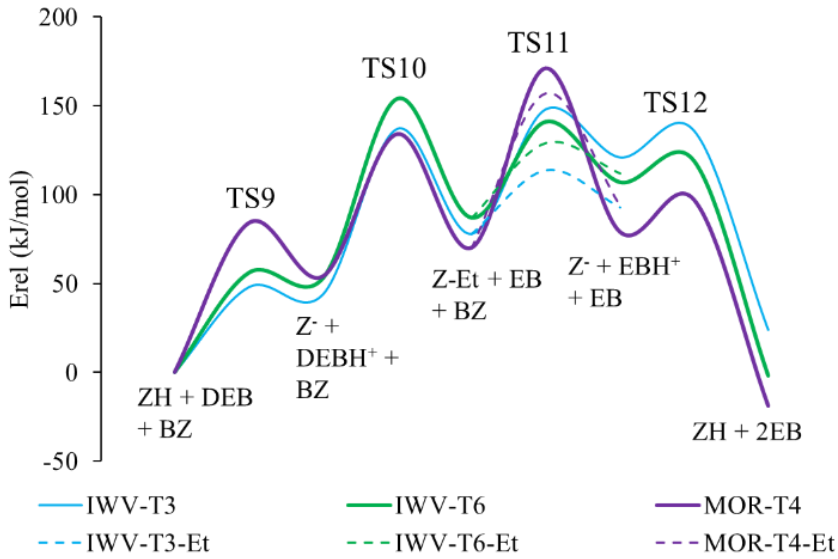

Figure 4.14. Calculated DFT energy profile for alkyl-transfer mechanism in IWV-T3, IWV-T6 and MOR-T4.

Table 4.11. DFT calculated activation and reaction energies (in kJ/mol) for the elementary steps of the alkyl-transfer mechanism.

Step	**IWV-T3**	**IWV-T6**	**MOR-T4**
	Eact	**Eact**	**Eact**
ZH + DEB →[TS9]→Z^-+$DEBH^+$	48	56	84
Z^-+$DEBH^+$→[TS10]→ Z-Et +EB	93	101	80
Z-Et +Bz →[TS11]→ Z^-+EBH^+	70	54	101
Z^-+EBH^+ →[TS12]→ ZH + EB	15	12	18
Z-Et →[TS13]→ ZH + C_2H_4	115	108	97

A proper explanation for the different behaviour of IWV and MOR catalysts is provided by the optimized geometries of the structures involved. The 12r channels in the two frameworks have similar dimensions, 6.2 × 6.9 Å in IWV and 6.5 × 7.0 Å in MOR, according to the IZA database. However, larger voids are present at the channels intersections in IWV. These wider regions are accessible irrespective of the Al location, and the $DEBH^+$ and EBH^+ cations involved in this pathway come close to the zeolite wall towards one side of the channel while getting far from the framework oxygen placed at the other side, losing the proper confinement effect conferred by the framework oxygen atoms when carbocations are placed in the centre of the zeolite channels (Figure 4.14). Taking the distance between the tertiary carbon atom of the DEB aromatic ring and the closest framework oxygen atom placed at the opposite side of the channel, rC-Of in Figure 4.15 and Table 4.12, as an indication of the situation of the cationic intermediates within the channels, we observe systematically larger values in IWV (between 6.5 and 9.1 Å) than in MOR (always below 5.7 Å). These values indicate that, in MOR, the reactant and intermediate species tend to be allocated in the centre of the straight 12r channel, fully surrounded by framework oxygen atoms at the right distance to maximize the stabilization by confinement. This positioning explains the low barrier for backward decomposition into DEB through TS9 in IWV, 4 kJ/mol, as the $DEBH^+$ carbocation cannot be properly confined. However, the first proton transfer through TS9 requires the approximation of the DEB to the Brønsted acid site, causing a deformation in its structure that gets more pronounced inside straight MOR channels than inside IWV intersection voids. This deformation explains the higher relative energy of TS9 in MOR when compared with IWV.

After the study presented in the two last sections for all possible non-desired side reactions for diethylbenzene transalkylation, namely disproportionation and dealkylation through the alkyl-transfer pathway, we can conclude than neither of them will be favoured when using 12r bi- or tri-dimensional zeolites as catalysts, hence increasing the experimental yield of EB. On the one hand, disproportionation is intrinsically disfavoured when compared to transalkylation. In addition, 12r channel systems cannot host properly the bulky diaryl intermediates formed by two DEB molecules reducing the probability of observing TEB as a side product. On the other hand, we can extrapolate the results for the alkyl-transfer pathway from IWV to other structures containing 12r channels systems with intersections like BEC, IWR or UTL. In these zeolites $DEBH^+$ carbocation will not be properly confined when approaching the zeolite framework, rendering the alkyl-transfer step through TS10 energetically non-competitive against backward proton transfer to the framework yielding DEB and lowering the amount of ethene generated as by-product.

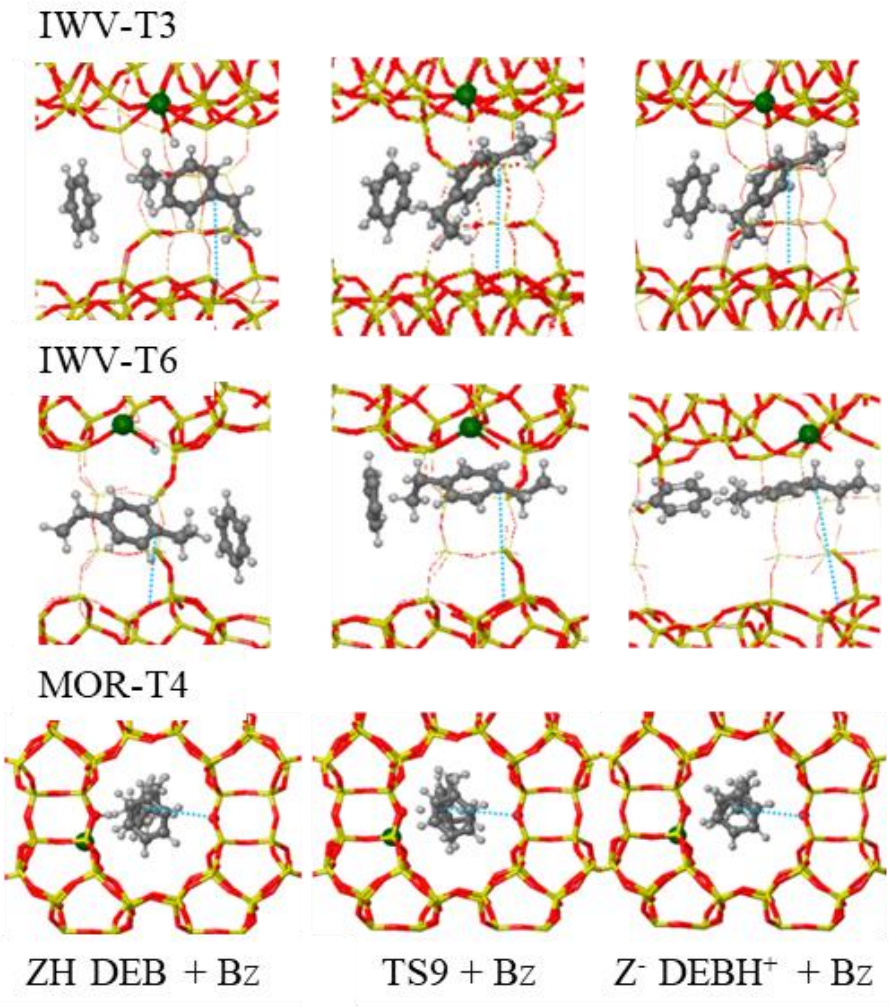

Figure 4.15. Optimized geometries of reactants, first transition state (TS9) and $DEBH^+$ carbonium ion intermediate involved in the alky-transfer pathway on IWV-T3, IWV-T6 and MOR-T4 sites. Dotted blue lines indicate the C – O_f distances given in Table 4.13.

Table 4.12. Optimized values (in Å) of selected distances of the structures involved in the alkyl transfer pathway. The rC-Of refers to the distance between the tertiary C atom of the aromatic ring and the closest oxygen atom at the opposite side of the zeolite channels as depicted in Figure 4.15.

	IWV-T3			**IWV-T6**			**MOR-T4**		
	rC-H	**rH-O**	**rC-Of**	**rC-H**	**rH-O**	**rC-Of**	**rC-H**	**rH-O**	**rC-Of**
ZH + DEB	3.47	1.01	6.47	2.74	1.00	7.70	2.60	1.01	5.18
TS9	1.32	1.41	7.28	1.33	1.45	8.16	1.41	1.35	5.68
Z^- + $DEBH^+$	1.16	1.78	7.09	1.19	1.72	8.60	1.13	2.69	5.36
	rC-C	**rC-O**	**rC-Of**	**rC-C**	**rC-O**	**rC-Of**	**rC-C**	**rC-O**	**rC-Of**
Z^- + $DEBH^+$	1.56	3.48	7.66	1.55	3.43	7.91	1.56	3.35	5.36
TS10	2.41	2.18	9.12	2.36	2.26	7.11	2.40	2.24	4.02
Z-Et + EB	3.46	1.53	4.94	3.98	1.52	6.77	3.79	1.53	4.83
Z-Et + Bz	5.13	1.53	7.66	3.97	1.52	7.91	4.06	1.53	4.83
TS11	2.35	2.35	8.57	2.38	2.30	7.55	2.36	2.31	5.72
Z^- + EBH^+	1.63	4.55	6.46	1.59	4.93	6.76	1.54	4.18	3.88
	rC-H	**rH-O**	**rC-Of**	**rC-H**	**rH-O**	**rC-Of**	**rC-H**	**rH-O**	**rC-Of**
Z^- + EBH^+	1.11	3.26	7.29	1.11	2.58	8.11	1.16	4.11	4.99
TS12	1.45	1.45	7.21	1.30	1.49	6.28	1.36	1.50	5.68
Z-H + EB	3.83	0.98	7.41	5.60	1.00	7.42	3.22	1.01	5.16

Subsequently to the alkyl-transfer study with acid zeolite models, it is also convenient to inspect the impact of acid site inclusion over diaryl mediated pathways. With that aim, we reproduced the mechanistic study performed in section **4.5** for all possible transalkylation diaryl mediated pathways inside the IWV-T3, IWV-T6 and MOR-T4 models (see Figure 4.16). Results obtained are disclosed at Table 4.13 and depicted at Figure 4.17.

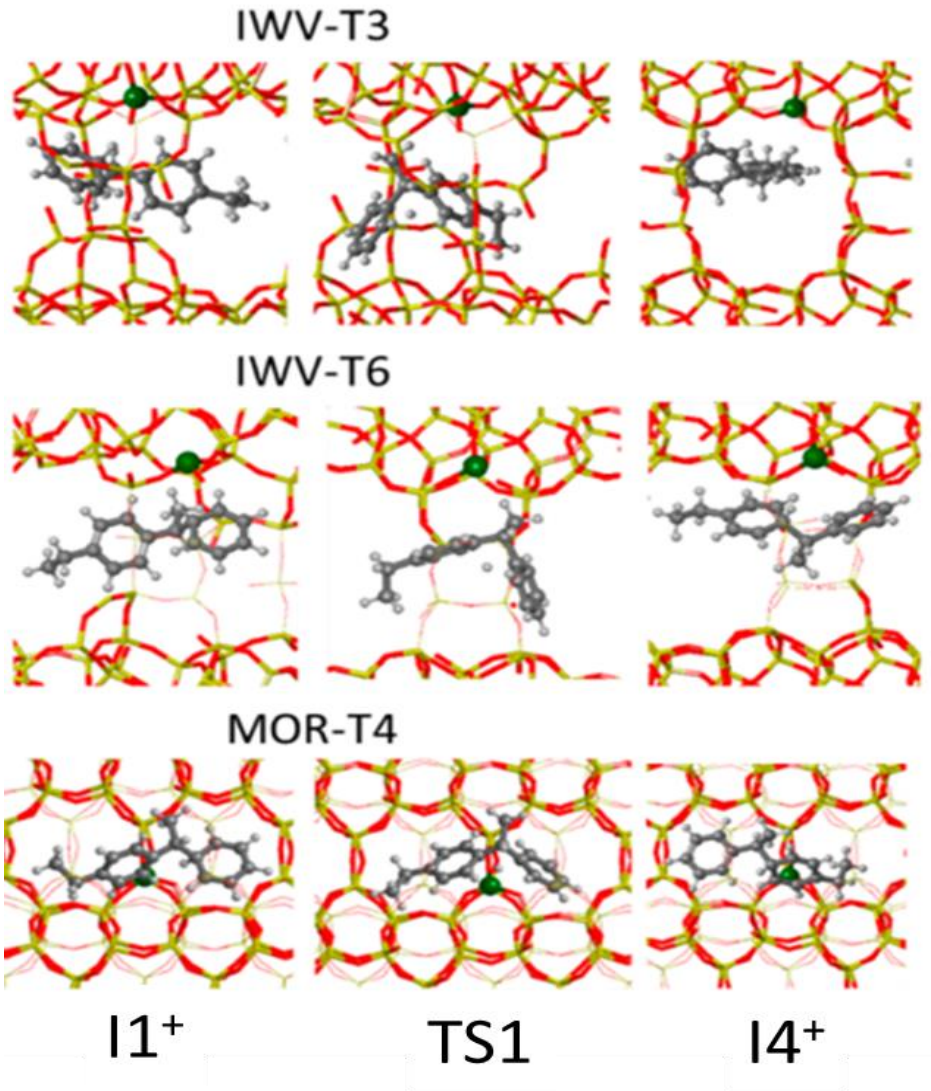

Figure 4.16. Optimized geometries of $I1^+$, TS1 and $I4^+$ involved in the transalkylation diaryl mediated pathway mechanism on IWV-T3, IWV-T6 and MOR-T4 sites.

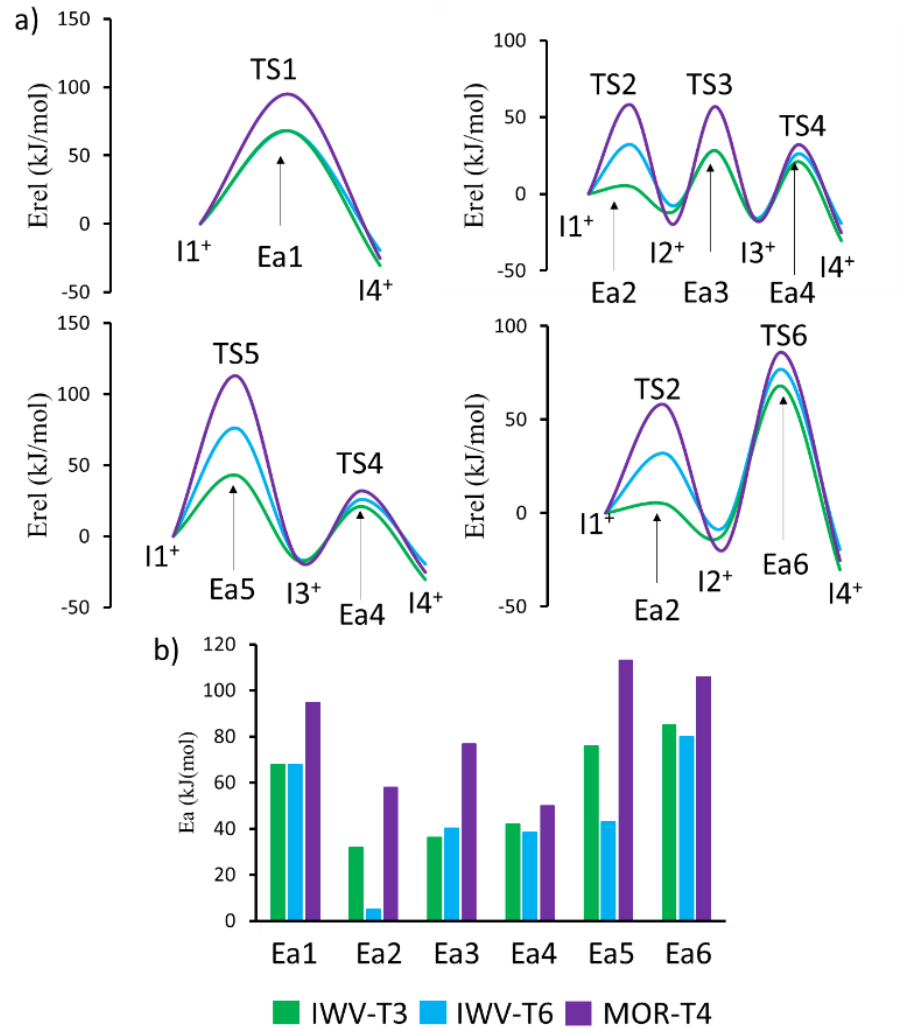

Figure 4.17. Energy profiles (a) and comparison of the activation energy barriers (b) for transalkylation diaryl mediated pathways in IWV-T3, IWV-T6 and MOR-T4 acid models.

Table 4.13. a) Relative stability and b) calculated activation barriers (in kJ/mol) of intermediates and transition states involved in the mechanisms of transalkylation in IWV-T3, IWV-T6 and MOR-T4 acid models.

a)	**IWV-T3**	**IWV-T6**	**MOR-T4**
$I1^+$	0	0	0
TS1	68	68	95
$I4^+$	-19	-30	-25
TS2	32	5	58
$I2^+$	-8	-12	-20
TS3	28	28	57
$I3^+$	-16	-18	-18
TS4	26	21	32
TS5	76	43	113
TS6	77	68	86

b)	**Ea1**	**Ea2**	**Ea3**	**Ea4**	**Ea5**	**Ea6**
IWV-T3	68	32	36	42	76	85
IWV-T6	68	5	40	39	43	80
MOR-T4	95	58	77	50	113	106

Comparing results obtained for both mechanisms inside acid models of IWV, it is possible to identify that calculated activation energies for the lowest energy path of the diaryl mediated pathways in IWV-T3 and IWV-T6, Ea2, Ea3 and Ea4 ~40 kJ/mol (see Table 4.13), are milder than the ones obtained for the TS9 and TS10 steps of the alkyl-transfer mechanism (see Table 4.11). Meanwhile for MOR-T4, activation energies around 80 kJ/mol obtained for alkyl-transfer mechanism steps TS9 and TS10 (Table 4.11) are competitive with the ones obtained for its lowest activation energy for the inter-ring H^+ transfer, Ea3 = 77 kJ/mol (see Table 4.13). These results reinforce the hypothesis given previously where IWV 2D 12x12 channel system is better suited to host diaryl intermediates than $DEBH^+$ cations, and MOR 12r straight channels host better the less space-demanding $DEBH^+$ cations than the diaryl intermediates.

Evaluating the impact of active site inclusion over the diaryl mediated paths by comparing Table 4.13 and Table 4.7 results, it is possible to conclude that the active site does not modify the diaryl mediated paths preferences. Both zeolites, IWV and MOR, with different channel systems still prefer the inter-ring H^+ transfer through Ea3 pathway inside both kinds of models. These results are reasonable because diaryl intermediates are big carbocationic molecules with a highly delocalized positive charge that does not interact in a strong manner with AlO_4^- units. Therefore, we can assume that pure silica models are accurate enough to describe the DEB transalkylation procedure.

Interestingly, when we compare IWV-T3 and IWV-T6 relative stability for $I2^+$, $I3^+$ and $I4^+$, it is possible to see that they are better stabilized in the IWV-T6 models. This better stabilization observed may suggest that placing the Al in determined positions of the IWV channel system helps to stabilize better the diaryl intermediates, it may also mean a poorer stabilization for $I1^+$. However, as we have seen that including an active site does not affect the diaryl mediated pathways mechanism activation energies relation, the issue of Al positioning effect is left for further work outside of this thesis dissertation.

To conclude the analysis about the acid site impact for the diaryl-mediated mechanism, we also considered the diaryl mediated pathway that involves the proton transfer to the negatively charged zeolite framework, generating a neutral diaryl molecule (I in Scheme 4.2, green path), which must be reprotonated by the Brønsted acid site. The models used are depicted in Figure 4.18.

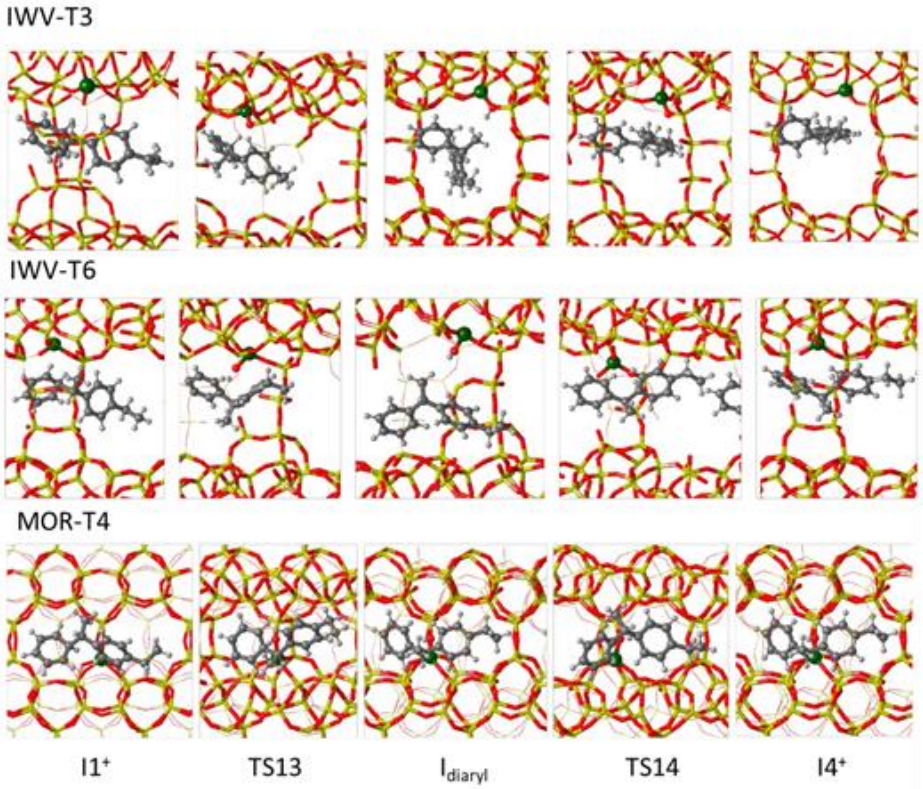

Figure 4.18. Optimized geometries of all structures involved in the proton transfer to the zeolite framework of the diaryl-mediated pathway on IWV and MOR zeolites.

The initial deprotonation step through TS7 is energetically affordable in all three cases, with activation energies ranging from 1 kJ/mol in IWV-T3 to 34 kJ/mol in MOR then generating a stable neutral intermediate I (see Table 4.14 and Figure 4.19). The subsequent protonation of the neutral species is similarly endothermic in all cases but involves much lower activation barriers in IWV zeolite, 50-55 kJ/mol, than in MOR, 121 kJ/mol (Table 4.14). In both cases, MOR presents barriers that double the ones of IWV for TS7 and TS8 because of the deformation that the diaryl intermediate undergoes when approaching the framework of a straight channel without intersections for the proton transfer process. On the other hand, the Ea7 and Ea8 values in IWV are quite similar to the activation energies found for the intrinsic proton transfer pathways (Table 4.7). Therefore, it is possible to conclude that the framework proton transfer route of the diaryl-mediated pathways is as viable as the inter-ring H^+ transfer pathways when using 2D or 3D zeolite channels.

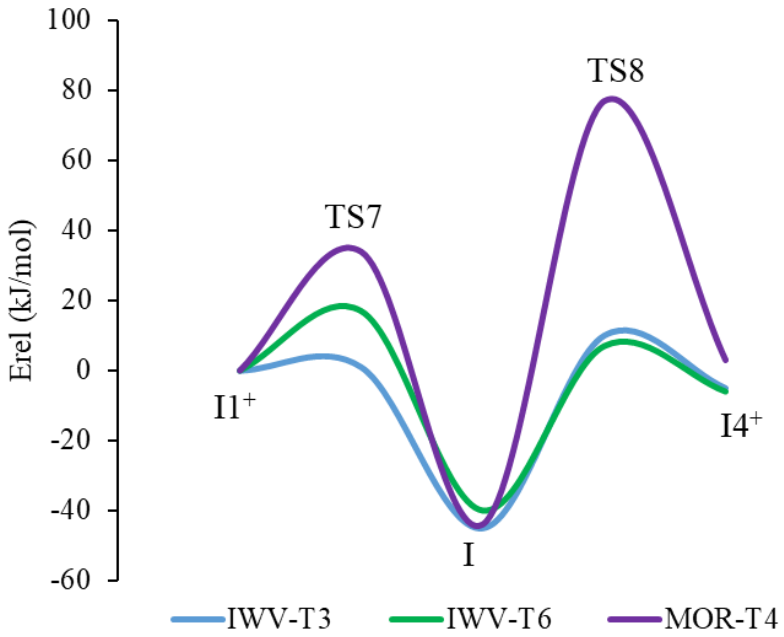

Figure 4.19. DFT energy profile for the framework route of the diaryl-mediated pathways.

Table 4.14. DFT calculated relative stabilities and activation energies (in kJ/mol) for the elementary steps for the framework route of the diaryl-mediated pathways.

	IWV-T3		**IWV-T6**		**MOR-T4**	
	Relative Stability	**Ea**	**Relative Stability**	**Ea**	**Relative Stability**	**Ea**
$I1^+$	0		0		0	
TS7	1	1	17	17	34	34
I	-45		-40		-44	
TS8	10	55	7	47	77	121
$I4^+$	-5		-6		3	

4.8 Synthesis and catalytic test of proposed zeolites.

To evaluate the trends proposed by the theoretical studies presented in previous sections, the following zeolites from the candidate set were synthesized and their catalytic activity was tested: extra-large pore ITQ-33 (ITT) and ITQ-15 (UTL), large-pore containing super-cages USY (FAU) large-pore with 3D channels ITQ-17 (BEC), large-pore with 2D channels ITQ-27 (IWV), intersecting large and medium-pore ITQ-47 (BOG) and ITQ-24 (IWR), and finally 1D large-pore mordenite (MOR).

Characterization data including PXRD patterns, FESEM images, 27Al MAS NMR spectra and pyridine adsorption/desorption IR-spectra for all samples can be found in Appendix II. Catalytic results obtained are disclosed in Table 4.15.

As expected, large-pore zeolites, such as ITT and UTL, produce remarkable amounts of TEB, 20.8% and 12.0%, respectively. Significant amounts of TEB, ~8%, are also observed for BEC with a 3D system of 12r channels of 7.5x6.3 Å, but not for FAU, with a supercage of 11.4 Å diameter. Regarding to 12r channel zeolites which dimensions are 7.0 Å or less, such as BOG, (7.0x7.0 Å), MOR (7.0x6.5 Å), IWV (6.9x6.2 Å) and ITQ-24 (IWR, 6.8x5.8 Å), results indicate a decrease of TEB formation due to steric restrictions for the bulky diaryl intermediates formation that are necessary for DEB disproportionation.

When linking theoretical and experimental results, a fairly good correlation between the selectivity to TEB and EB determined experimentally (TEB/EB ratio calculated from data in Table 4.14) and the theoretical Eint ratios I_{disp}/I_{trans} given in Table 4.7 is observed in Figure 4.20. There are only two structures out of this trend and the reason for these values can be properly explained. It is possible to see that MOR produces more TEB than predicted by the Eint ratios of the diaryl intermediates. That is because the aromatics transformations in this zeolite proceed in part through the alkyl-transfer pathway because of its mono-directionality as discussed in section 4.7. This assumption is confirmed by the observation of 4.6% ethene (see Table 4.15). In contrast, less TEB than expected from the theoretical Eint ratios I_{disp}/I_{trans} is experimentally observed in IWR because of an over-stabilization of the disproportionation diaryl intermediate at the intersection between the 12r and the two 10r channels that enhances I_{disp} value. From Figure 4.17 it is possible to identify that the two ethyl groups in one of the aromatic rings fit perfectly into the two narrow 10-ring channels of IWR at this specific position. However, the diffusion of TEB out of the crystal through 10r channels results hindered neglecting the possibility of observing a significant amount of TEB.

Table 4.15. Results of catalytic test in diethylbenzene-benzene transalkylation at 240ºC.

Zeolite	IZA code	DEB conv. (%)	r_{trans} (mol EB/mol acid h)	EB (%)	TEB (%)	C2H4 (%)	HP (%)	Ea exp[a] (kJ/mol)	Si/Ge
ITQ-33	ITT	11.9	717	76.4	20.8	0.6	2.1	75.2	2.3
ITQ-15	UTL	17.7	1599	85.7	12.0	0	2.3	56.1	49.7
USY	FAU	14.7	1075	90.1	2.7	2.7	4.5	66.5	
ITQ-17	BEC	20.8	628	88.8	8.3	0.5	2.3	59.5	3.4
ITQ-27	IWV	14.9	1926	94.1	0.5	2.3	3.0	58.3	
ITQ-24	IWR	15.2	676	95.1	2.5	0.4	2.0	69.4	
ITQ-47	BOG	14.4	349	90.4	4.4	4.8	0.4	66.2	85.5
mordenite	MOR	9.6	279	88.6	2.5	4.6	4.2	74.2	

The rate of transalkylation, r_{trans}, was measured as moles of EB formed per hour normalized by the moles of Brønsted acid sites present in each sample. Looking at data presented in Table 4.15, it is possible to see that the highest reaction rate obtained corresponds to IWV (12x12), followed by UTL (14x12). For ITT (18x10x10) and FAU, which contains a large cavity within its structure, the lower r_{trans} could be associated to a weaker confinement effect over the diaryl intermediates and transition states by their large pores causing a poorer stabilization. Looking at 12r channel zeolites, IWR with a 12x10x10 channel system exhibits a similar r_{trans} to BEC with wider 12x12x12 channels but without any large void at channels' intersections. In contrast, BOG catalytic activity which also presents a 12x10x10 channel system resulted much lower than the one observed for IWR despite the similarity in channel dimensions.

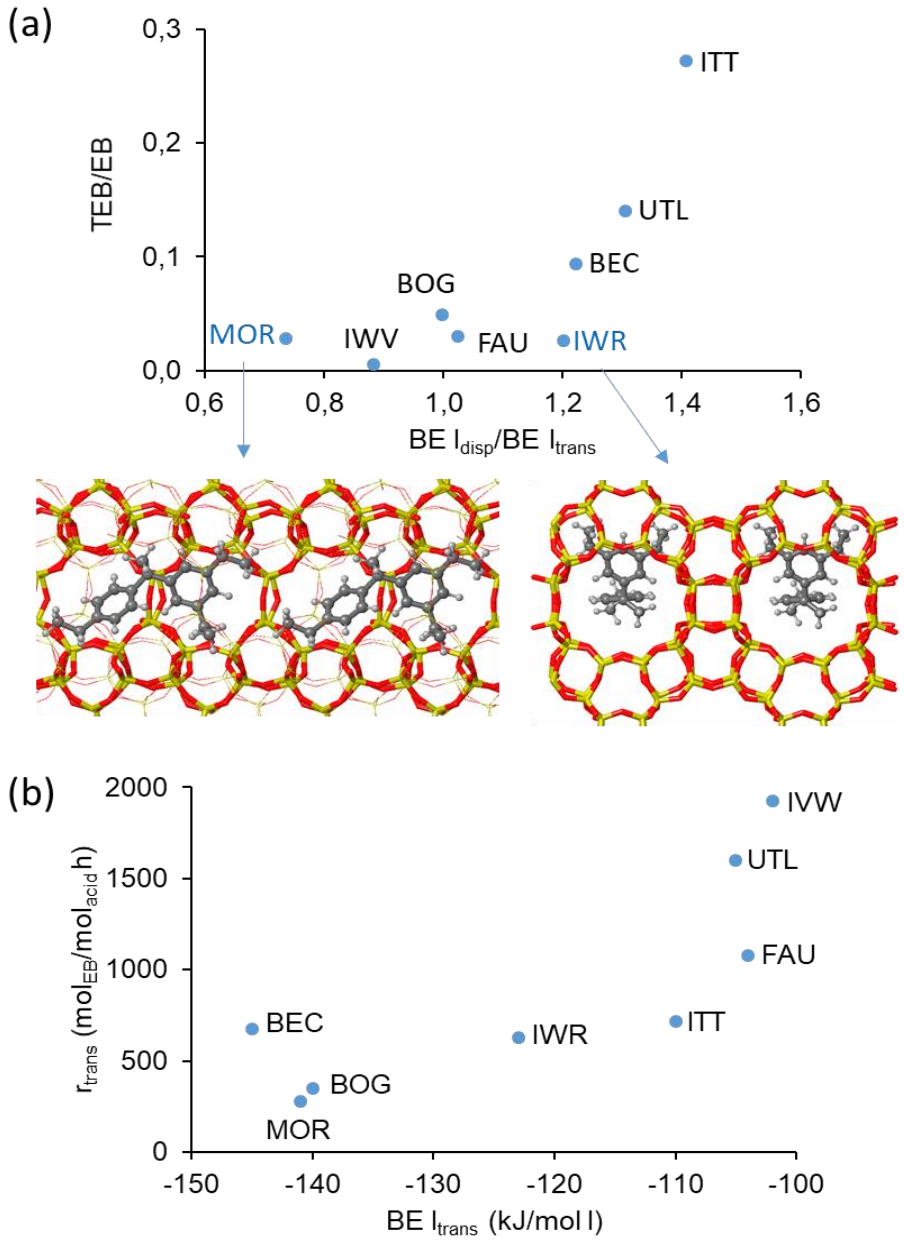

Figure 4.20. (a) Correlation between the experimental TEB/EB selectivity and the computational Eint Idisp /Itrans ratio. The optimized geometry of the diaryl Idisp intermediate inside the channels of MOR and IWR structures is shown. (b) Plot of experimental reaction rates for transalkylation r_{trans} versus DFT calculated Eint of the diaryl I_{trans} intermediate.

Comparing results presented in Table 4.15, BOG behaves similarly in terms of r_{trans} to MOR which presents mono-directional channels. The reasons for this similarity can be observed in the selectivity towards ethene which are the highest observed for any zeolite in the candidate set, 4.8 % for BOG and 4.6% for MOR. As it was theorized in section **4.7**, MOR straight channels with no intersections favour the alkyl-transfer pathway producing an important amount of ethene. As BOG three-dimensional channel system lacks of large void intersections, there might be a fraction of the concurring events that derive towards the alkyl-mediated pathway, most probably in the 10r channels, generating the amount of ethene observed. Finally, any clear correlation between the experimental reaction rates for transalkylation, r_{trans}, and the calculated Eint for Itrans intermediate was not found (Figure 4.20b).

Apparent activation energies (Ea exp) for each catalyst were calculated from the initial reaction rates r_{trans} measured at four different temperatures using the Arrhenius equation. The calculated Ea exp values are summarized in Table 4.15. In order to connect the experimental and computational information, the apparent activation energies Ea exp and the reaction rates for transalkylation r_{trans} were plotted against the DFT Ea3 activation energies obtained for the pure silica models summarized in Table 4.7 (Figure 4.21). The good correlation observed between the experimental and theoretical activation energies (Figure 4.21a) indicates that in these zeolite structures the DEB transalkylation reaction occurs preferentially through formation and transformation of diaryl intermediates. On the other hand, the experimental reaction rates for transalkylation r_{trans} decrease as the calculated Ea3 activation energies increase, with only one structure, BEC, out of this trend (Figure 4.21b). The explanation for this value not following the trend might be found at the synthesis because some of these large-pore zeolites can only be prepared if Ge is incorporated to the framework. In particular, the low Si/Ge ratio determined for BEC sample (Table 4.15) could result in a low framework stability that modifies the catalytic activity, breaking the correlation between reaction rates and DFT calculated activation energies.

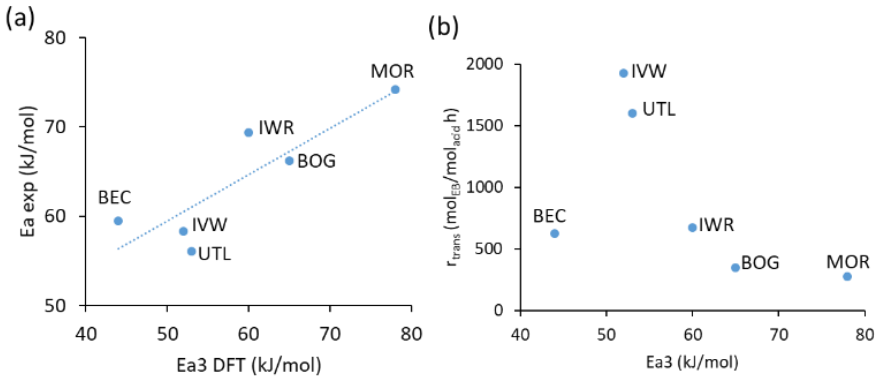

Figure 4.21. (a) Correlation between experimental and DFT calculated activation energies and (b) Correlation between experimental reaction rates for transalkylation r_{trans} and DFT calculated activation energies.

4.9. Conclusions

In this Chapter we have presented a combined computational approach that includes a fast force field screening of all zeolite structures able to stabilize the key intermediates of two competing reactions, DEB transalkylation and disproportionation. In a second step, a more accurate and time-demanding periodic DFT study for the competing reaction mechanisms and possible non-desired side reactions on the most promising catalyst candidates has been carried out. These studies pointed out several large pore zeolites as proper candidates to catalyse DEB transalkylation reaction that have been later synthesized, characterized and tested under reaction conditions. Comparison of the theoretical and experimental results validates the proposed methodology and leads to the following conclusions.

First, the theoretical study goes beyond the classical shape-selectivity or size-exclusion concept where some reactions are prevented because the intermediates or transition states involved require more space than available. In this case, the correlation between observed selectivity to TEB and EB in each zeolite and the relative stability of the diaryl intermediates involved in transalkylation (I_{trans}) and disproportionation (I_{disp}) determined by their calculated Eint is explained by a better fitting of one of the two slightly different diaryl intermediates within the zeolite microporous structure.

Second, a correlation between the catalytic activity of each zeolite, experimentally given by the rate of transalkylation r_{trans}, and the stability of the diaryl intermediate for transalkylation (I_{trans}) could not be established. However, the appropiate correlation was established with the calculated activation energy for the rate determining step of the pathway that contributes most at the

temperature of reaction. Thus, an accurate description of the catalytic activity requires an in depth mechanistic study that rationalises the reaction kinetics observed.

Third, the nature of the non-desired side reactions that compete with DEB transalkylation was studied and large pore zeolites containing 2D and 3D systems of 12r channels were appointed as the optimal candidates to restrict the formation of diaryl disproportionation bulky intermediates neglecting TEB production while lowering the contribution of the alkyl-transfer route, hence the ethene production.

Finally, theoretical and experimental results pointed out that the internal architecture of the IWV zeolite is the best suited for this reaction. These results are consistent with the synthesis of IWV framework when using diphenyldimehylphosphonium as structure directing agent.[69]

In summary, this Chapter has presented a new tool for the study of competing reactions catalyzed by zeolites. Using the methodology described we have been able to recognize and quantify subtle differences in the stabilization of intermediates and transition states within similar microporous voids, thus approaching the level of molecular recognition of enzymes. This procedure can be employed to select the most adequate zeolite structures, either existing or hypothetical, for many target reactions, reducing significantly the amount of expensive experimental trial and error work.

4.10 References

1. Perego, C. & Ingallina, P. Recent advances in the industrial alkylation of aromatics: New catalysts and new processes. *Catal. Today* **73**, 3–22 (2002).

2. Arsenova, N., Haag, W. O. & Karge, H. G. Kinetics study of ethylbenzene disproportionation with medium and large pore zeolites. *Stud. Surf. Sci. Catal.* **105 B**, 1293–1300 (1997).

3. Vermeiren, W. & Gilson, J. P. Impact of zeolites on the petroleum and petrochemical industry. *Top. Catal.* **52**, 1131–1161 (2009).

4. Yang, W., Wang, Z., Sun, H. & Zhang, B. Advances in development and industrial applications of ethylbenzene processes. *Cuihua Xuebao/Chinese J. Catal.* **37**, 16–26 (2016).

5. Perego, C. & Pollesel, P. *Advances in aromatics processing using Zeolite catalysts*. *Advances in Nanoporous Materials* vol. 1 (Elsevier, 2010).

6. Bellussi, G., Pazzuconi, G., Perego, C., Girotti, G. & Terzoni, G. Liquid-phase alkylation of benzene with light olefins catalyzed by β zeolites. *Journal of Catalysis* vol. 157 227–234 (1995).

7. Corma, A., Martínez-Soria, V. & Schnoeveld, E. Alkylation of benzene with short-chain olefins over MCM-22 zeolite: Catalytic behaviour and kinetic mechanism. *J. Catal.* **192**, 163–173 (2000).

8. Degnan, T. F., Smith, C. M. & Venkat, C. R. Alkylation of aromatics with ethylene and propylene: Recent developments in commercial processes. *Appl. Catal. A Gen.* **221**, 283–294 (2001).

9. Cheng, J. C. *et al.* A comparison of zeolites MCM-22, Beta, and USY for liquid phase alkylation of benzene with ethylene. *Stud. Surf. Sci. Catal.* **121**, 53–60 (1999).

10. Forni, L. *et al.* Transalkylation of m-diethylbenzene over large-pore zeolites. *Top. Catal.* **121**, 261–272 (1995).

11. Cavani, F., Corazzari, M., Bencini, E. & Goffredi, G. Liquid-phase transalkylation of diethylbenzenes with benzene over β-zeolite: Effect of operating parameters on the distribution of the products. *Appl. Catal. A Gen.* **226**, 31–40 (2002).

12. Gerzeliev, I. M., Khadzhiev, S. N. & Sakharova, I. E. Ethylbenzene synthesis and benzene transalkylation with diethylbenzenes on zeolite catalysts. *Pet. Chem.* **51**, 39–48 (2011).

13. Weckhuysen, B. M. *et al.* Zeolite Encaged Cu(Histidine) Complexes as

Mimics of Natural Cu Enzymes. *Angew. Chemie Int. Ed. English* **34**, 2652–2654 (1996).

14. Corma, A. Attempts to fill the gap between enzymatic, homogeneous, and heterogeneous catalysis. *Catal. Rev. - Sci. Eng.* **46**, 369–417 (2004).

15. Zecchina, A., Rivallan, M., Berlier, G., Lamberti, C. & Ricchiardi, G. Structure and nuclearity of active sites in Fe-zeolites: comparison with iron sites in enzymes and homogeneous catalysts. *Phys. Chem. Chem. Phys.* **9**, 3483 (2007).

16. Boronat, M., Martínez-Sánchez, C., Law, D. & Corma, A. Enzyme-like Specificity in Zeolites: A Unique Site Position in Mordenite for Selective Carbonylation of Methanol and Dimethyl Ether with CO. *J. Am. Chem. Soc.* **130**, 16316–16323 (2008).

17. Kwak, J. H. *et al.* A Common Intermediate for N 2 Formation in Enzymes and Zeolites: Side-On Cu-Nitrosyl Complexes. *Angew. Chemie Int. Ed.* **52**, 9985–9989 (2013).

18. Mahyuddin, M. H., Shiota, Y., Staykov, A. & Yoshizawa, K. Theoretical Overview of Methane Hydroxylation by Copper–Oxygen Species in Enzymatic and Zeolitic Catalysts. *Acc. Chem. Res.* **51**, 2382–2390 (2018).

19. Gallego, E. M., Paris, C., Cantín, Á., Moliner, M. & Corma, A. Conceptual similarities between zeolites and artificial enzymes. *Chem. Sci.* **10**, 8009–8015 (2019).

20. Bell, E. L. *et al.* Biocatalysis. *Nat. Rev. Methods Prim.* **1**, 46 (2021).

21. Sheldon, R. A., Brady, D. & Bode, M. L. The Hitchhiker's guide to biocatalysis: recent advances in the use of enzymes in organic synthesis. *Chem. Sci.* **11**, 2587–2605 (2020).

22. Gallego, E. M. *et al.* "Ab initio" synthesis of zeolites for preestablished catalytic reactions. *Science (80-.).* **355**, 1051–1054 (2017).

23. Gallego, E. M., Paris, C., Cantín, Á., Moliner, M. & Corma, A. Conceptual similarities between zeolites and artificial enzymes. *Chem. Sci.* **10**, 8009–8015 (2019).

24. Li, C. *et al.* Synthesis of reaction-adapted zeolites as methanol-to-olefins catalysts with mimics of reaction intermediates as organic structure-directing agents. *Nat. Catal.* **1**, 547–554 (2018).

25. Sievers, C. *et al.* Low-temperature activation of branched octane isomers over lanthanum-exchanged zeolite X catalysts. *J. Phys. Chem. C* **111**, 210–218 (2007).

26. Huang, J., Jiang, Y., Marthala, V. R. R. & Hunger, M. Insight into the

Mechanisms of the Ethylbenzene Disproportionation: Transition State Shape Selectivity on Zeolites. *J. Am. Chem. Soc.* **130**, 12642–12644 (2008).

27. Min, H.-K. & Hong, S. B. Mechanistic Investigations of Ethylbenzene Disproportionation over Medium-Pore Zeolites with Different Framework Topologies. *J. Phys. Chem. C* **115**, 16124–16133 (2011).

28. McCaulay, D. A. & Lien, A. P. Disproportionation of Alkylbenzenes. II. Mechanism of Alkyl-group Transfer. *J. Am. Chem. Soc.* **75**, 2411–2413 (1953).

29. Min, H. K., Chidambaram, V. & Hong, S. B. Diethylated diphenylethane species: Main reaction intermediates of ethylbenzene disproportionation over large-pore zeolites. *J. Phys. Chem. C* **114**, 1190–1193 (2010).

30. Clark, L. A., Sierka, M. & Sauer, J. Stable mechanistically-relevant aromatic-based carbenium ions in zeolite catalysts. *J. Am. Chem. Soc.* **125**, 2136–2141 (2003).

31. Clark, L. A., Sierka, M. & Sauer, J. Computational Elucidation of the Transition State Shape Selectivity Phenomenon. *J. Am. Chem. Soc.* **126**, 936–947 (2004).

32. Tiako Ngandjui, L. M., Louhibi, D. & Thyrion, F. C. Kinetic analysis of diethylbenzene-benzene transalkylation over faujasite Y. *Chem. Eng. Process. Process Intensif.* **36**, 133–141 (1997).

33. Shi, Q., Gonçalves, J. C., Ferreira, A. F. P., Plaza, M. G. & Rodrigues, A. E. Xylene isomerization side reactions over Beta zeolite: Disproportionation and transalkylation of C8 aromatics and toluene. *Appl. Catal. A Gen.* **562**, 198–205 (2018).

34. Yi, X. *et al.* Stability of the reaction intermediates of ethylbenzene disproportionation over medium-pore zeolites with different framework topologies: A theoretical investigation. *J. Phys. Chem. C* **117**, 23626–23637 (2013).

35. Mokoena, K. & Scurrell, M. S. Alkyl transfer reactions on solid acids. The disproportionation of ethylbenzene and toluene on H-mordenite and HY zeolites. *Pet. Sci. Technol.* **36**, 1208–1215 (2018).

36. Llopis, F. J., Sastre, G. & Corma, A. Isomerization and disproportionation of m-xylene in a zeolite with 9- and 10-membered ring pores: Molecular dynamics and catalytic studies. *J. Catal.* **242**, 195–206 (2006).

37. Margarit, V. J. *et al.* Control of the Reaction Mechanism of Alkylaromatics Transalkylation by Means of Molecular Confinement

Effects Associated to Zeolite Channel Architecture. *ACS Catal.* **9**, 5935–5946 (2019).

38. Byun, Y., Jo, D., Shin, D. N. & Hong, S. B. Theoretical investigation of the isomerization and disproportionation of m-xylene over medium-pore zeolites with different framework topologies. *ACS Catal.* **4**, 1764–1776 (2014).

39. Huang, J., Jiang, Y., Marthala, V. R. R., Ooi, Y. S. & Hunger, M. Regioselective H/D exchange at the side-chain of ethylbenzene on dealuminated zeolite H-Y studied by in situ MAS NMR-UV/Vis spectroscopy. *ChemPhysChem* **9**, 1107–1109 (2008).

40. Li, C. *et al.* Design and Synthesis of the Active Site Environment in Zeolite Catalysts for Selectively Manipulating Mechanistic Pathways. *J. Am. Chem. Soc.* **143**, 10718–10726 (2021).

41. Zhao, Y. & Truhlar, D. G. The M06 suite of density functionals for main group thermochemistry, thermochemical kinetics, noncovalent interactions, excited states, and transition elements: two new functionals and systematic testing of four M06-class functionals and 12 other functionals. *Theor. Chem. Acc.* **120**, 215–241 (2008).

42. Ditchfield, R., Hehre, W. J. & Pople, J. A. Self-Consistent Molecular-Orbital Methods. IX. An Extended Gaussian-Type Basis for Molecular-Orbital Studies of Organic Molecules. *J. Chem. Phys.* **54**, 724–728 (1971).

43. Hehre, W. J., Ditchfield, R. & Pople, J. A. Self—Consistent Molecular Orbital Methods. XII. Further Extensions of Gaussian—Type Basis Sets for Use in Molecular Orbital Studies of Organic Molecules. *J. Chem. Phys.* **56**, 2257–2261 (1972).

44. Frisch, M. J.; Trucks, G. W.; Schlegel, H. B.; Scuseria, G. E.; Robb, M. A.; Cheeseman, J. R.; Scalmani, G.; Barone, V.; Petersson, G. A.; Nakatsuji, H.; Li, X.; Caricato, M.; Marenich, A.; Bloino, J.; Janesko, B. G.; Gomperts, R.; Mennucci, B.; Hratchian, D. J. Gaussian 09. *Gaussian, Inc* **Wallingfor**, (2016).

45. Gale, J. D. GULP: A computer program for the symmetry-adapted simulation of solids. **93**, 629–637 (1997).

46. Gale, J. D. & Rohl, A. L. The General Utility Lattice Program (<scp>GULP</scp>). *Mol. Simul.* **29**, 291–341 (2003).

47. Schwalbe-Koda, D. & Gomez-Bombarelli, R. Benchmarking binding energy calculations for organic structure-directing agents in pure-silica zeolites. *ChemRxiv* 13270184 (2020) doi:10.26434/chemrxiv.13270184.v2.

48. Ch. Baerlocher and L.B. McCusker. Database of Zeolite Structures. *http://www.iza-structure.org/databases/* (2020).

49. Sanders, M. J., Leslie, M. & Catlow, C. R. A. Interatomic potentials for SiO2. *J. Chem. Soc. Chem. Commun.* 1271 (1984) doi:10.1039/c39840001271.

50. Jensen, Z. *et al.* Discovering Relationships between OSDAs and Zeolites through Data Mining and Generative Neural Networks. *Submitted* (2021).

51. Landrum, G. RDKit: Open-source cheminformatics. *RDKit: Open-source cheminformatics* (2006).

52. Halgren, T. A. Merck molecular force field. I. Basis, form, scope, parameterization, and performance of MMFF94. *J. Comput. Chem.* **17**, 490–519 (1996).

53. Tosco, P., Stiefl, N. & Landrum, G. Bringing the MMFF force field to the RDKit: implementation and validation. *J. Cheminform.* **6**, 37 (2014).

54. Schwalbe-Koda, D. & Gomez-Bombarelli, R. Supramolecular Recognition in Crystalline Nanocavities Through Monte Carlo and Voronoi Network Algorithms. *ChemRxiv* 13211012 (2020) doi:10.26434/chemrxiv.13211012.v1.

55. Mayo, S. L., Olafson, B. D. & Goddard, W. A. DREIDING: a generic force field for molecular simulations. *J. Phys. Chem.* **94**, 8897–8909 (1990).

56. Schwalbe-Koda, D. & Gómez-Bombarelli, R. Benchmarking binding energy calculations for organic structure-directing agents in pure-silica zeolites. *J. Chem. Phys.* **154**, 174109 (2021).

57. Perdew, J. P., Burke, K. & Ernzerhof, M. Generalized Gradient Approximation Made Simple. *Phys. Rev. Lett.* **77**, 3865–3868 (1996).

58. Perdew, J. P., Burke, K. & Ernzerhof, M. Generalized Gradient Approximation Made Simple [Phys. Rev. Lett. 77, 3865 (1996)]. *Phys. Rev. Lett.* **78**, 1396–1396 (1997).

59. Kresse, G. & Furthmüller, J. Efficient iterative schemes for *ab initio* total-energy calculations using a plane-wave basis set. *Phys. Rev. B* **54**, 11169–11186 (1996).

60. Blöchl, P. E. Projector augmented-wave method. *Phys. Rev. B* **50**, 17953–17979 (1994).

61. Grimme, S. Accurate description of van der Waals complexes by density functional theory including empirical corrections. *J. Comput. Chem.* **25**, 1463–1473 (2004).

62. Grimme, S. Semiempirical GGA-type density functional constructed with a long-range dispersion correction. *J. Comput. Chem.* **27**, 1787–1799 (2006).

63. Henkelman, G. & Jónsson, H. A dimer method for finding saddle points on high dimensional potential surfaces using only first derivatives. *J. Chem. Phys.* **111**, 7010–7022 (1999).

64. Heyden, A., Bell, A. T. & Keil, F. J. Efficient methods for finding transition states in chemical reactions: Comparison of improved dimer method and partitioned rational function optimization method. *J. Chem. Phys.* **123**, (2005).

65. Henkelman, G., Uberuaga, B. P. & Jónsson, H. Climbing image nudged elastic band method for finding saddle points and minimum energy paths. *J. Chem. Phys.* **113**, 9901–9904 (2000).

66. Sheppard, D., Xiao, P., Chemelewski, W., Johnson, D. D. & Henkelman, G. A generalized solid-state nudged elastic band method. *J. Chem. Phys.* **136**, (2012).

67. Baerlocher, C.; McCusker, L. B. Database of Zeolite Structures.

68. Kester, P. M., Crum, J. T., Li, S., Schneider, W. F. & Gounder, R. Effects of Brønsted acid site proximity in chabazite zeolites on OH infrared spectra and protolytic propane cracking kinetics. *J. Catal.* **395**, 210–226 (2021).

69. Dorset, D. L. *et al.* P-derived organic cations as structure-directing agents: Synthesis of a high-silica zeolite (ITQ-27) with a two-dimensional 12-ring channel system. *J. Am. Chem. Soc.* **128**, 8862–8867 (2006).

Chapter 5

Organic Structure Directing Agents for Zeolite Synthesis

5.1 Introduction.

Zeolites are microporous materials widely applied in industrial and sustainable catalysis, separations, adsorption and ion exchange, where their utility depends on the unique properties of each zeolite topology.[1,2] As we have seen in the past Chapters, topological diversity makes zeolites versatile because of their shape-selectivity. However, this diversity derives from complex nucleation mechanisms and phase competition between metastable polymorphs. These factors sum up during synthesis hindering the rational design of new synthetic routes for zeolites.[3–5] Despite decades of research, their synthesis still relies on trial-and-error approaches.

Zeolites well-defined crystalline frameworks facilitate connecting experimental data with theoretical insights of zeolite structure and function. This research field has become essential when aiming for tailored materials design.[6]
Nowadays, most of the research is currently split in two directions, creating new zeolite frameworks and compositions and lowering the synthesis cost of already known materials for specific industrial applications.[7]

As stated during Chapter 1 "Zeolites are commonly synthesized in the presence of an organic structure directing agent (OSDA), which strongly influences zeolite phase selectivity imprinting a significant influence on the size and shape of pores and channel systems." For the better comprehension of this Chapter, we must add that not only framework topology is a key factor for defining catalytic properties, the arrangement of their acid sites is also a crucial factor for the catalytic activity of zeolites. This distribution is modulated during synthesis with cationic OSDAs because these molecules facilitate the substitution of neutral framework SiO_4 tetrahedral units by anionic AlO_4^- tetraheas during zeolite crystallization.[8,9] Besides, many studies suggest that OSDAs influence the siting of Al at specific crystallographic locations based on the proximity between OSDAs cationic charges and anionic lattice AlO_4^- centers.[10–14] The influence of OSDAs over Al uptake and positioning has

been proven in many cases where two different OSDAs crystallize the same zeolite framework but each sample ends up with different Si/Al ratios, and perhaps different distributions, hence different catalytic activity towards the same test reaction.[15] Thus, designing the charge distribution for OSDAs becomes the main goal when aiming for tailored zeolite synthesis. In addition, it is important to note that zeolite synthesis is a multi-factor process where the nature of Si and Al sources, reaction conditions, crystallization times and laboratory equipment play an important role for success. Unfortunately, the effects of altering these variables cannot be studied in proper detail.

Theoretical simulations have aroused as a key tool for understanding OSDAs behavior and their effects over Al distribution and positioning. Initial studies found in literature started by predicting the affinity between OSDAs and targeted topologies providing a starting guide for the experimental work.[16–18] As structure crystallization from monomeric silica precursors is the most crucial part in synthesis, simulations of silica polymerization with Monte Carlo software showed that OSDA volume and its interactions with lattice oxygen atoms are key factors for stabilizing microporous voids during crystallization.[19–21] Obtaining theoretical interaction energies (Eint) between OSDAs and pure silica zeolite frameworks with different levels of theory enabled the creation of libraries of candidate OSDA molecules to identify more efficient synthesis routes towards known zeolite frameworks or new synthetic routes towards frameworks that were predicted to be stable.[7,22,23] These theory-guided approaches have been used successfully to design new OSDAs for the synthesis of AEI, SFW and STW zeolite frameworks.[24] In addition, as seen in Chapter 4, OSDAs that mimic transition state structures of a particular reaction have also been designed computationally and used to guide the synthesis of a zeolite framework that promotes a desired reaction mechanism.[5] Recent studies have focused on predicting the affinity between thousands of OSDAs and a few targeted zeolite frameworks.[25,26] However, these studies haven't succeeded in predicting whether the proposed OSDAs are more favorable towards another zeolite instead of the desired ones. Therefore, few experimental successes have been reported from such studies, because theoretically proposed OSDA candidates often fail to crystallize the specific desired structures as a consequence of the presence of intergrowths corresponding to undesired frameworks or due to a wrong theoretical prediction because interaction energies do not account for the whole set of real synthesis conditions such as temperature, nucleation time, etc. Moreover, design algorithms usually lead to molecules with low synthetic accessibility as a consequence of its expensive price or its troublesome synthetic route.[7] After this state-of-the-art review, it is possible to conclude that evolving from theoretical predictions to efficient experimental success poses a challenging task because of multiple factors associated with chemistry and economy.

In this Chapter, we devote our efforts to introduce new theoretical predictive tools based in DFT. We address two different topics of zeolite synthesis with OSDAs, on the one hand, we study the energetic affinity of very similar OSDAs for CHA synthesis and its effects on the quality of the material obtained. On the other hand, we present a new theoretical methodology to address Al positioning prediction in SSZ-39 zeolite comparing newly proposed templates with the classically used ones.

5.2 Methods and models.

Periodic density functional theory (DFT) calculations were performed using the Perdew−Burke−Ernzerhof (PBE) exchange-correlation functional within the generalized gradient approach (GGA)[27,28] as implemented in the Vienna Ab-initio Simulation Package (VASP) code.[29] The valence density was expanded in a plane wave basis set with a kinetic energy cutoff of 600 eV, and the effect of the core electrons in the valence density was taken into account by means of the projected augmented wave (PAW) formalism.[30] Integration in the reciprocal space was carried out at the Γ k-point of the Brillouin zone. Dispersion corrections to the energies were evaluated using the DFT-D3 Grimme's method.[31,32] Electronic energies were converged to 10^{-6} eV and geometries were optimized until forces on atoms were less than 0.015 eV/Å. During geometry optimizations, the positions of all atoms in the system were allowed to relax without any restriction. Static DFT optimizations correspond to structures optimized at T = 0 K.

In section **5.3,** the SSZ-13 (CHA) structure was modelled by means of a hexagonal unit cell with relaxed lattice a = b = 13.746 Å, c = 15.013 Å, α = β = 90°, and γ = 120° containing 36 T atoms (Si or Al) and 72 O atoms (see Appendix I). Realistic models with a Si/Al ratio of 5 were generated by replacing six framework Si atoms per unit cell by Al (locations described in section 5.3). Combinations of organic tetraethyl-ammonium (TEA), methyl-triethyl-ammonium (MTEA) and dimethyl-diethyl-ammonium (DMDEA) and inorganic sodium (Na^+) cations compensated the negative charges. Interaction energies per T atom were calculated as:

$$E_{int}/_{T} = [E(CHA_{6SDA}) - E(CHA) - 6 * E(SDA)]/_{36}$$

Where $E(CHA_{6SDA})$ is the total energy of the system with Si/Al = 5 containing six organic or inorganic (Na^+) structure directing agents, $E(CHA)$ is the total energy of the CHA unit cell with six framework Al atoms, and $E(SDA)$ is the total energy of the isolated organic or inorganic cations.

Experimental details that are not directly related to the work done by the author of this thesis and have been carried out by collaborators can be found in our published paper. There are the corresponding details about zeolite synthesis, Cu-exchange treatments, hydrothermal ageing treatments, material characterization, chemical analyses and morphology study of the samples.[33]

In section **5.4**, the SSZ-39 (AEI) structure was modeled by means of an orthorhombic unit cell (Cmcm) with lattice parameters a = 13.752, b = 12.646 Å, c = 18.482 Å, α = β = γ = 90°, containing 48 Si atoms and 96 O atoms (see Appendix I). Pure silica models and neutral versions of OSDAs were used during the whole subsection 5.4.1. In subsection 5.4.2 three different acid models with a Si/Al ratio of 47 were generated by replacing one framework Si atom per unit cell by Al. Only one OSDA molecule was introduced in the unit cell for each calculation. Interaction energies, Eint, were calculated as:

$$E_{int} = [E(AEI_{OSDA}) - E(AEI) - E(OSDA)]$$

Where $E(AEI_{OSDA})$ is the total energy of the system, either acid or pure silica, containing one OSDA, $E(AEI)$ is the total energy of the AEI unit cell, either acid or pure silica, and $E(OSDA)$ is the total energy of the isolated organic cation.

"Ab initio molecular dynamics" (AIMD) simulations were performed using the CP2K software package (CP2K 3.0).[34,35] Sampling of phase space occurs within the NVT ensemble using a timestep of 0.5 fs for integration of the equations of motion. The simulated temperature of 408 K was controlled by a Nosé-Hoover chain of five thermostat beads with a time constant of 100 wavenumbers.[36] As level of theory, the revPBE functional[27,37] was chosen because of its improved performance for solid-state calculations compared to the PBE functional[38] together with additional Grimme D3 dispersion corrections.[32] A combination of a Gaussian (TZVP) and plane wave basis set[39–41] with a cutoff of 320 Ry was used and GTH pseudopotentials were applied.[42,43] The self-consistent field convergence criterion was set at 10^{-6} Ha. All systems were first equilibrated for 5 ps, followed by a production run of 100 ps in section **5.4.1** and 75 ps in section **5.4.2**.

5.3 Preparation of CHA-type zeolites with low cost templates.

The selective catalytic reduction (SCR) of NO_x with NH_3 has been extensively studied during the last decade because of its importance for the automotive industry and its impact in public health due to pollutants produced by combustion engine vehicles.[44–46] For this reaction, Cu-containing small pore zeolites have been proven as the most efficient catalysts with CHA and AEI frameworks being commercialized by the automotive industry to mitigate NO_x emissions from diesel vehicles[46–49], especially the heavy-duty ones such as trucks that cannot migrate to electric engines yet. Nowadays, research efforts are focused on improving the synthesis routes of these small-pore zeolites to minimize manufacturing costs while maintaining, or even increasing, their SCR performance. As a clear example we can highlight CHA framework, which was usually synthesized with N,N,N-trimethyladamantammonium (TMAda) cation as its ideal OSDA because of its structural similarity with CHA cavities.[50,51] However, since the discovery of Cu-CHA as a very active and highly stable catalyst for the SCR of NO_x,[47] elementary OSDA molecules have been proposed as an alternative to the classically used TMAda. The most representative examples of OSDAs that have reported the successful crystallization of high-silica CHA zeolites with Si/Al molar ratios above 8 are benzyltrimethylammonium (BzTMA),[52,53] N-ethyl-N,N-dimethylcyclohexan-aminium (EMCyHA),[54,55] choline (Cho),[56,57] or tetraethylammonium (TEA)[58] (see Figure 5.1).

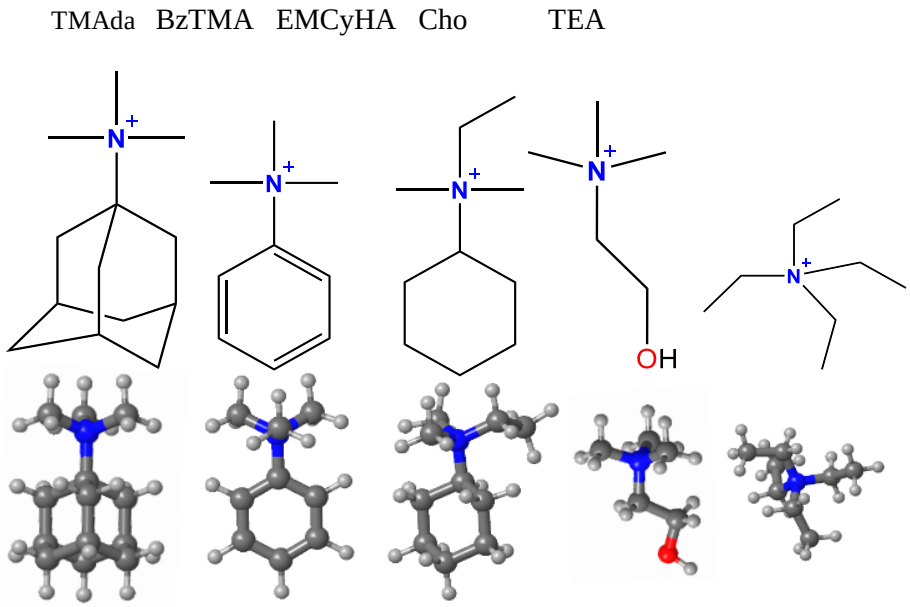

Figure 5.1. OSDAs used for CHA synthesis.

Combustion engine vehicles are spread all over the world. This means that the range of temperatures that will appear at the start of the catalyst function is very broad. Temperature is an important feature for SCR reaction because low temperatures act as an inhibitor for the Cu-exchanged zeolites activity. Recently, some studies pointed out that Cu-containing Al-rich small pore zeolites with Si/Al ~4-6,[59–61] show enhanced low-temperature SCR activity compared to their high-silica counterparts which presents a solution for this problem.[62] Therefore, the current research field is focused on exploring new synthesis routes to prepare CHA catalysts with low Si/Al ratios while keeping their production as cheap as possible. That is why our goal is to select the most adequate low-cost OSDA molecule to maximize the Al uptake during CHA zeolite crystallization.

5.3.1 DFT evaluation of host-guest stabilization with simple alkylammonium cations.

In the first step of this study, we evaluated the stabilization effect of different simple and commercially available cheap alkylammonium cations (see Figure 5.2) over CHA framework by calculating their Eint with periodic DFT methods.

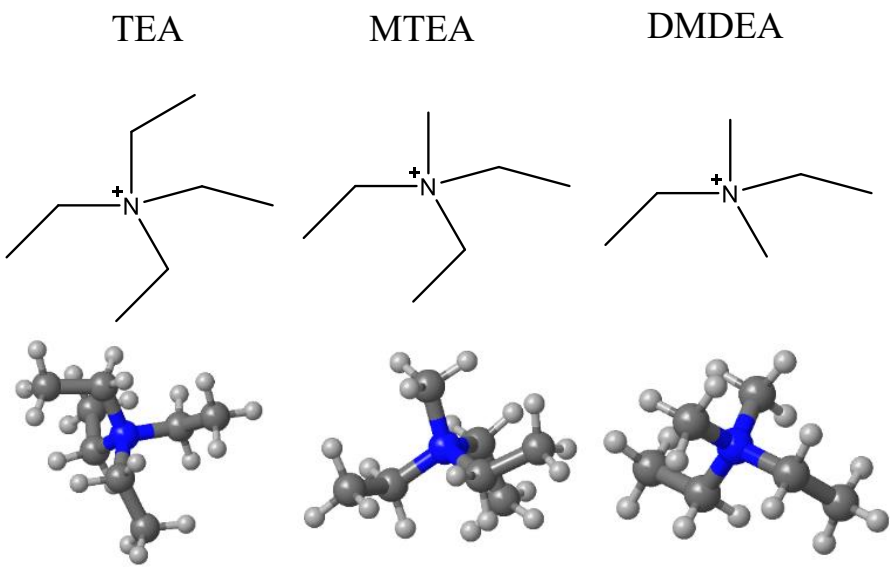

Figure 5.2: Simple alkylammonium cations employed as organic structure directing agents (OSDAs) in the present study.

As alkylammonium OSDAs introduce positive charges to the system, these cations must be compensated with negatively charged framework AlO_4^- units. Thus, three different catalyst models with a fixed Si/Al ratio of 5 have been designed to carry on this study. The CHA unit cell contains 36-T atoms and three CHA cages, hence, a Si/Al molar ratio of 5 implies the presence of six Al atoms, which translates into an average distribution of 2 Al atoms per CHA cage (see Figure 5.3). To analyze how different Al distributions may affect the host-guest interaction, Al pairs in six-rings (6r) (CHA_6Al_1), double-six-rings (d6r) (CHA_6Al_2 and CHA_6Al_3) have been included in these models. Additionally, both d6r models contain 8r windows with two Al atoms, as it can be seen in Figure 5.3.

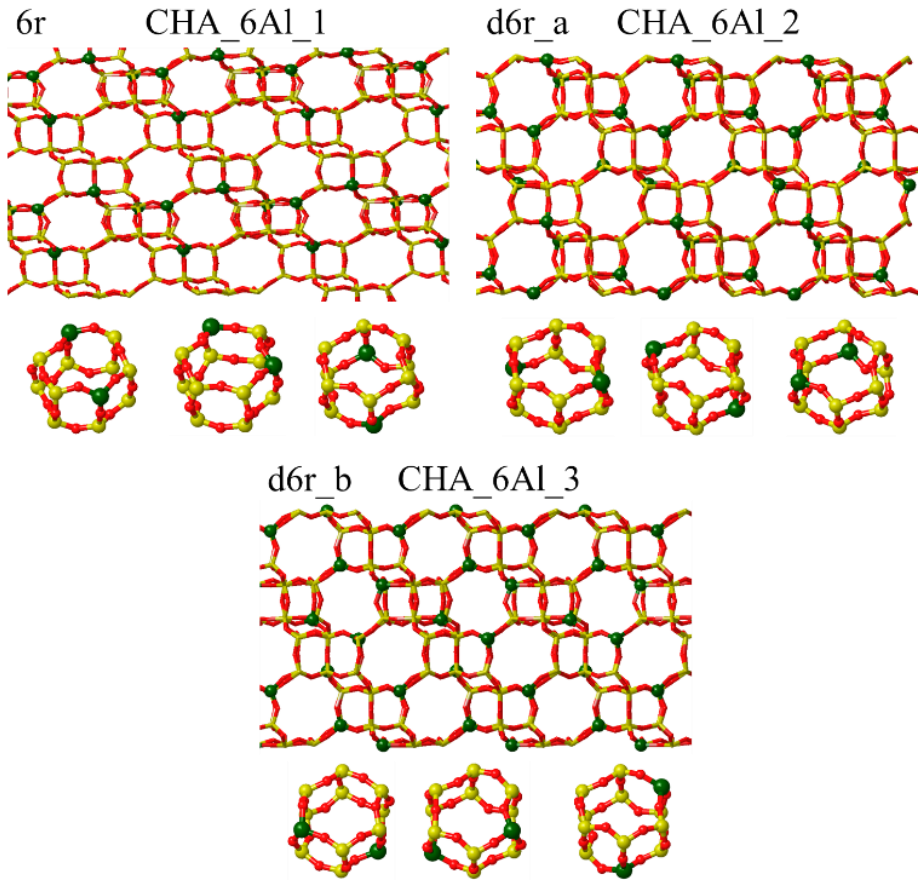

Figure 5.3: Three different Al distributions considered for the theoretical calculations. The three d6r units present in each unit cell are depicted below their corresponding model. Al, Si and O atoms are illustrated in green, yellow and red, respectively.

Since these models present six negative charges generated by the presence of Al in the framework, different OSDAs charge compensation alternatives have been considered approaching to real synthesis conditions with the inclusion of sodium cations which are always present in CHA synthesis. The different distributions considered range from two OSDA molecules to two sodium cations per CHA cage (see Figure 5.4).

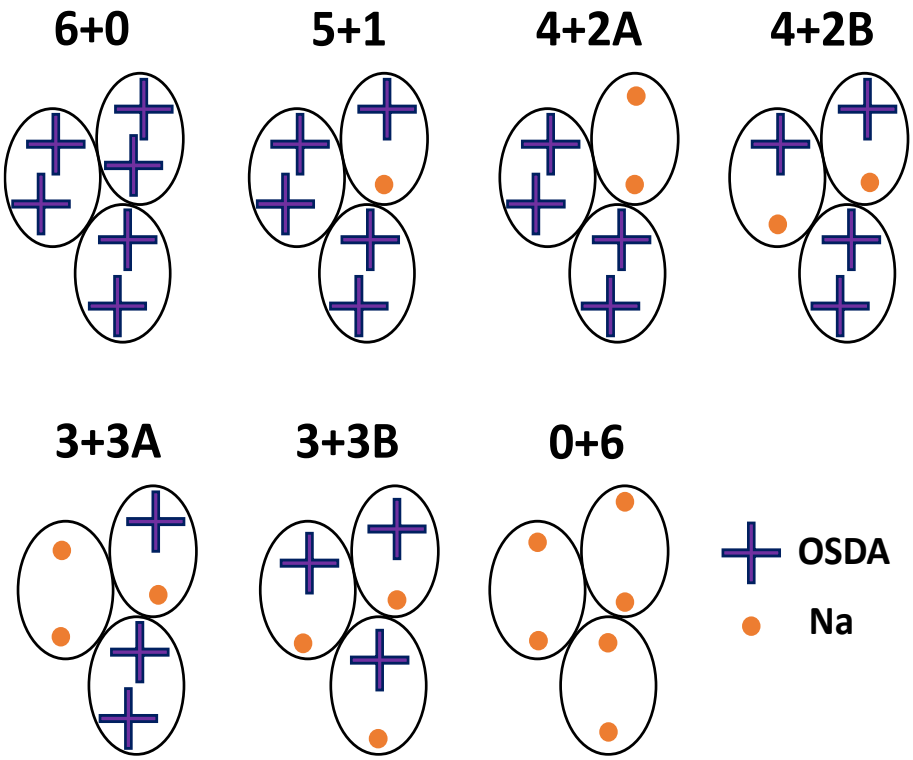

Figure 5.4. Proposed OSDA + Na^+ configurations within the unit cell of CHA considered for the DFT calculations.

All E_{int}/T values obtained in this study are presented in Tables 5.1 to 5.3. Looking at all the values shown, the first conclusion that can be observed is that the calculated interaction energies are not influenced by the initial Al distribution, because similar E_{int}/T values are obtained for each zeolite-cation pair with differences in the range of ± 1 - 2 kJ/mol.

Table 5.1. Eint calculated considering different configurations between OSDAs and CHA zeolite for the Al distribution number CHA_6Al_1 (see Figure 5.3).

OSDA[a]	6+0	5+1	4+2A	4+2B	3+3A	3+3B	0+6
DMDEA (tg)	-71	-72	-68	-71	-69	-71	-61
DMDEA (tt)	-63	-63	-61	-63	-62	-62	-61
MTEA (tg)	-89	-87	-81	-84	-77	-82	-61
MTEA (tt)	-93	-89	-83	-85	-73	-80	-61
TEA (tg)	-76	-76	-72	-80	-74	-82	-61
TEA (tt)	-75	-81	-74	-83	-75	-82	-61

Table 5.2: Stabilization energies calculated considering different configurations between OSDAs and CHA zeolite for the Al distribution number CHA_6Al_2 (see Figure 5.3).

OSDA[a]	6+0	5+1	4+2A	4+2B	3+3A	3+3B	0+6
DMDEA (tg)	-70	-70	-67	-70	-67	-68	-63
DMDEA (tt)	-62	-62	-58	-62	-59	-59	-63
MTEA (tg)	-89	-87	-80	-83	-77	-80	-63
MTEA (tt)	-92	-88	-82	-85	-71	-79	-63
TEA (tg)	-75	-76	-71	-78	-72	-81	-63
TEA (tt)	-74	-80	-73	-82	-73	-81	-63

Table 5.3: Stabilization energies calculated considering different configurations between OSDAs and CHA zeolite for the Al distribution number CHA_6Al_3 (see Figure 5.3).

OSDA[a]	6+0	5+1	4+2A	4+2B	3+3A	3+3B	0+6
DMDEA (tg)	-72	-71	-67	-71	-68	-68	-63
DMDEA (tt)	-62	-63	-59	-63	-59	-59	-63
MTEA (tg)	-89	-86	-80	-83	-77	-79	-63
MTEA (tt)	-92	-89	-82	-84	-72	-78	-63
TEA (tg)	-76	-76	-71	-78	-71	-80	-63
TEA (tt)	-74	-80	-73	-82	-74	-80	-63

[a] tt and tg refer to the conformation of the ethyl chains.

As there isn't any substantial difference between interaction energies found for each Al distribution, the E_{int}/T values obtained for the three different Al distributions have been averaged in Figure 5.5 to facilitate their comparison.

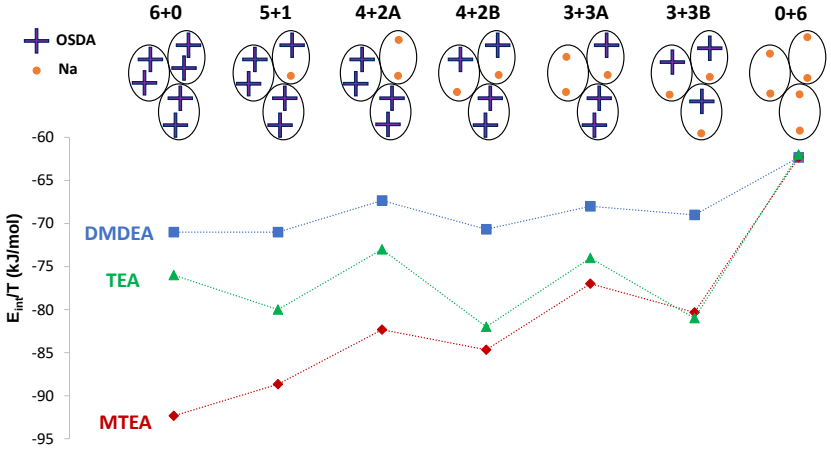

Figure 5.5. Theoretical stabilization energies, E_{int}/T, calculated for the different OSDA and Na^+ configurations within the unit cell of CHA.

From Figure 5.5 it is possible to see that the E_{int}/T obtained for DMDEA are worse for all OSDA-Na configurations compared to TEA and MTEA. This result indicates a better structure directing effect for TEA and MTEA towards Al-rich CHA compared to DMDEA. The interaction energy accounts majorly for the strong electrostatic interaction between the compensating cations and the negatively charged framework, but it also takes into account the weak Van der Waals and dispersion interactions between the hosted organic molecules and the framework oxygen atoms. The contribution of this last term is determined by the geometrical fitting between the hosted OSDA molecules and the zeolite framework. DMDEA structure, which is smaller than TEA and MTEA, is not large enough to fill the CHA cavity and explains the lower interaction energy obtained. It is important to note that the E_{int}/T values calculated for DMDEA remain almost constant around -70 kJ/mol for all configurations while substantial differences in the calculated E_{int}/T can be observed for TEA and MTEA depending on the distribution of the OSDA and Na^+ cations among CHA cages.

When considering configuration 3 + 3B (1 OSDA and 1 Na^+ per CHA cage, see Figure 5.5), TEA and MTEA present an identical E_{int}/T = -83 kJ/mol. In contrast, for the 3+3A configuration (2 OSDAs in a specific CHA cavity, see Figure 5.5), the E_{int}/T obtained for MTEA is slightly better than the one obtained for TEA, -77 and -74 kJ/mol, respectively. This difference becomes more pronounced as the number of OSDA molecules increases in configurations 4+2B, 4+2A, 5+1 and 6+0 with 4, 9, 9 and 16 kJ/mol difference between MTEA and TEA interaction energies, respectively. These results suggest that TEA may present a slight steric hindrance when compared to MTEA because of its slightly bigger chains (see Figures 5.6 and 5.7).

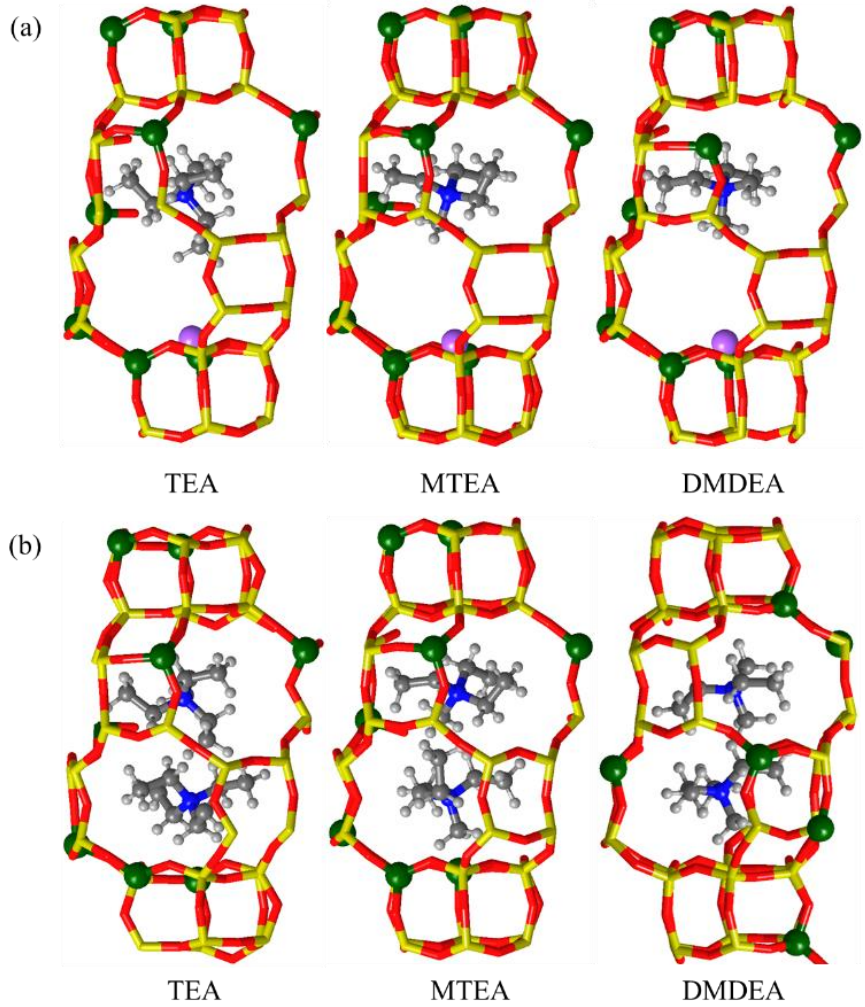

Figure 5.6: Optimized geometries of TEA, MTEA and DMDEA within the CHA cage in (a) 3+3B configuration containing Na or in (b) 6+0 configuration. Framework Si and O atoms are depicted as yellow and red sticks. Al, Na, C, N and H atoms are depicted as green, pink, grey, blue and white balls, respectively.

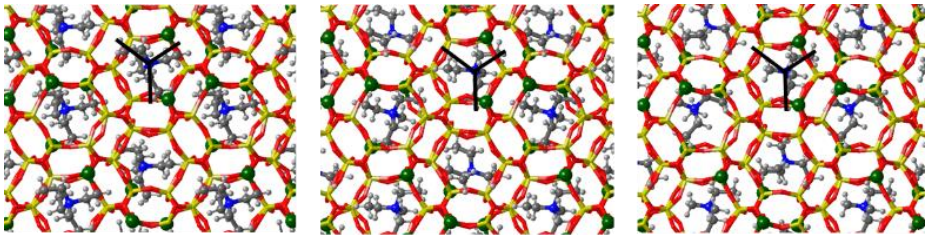

Figure 5.7. View along z axis of TEA, MTEA and DMDEA within the CHA cages. The black lines indicate the three 8-ring windows to which ethyl groups can point. Framework Si and O atoms are depicted as yellow and red sticks. Al, Na, C, N and H atoms are depicted as blue, pink, grey, blue and white balls, respectively.

Experimental zeolite synthesis is carried out in presence of inorganic cations, commonly Na^+. From the calculations performed, we can also add to the study some information about the interaction of Na^+ with OSDAs and with the CHA framework. From optimized structures we observed that the Na^+ cations always occupy positions close to the 6r plane of the small d6r units, irrespectively of the number of Al in the 6r, as already described in the literature (see Figure 5.6a).[63–65] Meanwhile, the bulkier organic cations are around the center of the CHA cavities with their alkyl chains pointing preferentially towards 8r windows (see Figure 5.7 black lines).

The results obtained for TEA and MTEA point towards a difference caused by the confinement of CHA cavities over OSDAs, where TEA presents a slight steric hindrance when two molecules are packed within the same CHA cavity meanwhile MTEA fits perfectly. As the structural difference between these molecules is just one methyl group, and considering the fact that our models include different variables such as electrostatic interactions between ammonium cations and framework Al and the presence of Na^+ cations in most of the systems considered, new neutral models have been generated in order to validate the steric hindrance hypothesis. The neutral models consist of a pure silica CHA unit cell containing six neutral OSDA molecules in which N is substituted by C to remove the positive charge (see Figure 5.8). This simple approximation proves that two TEA molecules cannot fit properly inside one CHA cavity because a positive interaction energy is obtained, E_{int}/T = 9 kJ/mol (see Table 5.4). Oppositely, the docking of two MTEA molecules inside the pure silica CHA cavity presents negative interaction energies of E_{int}/T = -9 kJ/mol confirming the steric hindrance results obtained with charged models. Therefore, all stabilization values shown for the charged and neutral models point towards MTEA cation as the preferred simple alkylammonium candidate to facilitate the synthesis of Al-rich CHA zeolites due to subtle but determinant structural differences.

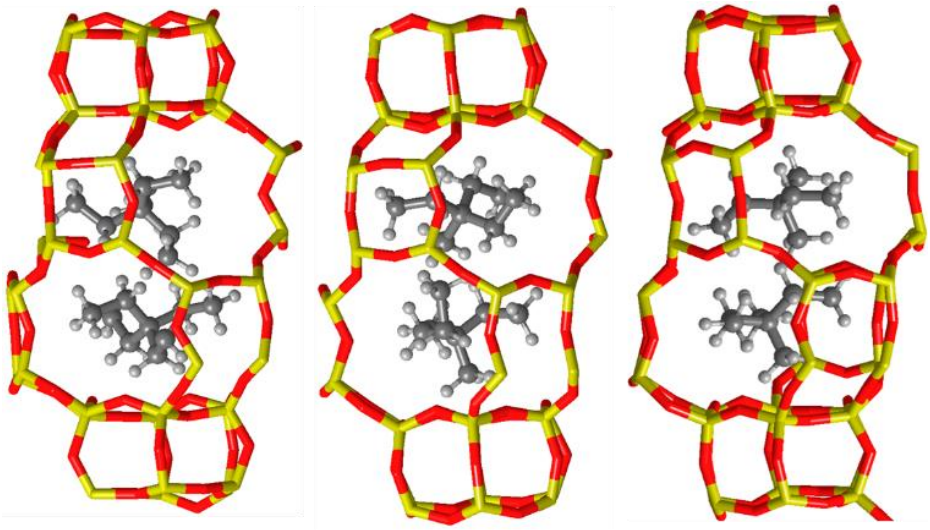

Figure 5.8: Optimized geometries of neutral models of TEA, MTEA and DMDEA within a pure silica CHA cage. Framework Si and O atoms are depicted as yellow and red sticks, C and H atoms are depicted as grey and white balls.

Table 5.4: Stabilization energies calculated for a neutral approximation in a pure silica CHA unit cell with 6 neutral OSDA molecules (2 OSDA/CHA cavity).

OSDA [a]	**Configuration**	**E_{int}/T (kJ/mol)**
TEA (tg)	CHA Si + 6 OSDA (neutral) [b]	11
TEA (tt)	CHA Si + 6 OSDA (neutral) [b]	9
MTEA (tg)	CHA Si + 6 OSDA (neutral) [b]	-4
MTEA (tt)	CHA Si + 6 OSDA (neutral) [b]	-9

[a] tt and tg refer to the conformation of the ethyl chains.
[b] The N atom of the ammonium group has been substituted by a C to achieve the neutral organic molecules

5.3.2 Zeolite synthesis, characterization and reaction.

The synthesis of Al-rich CHA-type zeolites was attempted using TEA, MTEA and DMDEA under identical molar gel compositions. Material characterization techniques confirmed the main formation of the CHA structure when using TEA or MTEA, meanwhile the sample prepared with DMDEA presented a mixture of cage-based small pore zeolites LEV and ESV phases that present smaller cavities than CHA zeolite. LEV is usually obtained using small cyclic cations, but this result is also in agreement with literature because the preparation of LEV has also been described using DMDEA as OSDA.[66–68] This experimental result, coupled with the low E_{int}/T values obtained in the theoretical study for DMDEA suggests that the smaller size of DMDEA would favor the formation of smaller LEV and ESV cavities instead of CHA.

When comparing the samples obtained with TEA and MTEA, the latter acquired an almost perfect crystallization of CHA, while TEA produced less pure crystals with stacking intergrowths of GME that alter the structure and create a larger cage, as revealed by electron diffraction and high-resolution transmission electron microscopy (HRTEM) (see Figure 5.9b highlighted cages and Figure 5.10). From the HRTEM study, is possible to see that the regions of GME-type stacking do not present a considerable extension along the material (see Figure 5.9a).

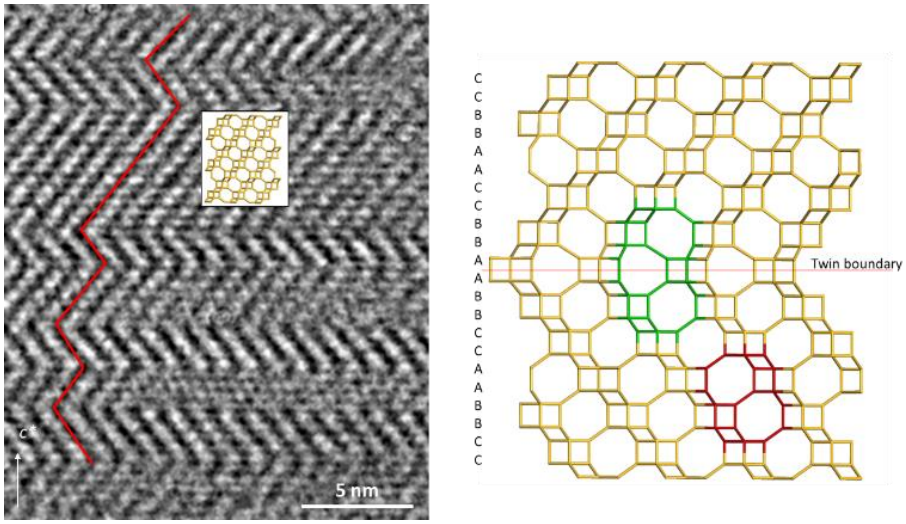

Figure 5.9. (a) HRTEM image acquired along the [100] direction of the CHA-type zeolite synthesized with TEA. Twinning in small domains is present as indicated by the red guideline. CHA structure is shown as inset for reference. (b) Structure model for the twin boundary in the structure of CHA with the larger cage (in green) created around the twin boundary. A CHA cage is shown in red. Oxygen atoms are omitted for clarity in the structure models.

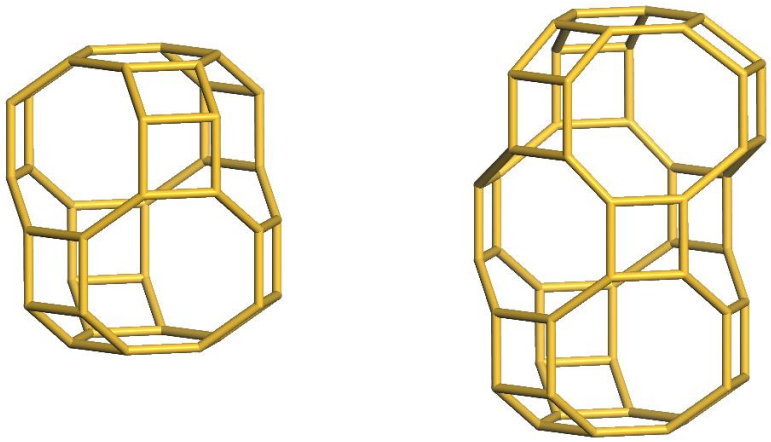

Figure 5.10. Structure models for CHA cage (a) and for the cage present at the CHA twin-boundary (b). Oxygen atoms are omitted in the structure models for clarity.

This experimental result for the CHA sample synthesized with TEA is in good agreement with the DFT results shown in the previous section where local stacking of two TEA molecules within the CHA cage presents steric hindrance causing the formation of larger cavities when using TEA as compared to MTEA. Characterization and further details of this part of the study can be found in our published paper.[38]

The chemical composition of the as-prepared CHA samples was evaluated by ICP and thermogravimetric analysis. Both materials presented analogous Si/Al ratios (~4.6 - 4.9) and Na contents (~4.0%wt). As each CHA unit cell contains 36-T atoms that build up three cavities, it is possible to estimate that there are ~2 - 2.2 Al and ~1.1-1.3 Na^+ cations present in each cavity on average. These results also point out that the average number of OSDA molecules per cavity approaches ~1 OSDA, being 0.9 and 0.8 for MTEA and TEA, respectively. Therefore, from these results we can extract that the most probable configuration of TEA and MTEA organic molecules would be the 3+3B model, where the CHA cages are filled by 1 OSDA molecule and 1 Na^+ cation. This is consistent with the interaction energy results shown in Figure 5.5 because the stabilization energies for the 3+3B model using TEA and MTEA are very similar and explain the excellent ability of both OSDAs to direct the crystallization of CHA. An explanation for the CHA/GME intergrowth with the formation of cavities larger than CHA cages when employing TEA as OSDA can be found in local alterations of the 3+3B model during the nucleation/crystallization processes towards OSDA-rich or Na-rich regions. These areas would present 4+2A or 3+3A conformations that are less stable

from the host-guest interaction energy point of view with two OSDA molecules in the same cavity causing the GME intergrowth for the TEA sample.

Finally, the NH_3-SCR catalytic performance for NO_x abatement of the Cu-exchanged CHA catalyst prepared with TEA and MTEA was evaluated under fresh and aged conditions. Both presented excellent catalytic activity and hydrothermal stability for their potential application as SCR catalysts for heavy-duty diesel vehicles. Further details for this part of the work can be found in the published paper.[33]

5.3.3 Conclusions.

In this section of the Chapter, we have implemented a theoretical methodology for zeolite synthesis using OSDA molecules that is able to distinguish small stabilization effects caused by slight structural differences between molecules that have an impact on the final structure synthesized. In this case, we focused on cheap commercially available alkylammonium cations with slight differences on their alkyl chain groups, as TEA, MTEA and DMDEA for Al-rich CHA zeolites. We evaluated the host-guest interaction energies of different combinations of OSDAs and Na^+ cations with periodic DFT methods. From this study we obtained important differences in interaction energies for TEA and MTEA as compared to DMDEA despite the small structural differences between these molecules. Moreover, these subtle differences also aroused when simulating a complete load of two OSDA in one CHA cavity with MTEA and TEA. While MTEA molecules presented an improved host-guest confinement, TEA molecules are limited by steric hindrance and this is translated into a non-negligible difference in interaction energies.

After the theoretical study, the preparation of Al-rich CHA zeolites was attempted using TEA, MTEA and DMDEA. When using DMDEA, a mixture of LEV and SEV was obtained. Synthesis attempted with TEA produced CHA with narrow GME intergrowths that formed larger cavities meanwhile MTEA produced a perfect CHA material. Finally, the two Al-rich CHA-type materials prepared with TEA and MTEA were exchanged with copper and their catalytic performance in the NH_3-SCR reaction was evaluated with success.

5.4 Theoretical Prediction for Disperse Al Distribution in AEI Zeolite.

In this section, we focus on AEI zeolite synthesis because it is one of the most commercially useful small-pore zeolites. Its structure its formed by a three-dimensional pore system with 3.8 Å × 3.8 Å 8r windows and large unsymmetrical avocado-like cages (12.6 Å × 11.2 Å)[26,69] (see Fig. 5.11). The AEI framework can be synthesized with two different chemical compositions, aluminosilicate, SSZ-39, and silicoaluminophosphate, SAPO-18. Both materials are widely used to catalyze chemical reactions with industrial interest such as methanol-to-olefins reaction as seen in Chapter 3 section **3.4**, where SSZ-39 and SAPO-18 are studied in depth. Moreover, metal-exchanged SSZ-39 zeolites display excellent performance for direct conversion of methane to methanol and ammonia SCR of NO_x.[49,70,71]

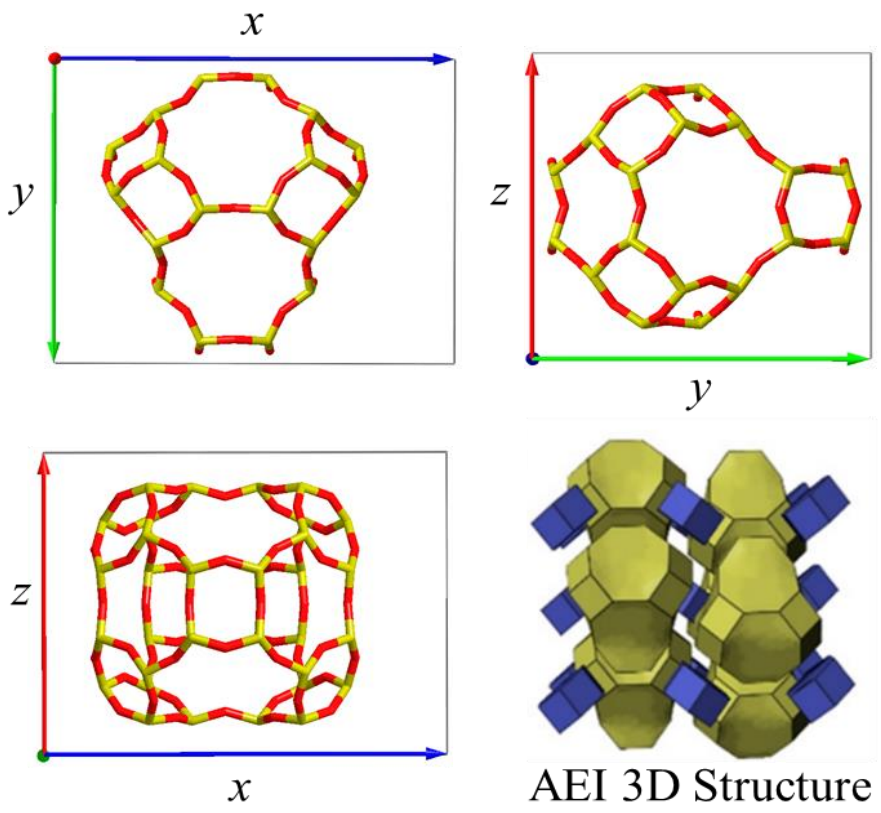

Fig 5.11. AEI framework topology.

The first successful synthesis of SSZ-39 zeolite was reported in 1999 by Zones et al, using cyclic or polycyclic quaternary ammonium cations as OSDAs.[72] Since then, diverse synthetic conditions have been developed to produce AEI zeolites with improved hydrothermal stability and catalytic performance. Nowadays, SSZ-39 is commonly synthesized using a wide range of piperidinium based OSDAs under a variety of inorganic synthesis conditions.[73,74] Following these achievements, other piperidinium related molecules have been proposed theoretically as possible OSDAs for SSZ-39 synthesis because of their good interaction energy affinity and their low synthesis difficulty that translates into economic prices.[26]

Despite achieving the synthesis of the AEI framework with aluminosilicate and silicoaluminophosphate compositions, the effect of the OSDAs over acid site positioning is unclear yet. Some studies in literature have reported frameworks with disperse acid site distribution in SAPO-18 framework neglecting the formation of silicon islands.[75] However, the effects of OSDAs over Al positioning in SSZ-39 synthesis remain unclear. There are examples of SSZ-39 samples synthesized with different cis/trans isomers of piperidinium derivatives that present slight differences in deactivation lifetimes and activities towards SCR of NO_x at different temperatures,[49,76,77] but it results bold to attribute these observed differences specifically to different Al distributions when using highly similar molecules or even molecular isomers as directing agents. In this section, we aim to understand the behavior of some selected OSDAs inside SSZ-39 cavities rationalizing and predicting their Al directing ability and the differences that would be expected between the corresponding SSZ-39 samples if they were synthesized with each template. First, we evaluate the mobility and Al directing ability of classic piperidinium based OSDAs for SSZ-39 framework. In a second step, we compare the initial set with a new set of OSDAs with different molecular structures and charge distributions.

5.4.1 Mobility of piperidinium based OSDAs.

To start the first part of this study, we performed regular AIMD simulations of three widely used OSDAs for SSZ-39 synthesis inside a pure silica AEI unit cell (Appendix I) considering experimental synthesis temperature, T = 408 K. These simulations aim to observe the mobility and feasible orientations of the different OSDAs inside AEI cages. The OSDAs selected were, *N*,*N*-dimethyl-2,6-dimethylpiperidinium (OSDA1)[15], *N*,*N*-dimethyl-3,5-dimethylpiperidinium (OSDA2)[78] and *N*,*N*-diethyl-2,6-dimethylpiperidinium (OSDA3)[15] (Fig 5.12), both cis and trans conformations were taken into account for each OSDA.

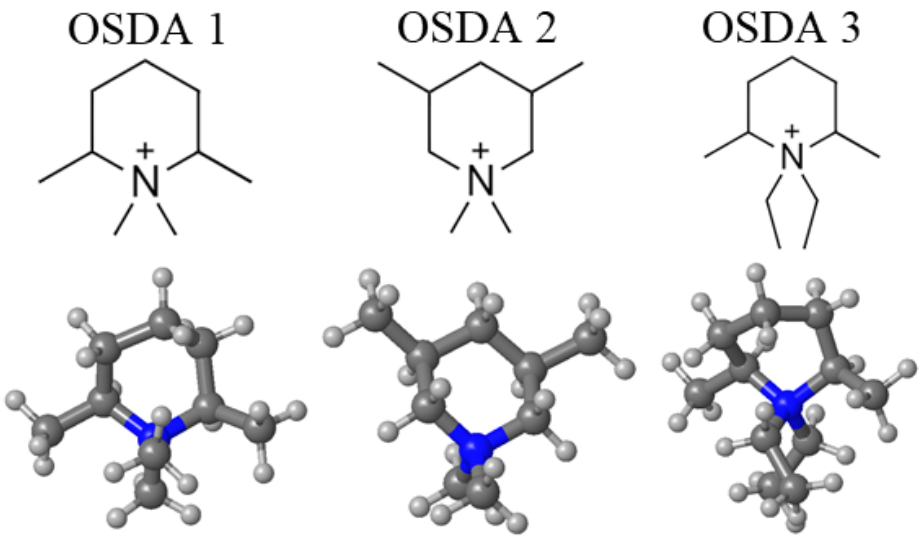

Figure 5.12. cis isomers of OSDAs studied: *N*,*N*-dimethyl-2,6-dimethylpiperidinium (OSDA1), *N*,*N*-dimethyl-3,5 dimethylpiperidinium (OSDA2) and *N*,*N*-diethyl-2,6-dimethylpiperidinium (OSDA3). N, C and H atoms depicted as blue, grey and white balls respectively.

As the goal is to observe the mobility of each OSDA inside the AEI cavities, mainly all possible rotations and complete inversions, in a first step the positive charge of these piperidinium molecules was eliminated by substituting the N atom by a C atom. By this procedure, a neutral molecule with the same size and mobility is obtained while effects associated to the presence of positive (OSDA) and negative (framework Al) charges are neglected; they will be taken into account in next sections. From now on, "N" refers to the C atom that is replacing the N atom in the original piperidinium cation, it is depicted with blue colour in all Figures of this section. In addition, to evade disturbances caused by OSDAs located in neighbouring cavities, only one OSDA was introduced per unit cell leaving one empty cavity in each direction (top, bottom, left, right, front and back) when the system is periodically replicated during the simulations.

Two different initial orientations were selected for each OSDA as starting points for the regular AIMD runs, one with the substituted "N" atom (blue atom in Fig 5.13) pointing towards the narrow part of the AEI cavity (O1) and other with the substituted "N" atom pointing towards the wide part of the cavity (O2), (Fig 5.13).

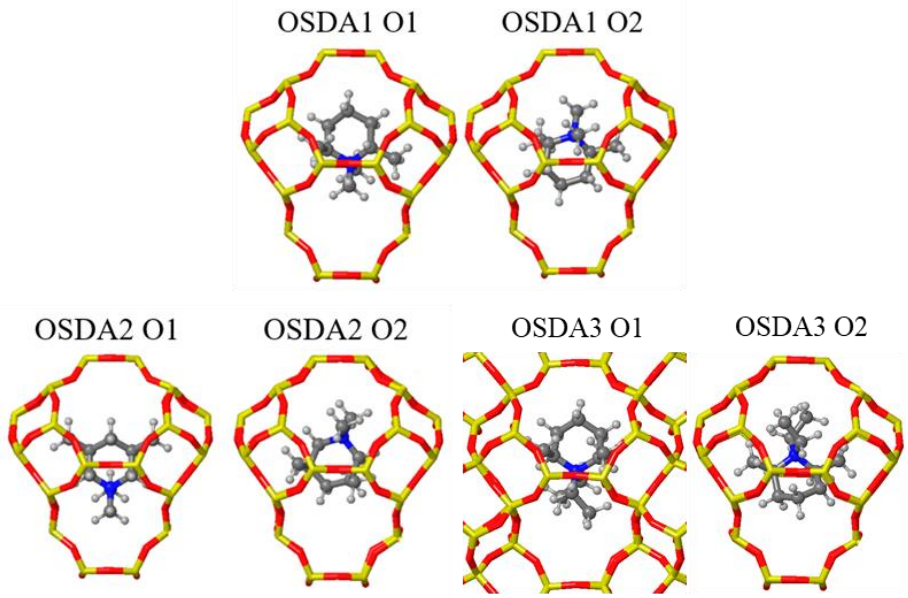

Fig 5.13. Initial orientations selected for each OSDA. Framework Si and O atoms are depicted as yellow and red sticks, N, C and H atoms are depicted as blue, grey and white balls.

Each regular AIMD simulation ran for 100 ps and scatterplots for "N" atom movement were produced for each run (see Fig 5.14). After observing all the different cases, we did not find any complete inversion of any OSDA from O1 to O2 or vice versa in any case. The general lack of mobility can be confirmed by scatterplots corresponding to the position of the ring methyl substituents in Figure 5.15 where it is possible to see how methyl groups, M1 (green) and M2 (purple), never swap places through rotations or inversions.

From these scatterplots it is possible to see that OSDA3 presents a very low mobility because the two ethyl chains reduce the space where the "N" atom is able to reach, making OSDA3 stay always at the centre of the cavity (see Fig 5.14*i-l*). Only its trans configuration presents a slight rotation for its O2 simulation, see M1 and M2 scatterplots in Figure 5.15*l*, however, it does not affect the "N" atom position (Figure 5.14*l*). Scatterplots for OSDA1 show a similar behaviour to that of OSDA3, but with a slightly increased mobility in the x and y axes due to the smaller substituents at the "N" atom (see Figure 5.14 and 5.15 *a, b, e, f*). For OSDA1, pronounced rotations are observed for both

orientations of the trans isomer, Figure 5.15 *b, f,* however, a complete inversion from O1 to O2 or vice versa is never observed. For OSDA2 a new orientation was found, named as O3, with the substituents on the "N" atom pointing towards the wide side of the cage after a 60-degree rotation in the xy plane from the starting O2. This rotation occurred during the first 10 ps of the run for cis and trans isomers, then, O3 position was maintained for the rest of the simulation because of the good fitting of the methyl groups with the AEI cavity topology (see Fig 5.14 and Figure 5.15 *g,h*).

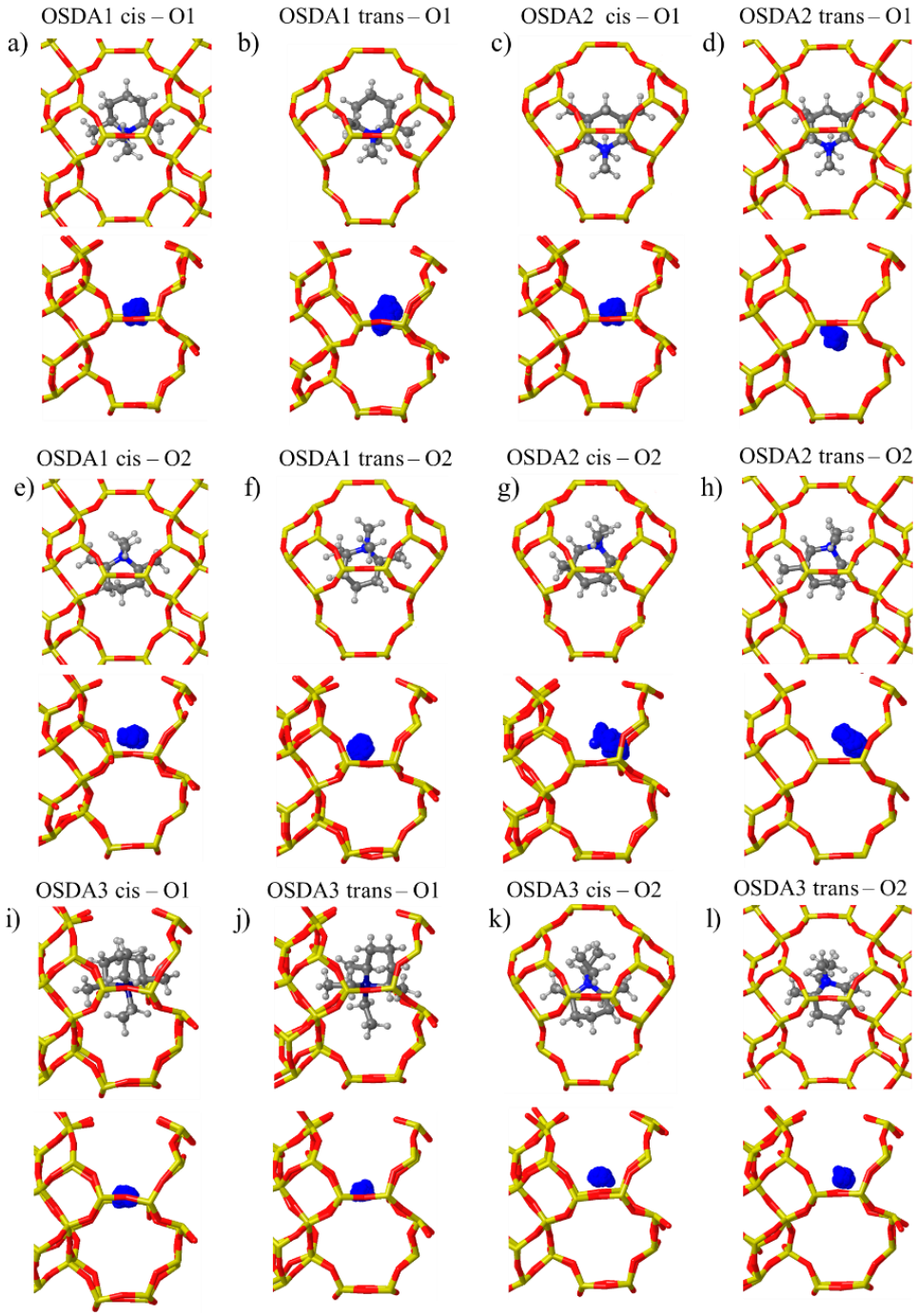

Fig 5.14. 100ps scatterplots for the "N" atom position (blue).

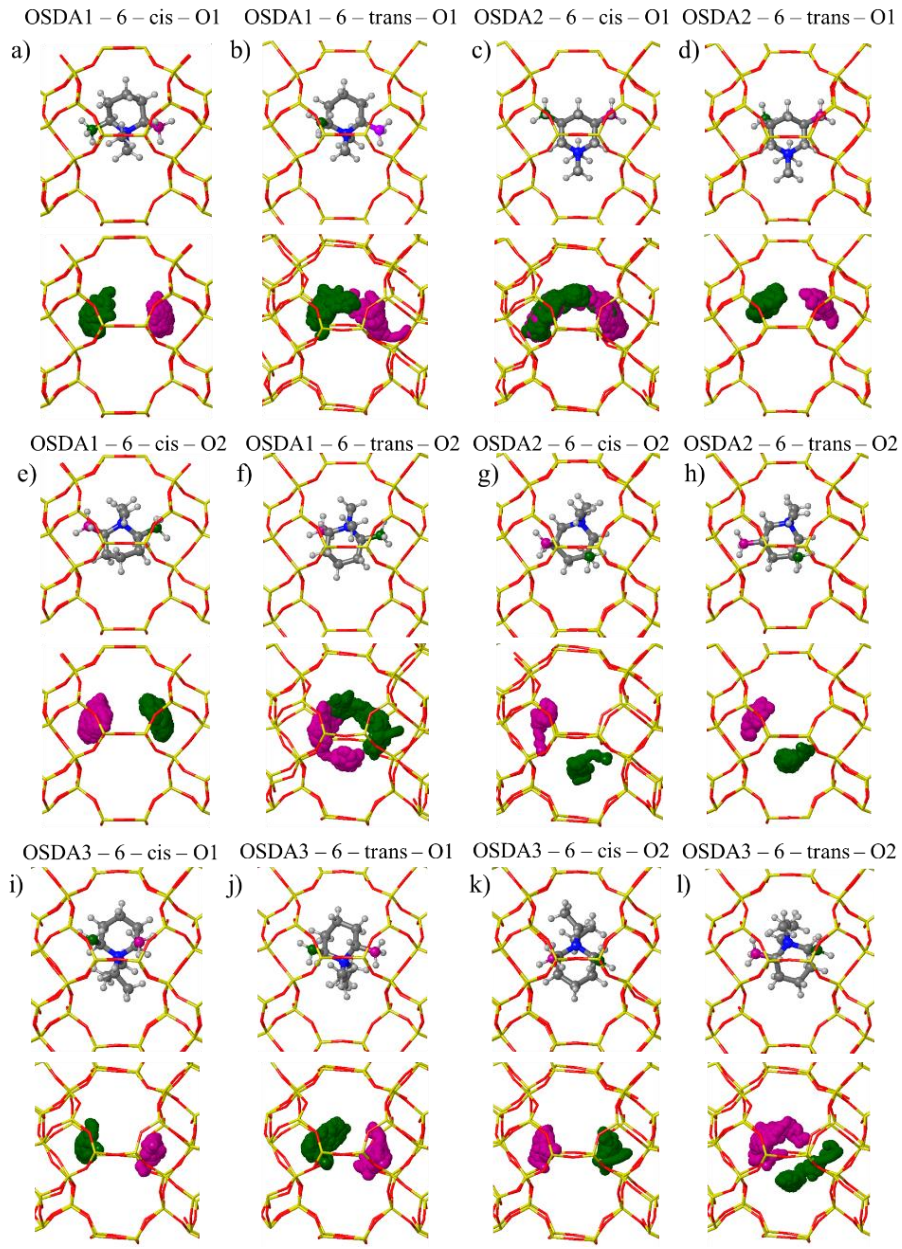

Figure 5.15. 100ps scatterplots for M1 (green) and M2 (purple) positions.

Therefore, from these regular AIMD simulations we can conclude that all these OSDAs present similar and low mobility, with only small differences due to the different substituents position around the piperidinium ring and different chain size. This effect should be taken into account when looking for disperse Al distributions around the catalyst framework, because since these kind of OSDAs are immobile, the Al will be directed always towards the same positions.

After running the AIMD simulations, it is reasonable to consider that the majority of orientation probabilities for the selected OSDAs inside AEI cavities have been observed with just O3 appearing as a new orientation specifically for OSDA2. At this point, static DFT calculations with VASP 5.4 software were performed using the same models employed as starting points for AIMD simulations in order to quantify the stability of the different orientations for neutral versions of OSDA1 and OSDA2 by means of their Eint (Fig 5.16). Looking at Table 5.5 we can see that only O2 is disfavoured for OSDA2 because the methyl substituents on the pyridine ring collide with the narrow part of the AEI cavity. These results for OSDA2 explain the observed rotation from O2 to O3 during the AIMD simulations. The Eint values for OSDA1 suggest that it could be found in any of the three orientations during the synthesis meanwhile OSDA2 will be mostly found in O1and O3.

Table 5.5. Eint (in kJ/mol) of OSDA1 and OSDA2 for each orientation.

OSDA	**O1**	**O2**	**O3**
1 cis	-105	-105	-105
1 trans	-100	-106	-107
2 cis	-101	-61	-104
2 trans	-101	-95	-107

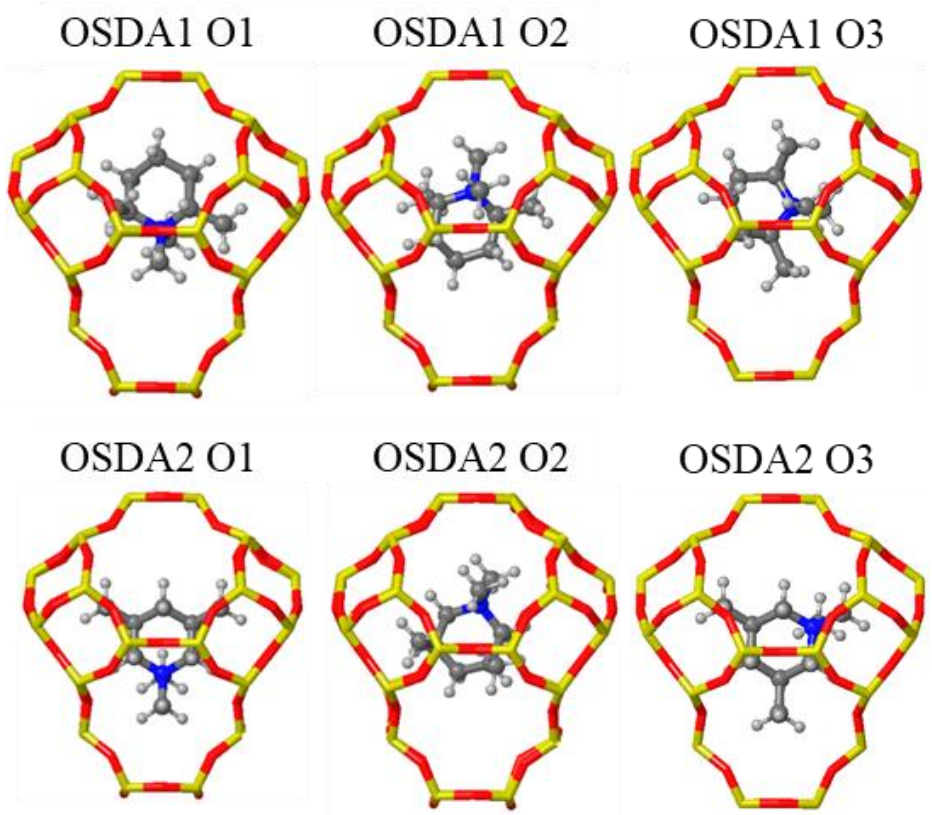

Figure 5.16. Orientations tested with static DFT (VASP). Framework Si and O atoms are depicted as yellow and red sticks, "N", C and H atoms are depicted as blue, grey and white balls.

The first part of the OSDA mobility study within pure silica AEI cavities focused on the degree of mobility of each OSDA and the differences found between them because of the size of their N-substituents and their position around the piperidinium ring.

In this second part, it focuses on the ring size and its impact over mobility and stability. A set of models of entrapped neutral versions of OSDA1 with different ring sizes was designed, ranging from five carbon atoms (5-C) to ten carbon atoms (10-C), and their corresponding Eint were calculated with orientations O1and O2 (see Fig 5.17).

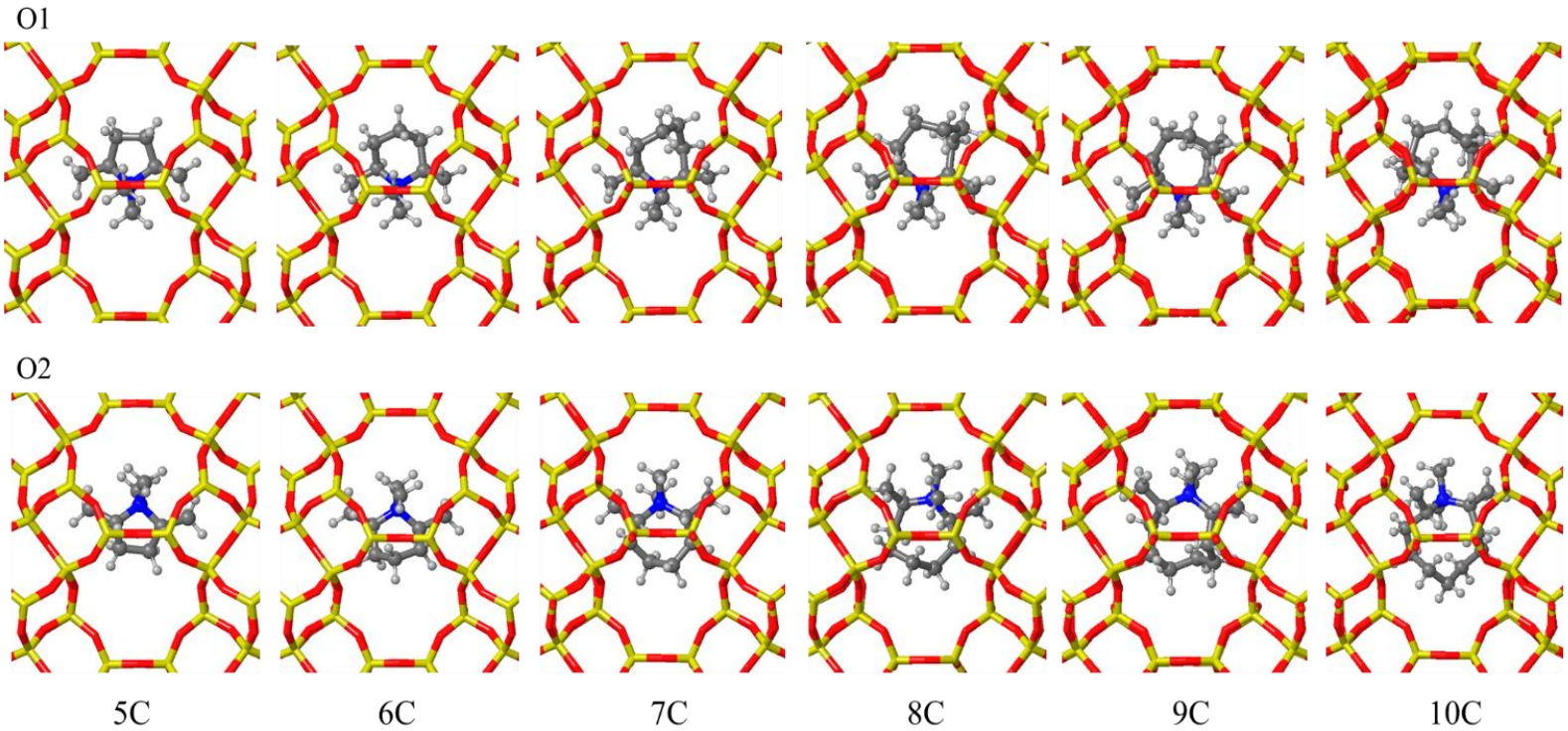

Figure 5.17. OSDA1 different ring sizes ranging 5-C to 10-C. “N”, C, H depicted in blue, grey and white.

Interaction energies obtained for this set of calculations and interaction energies normalized by the number of carbon atoms in each molecule (Eint/C) are summarized in Table 5.6 and depicted in Figure 5.18.

Table 5.6. Absolute Eint values (in kJ/mol) and Eint/C values normalized per number of C atoms (in kJ/mol C) obtained for OSDA1 with ring size from 5-C to 10-C.

OSDA1		**O1**		**O2**	
		BE (kJ/mol)	**BE/C (kJ/mol C)**	**BE (kJ/mol)**	**BE/C (kJ/mol C)**
5-C	cis	-93	-10	-93	-10
	trans	-90	-10	-99	-11
6-C	cis	-105	-10	-105	-10
	trans	-100	-10	-106	-11
7-C	cis	-118	-11	-133	-12
	trans	-130	-12	-133	-12
8-C	cis	-117	-10	-117	-10
	trans	-101	-8	-111	-9
9-C	cis	-117	-9	-109	-8
	trans	-114	-9	-119	-10
10-C	cis	-86	-6	-78	-6
	trans	-105	-8	-128	-9

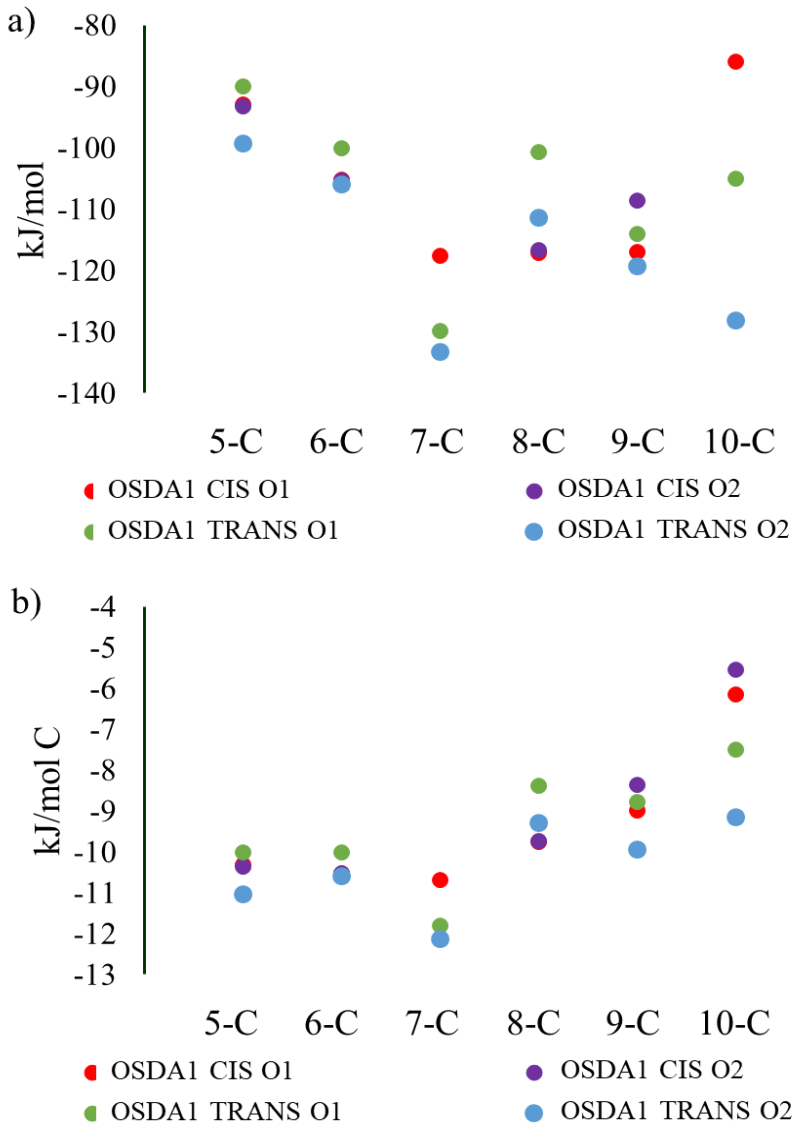

Figure 5.18. a) Eint vs ring size b) Eint/C vs ring size.

From these results it is possible to identify that the lowest value found, either for absolute Eint or normalized Eint/C, corresponds to the 7-C OSDA1. This fact indicates that any kind of substituted piperidinium rings that exceed this number of ring units is not going to fit properly inside AEI cages, therefore, it will direct the synthesis towards other kind of framework arrangements, perhaps cavity systems with wider cages. Then, we delimited our study about ring size and OSDA mobility to systems with 5-, 6- and 7-C atoms in the ring, and ran molecular dynamics simulations for the corresponding neutral structures of OSDA1, OSDA2 and OSDA3 with initial orientations O1 and O2. Scatterplots for each run are presented in Figures 5.19 to 5.21.

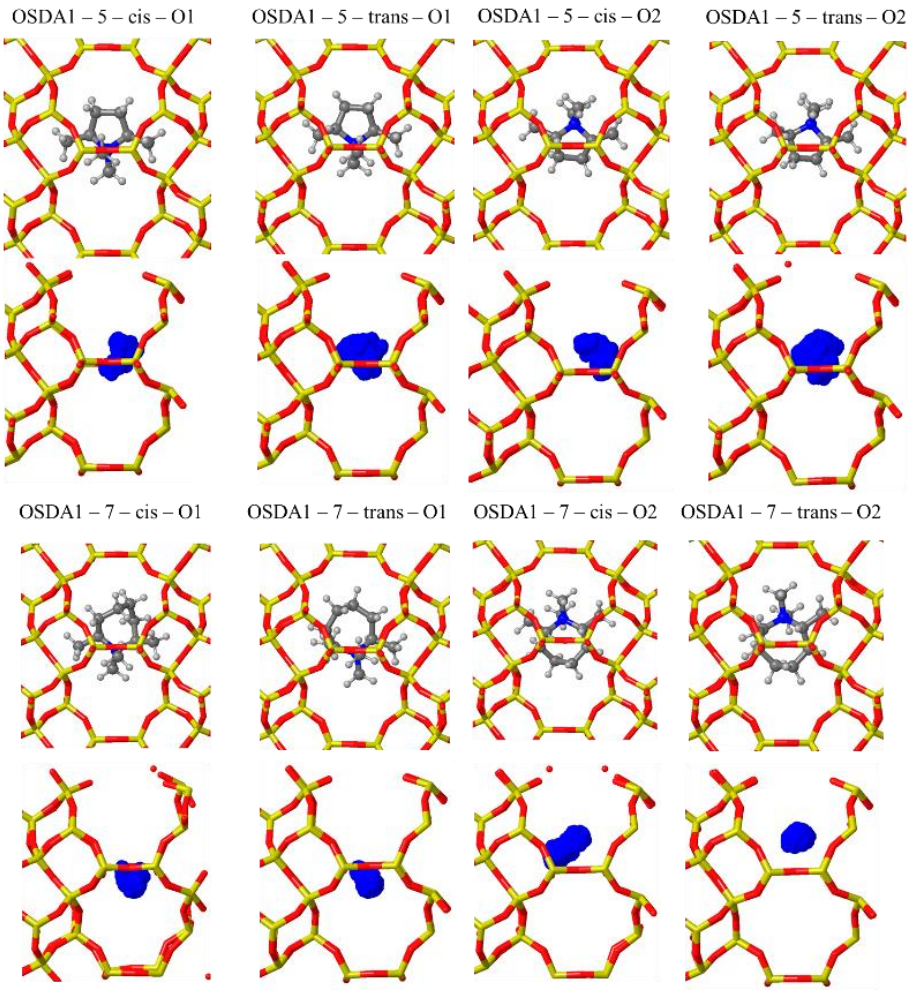

Figure 5.19. Scatterplots of 100 ps for 5-C and 7-C structures of OSDA1. Framework Si and O atoms are depicted as yellow and red sticks, "N", C and H atoms are depicted as blue, grey and white balls.

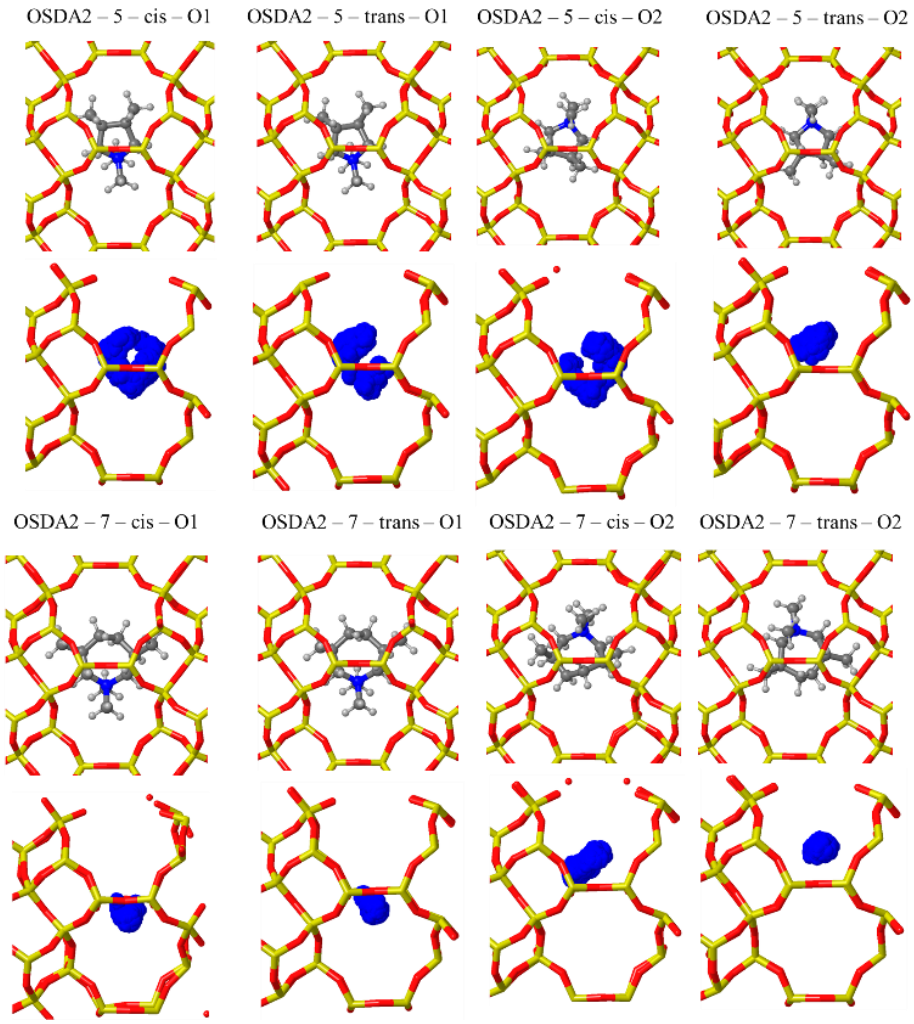

Figure 5.20. Scatterplots of 100 ps for 5-C and 7-C structures of OSDA2. Framework Si and O atoms are depicted as yellow and red sticks, "N", C and H atoms are depicted as blue, grey and white balls.

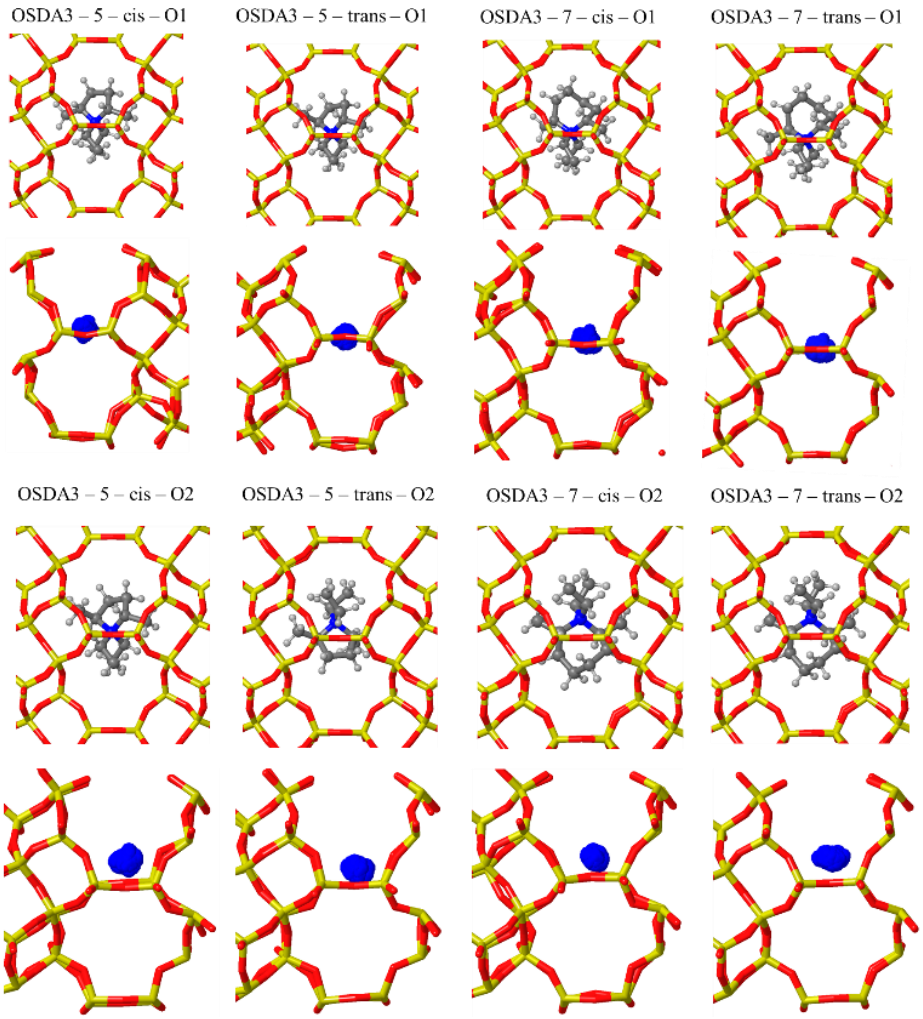

Figure 5.21. Scatterplots of 100 ps for 5-C and 7-C structures of OSDA 3. Framework Si and O atoms are depicted as yellow and red sticks, "N", C and H atoms are depicted as blue, grey and white balls.

Looking at Figure 5.21, that shows 5- and 7-C ring versions of OSDA3, it is possible to see that this molecule remains immobile independently of the ring size because of its bulky substituents over the "N" atom as it happens in Figure 5.14 for the corresponding 6-C ring structure. From Figure 5.19 and 5.20, with scatterplots for 5- and 7-C versions of OSDA1 and OSDA2, it is possible to observe that 5-C ring molecules show an enhanced mobility when compared to their original 6-C version (Figure 5.14), In contrast, systems with 7-C rings are clearly less mobile not presenting much movement away from their initial position. From the qualitative results presented in this section as scatterplots of OSDA mobility, it can be concluded that the size of the N-substituents has a more pronounced effect on mobility than the ring size (in the 5-C to 7-C range).

Thus, when the N-substituents size decreases from ethyl in OSDA3 to methyl in OSDA1 an enhanced mobility is observed for all ring sizes. On the other hand, in OSDA1 and OSDA2 with methyl substituents on the "N" atom, increasing the ring size from 5-C to 7-C only leads to a slight decrease in mobility.

5.4.2 Aluminium Distribution in AEI cavities using piperidinium-based OSDAs.

In the previous subsection, mobility of neutral OSDAs was studied inside AEI cavities identifying OSDA3 as an immobile directing agent and OSDA1 and OSDA2 as molecules with low mobility because of the optimal confinement given by AEI cages to piperidinium substituted molecules. In this section we study the behaviour of these OSDAs when electrostatic charges are present. Besides, other hypothesized OSDAs for SSZ-39 synthesis are also included in this part of the study in order to compare how their molecular structure is able to direct the Al positioning in different manners around the framework.

First, we need to describe in detail the Al distribution in an AEI cavity structure. It presents a framework made up of d6r with three different tetrahedral, T-site, positions. These d6r units sum up to form the whole AEI structure, composed by pear-like cavities each of which is accessible through six 8r windows. Not all the 8r windows present the same T-site distribution. For each cavity there are four 8r windows that contain the three possible T-sites, 4 T1, 2 T2 and 2 T3, these windows are found on the upper and the lower part of each cavity (see Fig 5.21). Windows that connect the cavities through the x axis contain 4 T2 and 4 T3 sites without any presence of T1 positions, (see Fig 5.22). To compare the stability of each T-site, we generated three different models with one Si atom substituted by one Al atom leaving the AlO_4^- negative charge uncompensated, each model corresponding to a different T-site. Comparing the intrinsic stability of these models, we found that T1 is the most stable position (see Table 5.7). Thus, if an OSDA that would direct Al towards T2 or T3 instead of T1 was used in AEI synthesis, a difference in the catalytic behaviour of the material obtained or in the diffusion of reactants or products might be observed.

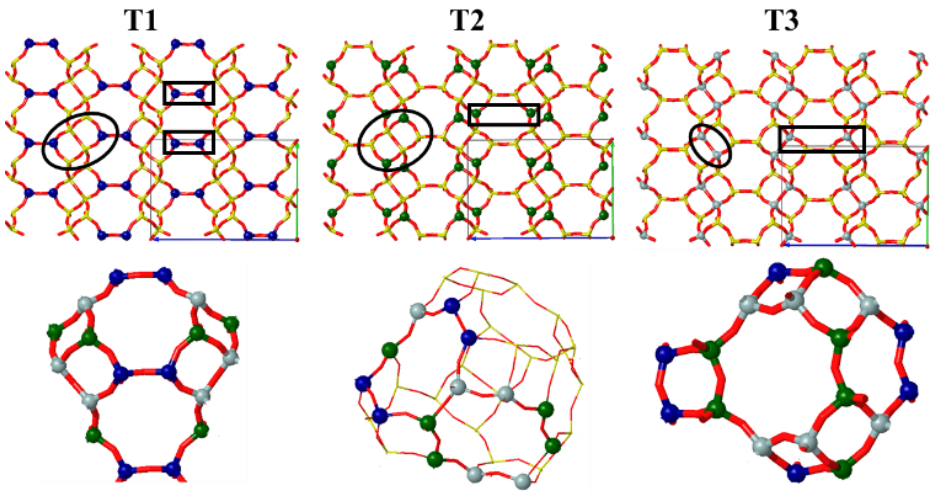

Fig 5.22. AEI T-site distribution; blue (T1), green (T2), grey (T3).

Table 5.7. Relative electronic energy for the different AEI T-site positions (kJ/mol).

	T1	**T2**	**T3**
Erel (kJ/mol)	0	3	4

To start the study, we selected OSDA1, OSDA2, OSDA3 and included another piperidinium cation, *N*-ethyl-*N*-methyl-2,6-dimethyl-piperidinium (OSDA4, see Figure 5.23), which has been theorized as the best directing agent for AEI framework synthesis.[15] The Eint between the cationic form of each OSDA and the negatively charged AEI framework containing one Al atom was calculated using static DFT as described in section **5.2**. Al was placed in each of the three different T-positions, always selecting the location closest to the N atom of the OSDA (see Fig 5.24 to 5.27). The three orientations observed from regular MD simulations during the previous subsection, O1, O2 and O3, were considered in each case and only *cis* configurations were taken into account in order to reduce the number of variables and extract comparable results.

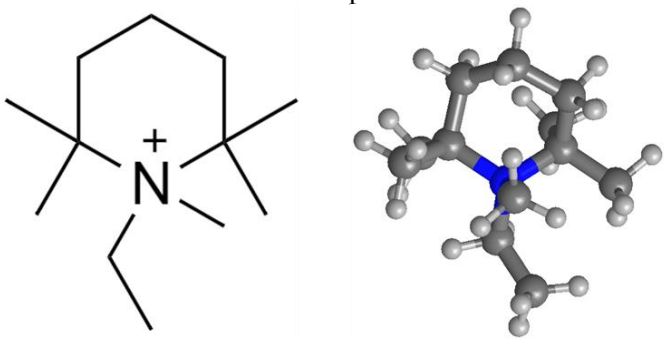

Figure 5.23. *N*-ethyl-*N*-methyl-2,6-dimethyl-piperidinium (OSDA4).

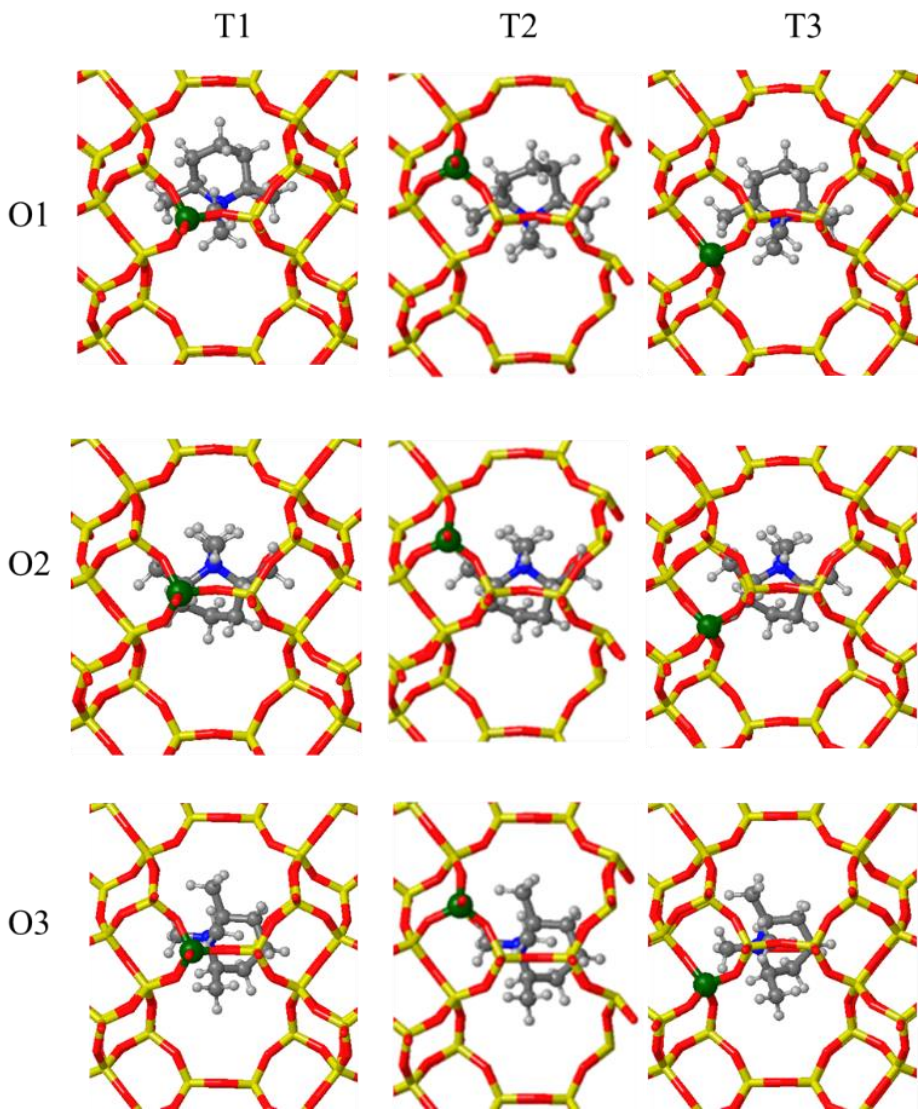

Fig 5.24. Static DFT VASP calculations for each possible AEI T-site using OSDA1. Framework Si and O atoms are depicted as yellow and red sticks, Al, N, C and H atoms are depicted as green, blue, grey and white balls.

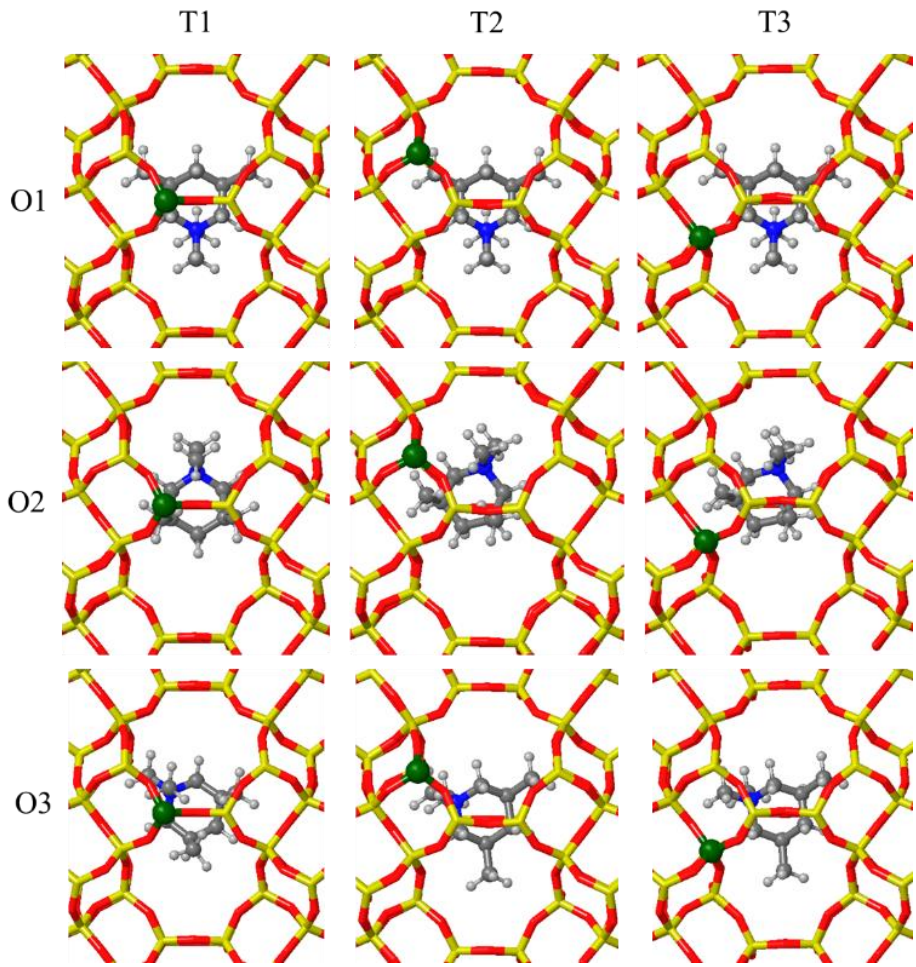

Fig 5.25. Static DFT VASP calculations for each possible AEI T-site using OSDA2. Framework Si and O atoms are depicted as yellow and red sticks, Al, N, C and H atoms are depicted as green, blue, grey and white balls.

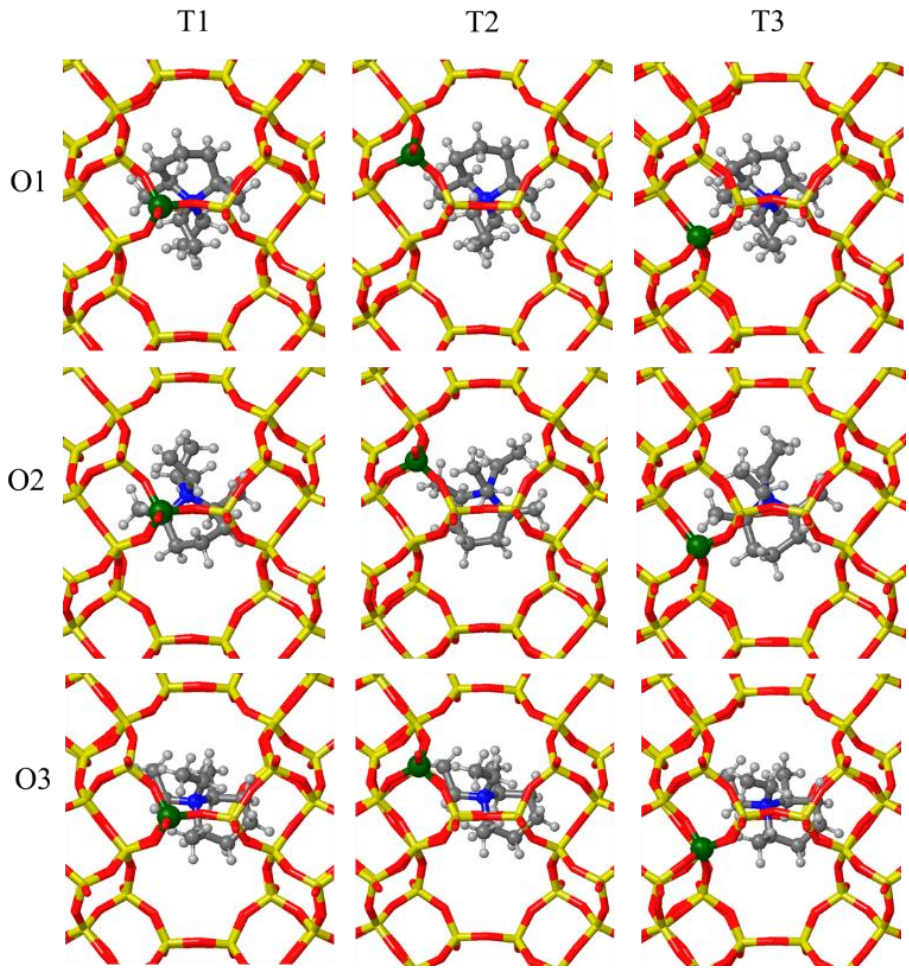

Fig 5.26. Static DFT VASP calculations for each possible AEI T-site using OSDA3. Framework Si and O atoms are depicted as yellow and red sticks, Al, N, C and H atoms are depicted as green, blue, grey and white balls.

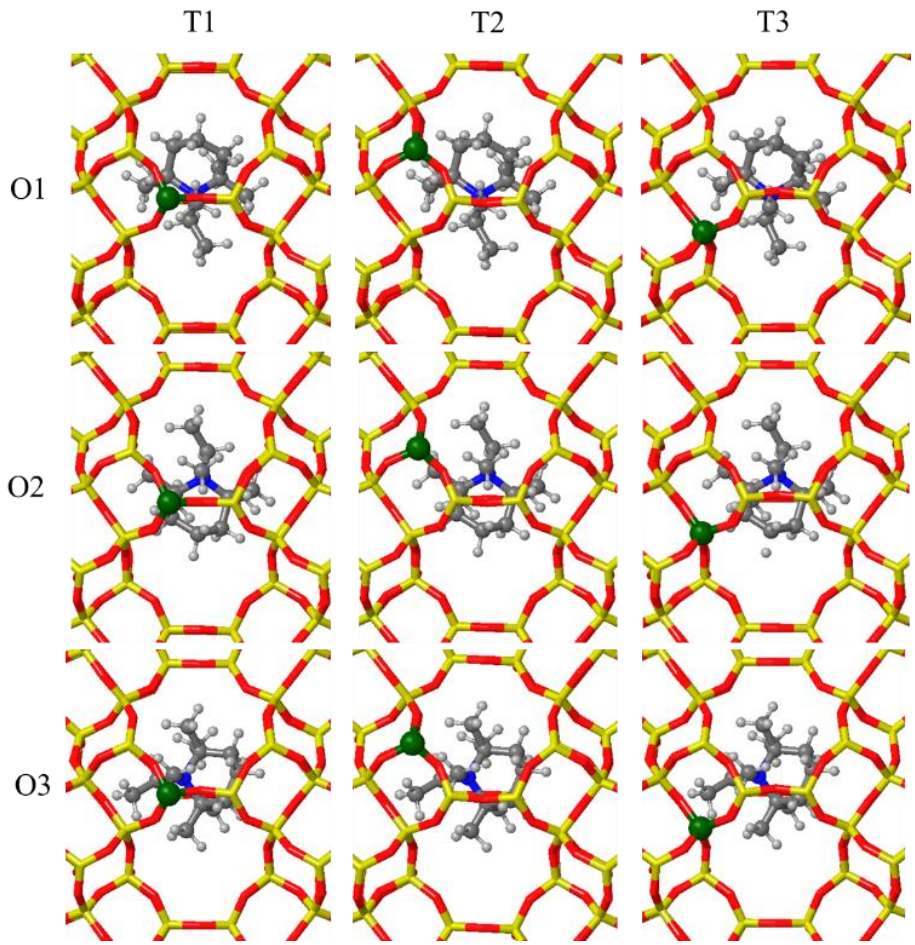

Fig 5.27. Static DFT VASP calculations for each possible AEI T-site using OSDA4. Framework Si and O atoms are depicted as yellow and red sticks, Al, N, C and H atoms are depicted as green, blue, grey and white balls.

All Eint values are summarized in Table 5.8. Looking at results globally, all OSDAs present high negative values for Eint, ~ -600 kJ/mol, which accounts for the strong electrostatic interactions between AlO_4^- tetrahedra and positively charged OSDAs coupled with their good templating effect for AEI framework. When analysing these data in more detail, it is possible to see that the more stable structures for each OSDA, highlighted in Table 5.8, correspond to T1 models. There are only two cases, OSDA1 T3 O3 Eint -648 kJ/mol and OSDA4 T3 O1 Eint -646 kJ/mol, where T3 structures present a similar Eint to their respective most stable T1 models, ~ 2-3 kJ/mol difference. An OSDA preference for Al in T2 position was not found in any case. Regarding to the different orientations studied, the worse Eint observed in the previous section for OSDA2 O2 (Table 5.5) gets diluted when electrostatic charges are introduced, and the values obtained for O2 are similar to the other orientations.

In this case, a feature to highlight about OSDA4 are the worse Eint values obtained for its O2 models when compared to O1 and O3 with differences between their calculated Eint of 14 and 42 kJ/mol. From these results it is possible to extract a clear conclusion about ring substituted charge-centred piperinium-based OSDAs, they tend to position the Al in T1, with a few exceptions pointing towards small portions of Al in T3 because their Eint is close to T1 values.

The central position of T1 in AEI cages allows a better interaction and stabilization for these OSDAs that position their positive charge at the centre of the cavities and show a very limited mobility. This assumption is strengthened when looking at the literature, in 2015 Davis et al. used dimethylpiperidine based OSDAs (OSDA1 and OSDA2) to prepare SSZ-39 while studying the influence of diastereo- and structural isomeric mixtures on the synthesis. Independently of the mixture used, they achieved a proper synthesis of SSZ-39 with similar Si/Al ratios. These results indicate that piperidinium based OSDAs behave similarly leading to analogous SSZ-39 samples.[79]

Table 5.8. DFT Eint calculated for OSDA1, OSDA2, OSDA3 and OSDA4 (kJ/mol).

OSDA		**T1**	**T2**	**T3**
1	O1	**-651**	-638	-640
1	O2	-646	-641	-625
1	O3	-647	-633	-648
2	O1	-622	-607	-614
2	O2	-621	-606	-616
2	O3	**-627**	-618	-621
3	O1	**-640**	-624	-636
3	O2	-635	-610	-619
3	O3	-621	-614	-614
4	O1	**-644**	-635	-642
4	O2	-616	-606	-600
4	O3	-630	-632	-634

In order to check whether the low mobility around the cage centre of this kind of OSDAs is maintained when electrostatic charges are introduced in the simulations, we performed 75 ps long AIMD simulations at 408 K of OSDA1 and OSDA2 inside AEI cavities with one Al in each of the three different T-sites. As starting orientations, we selected O1 and O2 for OSDA1, and O1, O2 and O3 for OSDA2, resulting in a total of 15 MD simulations.

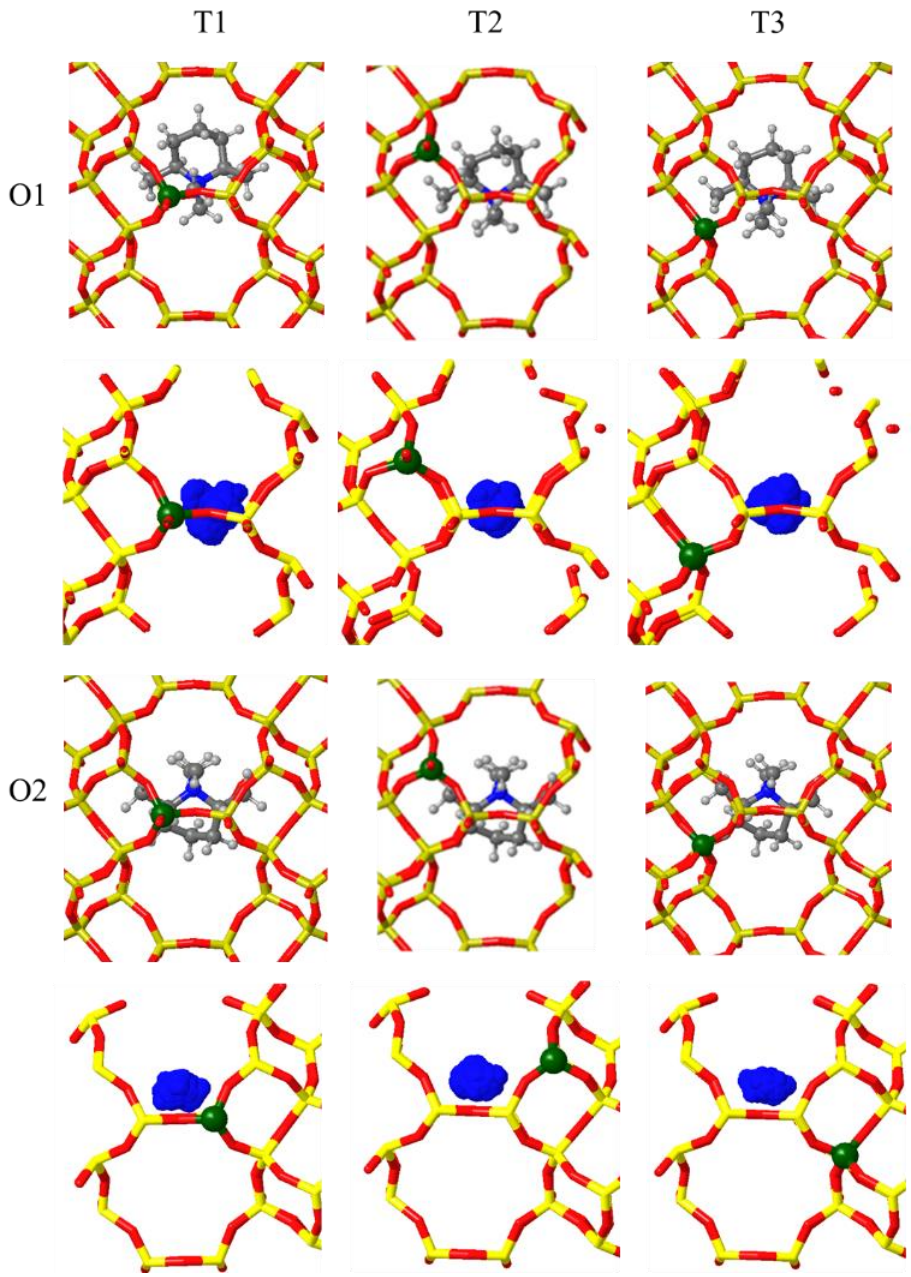

Figure 5.28. OSDA1 75 ps scatterplots. Framework Si and O atoms are depicted as yellow and red sticks, Al, N, C and H atoms are depicted as green, blue, grey and white balls.

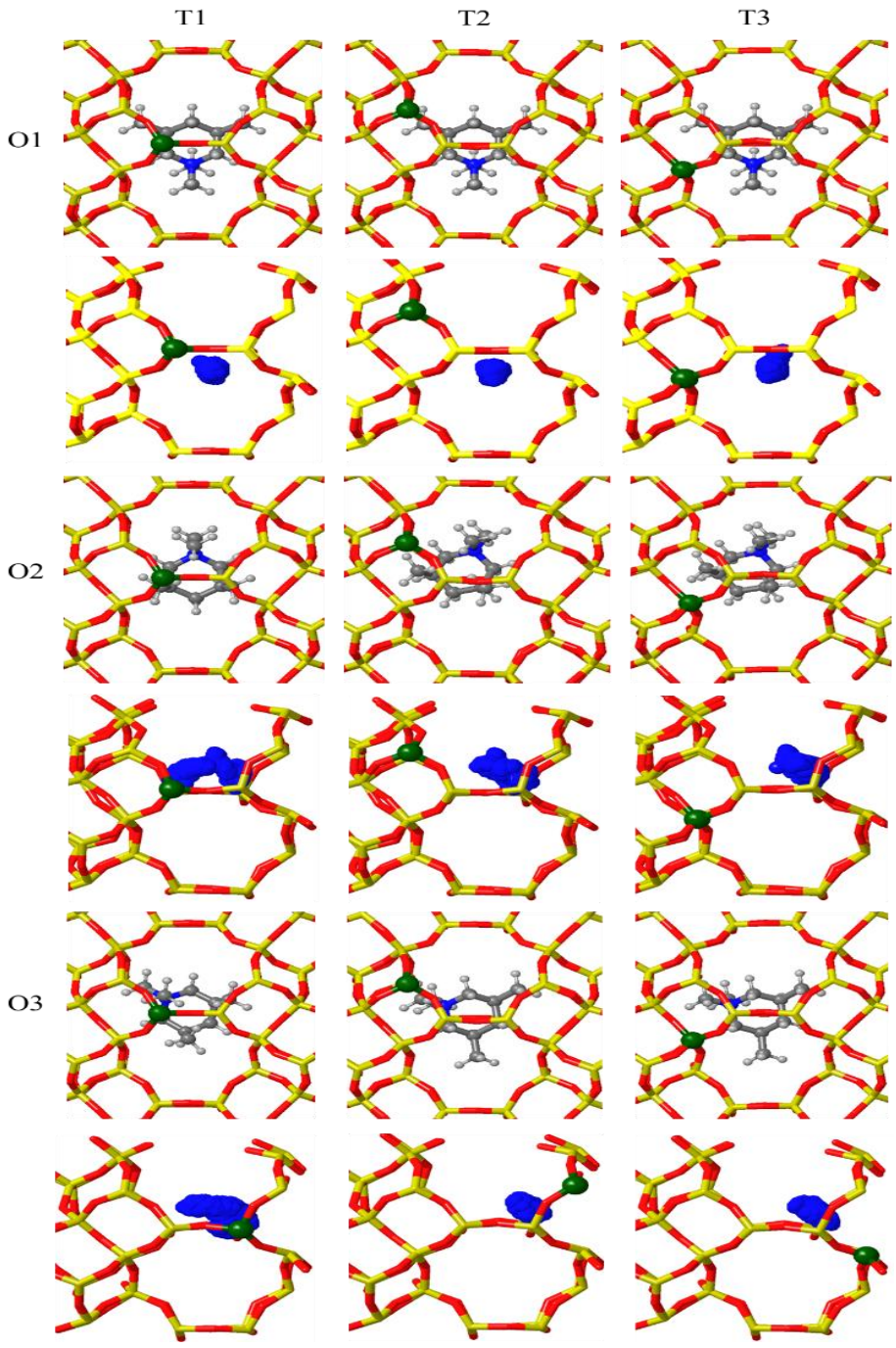

Figure 5.29. OSDA2 75 ps scatterplots.

As it can be seen from the scatterplots, the mobility of the charged OSDAs does not change with respect to the neutral versions studied in the previous section (Figure 5.14) and the N atom is mainly found at the centre of the AEI cavity most of the simulation time. To correlate the static and dynamic DFT data produced, the distance between the OSDA N atom and the framework Al atom was measured in the static optimized structures and an average N-Al distance was computed from AIMD simulations (see Table 5.9). The good correlation (R^2=0.946) between the static and dynamic N-Al distances observed in Figure 5.30 can be taken as a numerical way of proving the immobility of ring-substituted piperidinum OSDAs when confined within the AEI cages, evidencing that no important displacements, rotations or other movements of the whole OSDAs are taking place. On the other hand, despite the N-Al distances are shorter when Al is in T1 and longer when Al occupies T2 (see Figure 5.30), no correlation was found between the calculated Eint and any kind of distances measured.

Table 5.9. Calculated N-Al distances (Å) from static geometry optimizations and averaged N-Al distances (Å) from AIMD simulations of OSDA1 and OSDA2 within AEI cages.

OSDA		T1		T2		T3	
		Static	MD	Static	MD	Static	MD
1	O1	5.2	5.4	6.5	6.8	5.1	5.2
1	O2	5.0	5.3	5.8	6.1	5.5	5.7
2	O1	5.1	5.3	7.2	7.2	5.1	5.0
2	O2	5.1	5.1	6.8	7.1	6.8	6.6
2	O3	4.8	5.1	5.6	5.8	4.8	5.1

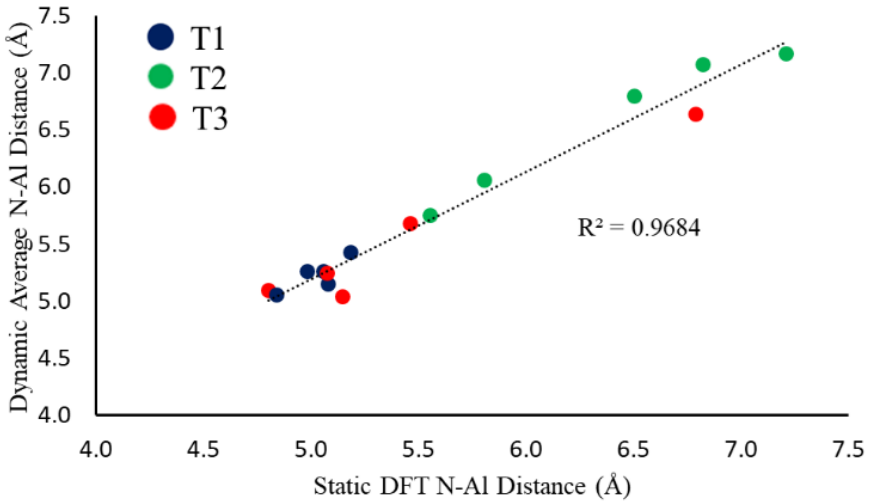

Figure 5.30. Correlation between N-Al optimized distances from static DFT calculations and averaged N-Al distances from AIMD simulations for OSDA1 and OSDA2 within AEI cages.

Once the piperidinium based OSDAs classically used in AEI synthesis have been identified as directing agents unable to spread the Al around the three possible T-site positions in AEI framework, leading in all cases to T1 positioning, a new set of OSDAs with different molecular structures and positive charge placement that had been theorized as good directors for AEI synthesis, 2,2,7,7-tetramethyl-2-azoniabicyclo[4.1.1]octane (OSDA5) and 1,3,3,6,6-pentamethyl-6-azoniabicyclo [3.2.1] octane (OSDA 6) were investigated (see Figure 5.31).[15]

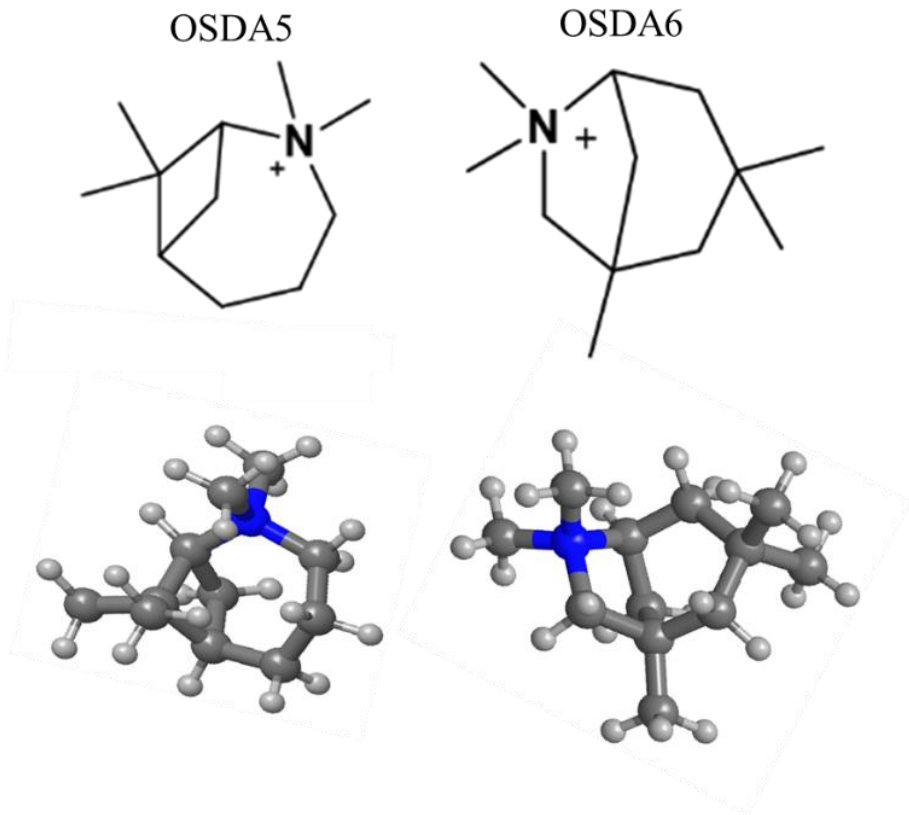

Figure 5.31. 2,2,7,7-Tetramethyl-2-azoniabicyclo [4.1.1]octane (OSDA5) and 1,3,3,6,6-Pentamethyl-6-azoniabicyclo[3.2.1]octane (OSDA6).

Both molecules present a similar molecular structure based on azepane molecule, both present methyl substituents, four in OSDA5 and five in OSDA6, but their positioning around the azepane ring is different (see Figure 5.31). Also, a three-membered bridge that confers three-dimensionality is present in both molecules. Comparing OSDA5 and OSDA6 with the molecules studied previously, the most important difference is found in the asymmetric position occupied by the positive charge (see Figure 5.31). This feature allows the N atom, and the positive charge associated, to be placed in different regions of the AEI cavity that are slightly displaced from the cage centre, hence suggesting the possibility of a better contact with T2 and T3 crystallographic positions

instead of T1 ones (see Figures 5.32 and 5.33). The same methodology employed previously was applied to the new set of OSDAs, starting with static DFT optimizations of each OSDA inside negatively charged AEI frameworks in order to obtain information about their stabilities and preferred orientations. The Eint values obtained from these calculations are summarized in Table 5.10.

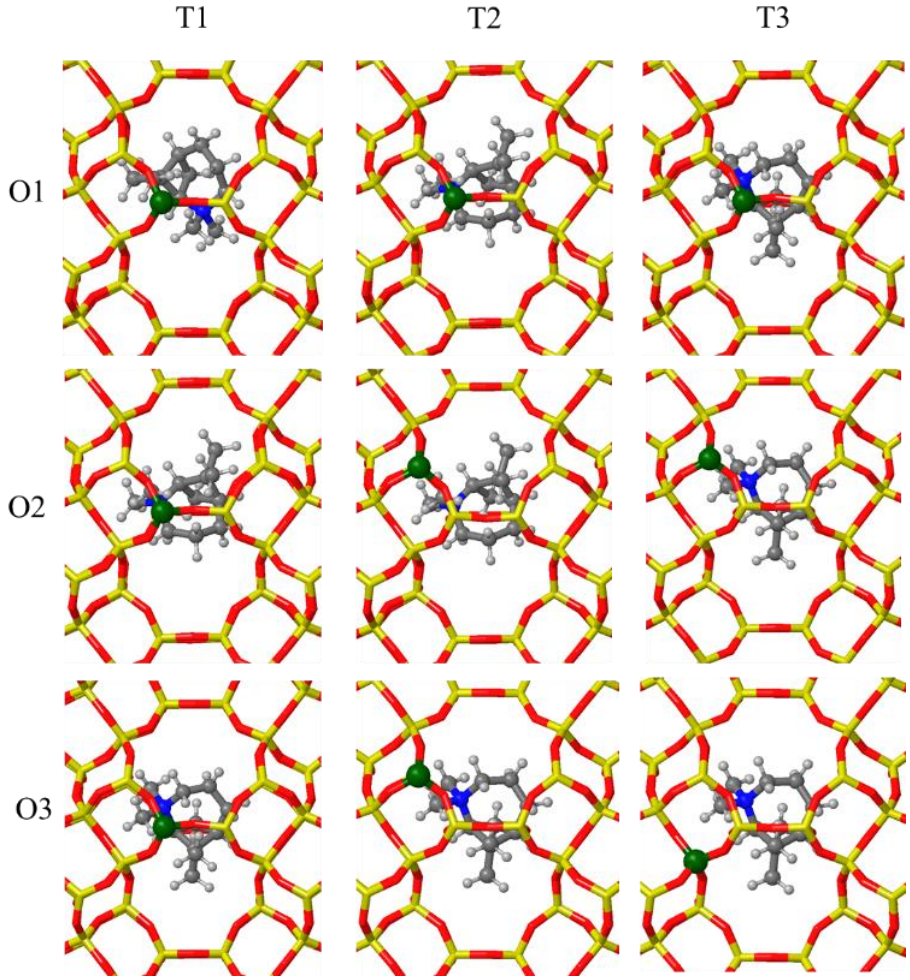

Fig 5.32. Static DFT VASP calculations for each possible AEI T-site using OSDA5. Framework Si and O atoms are depicted as yellow and red sticks, Al, N, C and H atoms are depicted as green, blue, grey and white balls.

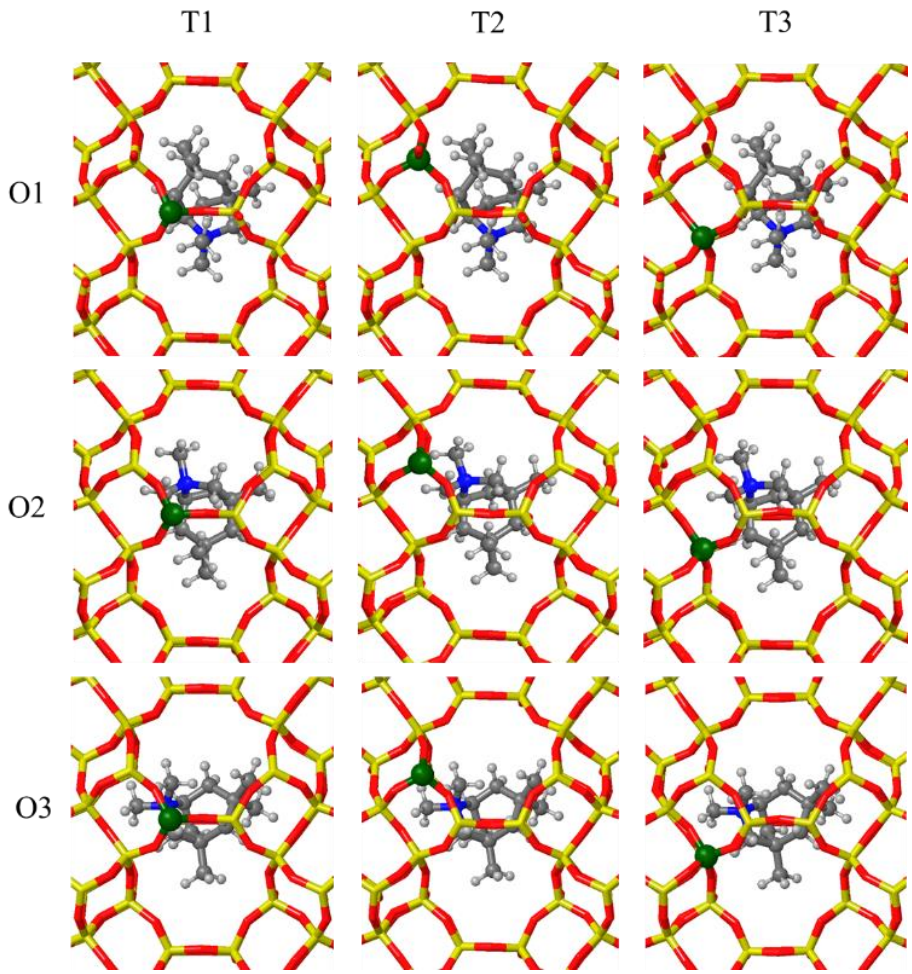

Fig 5.33. Static DFT VASP calculations for each possible AEI T-site using OSDA6. Framework Si and O atoms are depicted as yellow and red sticks, Al, N, C and H atoms are depicted as green, blue, grey and white balls.

Table 5.10. DFT Eint calculated for OSDA5 and OSDA6 (kJ/mol).

OSDA		**T1**	**T2**	**T3**
5	O1	-619	-607	-618
5	O2	-626	-617	-625
5	O3	**-638**	-630	-632
6	O1	-626	-613	-621
6	O2	-643	-634	-635
6	O3	**-644**	-639	-642

From highlighted results in Table 5.10, it is possible to identify that the best Eint values obtained for both OSDAs correspond to their O3. These structures present their positive charge displaced towards one of the sides of the AEI cage instead of being in the centre of the cavity centre (see Figures 5.32 and 5.33). Despite this, the T1 position resulted again the most stable for both OSDAs. It is important to note that the Eint difference between O3 T1 and O3 T3 positioning for OSDA6 is 2 kJ/mol, suggesting a possible spreading of Al around T1 and T3 positions when using this OSDA similar to the spread predicted for OSDA1 and OSDA4 where the same Eint difference between T1 and T3 was found.

Following the method defined previously, regular AIMD simulations of 75 ps at 408 K were performed only for the most stable O3 orientation of OSDA5 and OSDA6 within charged models of AEI framework with Al placed in T1, T2 and T3 sites. Results from these simulations are given as N position scatterplots in Figure 5.34.

From Figure 5.34 it is possible to see how immobile these OSDAs are, with the N atom always remaining around its initial position in every case. This is because of the good fitting of their structures within the AEI cages. As described in previous section, seven membered rings are the best suited to fill the AEI cavities. Moreover, their substituents docked into the narrow part of the cavity restrict the rotations that can take place because of their steric hindrance, and as a result OSDA5 and OSDA6 are less mobile than OSDA1-OSDA4. The distance between the N atom and the framework Al was obtained from static calculations and averaged from AIMD simulations repeating the procedure presented before (see Table 5.11), and the correlation between the data obtained is depicted in Figure 5.35.

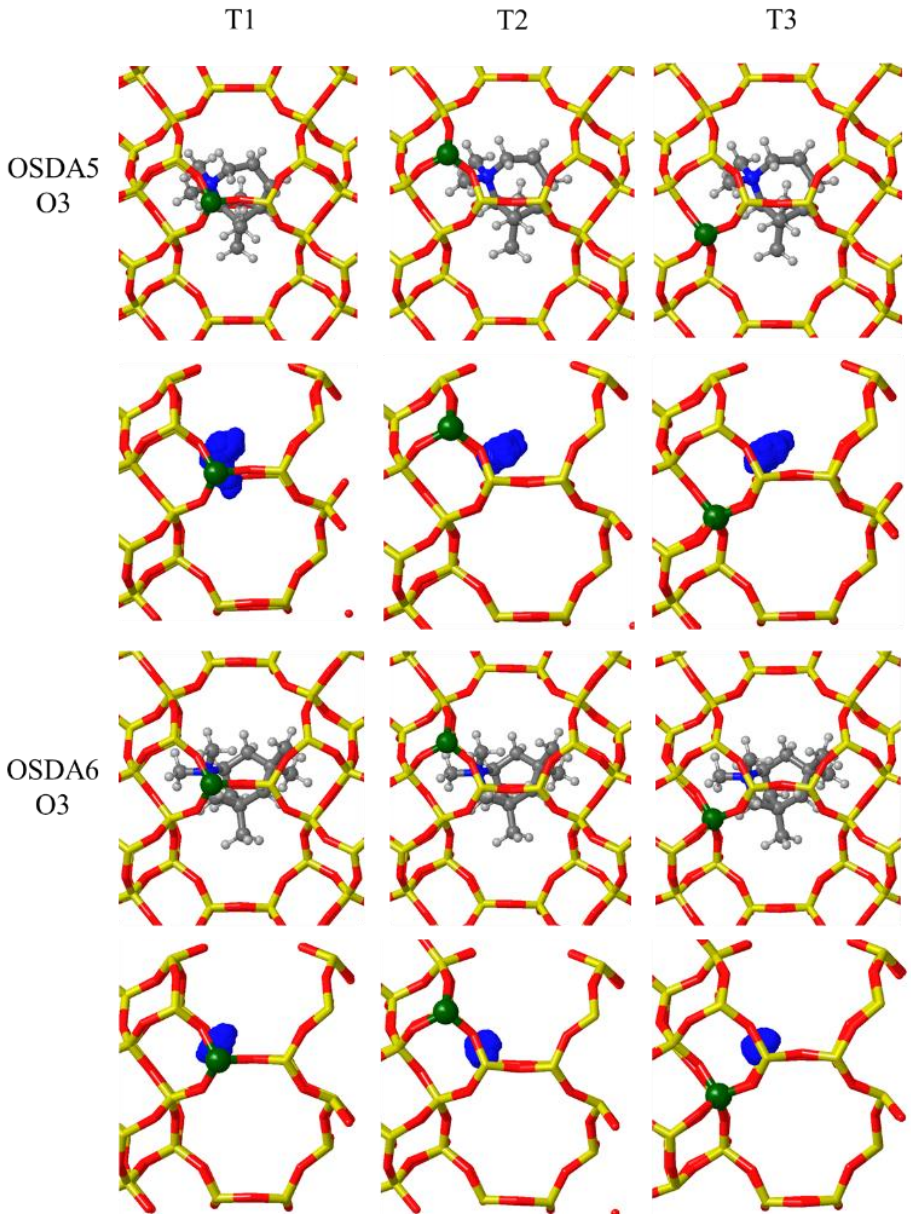

Figure 5.34. 75 ps scatterplots for N position in OSDA5 and OSDA6. Framework Si and O atoms are depicted as yellow and red sticks, Al, N, C and H atoms are depicted as green, blue, grey and white balls.

Table 5.11. Calculated N-Al distances (Å) from static geometry optimizations and averaged N-Al distances (Å) from AIMD simulations of OSDA5 and OSDA6 within AEI cages.

OSDA	T1		T2		T3	
	Static	MD	Static	MD	Static	MD
5	4.8	5.3	5.4	5.8	4.9	5.2
6	4.7	5.0	5.4	5.6	4.4	4.5

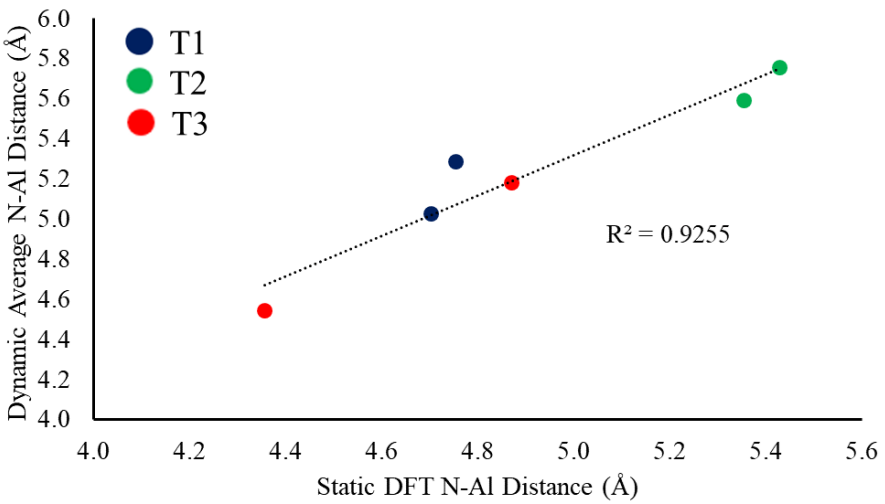

Figure 5.35. Correlation of N-Al distances (Å) from static geometry optimizations and AIMD averaged N-Al distances (Å) from MD simulations of OSDA5 and OSDA6 within AEI cages.

A good correlation was obtained between static and dynamic N-Al distances. Therefore, results point towards an Al positioning in T1 for OSDA5. Despite T1 and T3 static and MD distances being short for OSDA5, ~ 5 Å, which accounts for a good interaction between N and Al atoms (see Table 5.11), a 6 kJ/mol difference between T1, most stable, and T3 Eint becomes an immense difference at synthesis temperatures. Similarly, Eint values obtained for OSDA6 anticipate a major Al positioning in T1, nonetheless, the possibility of a disperse distribution of Al between T1 and T3 is more probable when compared with OSDA5 and OSDA1. For OSDA6, T3 Eint only differs 2 kJ/mol from T1 Eint, moreover, T3 distances static, 0 K, and dynamic, 408 K, are shorter than T1 ones which accounts for a better contact between N and Al atoms when Al is placed at T3. In OSDA1 case, the difference between Eint was also 2 kJ/mol but distances were similar for T1 and T3 and in both cases they were larger than the ones calculated for OSDA6 (see Tables 5.8 and 5.9).

During this study, we have examined many piperidinium and azepane rings that are substituted in different manners. Independently of their positions, methyl and ethyl substituent chains always fix the OSDA by docking with the AEI cavity topology. Therefore, as the last part of this section, we selected 9,9-dimethyl-9-azabicyclo [3.3.1]nonane-9-ium (OSDA7),[80] a successfully proven OSDA for AEI framework synthesis that lacks of substituents around its ring and has its positive charge located outside it (see Figure 5.36), in order to compare and contrast the results previously obtained and determine the role of substituents in OSDA mobility and Al directing capacity.

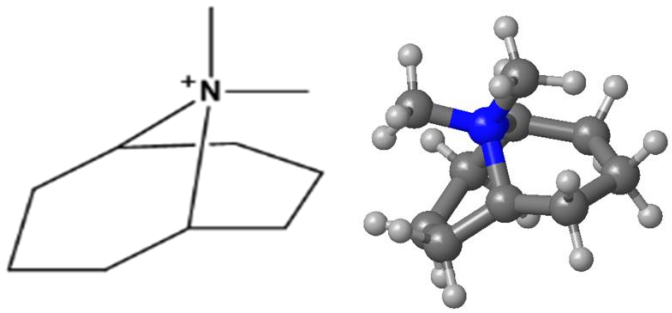

Figure 5.36. 9,9-dimethyl-9-azabicyclo[3.3.1]nonane-9-ium (OSDA7).

As OSDA7 is expected to be mobile within AEI cages because of its molecular structure without substituents in its nonane ring, that should allow considerable rotations, we considered a total of seven different initial orientations for the static DFT optimizations carried out as the initial step of our analysis method (Figure 5.37). Considering the seven different orientations within each of the three Al-containing AEI models (with Al in T1, T2 and T3) led up to twenty-one different optimized structures (Figure 5.37), with all the data obtained being presented in Table 5.12. The mobility of these systems was evaluated with 75 ps AIMD simulations at 408 K, and scatterplots for N atom position in each simulation were generated (see Figures 5.38 and 5.39). Besides, we marked one C atom corresponding to a methyl substituent over the N atom with purple colour in Figure 5.37, and scatterplots for the positions of this atom have been generated in combination with positions of the N atom in order to evaluate the rotation of the whole OSDA7 (see Figure 5.40).

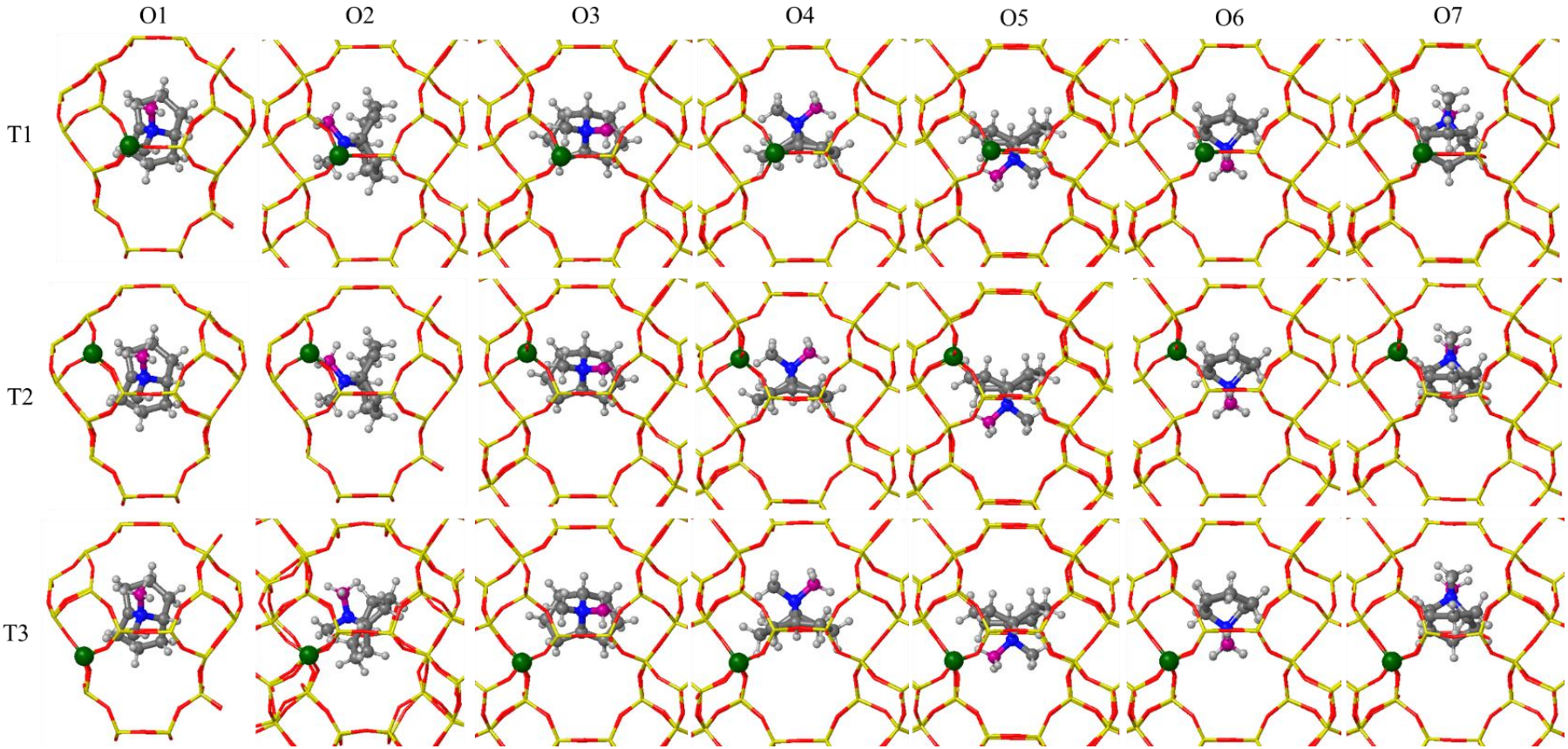

Figure 5.37. Static DFT VASP calculations for each possible AEI T-site using OSDA7 with 7 different orientations. Framework Si and O atoms are depicted as yellow and red sticks, Al, N, C and H atoms are depicted as green, blue, grey and white balls. Purple C atom marked as a reference for Figure 5.40 scatterplots.

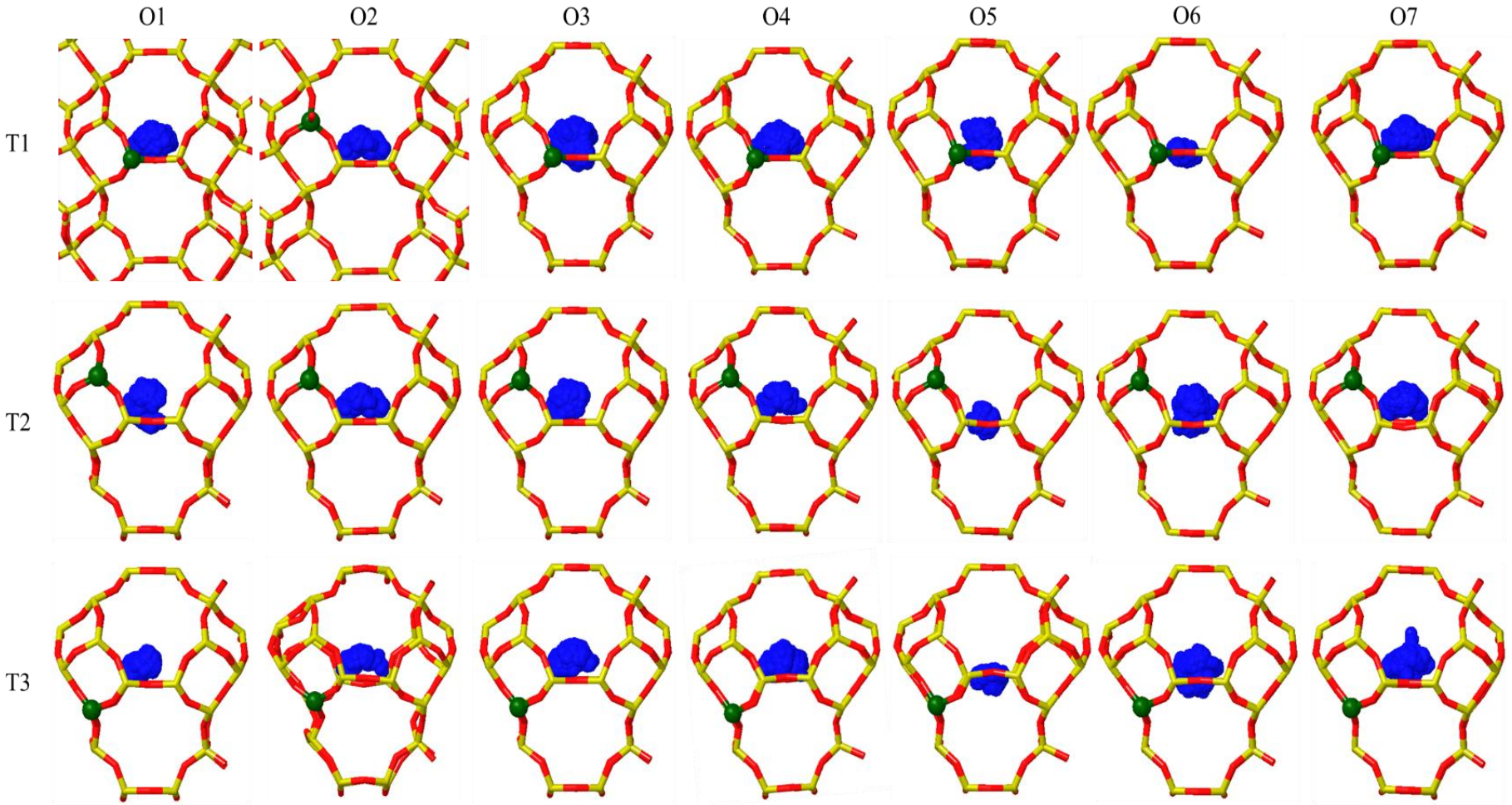

Figure 5.38. 75 ps scatterplots for N position in OSDA7 seen from z axis. Framework Si and O atoms are depicted as yellow and red sticks, Al and N atoms are depicted as green and blue balls.

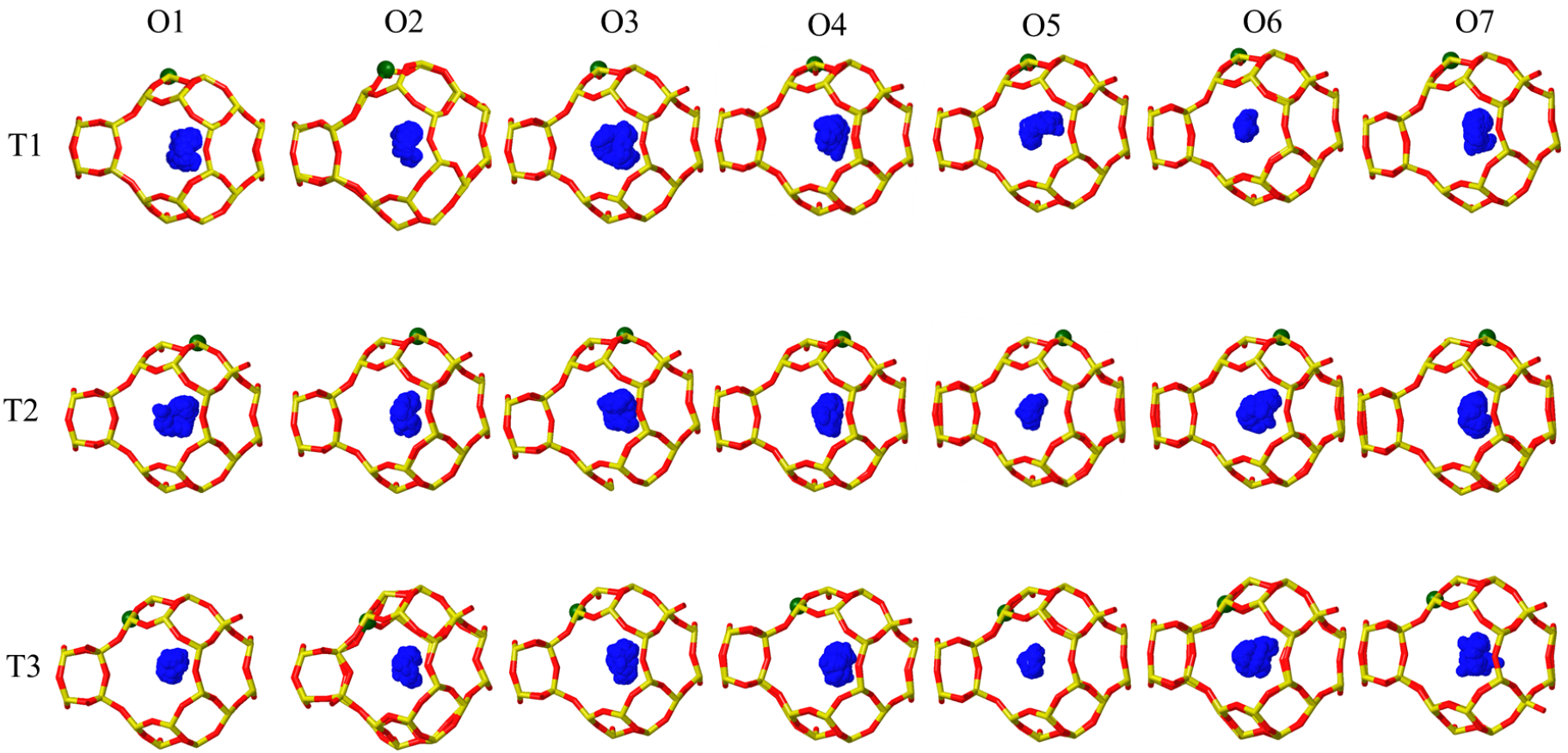

Figure 5.39. 75 ps scatterplots for N position in OSDA7 seen from x axis. Framework Si and O atoms are depicted as yellow and red sticks, Al and N atoms are depicted as green and blue balls.

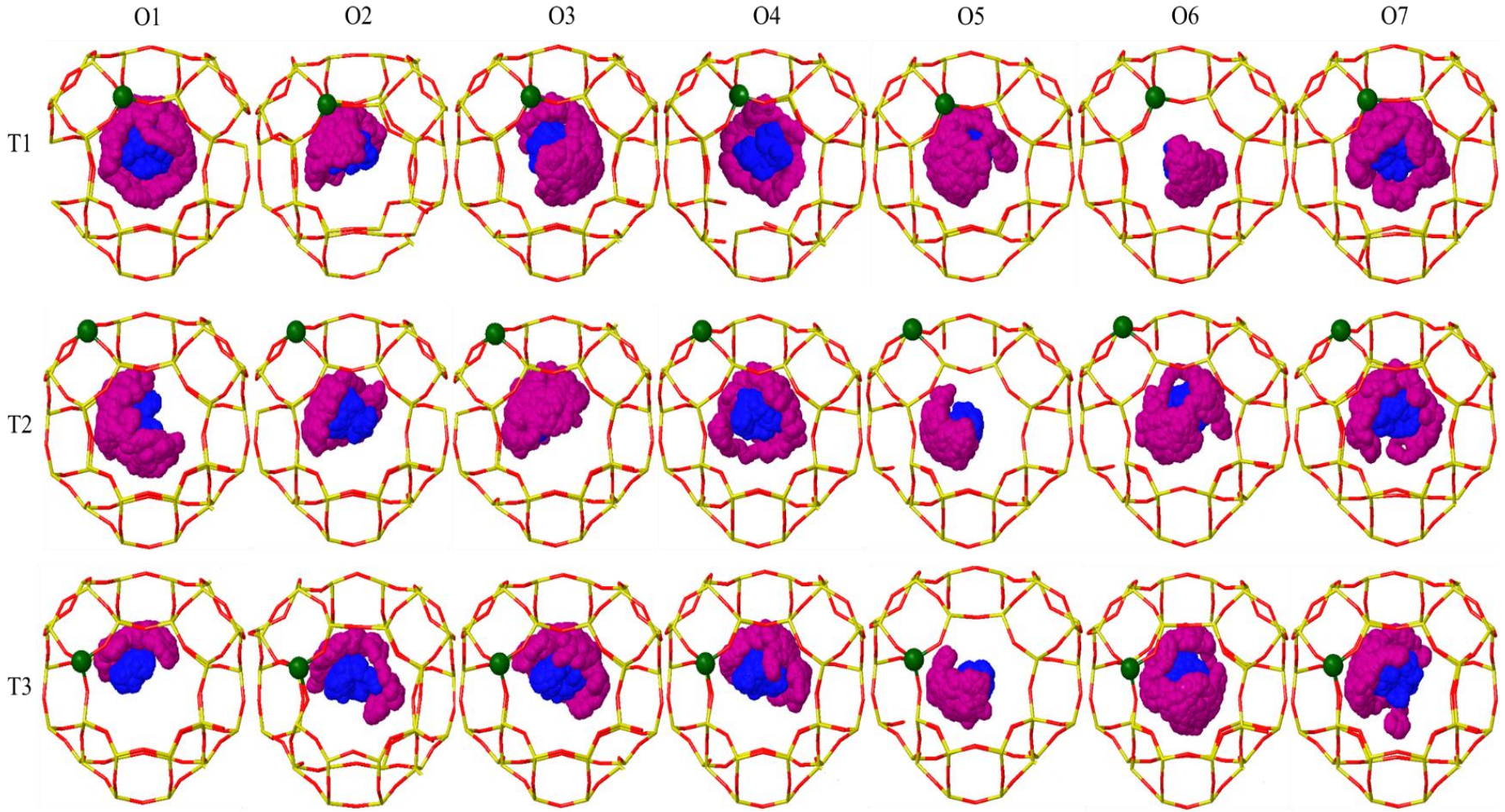

Figure 5.40. 75 ps scatterplots for N and C, marked with purple colour in Figure 5.37, position for OSDA7. Framework Si and O atoms are depicted as yellow and red sticks, Al, N and C atoms are depicted as green, blue and purple balls.

Table 5.12. DFT Eint calculated for OSDA7 (kJ/mol).

OSDA7	T1	T2	T3
O1	-623	-608	-613
O2	**-625**	**-620**	**-630**
O3	-623	-614	-611
O4	-620	-612	-613
O5	-616	-610	-616
O6	-624	-615	-619
O7	-607	-603	-598

Comparing the Eint summarized in Table 5.12 it is possible to identify that O2 values are the best ones for each Al position (highlighted in Table 5.12). In opposition to all other OSDAs studied, in this case the best Eint value obtained corresponds to T3. These results hint a significant probability of spreading part of the Al towards T3 using OSDA7, however, to attain a proper conclusion it is necessary to observe the mobility of OSDA7 given by AIMD simulations (see Figure 5.38 to 5.40).

From these scatterplots we can see how the OSDA mobility is clearly enhanced by the lack of substituents around the nonane ring with bulkier scatterplots for the N atom position in Figures 5.38 and 5.39 when compared to the ones obtained for OSDA1, OSDA2, OSDA5 and OSDA6 in Figures 5.28, 5.29 and 5.34 respectively. It is worth to note the impact of substituents absence because a non-substituted nonane ring presents a much higher mobility than methyl substituted piperidinium OSDAs. Looking at Figure 5.40 it is possible to observe full rotations of the complete OSDA in specific cases, see O1 T1, O4 T1 and T2, O6, T2 and T3 and O7 T1 and T2 where the purple scatterplots for the marked C atom cover a whole circle around the cavity. Besides, these rotations lead to interconversion between different orientations despite the Al positions of the model. Consequently, the hypothesis about OSDA7 Al positioning ability cannot be established taking into account only the static Eint energy values as an absolute parameter for preferred orientations because unequivocal interconversions between orientations have been observed for all three Al positions when the different systems have been studied dynamically (Figure 5.40). In addition, these features identified for OSDA7 mobility constitute a conclusion about the role of ring substituents over OSDA mobility as itself. Regarding to preferred orientations for OSDA7 regardless of its mobility, from these AIMD simulations we cannot make the assumption of O2 being the most probable one because it is the most stable orientation determined by static DFT values (see Table 5.12). A simulation time of 75 ps results rather short to extract any conclusion of that kind. This timescale serves to scrutinize accurately OSDAs mobility, or immobility, as we have been doing during this chapter, but larger simulation times are necessary in order to explore all the accessible states of a system and derive a conclusion about preferred

orientations, especially when talking about such mobile OSDAs as OSDA7 and high temperatures of 408 K.

Converting the mobility observed in numerical data (see Table 5.13) and establishing a correlation between static and averaged dynamic N-Al distances (Figure 5.41), it becomes clear from the R^2 value obtained, $R^2 = 0.4779$, that there is a poor correlation between static and dynamic distances because of the high mobility of OSDA7.

Table 5.13. Calculated N-Al distances (Å) from static optimizations (VASP) and averaged AIMD N-Al distances (Å) from dynamic runs for OSDA7 with O1, O2, O3, O4, O5 and O6 and O7 positions (CP2K).

OSDA7	T1		T2		T3	
	Static	MD	Static	MD	Static	MD
O1	4.5	5.0	5.6	6.5	5.0	5.1
O2	4.9	5.2	5.7	6.0	4.8	5.0
O3	4.8	5.2	5.6	5.8	5.4	5.3
O4	5.5	5.1	6.2	6.3	6.2	5.6
O5	5.0	5.1	6.5	6.6	5.0	5.3
O6	5.1	5.3	6.4	6.5	4.9	5.2
O7	6.2	5.2	6.5	6.2	6.4	5.2

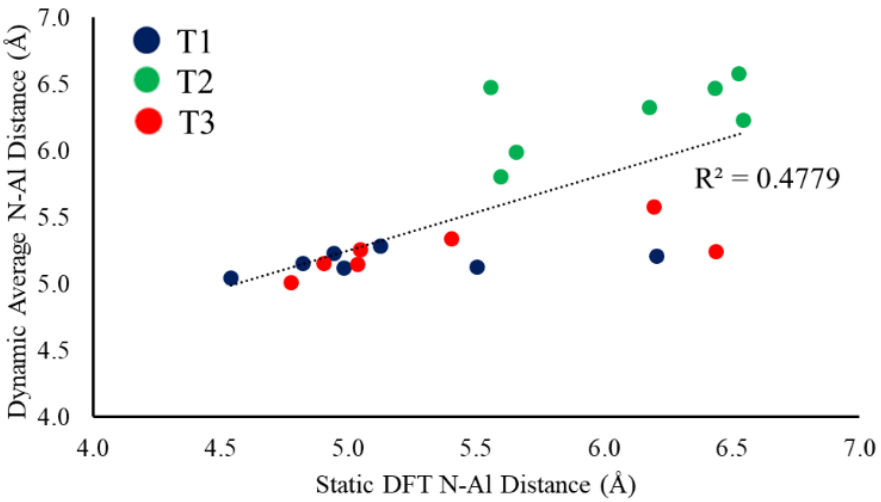

Figure 5.41. Correlation of N-Al distances (Å) from static optimizations and averaged AIMD N-Al distances (Å) from dynamic runs for OSDA7 with O1, O2, O3, O4, O5, O6 and O7 positions (CP2K).

Due to OSDA7 proven mobility we should focus the analysis in the averaged N-Al MD distances because they account for a more real system. It is possible to identify T2 N-Al distances as the largest ones found for each orientation meanwhile T1 and T3 N-Al distances are similar in simulations O1-3 and O5-7, ~ 0.1-0.2 Å, with just O4 simulation obtaining a difference of 0.5 Å. As OSDA7 is able to freely rotate and interconvert from one orientation to other, the differences and similarities exposed can be better seen if the average of the seven simulations for the distances to each T-site position is calculated obtaining an average distance of 5.1 Å for T1, 6.3 Å for T2 and 5.2 Å for T3 Al positions.

From the mobility shown by OSDA7 in the molecular dynamics simulations and the N-Al distance values derived from them, it is possible to hypothesize an Al spreading towards T1 and T3 crystallographic sites of the AEI cavities because, despite OSDA7 ability to freely rotate around itself, these are the closer positions to the OSDA positive charge, hence the better interacting ones.

5.4.3. Conclusions.

In this section of the Chapter, we have implemented a novel theoretical methodology for zeolite synthesis using OSDA molecules that is able to describe comprehensively the behavior of different OSDAs when confined in AEI cavities. We have studied OSDA stability and mobility with static DFT and AIMD simulations, and the data obtained have been correlated with the most probable Al T-site positions of the SSZ-39 framework for each OSDA.

From the mobility study with 100ps AIMD simulations we observed that OSDAs with substituted rings in a range of 5- to 7-C atoms are mainly immobile. OSDA1, OSDA2, OSDA3, OSDA4, consisting of piperidium rings with methyl and ethyl substituents over the N atom and at different positions of the ring, as well as OSDA5 and OSDA6 formed by azepane rings with methyl substituents, cannot undergo full rotations in any of three spatial axes inside AEI cavities. Au contraire, OSDA7 formed by a nonane ring without substituents at the ring is able to rotate freely.

Comparing the 5-C versions of OSDA1 and OSDA3 with their original 6-C molecule, it was possible to identify an enhanced mobility for OSDA1 5-C and a similar mobility for OSDA3 5-C because of its ethyl substituents over the N atom restricting its possible movement. This observation paired with the mobility observed for OSDA7 pointed out that substituents size has a bigger impact over mobility than ring size.

Applying the methodology described to Al positioning study we have been able to distinguish between different kinds of OSDAs that led up to different crystallographic T-site preferences for Al atoms. On the one hand, all Eint values obtained for piperidinium based OSDAs that are symmetrically ring substituted, OSDA1 to OSDA4, indicate that the preferred position for Al is T1 because of its central placement in the AEI cavity. Only OSDA1 and OSDA3 suggest a slight possibility of a portion of Al being placed in T3 because of the small differences observed between the corresponding Eint values. Moreover, AIMD simulations for these immobile OSDAs displayed a good correlation for the averaged N-Al distance with the values calculated from static DFT calculations for this magnitude. The high degree of correlation observed accounts for OSDA immobility and allows us to use Eint as a predictive parameter for Al positioning. Besides, azepanium based OSDAs that are unsymmetrically substituted, OSDA5 and OSDA6, are able to position its positive charge far from the centre of the AEI cage. Nonetheless, the calculated Eint for these kind of OSDAs also showed preference for T1, with OSDA6 suggesting a considerable probability for positioning Al in T3 due to the similar Eint and the low MD distances measured.

On the other hand, OSDA7 based in an unsubstituted nonane ring points towards a disperse Al distribution through T1 and T3. In this case the best Eint values obtained corresponded to T3, however, because of the high mobility displayed by OSDA7, the assumption of T3 being the preferred position for Al cannot be made from static Eint values. Studying the calculated N-Al distances from each of the seven simulations for each Al position carried out for OSDA7, we calculated an average of N-Al distances that resulted in 5.1 Å for T1, 6.3 Å for T2 and 5.2 Å for T3 Al positions. Therefore, thinking the N-Al distances as a measure for the strength interaction between cationic N atoms and anionic AlO_4^- tetrahedra, we anticipate a disperse Al distribution between T1 and T3 for the AEI framework synthesized with OSDA7.

In conclusion, in accordance with the aim of this study, we have identified the structural features of different OSDAs for AEI synthesis that improve the probabilities of spreading Al through different T-site positions other than T1 obtaining an AEI catalyst different from the classically synthesized with OSDA1 and OSDA2. If the AEI synthesis was conducted with the remarkably mobile OSDA7, allowing the OSDA positive charge to round about all positions inside the cavity, an AEI catalyst with perhaps enhanced diffusion of short-chain olefins or NH_3-SCR species should be obtained because of all the different 8r windows of each cavity containing at least one acid site.

5.5. References

1. Vermeiren, W. & Gilson, J. P. Impact of zeolites on the petroleum and petrochemical industry. *Top. Catal.* **52**, 1131–1161 (2009).
2. Li, Y., Li, L. & Yu, J. Applications of Zeolites in Sustainable Chemistry. *Chem* **3**, 928–949 (2017).
3. Moliner, M., Rey, F. & Corma, A. Towards the rational design of efficient organic structure-directing agents for zeolite synthesis. *Angew. Chemie - Int. Ed.* **52**, 13880–13889 (2013).
4. Eliášová, P. *et al.* The ADOR mechanism for the synthesis of new zeolites. *Chem. Soc. Rev.* **44**, 7177–7206 (2015).
5. Gallego, E. M. *et al.* "Ab initio" synthesis of zeolites for preestablished catalytic reactions. *Science* **355**, 1051–1054 (2017).
6. Knott, B. C. *et al.* Consideration of the Aluminum Distribution in Zeolites in Theoretical and Experimental Catalysis Research. *ACS Catal.* **8**, 770–784 (2018).
7. Pophale, R., Daeyaert, F. & Deem, M. W. Computational prediction of chemically synthesizable organic structure directing agents for zeolites. *J. Mater. Chem. A* **1**, 6750–6760 (2013).
8. Burton, A. W.; Zones, S. I.; Elomari, S. The Chemistry of Phase Selectivity in the Synthesis of High-Silica Zeolites. *Curr. Opin. Colloid Interface Sci.* **10**, 211–219 (2005).
9. Shantz, D. F., Fild, C., Koller, H. & Lobo, R. F. Guest - Host Interactions in As-Made Al-ZSM-12: Implications for the Synthesis of Zeolite Catalysts. *J. Phys. Chem. B* **103**, 10858–10865 (1999).
10. Pinar, A. B., Gómez-Hortigüela, L., McCusker, L. B. & Pérez-Pariente, J. Controlling the aluminum distribution in the zeolite ferrierite via the organic structure directing agent. *Chem. Mater.* **25**, 3654–3661 (2013).
11. Shantz, D. F.; Lobo, R. F.; Fild, C. . Koller, H. Controlling the Distribution of Framework Aluminum in High-Silica Zeolites. *Stud. Surf. Sci. Catal.* **130**, 845– 850 (2000).
12. Sklenak, S. *et al.* Aluminium siting in the ZSM-5 framework by combination of high resolution 27Al NMR and DFT/MM calculations. *Phys. Chem. Chem. Phys.* **11**, 1237–1247 (2009).
13. Sklenak, S. *et al.* Aluminum siting in silicon-rich zeolite frameworks: A combined high-resolution 27Al NMR spectroscopy and quantum mechanics/molecular mechanics study of ZSM-5. *Angew. Chemie - Int. Ed.* **46**, 7286–7289 (2007).
14. Yokoi, T., Mochizuki, H., Namba, S., Kondo, J. N. & Tatsumi, T. Control of the Al Distribution in the Framework of ZSM-5 Zeolite and Its Evaluation by Solid-State NMR Technique and Catalytic Properties. *J. Phys. Chem. C* **119**, 15303–15315 (2015).
15. Schmidt, J. E.; Deem, M. W.; Lew, C.; Davis, T. M. Computationally-Guided Synthesis of the 8-Ring Zeolite AEI. *Top. Catal.* **58**, 410– 415

(2015).
16. Lewis, D. W., Willock, D. J., Catlow, C. R. A., Thomas, J. M. & Hutchings, G. J. De novo design of structure-directing agents for the synthesis of microporous solids. *Nature* vol. 382 604–607 (1996).
17. Sastre, G., Cantin, A., Diaz-Cabañas, M. J. & Corma, A. Searching organic structure directing agents for the synthesis of specific zeolitic structures: An experimentally tested computational study. *Chem. Mater.* **17**, 545–552 (2005).
18. Schmidt, J. E., Deem, M. W. & Davis, M. E. Synthesis of a specified, silica molecular sieve by using computationally predicted organic structure-directing agents. *Angew. Chemie - Int. Ed.* **53**, 8372–8374 (2014).
19. Bores, C., Auerbach, S. M. & Monson, P. A. Modeling the Role of Excluded Volume in Zeolite Structure Direction. *J. Phys. Chem. Lett.* **9**, 3703–3707 (2018).
20. Chien, S. C., Auerbach, S. M. & Monson, P. A. Modeling the self-assembly of silica-templated nanoparticles in the initial stages of zeolite formation. *Langmuir* **31**, 4940–4949 (2015).
21. Khan, M. N., Auerbach, S. M. & Monson, P. A. Lattice Monte Carlo Simulations in Search of Zeolite Analogues: Effects of Structure Directing Agents. *J. Phys. Chem. C* **119**, 28046–28054 (2015).
22. Daeyaert, F. & Deem, M. W. In silico design of chiral dimers to direct the synthesis of a chiral zeolite. *Mol. Phys.* **116**, 2836–2855 (2018).
23. Li, Y., Cao, H. & Yu, J. Toward a New Era of Designed Synthesis of Nanoporous Zeolitic Materials. *ACS Nano* **12**, 4096–4104 (2018).
24. Schmidt, J. E.; Deem, M. W.; Lew, C. Davis, T. M. Computationally-Guided Synthesis of the 8-Ring Zeolite AEI. *Top. Catal.* **58**, 410–415 (2015).
25. Daeyaert, F., Ye, F. & Deem, M. W. Machine-learning approach to the design of OSDAs for zeolite beta. *Proc. Natl. Acad. Sci. U. S. A.* **116**, 3413–3418 (2019).
26. Muraoka, K., Chaikittisilp, W. & Okubo, T. Multi-objective: De novo molecular design of organic structure-directing agents for zeolites using nature-inspired ant colony optimization. *Chem. Sci.* **11**, 8214–8223 (2020).
27. Perdew, J. P., Burke, K. & Ernzerhof, M. Generalized Gradient Approximation Made Simple. *Phys. Rev. Lett.* **77**, 3865–3868 (1996).
28. Perdew, J. P., Burke, K. & Ernzerhof, M. Generalized Gradient Approximation Made Simple [Phys. Rev. Lett. 77, 3865 (1996)]. *Phys. Rev. Lett.* **78**, 1396–1396 (1997).
29. Kresse, G. & Furthmüller, J. Efficient iterative schemes for *ab initio* total-energy calculations using a plane-wave basis set. *Phys. Rev. B* **54**, 11169–11186 (1996).
30. Blöchl, P. E. Projector augmented-wave method. *Phys. Rev. B* **50**, 17953–17979 (1994).

31. Grimme, S. Accurate description of van der Waals complexes by density functional theory including empirical corrections. *J. Comput. Chem.* **25**, 1463–1473 (2004).
32. Grimme, S., Antony, J., Ehrlich, S. & Krieg, H. A consistent and accurate ab initio parametrization of density functional dispersion correction (DFT-D) for the 94 elements H-Pu. *J. Chem. Phys.* **132**, (2010).
33. Bello, E. *et al.* NH3-SCR catalysts for heavy-duty diesel vehicles: Preparation of CHA-type zeolites with low-cost templates. *Appl. Catal. B Environ.* **303**, (2022).
34. Vandevondele, J. *et al.* Quickstep: Fast and accurate density functional calculations using a mixed Gaussian and plane waves approach. *Comput. Phys. Commun.* **167**, 103–128 (2005).
35. Hutter, J., Iannuzzi, M., Schiffmann, F. & Vandevondele, J. Cp2k: Atomistic simulations of condensed matter systems. *Wiley Interdiscip. Rev. Comput. Mol. Sci.* **4**, 15–25 (2014).
36. Nosé, S. Molecular Physics: An International Journal at the Interface Between Chemistry and Physics A molecular dynamics method for simulations in the canonical ensemble A molecular dynamics method for simulations in the canonical ensemblet. *An Int. J. Interface Between Chem. Phys. Mol. Phys.* **52**, 255–268 (1984).
37. Zhang, Y. & Yang, W. Comment on "generalized gradient approximation made simple". *Phys. Rev. Lett.* **80**, 890 (1998).
38. Yang, K., Zheng, J., Zhao, Y. & Truhlar, D. G. Tests of the RPBE, revPBE, τ -HCTHhyb, ωb97X-D, and MOHLYP density functional approximations and 29 others against representative databases for diverse bond energies and barrier heights in catalysis. *J. Chem. Phys.* **132**, (2010).
39. LIPPERT, G., HUTTER, J. & PARRINELLO, M. A hybrid Gaussian and plane wave density functional scheme. *Mol. Phys.* **92**, 477–487 (1997).
40. Lippert, G., Hutter, J. & Parrinello, M. The Gaussian and augmented-plane-wave density functional method for ab initio molecular dynamics simulations. *Theor. Chem. Acc.* **103**, 124–140 (1999).
41. VandeVondele, J. & Hutter, J. Gaussian basis sets for accurate calculations on molecular systems in gas and condensed phases. *J. Chem. Phys.* **127**, (2007).
42. Goedecker, S. & Teter, M. Separable dual-space Gaussian pseudopotentials. *Phys. Rev. B - Condens. Matter Mater. Phys.* **54**, 1703–1710 (1996).
43. C. Hartwigsen, S. Goedecker, J. H. Relativistic separable dual-space Gaussian pseudopotentials from H to Rn. *Phys. Rev. B* **58**, 3641–3662 (1998).
44. Fickel, D. W., D'Addio, E., Lauterbach, J. A. & Lobo, R. F. The ammonia selective catalytic reduction activity of copper-exchanged

small-pore zeolites. *Appl. Catal. B Environ.* **102**, 441–448 (2011).
45. Beale, A. M., Gao, F., Lezcano-Gonzalez, I., Peden, C. H. F. & Szanyi, J. Recent advances in automotive catalysis for NO x emission control by small-pore microporous materials. *Chem. Soc. Rev.* **44**, 7371–7405 (2015).
46. Kwak, J. H., Tonkyn, R. G., Kim, D. H., Szanyi, J. & Peden, C. H. F. Excellent activity and selectivity of Cu-SSZ-13 in the selective catalytic reduction of NOx with NH3. *J. Catal.* **275**, 187–190 (2010).
47. Bull, I. *et al.* Copper CHA zeolite catalysts. (2009).
48. Moliner-Marin, M. *et al.* Method and system for the purification of exhaust gas from an internal combustion engine. (2013).
49. Moliner, M., Franch, C., Palomares, E., Grill, M. & Corma, A. Cu-SSZ-39, an active and hydrothermally stable catalyst for the selective catalytic reduction of NOx. *Chem. Commun.* **48**, 8264–8266 (2012).
50. Stacey I. Zones. Zeolite SSZ-13 and Its Method of Preparation. *U S Patent* 4,544,538 (1985).
51. Zones, S. I. Conversion of faujasites to high-silica chabazite SSZ-13 in the presence of N,N,N-trimethyl-1-adamantammonium iodide. *J. Chem. Soc. Faraday Trans.* **87**, 3709 (1991).
52. Zones, S. I. Preparation of Molecular Sieves Using a Structure Directing Agent and An N, N, N-Triakyl Benzyl Quaternary Ammonium Cation. (2008).
53. Zones, S. I. Translating new materials discoveries in zeolite research to commercial manufacture. *Microporous Mesoporous Mater.* **144**, 1–8 (2011).
54. Jose, S. Synthesis of chabazite-containing molecular sieves and their use in the conversion of oxygenates to olefins US Patent 7670589 B2. **2**, (2010).
55. Wang, X. *et al.* Atom-economical synthesis of a high silica CHA zeolite using a solvent-free route. *Chem. Commun.* **51**, 16920–16923 (2015).
56. Chen, B., Xu, R., Zhang, R. & Liu, N. Economical Way to Synthesize SSZ-13 with Abundant Ion-Exchanged Cu + for an Extraordinary Performance in Selective Catalytic Reduction (SCR) of NO x by Ammonia. *Environ. Sci. Technol.* **48**, 13909–13916 (2014).
57. Wang, X., Zhang, R., Wang, H. & Wei, Y. Strategy on Effective Synthesis of SSZ-13 Zeolite Aiming at Outstanding Performances for NH3-SCR Process. *Catal. Surv. from Asia* **24**, 143–155 (2020).
58. Martín, N., Moliner, M. & Corma, A. High yield synthesis of high-silica chabazite by combining the role of zeolite precursors and tetraethylammonium: SCR of NOx. *Chem. Commun.* **51**, 9965–9968 (2015).
59. Shan, Y. *et al.* A comparative study of the activity and hydrothermal stability of Al-rich Cu-SSZ-39 and Cu-SSZ-13. *Appl. Catal. B Environ.* **264**, 118511 (2020).

60. Paolucci, C. *et al.* Catalysis in a Cage: Condition-Dependent Speciation and Dynamics of Exchanged Cu Cations in SSZ-13 Zeolites. *J. Am. Chem. Soc.* **138**, 6028–6048 (2016).
61. Zhao, Z. *et al.* Rare-earth ion exchanged Cu-SSZ-13 zeolite from organotemplate-free synthesis with enhanced hydrothermal stability in NH 3 -SCR of NO x. *Catal. Sci. Technol.* **9**, 241–251 (2019).
62. Gao, F. & Szanyi, J. On the hydrothermal stability of Cu/SSZ-13 SCR catalysts. *Appl. Catal. A Gen.* **560**, 185–194 (2018).
63. Ramsahye, N. A. & Bell, R. G. Cation mobility and the sorption of chloroform in zeolite NaY: Molecular dynamics study. *J. Phys. Chem. B* **109**, 4738–4747 (2005).
64. Feuerstein, M., Hunger, M., Engelhardt, G. & Amoureux, J. P. Characterisation of sodium cations in dehydrated zeolite NaX by 23Na NMR spectroscopy. *Solid State Nucl. Magn. Reson.* **7**, 95–103 (1996).
65. Jaramillo, E. & Auerbach, S. M. New Force Field for Na Cations in Faujasite-Type Zeolites. *J. Phys. Chem. B* **103**, 9589–9594 (1999).
66. Campbell, B. J. *et al.* The synthesis of the new zeolite, ERS-7, and the determination of its structure by simulated annealing and synchrotron X-ray powder diffraction. *Chem. Commun.* 1725–1726 (1998) doi:10.1039/a803572e.
67. Tuoto, C. V., Nagy, J. B. & Nastro, A. Synthesis and characterization of levyne type zeolite obtained from gels with different SiO2/Al2O3 ratios. *Stud. Surf. Sci. Catal.* **105**, 213–220 (1997).
68. Yamamoto, K. *et al.* Synthesis and structure analysis of RUB-50, an LEV-type aluminosilicate zeolite. *Microporous Mesoporous Mater.* **128**, 150–157 (2010).
69. Li, C. *et al.* Synthesis of reaction-adapted zeolites as methanol-to-olefins catalysts with mimics of reaction intermediates as organic structure-directing agents. *Nat. Catal.* **1**, 547–554 (2018).
70. Mahyuddin, M. H., Staykov, A., Shiota, Y., Miyanishi, M. & Yoshizawa, K. Roles of Zeolite Confinement and Cu-O-Cu Angle on the Direct Conversion of Methane to Methanol by [Cu2(μ-O)]2+-Exchanged AEI, CHA, AFX, and MFI Zeolites. *ACS Catal.* **7**, 3741–3751 (2017).
71. Liu, C., Bi, Y., Han, J., Guo, M. & Liu, Q. A Perspective on the Relationship Between Microstructure and Performance of Cu-Based Zeolites for the Selective Catalytic Reduction of NOx. *Catal. Surv. from Asia* **24**, 179–195 (2020).
72. Paul Wagner, † *et al.* Guest/Host Relationships in the Synthesis of the Novel Cage-Based Zeolites SSZ-35, SSZ-36, and SSZ-39. (1999) doi:10.1021/JA990722U.
73. Wagner, P. *et al.* Guest / Host Relationships in the Synthesis of the Novel Cage-Based. *J. Am. Chem. Soc.* **5**, 263–273 (2000).
74. Nakagawa, Y., Lee, G. S., Harris, T. V., Yuen, L. T. & Zones, S. I. Guest/host relationships in zeolite synthesis: Ring-substituted

piperidines and the remarkable adamantane mimicry by 1-azonio spiro [5.5] undecanes. *Microporous Mesoporous Mater.* **22**, 69–85 (1998).
75. Martínez-Franco, R., Li, Z., Martínez-Triguero, J., Moliner, M. & Corma, A. Improving the catalytic performance of SAPO-18 for the methanol-to-olefins (MTO) reaction by controlling the Si distribution and crystal size. *Catal. Sci. Technol.* **6**, 2796–2806 (2016).
76. Martín, N., Boruntea, C. R., Moliner, M. & Corma, A. Efficient synthesis of the Cu-SSZ-39 catalyst for DeNOx applications. *Chem. Commun.* **51**, 11030–11033 (2015).
77. Martín, N., Vennestrøm, P. N. R., Thøgersen, J. R., Moliner, M. & Corma, A. Iron-Containing SSZ-39 (AEI) Zeolite: An Active and Stable High-Temperature NH3-SCR Catalyst. *ChemCatChem* **9**, 1754–1757 (2017).
78. S.I. Zones, Y. Nakagawa, S.T. Evans, G. S. L. US Pat 5958370. (1999).
79. Dusselier, M. *et al.* Influence of organic structure directing agent isomer distribution on the synthesis of ssz-39. *Chem. Mater.* **27**, 2695–2702 (2015).
80. Wilt, J. & Us, M. A. (19) United States (12) Patent Application Publication quaternary ammonium hydroxide. **9**, (2018).

Conclusions

In this work, we have successfully applied computational chemistry methods to the study of two heterogeneous catalytic systems and to study the behaviour of different organic directing agents when being used for zeolite synthesis. Specific conclusions are given at the end of the corresponding chapters, however, some comments are dedicated here to more general conclusions.

In Chapter 3, we studied the methanol to olefins reaction catalysed by small-pore cage-like zeolites focusing on the hydrocarbon pool, confined polymehtylated aromatic species, mechanism and the different routes which it can proceed through. We started with a comprehensive gas phase study of all possible methylation steps for the hydrocarbon pool, concluding that its complete methylation producing heptamethylbenzenium cation is an energetically favoured process. We identified that only fully methylated hydrocarbon pool molecules are able to follow the paring route of the mechanism producing mainly propene, meanwhile partially methylated hydrocarbon pool molecules present a more feasible way towards the side-chain mechanism with a higher production of ethene associated. As a result of these findings, we proposed a theoretical parameter, $E_{int(7/5)}$, that is able to describe the confinement effect of different small-pore cage-like zeolite topologies over the key hydrocarbon pool intermediates, penta- and hepta-methylated benzenium cations, which is also able to discern between silica and AlPO compositions with the same framework. When $E_{int(7/5)}$ parameter showcases values close to 1 or higher for an specific zeolite, it indicates that fully methylated hydrocarbon pool is likely to form inside zeolite cavities enhancing the paring route of the mechanism, propene production, of that catalyst. On the other hand, when $E_{int(7/5)}$ presents low values, it indicates that zeolite confinement will force hydrocarbon pool methylation to stop earlier producing partially methylated species favouring the side chain route of the mechanism, thus enhancing ethene production. This parameter was validated by presenting good correlation with experimental selectivity ratio of propene and ethene ($C_3^=/C_2^=$) observed for six zeolite topologies. In the last part of Chapter 3, the limits of $E_{int(7/5)}$ parameter were tested with all existing small-pore cage-like zeolite topologies and compositions establishing its limits to zeolites that present an optimal confinement for the hydrocarbon pool molecules. Zeolites with small cavities do not allow the hydrocarbon pool to form and proceed through alkene cracking mechanism meanwhile zeolites with wider cavities present enough space for the hydrocarbon pool and other non-desired reactions to co-exist, though the distribution of the light olefins still correlates with the $E_{int(7/5)}$ parameter, the formation of alkanes and other products is significant.

The second reaction studied in this work is the diethylbenzene transalkylation with benzene, an industrial reaction used to produce ethylbenzene. This reaction also produces ethene and triethylbenzene as non-desired secondary products. The ethylbenzene production by transalkylation reaction can proceed through two different mechanistic routes, the alkyl-transfer mechanism, with a considerable yield of ethene, and the diaryl mediated pathway which neglects ethene production but increases the triethylbenzene yield because of the disproportionation reaction of two diethybenzene molecules. In Chapter 4 we started with a force field computational screening of 50 different zeolites that stabilize the key intermediates of the diaryl-mediated pathway in order to find candidate catalysts that enhance this mechanism and hinder the alkyl-transfer one reducing the non-desired production of ethene. From the results obtained in the initial screening we selected 12 candidates, BEA, BEC, BOG, CON, FAU, ITT, IWR, IWV, MOR, SEW, USI and UTL, whose structure presents at least one 12r channel within a bi-directional channel system, and reproduced the force field study with DFT methods, finding a good correlation between them and being able to discern between the stabilization of key transalkylation and disproportionation intermediates. From this set we selected relevant zeolites with channels arrangements 12x10, BOG and IWR, 12x12, BEC and IWV and 14x12, UTL, with MOR 12x8 being added as check for the mono-dimensional catalysts. Each candidate catalyst was studied in depth analysing the influence of their different topologies, channel system arrangement and intersection voids over all possible diaryl-mediated pathways for transalkylation and disproportionation, identifying the key mechanistic steps and the minimum energy path in each case. Comparing results for transalkylation and disproportionation we were able to select catalysts that enhance the production of ethylbenzene while decreasing triethylbenzene yield coming from the same mechanism as a non-desired product. The low production of ethene and the good correlation found between the theoretical data proposed about the diaryl mediated pathways and the experimental selectivity obtained for ITT, UTL, FAU, BEC, IWV, IWR, BOG and MOR catalysts validated our method for mechanistic selection inside zeolite channels.

The last topic studied was the synthesis of zeolites with organic structure directing agents, Chapter 5 presented two separated studies about CHA and AEI synthesis. The first part of Chapter 5 was dedicated to implement a theoretical methodology for zeolite synthesis using OSDA molecules that is able to distinguish small stabilization effects caused by slight structural differences between molecules that have an impact on the final structure synthesized. In this case, we focused on cheap commercially available alkylammonium cations with slight differences on their alkyl chain groups, as TEA, MTEA and DMDEA. We evaluated the host-guest interaction energies of different combinations of OSDAs and Na^+ cations with periodic DFT methods. From

this study we obtained important differences in interaction energies for the three OSDAs despite the small structural differences between these molecules. DMDEA was the worst stabilized molecule inside CHA cages meanwhile two TEA molecules could not be packed inside the same cage because of steric hindrance. MTEA showcased the best stabilization values when interacting with Na^+ and when two MTEA molecules were packed inside the same CHA cage suggesting a better directing effect for CHA framework. These theoretical results were confirmed when attempting CHA synthesis with each OSDA studied, MTEA crystallized in a perfect CHA material meanwhile TEA produced CHA samples with narrow GME intergrowths that formed larger cavities and DMDEA led to crystallization of a LEV framework.

The second part of Chapter 5 implemented a novel theoretical methodology for zeolite synthesis using OSDA molecules that is able to describe comprehensively the behavior of different OSDAs when confined by AEI cavities. We studied OSDA stability and mobility with static DFT and AIMD simulations, respectively, and the data obtained were correlated with the most probable Al T-site positions of the SSZ-39 framework for each OSDA. Using AIMD simulations, we identified substituted piperidinium based OSDAs (OSDA1 to OSDA4) and substituted azepanium based OSDAs (OSDA5 and OSDA6) as immobile molecules when confined inside AEI cages. The lack of mobility observed allowed us to predict their Al positioning by using static DFT optimizations in order to calculate their interaction energies. All results pointed towards T1 position as the most stable one for each OSDA with OSDA1, OSDA3 and OSDA6 showing close Eint values for T3, suggesting that a small portion of Al may be placed in T3 when using these OSDAs. Au contraire, OSDA7 based in a nonane ring without substituents at the ring presented high mobility being able to rotate freely inside the AEI cavity. From the averaged N-Al distances obtained from AIMD simulations we obtained almost equal distances for T1 and T3, therefore, thinking the N-Al distances as a measure for the strength interaction between cationic N atoms and anionic AlO_4^- tetrahedrons, we anticipate a disperse Al distribution between T1 and T3 for the AEI framework synthesized with OSDA7.

Summary

In this work, we have studied two heterogeneous catalytic reactions and we have compared the behaviour of different organic directing agents when being used for zeolite synthesis. Since the various topics of this thesis are not related to each other, a general introduction about the whole subject is not provided. Instead, each topic is introduced independently in its corresponding chapter. The structure of this manuscript is outlined below.

In Chapter 1, we provide an outline of the fundamental concepts of heterogeneous catalysis that will appear in the discussion of the results presented in chapters 3 to 5. A brief description of different zeolite topologies and their chemical compositions is also given. This chapter ends with some general comments on the motivation for this work.

Computational chemistry has been used as the fundamental tool during the whole work. Therefore, the theoretical models and methods on this subject are explained in Chapter 2. The first part sketches the fundamentals of quantum chemistry and specifically explains the Density Functional Theory that constitutes the basis of the computational methods applied. In this section, basic notions of the Hartree-Fock method serve as prologue for DFT after which more practical aspects are elucidated, such as the concept of Potential Energy Surface and the techniques for its exploration. The fundamentals of ab initio molecular dynamics are also introduced towards the end of this chapter. To conclude, a general description of the different zeolite models used for is given.

Chapter 3 presents the first results of this work corresponding to the methanol to olefins reaction catalysed by different small-pore cage-like zeolites. This reaction is a relevant process that produces short chain olefins such as ethene ($C_2^=$), propene ($C_3^=$) and butene ($C_4^=$) at industrial scale from biomass. The catalytic system comprises both the zeolite inorganic framework containing the Brønsted acid sites and the confined organic species, that form the hydrocarbon pool and produce light olefins by successive methylation and cracking steps. Our efforts are focused on understanding the nature of the hydrocarbon pool, a polymethylated benzene molecule, and its reaction mechanisms in order to be able to discern between them and identify the proper catalysts to enhance propene or ethene production based on each zeolite cavity topology. We have been able to identify the hydrocarbon pool methylation degree as the key factor to enhance paring route mechanism where propene is the predominant product, or side-chain mechanism, with ethene being the predominant product. This finding enables us to establish a relation between the stabilization of the two key intermediates and the experimental selectivity observed with a high degree of correlation.

In another matter, we also investigate the nature of diethylbenzene transalkylation reaction and the main results are presented in Chapter 4. In this chapter we present a new tool for the study of competing reactions catalyzed by zeolites. Using a fast computational screening with force fields for the key intermediates of the reaction and a detailed density functional theory mechanistic study we are able to recognize and quantify subtle differences in the stabilization of intermediates and transition states within similar microporous voids, thus approaching the level of molecular recognition of enzymes. With these tools we are able to select a zeolite catalyst that hinders alkyl-transfer mechanism reducing the production of non-desired ethene while enhancing the diaryl-mediated pathyways mechanism. Once we discard the non-desired mechanism, we are also able to hinder the diethylbenzene disproportionation, a non-desired route of the diaryl-mediated pathways that leads to triethylbenzene production, while favouring diethylbenzene transalkylation increasing the obtained yield of ethylbenzene. To close this chapter, the theoretical results are compared with experimental selectivities obtained for eight candidate zeolites obtaining a good correlation between theory and experiment.

Finally, during the las chapter we introduce new theoretical predictive tools based in DFT addressing two different topics of zeolite synthesis with OSDAs. On the one hand, in the first section of Chapter 5, we study the energetic affinity of commercially available alkylammonium cations with slight differences on their alkyl chain groups, as TEA, MTEA and DMDEA, for CHA synthesis and its effects on the quality of the material obtained. We evaluate the host-guest interaction energies of different combinations of OSDAs and Na^+ cations with periodic DFT methods being able to distinguish small stabilization effects caused by slight structural differences between molecules that have an impact on the final structure synthesized. The conclusions of this study point towards MTEA as the best alkylammonium OSDA for CHA synthesis. To end this section, our theoretical predictions are tested with experimental synthesis of CHA samples using the alkylammonium OSDAs studied. The structural analysis of the samples obtained confirm that the synthesis using MTEA crystallizes in a perfect CHA material meanwhile the sample prepared with TEA presents GME intergrowths and DMDEA produces a LEV framework.

On the other hand, we present a new theoretical methodology to address Al positioning prediction in SSZ-39 zeolite with the AEI framework. During the second section of Chapter 5, we identify the structural features of different OSDAs for AEI synthesis that improve the probabilities of spreading Al through different T-site positions other than T1 obtaining an AEI catalyst different from the classically synthesized with *N*,*N*-dimethyl-2,6-dimethylpiperidinium and *N*,*N*-dimethyl-3,5 dimethylpiperidinium. Studying

the stabilization and mobility of different OSDA candidates inside AEI cavities with DFT methods, we arrive to the conclusion that if the AEI synthesis was conducted with the remarkably mobile 9,9-dimethyl-9-azabicyclo [3.3.1]nonane-9-ium, allowing the OSDA positive charge to round about all positions inside the cavity, an AEI catalyst with an Al distribution dispersed between T1 and T3 positions should be obtained.

Resumen

En esta tesis hemos estudiado dos reacciones catalíticas heterogéneas y hemos comparado el comportamiento de diferentes agentes orgánicos directores de estructura utilizados en la síntesis de zeolitas. Dado que los distintos temas de esta tesis no están relacionados entre sí, no se ofrece una introducción general sobre toda la materia. En su lugar, cada tema se introduce de forma independiente en su capítulo correspondiente. A continuación se esboza la estructura de este manuscrito.

En el Capítulo 1 se ofrece una introducción a los conceptos fundamentales de la catálisis heterogénea que aparecerán en la discusión de los resultados presentados desde el Capítulo 3 al Capítulo 5. También se ofrece una breve descripción de las diferentes topologías de zeolitas existentes y de sus composiciones químicas. Este capítulo termina con algunos comentarios generales sobre la motivación de este trabajo.

Toda esta disertación ha utilizado la química computacional como herramienta fundamental para el análisis científico. Por ello, en el Capítulo 2 se explican los modelos y métodos teóricos sobre este tema. La primera parte del capítulo se centra en los fundamentos de la química cuántica y, en concreto, se explica con detalle la Teoría del Funcional de la Densidad la cual constituye la base de los métodos computacionales aplicados. En esta sección, las nociones básicas del método Hartree-Fock sirven de prólogo a la DFT, tras lo cual se dilucidan aspectos más prácticos, como el concepto de Superficie de Energía Potencial y las técnicas para su exploración. Los fundamentos de la dinámica molecular ab initio también se introducen hacia el final de este capítulo. Para concluir, se ofrece una descripción general de los distintos modelos de zeolitas utilizados.

El Capítulo 3 presenta los primeros resultados de este trabajo correspondientes a la reacción de metanol a olefinas catalizada por diferentes zeolitas con cavidades de poro pequeño. Esta reacción es un proceso industrial relevante que produce olefinas de cadena corta como eteno ($C_2^=$), propeno ($C_3^=$) y buteno ($C_4^=$) a escala industrial a partir de la biomasa. El sistema catalítico comprende tanto la estructura inorgánica de la zeolita que contiene los sitios ácidos Brønsted como las especies orgánicas confinadas, que forman la "*hydrocarbon pool*" y producen olefinas ligeras mediante pasos sucesivos de metilación y craqueo. Hemos centrado nuestros esfuerzos en comprender la naturaleza de la "*hydrocarbon pool*", una molécula de benceno polimetilada, y sus mecanismos de reacción para poder discernir entre ellos e identificar los catalizadores adecuados para mejorar la producción de propeno o eteno en función de la topología de cada cavidad zeolitica. Hemos podido identificar el grado de metilación de la "*hydrocarbon pool*" como el factor clave para potenciar el mecanismo de la ruta *"paring"*, donde el propeno es el producto mayoritario,

o el mecanismo de la ruta *"side-chain"*, siendo el eteno el producto predominante. Este hallazgo nos permite establecer una relación entre la estabilización de los dos intermedios clave y la selectividad experimental observada con un alto grado de correlación.

Por otra parte, también investigamos la naturaleza de la reacción de transalquilación del dietilbenceno y los principales resultados obtenidos se presentan en el Capítulo 4. En este capítulo presentamos una nueva herramienta para el estudio de reacciones competitivas catalizadas por zeolitas. Utilizando un cribado computacional rápido con *"force fields"* para los intermedios clave de la reacción y un detallado estudio mecanístico usando la teoría del funcional de la densidad somos capaces de reconocer y cuantificar sutiles diferencias en la estabilización de intermedios y estados de transición dentro de huecos microporosos similares, aproximándonos así al nivel de reconocimiento molecular de las enzimas. Con estas herramientas somos capaces de seleccionar como catalizador una zeolita que obstaculice el mecanismo *"alkyl-transfer"* reduciendo la producción de eteno no deseado y potenciando al mismo tiempo el mecanismo *"diaryl-mediated pathway"*. Una vez descartado el mecanismo no deseado, también somos capaces de obstaculizar la desproporción de dietilbenceno, una ruta no deseada del mecanismo *"diaryl-mediated pathway"* que conduce a la producción de trietilbenceno, mientras que se favorece la transalquilación de dietilbenceno aumentando el rendimiento obtenido de etilbenceno. Para cerrar este capítulo, se comparan los resultados teóricos con las selectividades experimentales obtenidas para ocho zeolitas candidatas obteniéndose una buena correlación entre teoría y experimento.

Finalmente, durante el último capítulo introducimos nuevas herramientas predictivas basadas en la teoria del funcional de la densidad que abordan dos temas diferentes sobre la síntesis de zeolitas con agentes directores de estructura. Por un lado, en la primera sección del Capítulo 5, estudiamos la afinidad energética de cationes alquilamonio comercialmente disponibles con ligeras diferencias en sus grupos alquilo, TEA, MTEA y DMDEA, para la síntesis de CHA y sus efectos sobre la calidad del material obtenido. Evaluamos las energías de interacción entre la zeolita y el catión de diferentes combinaciones de agentes directores y cationes Na^+ con métodos DFT periódicos pudiendo distinguir pequeños efectos de estabilización causados por ligeras diferencias estructurales entre moléculas que repercuten en la estructura final sintetizada. Las conclusiones de este estudio apuntan hacia MTEA como el mejor agente director de estructura para la síntesis de CHA. Para finalizar esta sección, nuestras predicciones teóricas se comprueban con la síntesis experimental de muestras de CHA utilizando los agentes directores de estructura estudiados. El análisis estructural de las muestras obtenidas confirma que la síntesis realizada con MTEA cristaliza en un material CHA perfecto,

mientras que la muestra obtenida usando TEA presenta intercrecimientos GME y DMDEA produce una estructura tipo LEV.

Como final de esta tesis, presentamos una nueva metodología teórica para abordar la predicción del posicionamiento del Al en la zeolita SSZ-39 con estructura AEI. Durante la segunda sección del Capítulo 5, identificamos las características estructurales de diferentes agentes directores de estructura para la síntesis de AEI que mejoran las probabilidades de dispersión del Al en posiciones tetraédricas distintas de T1 obteniendo un catalizador AEI diferente de los sintetizados clásicamente con N,N-dimetil-2,6-dimetilpiperidinio y N,N-dimetil-3,5 dimetilpiperidinio. Estudiando la estabilización y movilidad de diferentes agentes directores de estructura candidatos dentro de las cavidades AEI con métodos DFT, llegamos a la conclusión de que si la síntesis AEI se realiza con el notablemente móvil 9,9-dimetil-9-azabiciclo [3.3.1]nonano-9-io, permitiendo que la carga positiva ronde todas las posiciones dentro de la cavidad, debería obtenerse un catalizador AEI con una distribución de Al dispersa entre de las posiciones T1 y T3.

Resum

En aquesta tesi hem estudiat dues reaccions catalítiques heterogènies i hem comparat el comportament de diferents agents orgànics directors d'estructura utilitzats a la síntesi de zeolites. Atès que els diferents temes d'aquesta tesi no estan relacionats entre si, no s'ofereix una introducció general sobre tota la matèria. En canvi, cada tema s'introdueix de manera independent al seu capítol corresponent. A continuació s'esbossa l'estructura d'aquest manuscrit.

En el Capítol 1 s'ofereix una introducció als conceptes fonamentals de la catàlisi heterogènia que apareixeran en la discussió dels resultats presentats des del Capítol 3 al Capítol 5. També s'ofereix una breu descripció de les diferents topologies de zeolites existents i de les seves composicions químiques. Aquest capítol acaba amb alguns comentaris generals sobre la motivació d'aquest treball.

Tota aquesta dissertació utilitza la química computacional com eina fonamental per a l'anàlisi científica. Per això, en el Capítol 2 s'expliquen els models i mètodes teòrics sobre aquest tema. La primera part del capítol es centra en els fonaments de la química quàntica i, en concret, s'explica amb detall la Teoria del Funcional de la Densitat la qual constitueix la base dels mètodes computacionals aplicats. En aquesta secció, les nocions bàsiques del mètode Hartree-Fock serveixen de pròleg a la DFT, tot seguit es diluciden aspectes més pràctics, com el concepte de Superfície d'Energia Potencial i les tècniques per a la seva exploració. Els fonaments de la dinàmica molecular ab initio també s'introdueixen cap al final d'aquest capítol. Per a concloure, s'ofereix una descripció general dels diferents models de zeolites utilitzats.

El Capítol 3 presenta els primers resultats d'aquest treball corresponents a la reacció de metanol a olefines catalitzada per diferents zeolites amb cavitats de porus petit. Aquesta reacció és un procés industrial rellevant que produeix olefines de cadena curta com etè ($C_2^=$), propè ($C_3^=$) i butè ($C_4^=$) a escala industrial a partir de la biomassa. El sistema catalític comprèn tant l'estructura inorgànica de la zeolita que conté els llocs àcids Brønsted com les espècies orgàniques confinades, que formen la "hydrocarbon pool" i produeixen olefines lleugeres mitjançant passos successius de metilació i craqueig. Hem centrat els nostres esforços en comprendre la naturalesa de la *"hydrocarbon pool"*, una molècula de benzè polimetilada, i els seus mecanismes de reacció per a poder discernir entre ells i identificar els catalitzadors adequats per millorar la producció de propè o etè en funció de la topologia de cada cavitat zeolitica. Hem pogut identificar el grau de metilació de la *"hydrocarbon pool"* com el factor clau per a potenciar el mecanisme de la ruta *"paring"*, on el propè és el producte majoritari, o el mecanisme de la ruta *"side-chain"*, sent l'etè el producte predominant. Aquesta troballa ens

permet establir una relació entre l'estabilització dels dos intermedis clau i la selectivitat experimental observada amb un alt grau de correlació.

D'altra banda, també investiguem la naturalesa de la reacció de transalquilació del dietilbenzè i els principals resultats obtinguts es presenten en el Capítol 4. En aquest capítol presentem una nova eina per a l'estudi de reaccions competitives catalitzades per zeolites. Utilitzant un cribratge computacional ràpid amb *"force fields"* per als intermedis clau de la reacció i un detallat estudi mecanístic amb la teoria del funcional de la densitat som capaços de reconèixer i quantificar subtils diferències en l'estabilització d'intermedis i estats de transició dins de buits microporosos similars, aproximant-nos així al nivell de reconeixement molecular dels enzims. Amb aquestes eines som capaces de seleccionar una zeolita com a catalitzador que obstaculitzi el mecanisme *"alkyl-transfer"* reduint la producció de eteno no desitjat i potenciant al mateix temps el mecanisme *"diaryl-mediated pathway"*. Una vegada descartat el mecanisme no desitjat, també som capaços d'obstaculitzar la desproporció de dietilbenzè, una ruta no desitjada del mecanisme *"diaryl-mediated pathway"* que condueix a la producció de trietilbenzè, mentre que s'afavoreix la transalquilació de dietilbenzè augmentant el rendiment obtingut d'etilbenzè. Per tancar aquest capítol, es comparen els resultats teòrics amb les selectivitats experimentals obtingudes per a huit zeolites candidates obtenint una bona correlació entre teoria i experiment.

Finalment, durant l'últim capítol introduïm noves eines predictives basades en la teoria del funcional de la densitat que aborden dos temes diferents sobre la síntesi de zeolites amb agents directors d'estructura. D'una banda, en la primera secció del Capítol 5, estudiem l'afinitat energètica de cations alquilamoni comercialment disponibles amb lleugeres diferències als seus grups alquil, TEA, MTEA i DMDEA, per a la síntesi de CHA i els seus efectes sobre la qualitat del material obtingut. Avaluem les energies d'interacció entre la zeolita i el catió entre diferents combinacions d'agents directors i cations Na^+ amb mètodes DFT periòdics podent distingir petits efectes d'estabilització causats per lleugeres diferències estructurals entre molècules que repercuteixen en l'estructura final sintetitzada. Les conclusions d'aquest estudi apunten cap a MTEA com el millor agent director d'estructura per a la síntesi de CHA. Per finalitzar aquesta secció, les nostres prediccions teòriques es comproven amb la síntesi experimental de mostres de CHA utilitzant els agents directors d'estructura estudiats. L'anàlisi estructural de les mostres obtingudes confirma que la síntesi realitzada amb MTEA cristal·litza en un material CHA perfecte, mentre que la mostra obtinguda amb TEA presenta intercreixements GME i DMDEA produeix una estructura tipus LEV.

Per finalitzar aquesta tesi, presentem una nova metodologia teòrica per a abordar la predicció del posicionament de l'Al a la zeolita SSZ-39 amb estructura AEI. Durant la segona secció del Capítol 5, identifiquem les característiques estructurals de diferents agents directors d'estructura per a la síntesi d'AEI que milloren les probabilitats de propagació de l'Al a través de posicions tetrahedriques diferents de T1 obtenint un catalitzador AEI diferent dels sintetitzats clàssicament amb N,N-dimetil-2,6-dimetilpiperidini i N,N-dimetil-3,5 dimetilpiperidini. Estudiant l'estabilització i mobilitat de diferents agents directors d'estructura candidats dins de les cavitats AEI amb mètodes DFT, arribem a la conclusió que si la síntesi AEI es realitza amb el notablement mòbil 9,9-dimetil-9-azabicicle [3.3.1] nonà-9-i, permetent que la càrrega positiva rondi totes les posicions dins de la cavitat, hauria d'obtenir-se un catalitzador AEI amb una distribució d'Al dispersa entre de les posicions T1 i T3.

APPENDIX I

Catalyst Models Employed

This appendix to the work describes all unit cells used for all the materials studied in this thesis. Catalysts are listed alphabetically by the code name given by IZA database.

All unit cells presented were obtained after full relaxation of the experimental lattice parameters using calculations based on DFT and performed with PBE exchange-correlation functional within the GGA as implemented in the VASP code. The valence density was expanded in a plane wave basis set with a kinetic energy cutoff of 600 eV, and the effect of the core electrons in the valence density was taken into account by means of the PAW formalism. Integration in the reciprocal space was carried out at the Γ k-point of the Brillouin zone. Dispersion corrections to the energies were evaluated using the DFT−D Grimme's method. To achieve full relaxation of lattice parameters, atomic positions, cell shape and cell volume were considered as degrees of freedom for calculations. For more detailed explanation about methodology, refer to Chapter 2 of this work.

Materials that were studied with silica and AlPO chemical compositions have the different unit cell parameters obtained specified on their section.

AI.1. AEI

AI.2. AFX

AI.3. BEA

AI.4. BEC

AI.5. BOG

AI.6. CHA

AI.7. CON

AI.8. DDR

AI.9. ERI

AI.10. FAU

AI.11. ITE

AI.12. ITT

AI.13. IWR

AI.14. IWV

AI.15. KFI

AI.16. LEV

AI.17. LTA

AI.18. MOR

AI.19. RHO

AI.20. RTH

AI.21. SAV

AI.22. SEW

AI.23. UFI

AI.24. USI

AI.25. UTL

AI.1. AEI

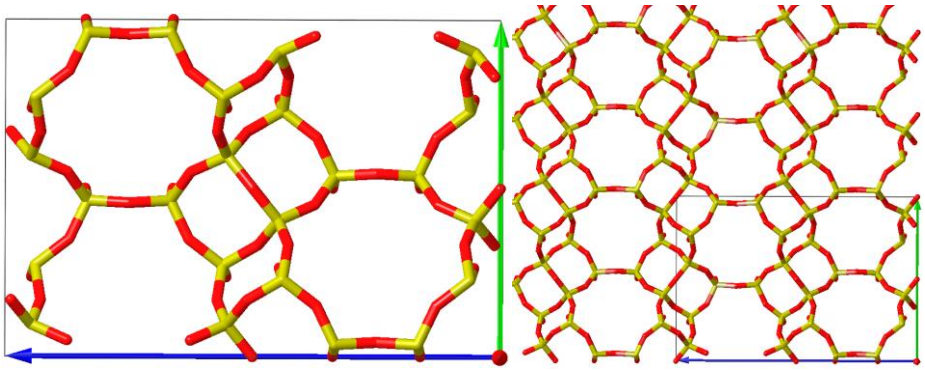

Figure AI.1. AEI unit cell (left). AEI structure expanded (right).

For AEI framework, SSZ-39 structure was modeled by means of an orthorhombic unit cell (Cmcm) with lattice parameters a = 13.752, b = 12.646 Å, c = 18.482 Å, $\alpha = \beta = \gamma = 90°$, containing 48 Si atoms and 96 O atoms. Meanwhile, AlPO-18 structure presented an orthorhombic unit cell with lattice parameters a = 13.976, b = 12.715 Å, c = 18.641 Å, $\alpha = \beta = \gamma = 90°$, containing 24 Al atoms, 24 P atoms and 96 O atoms.

AI.2. AFX

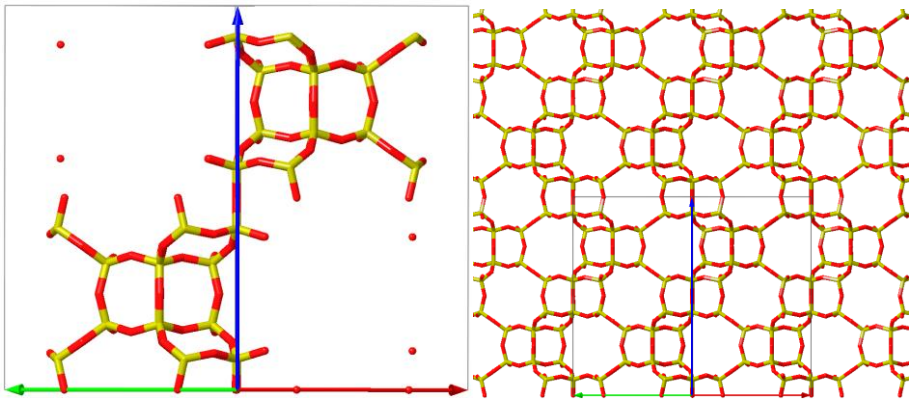

Figure AI.2. AFX unit cell (left). AFX structure expanded (right).

For AFX framework, hypothetical pure silica structure was modeled by means of a hexagonal unit cell (P6(3)/mmc) with lattice parameters a = b = 13.709 Å, c = 19.809 Å, $\alpha = \beta = 90°$, and $\gamma = 120°$, containing 48 Si atoms and 96 O atoms. Meanwhile, AlPO-56 structure presented a hexagonal unit cell with lattice parameters a = b = 13.756 Å, c = 15.756 Å, $\alpha = \beta = 90°$, and $\gamma = 120°$, containing 24 Al atoms, 24 P atoms and 96 O atoms.

AI.3. *BEA

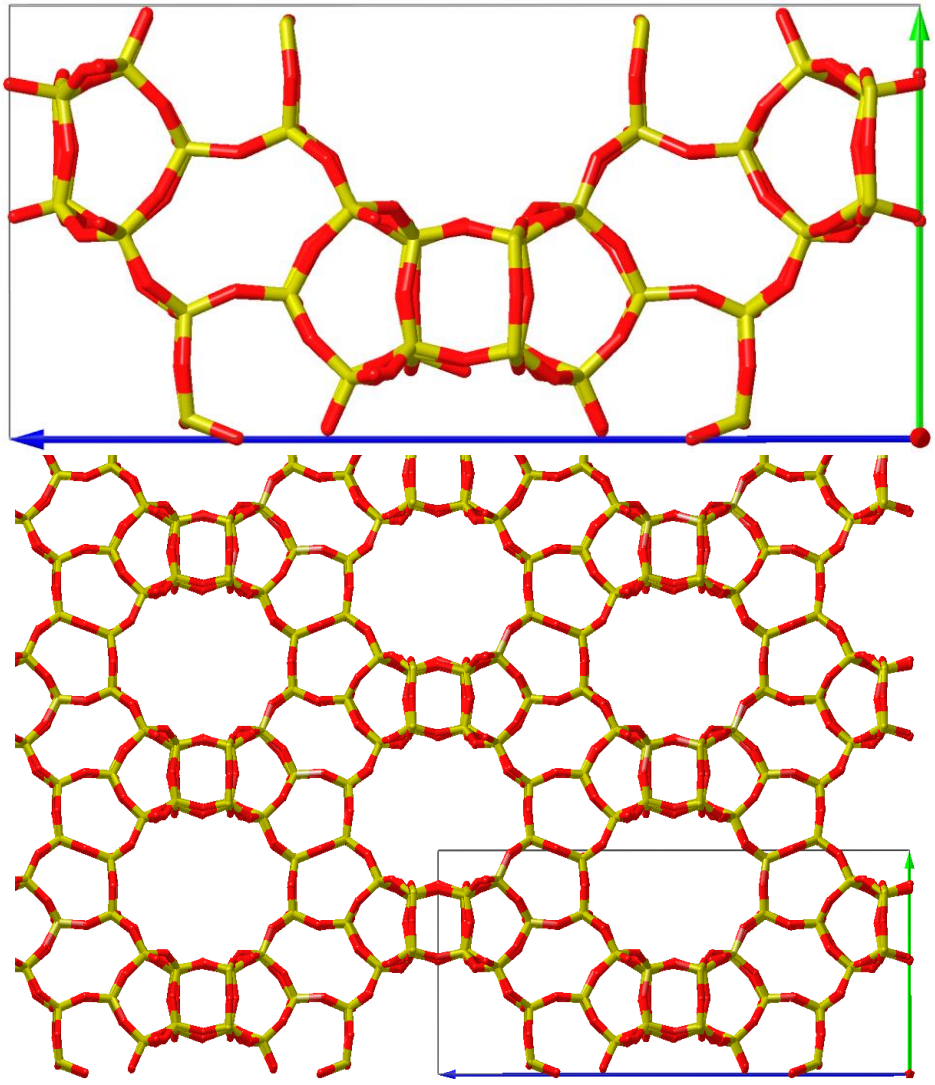

Figure AI.3. *BEA unit cell (top). *BEA structure expanded (bottom).

For Beta Polymorph A framework, *BEA structure was modeled by means of a tetragonal unit cell (P4122) with lattice parameters a = b = 12.593 Å, c = 26.495 Å, $\alpha = \beta = \gamma = 90°$, containing 64 Si atoms and 128 O atoms.

AI.4. BEC

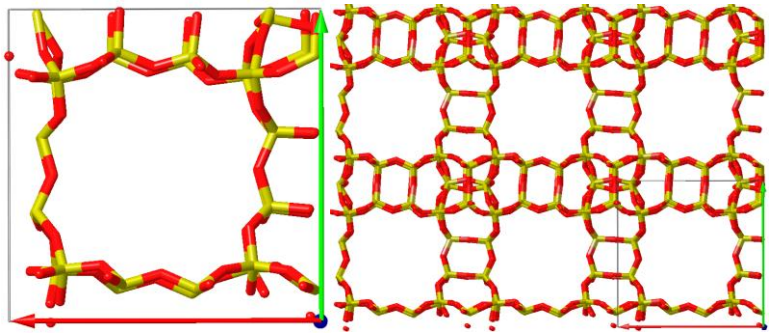

Figure AI.4. BEC unit cell (left). BEC structure expanded (right).

For Beta Polymorph C (BEC) framework, FOS-5 structure was modeled by means of a tetragonal unit cell (P42/mmc) with lattice parameters a = 12.935, b = 12.822 Å, c = 12.676 Å, α = β = γ = 90°, containing 32 Si atoms and 64 O atoms.

AI.5.1. BOG-Full

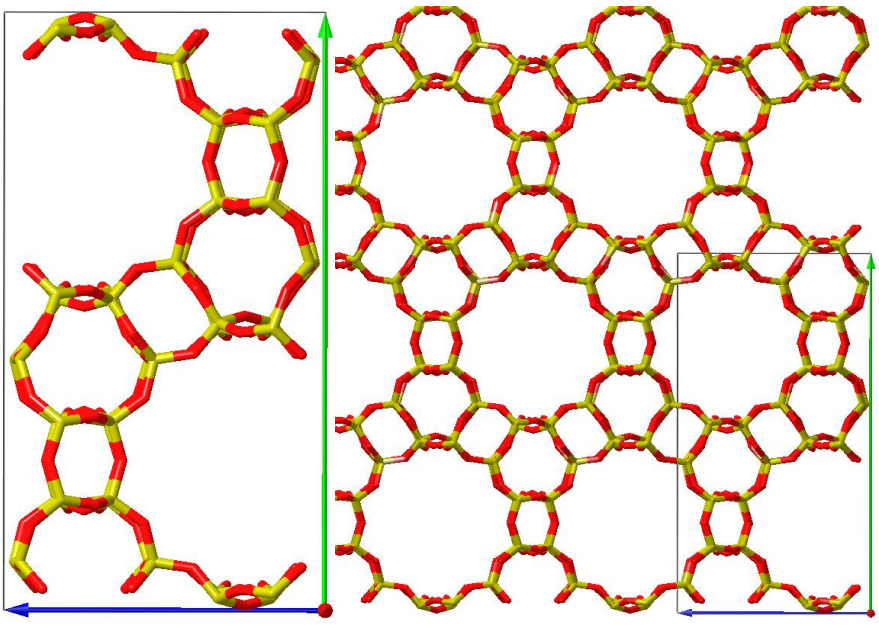

Figure AI.5. BOG unit cell (left). BOG structure expanded (right).

For Boggsite (BOG) framework, its structure was modeled by means of an orthorhombic unit cell (Imma) with lattice parameters a = 20.104, b = 23.659 Å, c = 12.799 Å, α = β = γ = 90°, containing 96 Si atoms and 192 O atoms.

AI.5.2. BOG-Reduced

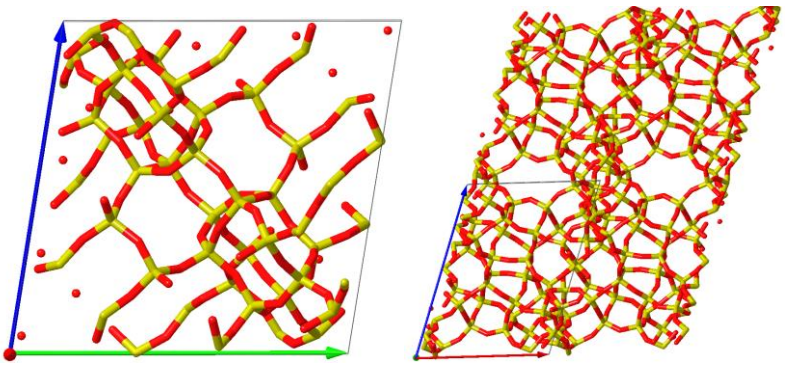

Figure AI.6. BOG primitive reduced unit cell (left). BOG structure expanded (right).

For certain simulations of Boggsite (BOG) framework in Chapter 4 we used a smaller primitive reduced unit cell obtained through the transformation matrix: c,-1/2a-1/2b+1/2c,1/2a-1/2b+1/2c that has a 2 times smaller volume. This unit cell presents triclinic symmetry (P1) and lattice parameters a = 12.812 Å, b = c = 16.791 Å, α = 74, β = 68 and γ = 68 containing 48 Si atoms and 96 O atoms.

AI.6. CHA

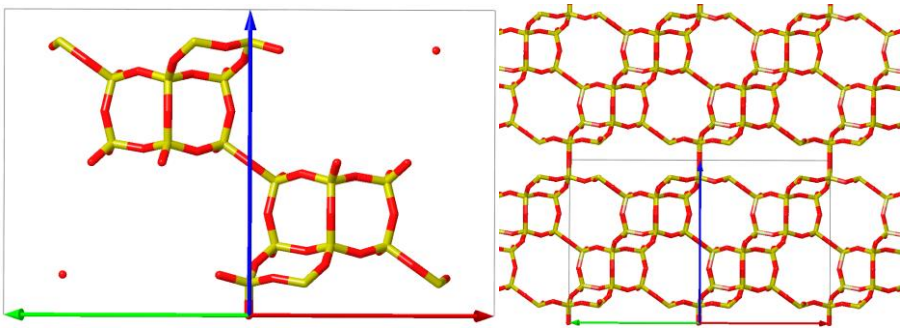

Figure AI.7. CHA unit cell (left). CHA structure expanded (right).

For chabazite (CHA) framework, SSZ-13 structure was modeled by means of a trigonal unit cell (R3-M) with lattice parameters a = b = 13.746 Å, c = 15.013 Å, α = β = 90°, and γ = 120°, containing 36 Si atoms and 72 O atoms. Meanwhile, AlPO-34 structure presented a hexagonal unit cell with lattice parameters a = b = 13.803 Å, c = 15.075 Å, α = β = 90°, and γ = 120°, containing 18 Al atoms, 18 P atoms and 72 O atoms.

AI.7. CON

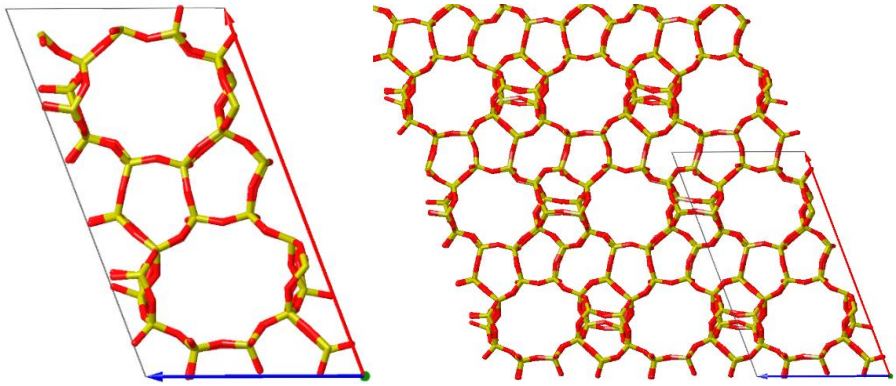

Figure AI.8. CON unit cell (left). CON structure expanded (right).

For CON framework, CIT-1 structure was modeled by means of a monoclinic unit cell (C12/m1) with lattice parameters a = 22.459, b = 13.613 Å, c = 12.409 Å, $\alpha = \gamma = 90°$, $\beta = 70°$, containing 56 Si atoms and 112 O atoms.

AI.8. DDR

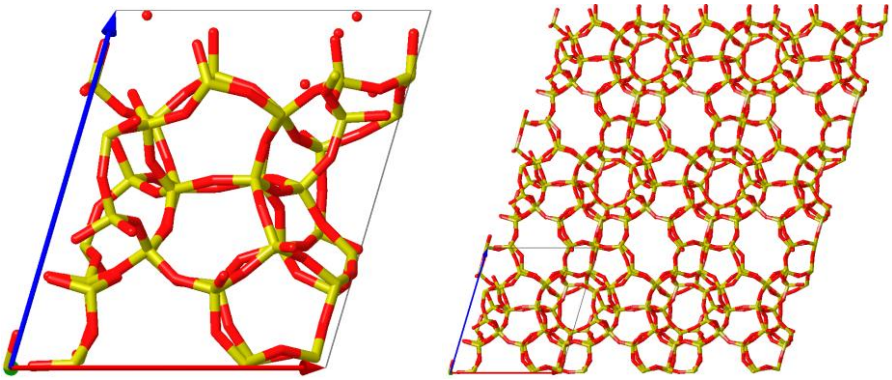

Figure AI.9. DDR primitive reduced unit cell (left). DDR structure expanded (right).

For deca-dodecasil 3R (DDR) framework, ZSM-58 structure was modeled by means of a trigonal (R3-M) unit cell with lattice parameters a = b = 13.795 Å, c = 40.750 Å, $\alpha = \beta = 90°$, and $\gamma = 120°$, containing 120 Si atoms and 240 O atoms. For simulations of the DDR structure in Chapter 3 we have used a smaller primitive reduced unit cell obtained through the transformation matrix: a,-b,1/3a-1/3b-1/3c that has a 3 times smaller volume. This unit cell presents triclinic symmetry (P1) and lattice parameters a = b = 13.882 Å, c= 15.816 Å, $\alpha = \beta = 64$, and $\gamma = 77.742$ containing 40 Si atoms and 80 O atoms.

AI.9. ERI

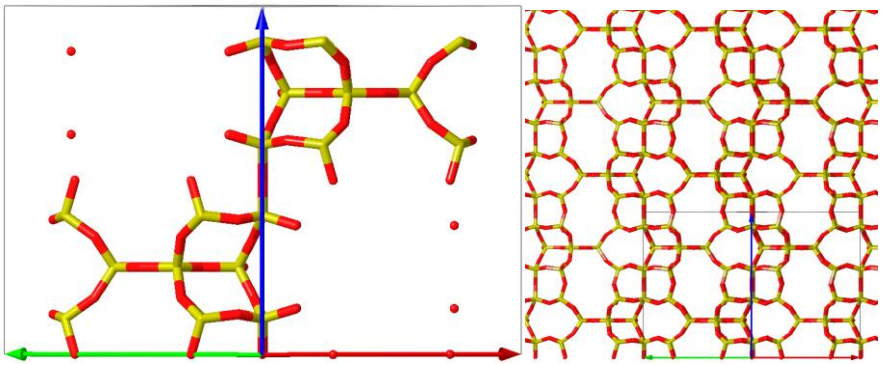

Figure AI.10. ERI unit cell (left). ERI structure expanded (right).

For erionite (ERI) framework, SSZ-16 structure was modeled by means of a hexagonal unit cell (P6(3)/mmc) with lattice parameters a = b = 13.121 Å, c = 15.230 Å, α = β = 90°, and γ = 120°, containing 36 Si atoms and 72 O atoms. Meanwhile, AlPO-17 structure presented a hexagonal unit cell with lattice parameters a = b = 13.279 Å, c = 15.406 Å, α = β = 90°, and γ = 120°, containing 18 Al atoms, 18 P atoms and 72 O atoms.

AI.10. FAU

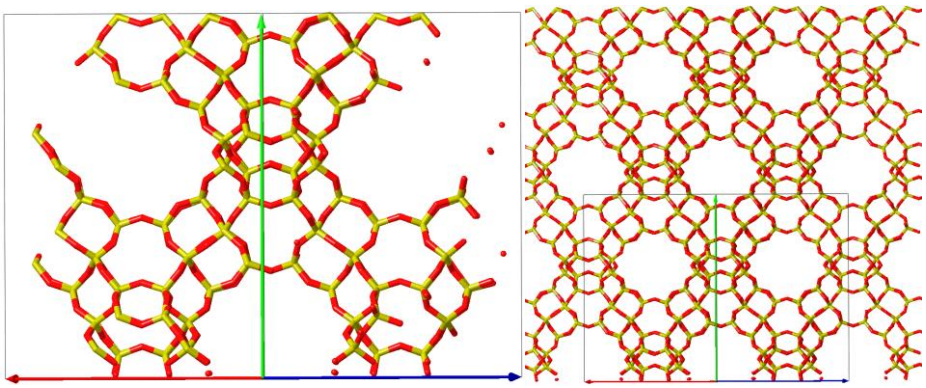

Figure AI.11. FAU unit cell (left). FAU structure expanded (right).

For Faujasite framework, FAU structure was modeled by means of a cubic unit cell Fd-3m with lattice parameters a = b = c = 24.345 Å, α = β = γ = 90°, containing 192 Si atoms and 384 O atoms.

AI.11. ITE

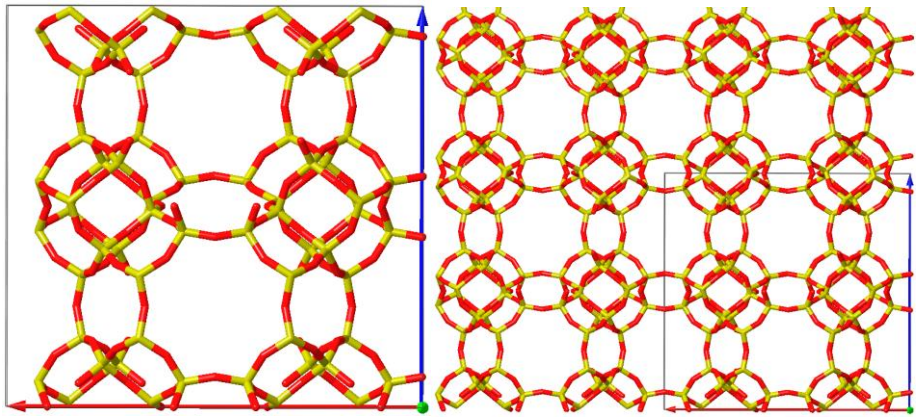

Figure AI.12. ITE unit cell (left). ITE structure expanded (right).

For ITE framework, ITQ-3 structure was modeled by means of a monoclinic unit cell (Cmcm) with lattice parameters a = 20.585, b = 9.757 Å, c = 19.860 Å, $\alpha = \beta = \gamma = 90°$, containing 64 Si atoms and 128 O atoms.

AI.12. ITT

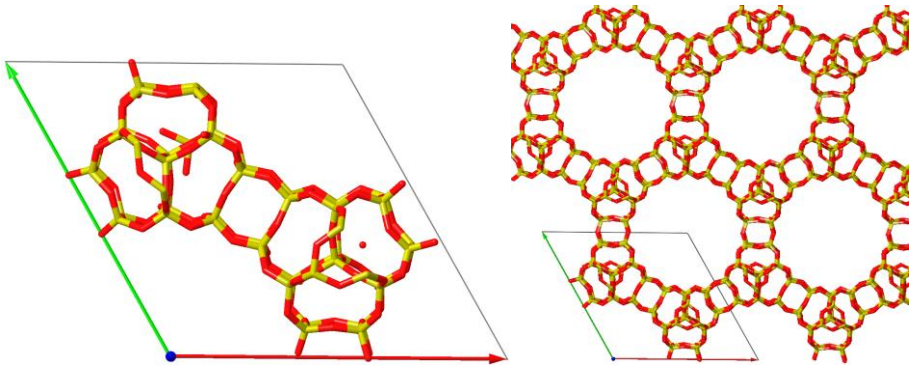

Figure AI.13. ITT unit cell (left). ITT structure expanded (right).

For ITT framework, ITQ-33 structure was modeled by means of a hexagonal unit cell (P6/mmm) with lattice parameters a = 19.039, b = 19.027 Å, c = 11.512 Å, $\alpha = \beta = 90°$, $\gamma = 120°$, containing 46 Si atoms and 92 O atoms.

AI.13. IWR

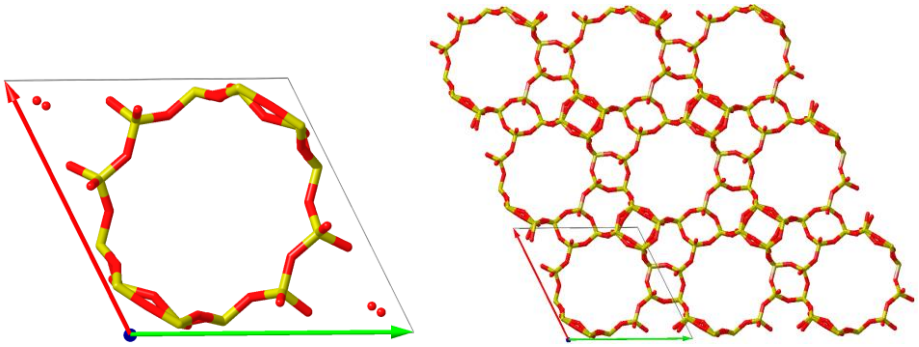

Figure AI.14. IWR unit cell (left). IWR structure expanded (right).

For IWR framework, ITQ-24 structure was modeled by means of an orthorhombic unit cell (Cmmm) with lattice parameters a = 21.112, b = 13.570 Å, c = 12.608 Å, $\alpha = \beta = \gamma = 90°$, containing 56 Si atoms and 112 O atoms.

AI.14. IWV

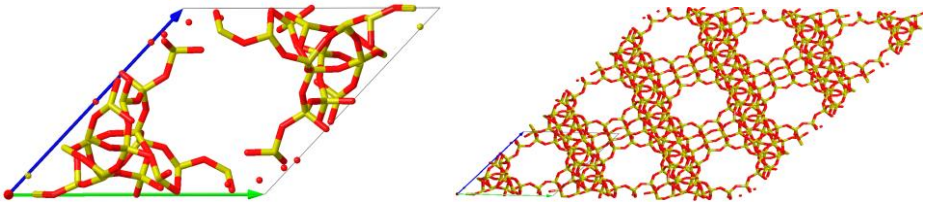

Figure AI.15. IWV primitive reduced unit cell (left). IWV structure expanded (right).

For IWV framework, ITQ-27 structure presents a conventional orthorhombic unit cell (Fmmm) with lattice parameters a = 27.826 Å, b = 26.081 Å, and c = 13.944 Å, containing 152 Si atoms and 304 O atoms. For simulations of IWV structure in Chapter 4 we used a smaller primitive reduced unit cell obtained through the transformation matrix: -c,-1/2b-1/2c,-1/2a-1/2c that has a 4 times smaller volume. This unit cell presents triclinic symmetry (P1) and lattice parameters a = 14.544 Å, b = 15.784 Å, c= 19.055 Å, $\alpha = 48$, $\beta = 54$ and $\gamma = 78$ containing 38 Si atoms and 76 O atoms.

AI.15. KFI

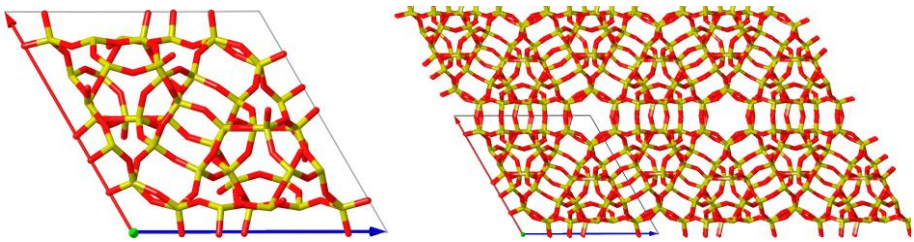

Figure AI.16. KFI primitive reduced unit cell (left). KFI structure expanded (right).

For KFI framework, ZK-5 structure presents a cubic unit cell (Im-3m) with lattice parameters a = b = c = 18.578 Å α = β = γ = 109, containing 96 Si atoms and 192 O atoms. For simulations the KFI structure in Chapter 3 we used a smaller primitive reduced unit cell obtained through the transformation matrix: 1/2a-1/2b+1/2c,-1/2a-1/2b-1/2c,1/2a+1/2b-1/2c that has a 2 times smaller volume. This unit cell presents cubic symmetry (Im-3m) and lattice parameters a = b = c = 16.153 Å α = β = γ = 109 containing 48 Si atoms and 96 O atoms. Meanwhile, STA-14 structure presented a cubic unit cell with lattice parameters a = b = c = 16.075 Å, α = β = γ = 110°, containing 24 Al atoms, 24 P atoms and 96 O atoms.

AI.16. LEV

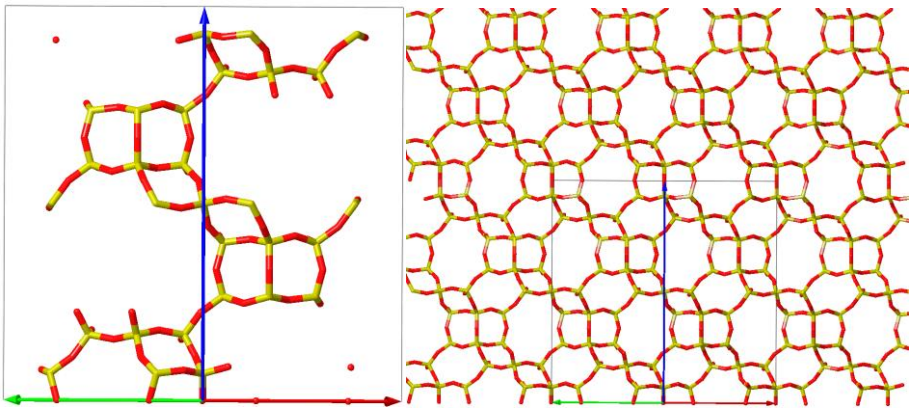

Figure AI.17. LEV unit cell (left). LEV structure expanded (right).

For levyne (LEV) framework, SSZ-17 structure was modeled by means of a trigonal unit cell (R3-M) with lattice parameters a = b = 13.202 Å, c = 22.682 Å, α = β = 90°, and γ = 120°, containing 54 Si and 108 O atoms. Meanwhile, AlPO-35 structure presented a hexagonal unit cell with lattice parameters a = b = 13.310 Å, c = 23.033 Å, α = β = 90°, and γ = 120°, containing 27 Al atoms, 27 P and 108 O atoms.

AI.17. LTA

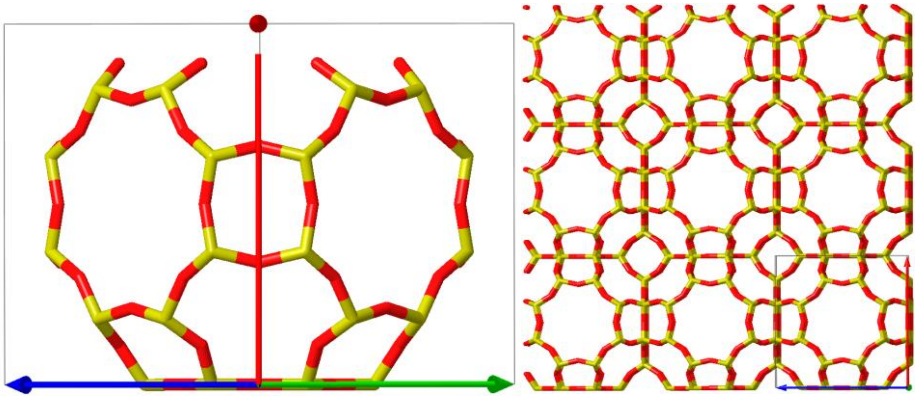

Figure AI.18. LTA unit cell (left). LTA structure expanded (right).

For LTA framework, zeolite A structure was modeled by means of a cubic unit cell (Pm-3m) with lattice parameters a = b = c = 11.968 Å, α = β = γ = 90°, containing 24 Si atoms and 48 O atoms. Meanwhile, AlPO-42 structure presented a monoclinic unit cell with lattice parameters a = b = c = 11.984 Å, α = β = γ = 90°, containing 24 Al atoms, 24 P atoms and 96 O atoms.

AI.18. MOR

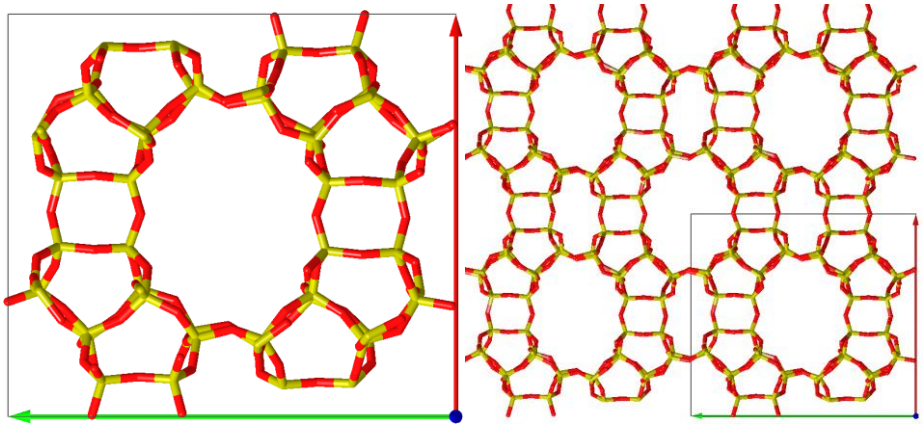

Figure AI.19. MOR unit cell (left). MOR structure expanded (right).

For Mordenite framework, MOR structure was modeled by means of an orthorhombic unit cell (Cmcm) with lattice parameters a = 18.023, b = 20.042, and c = 7.432 Å, α = β = γ = 90.0°, containing 48 Si atoms and 96 O atoms. To model the MOR structure in Chapter 4 we used a larger 1 × 1 × 2 supercell containing 96 Si atoms and 192 O atoms, with lattice parameters a = 18.023, b = 20.042, and c = 14.864 Å, α = β = γ = 90°.

AI.19. RHO

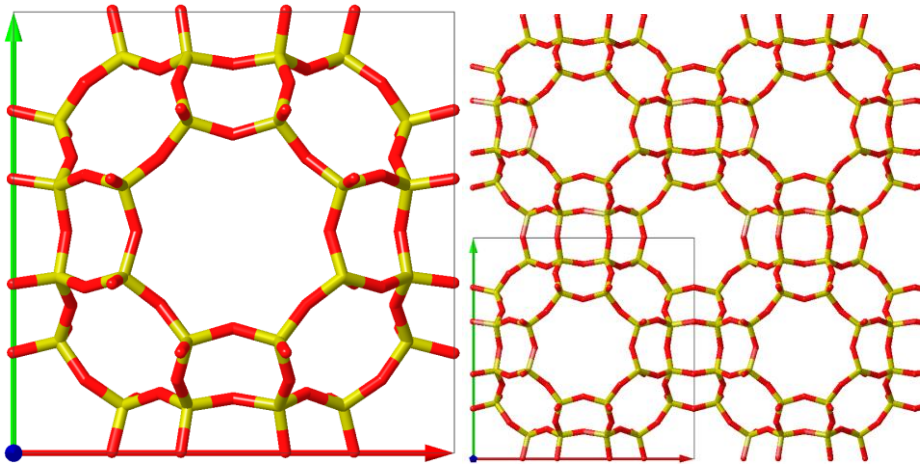

Figure AI.20. RHO unit cell (left). RHO structure expanded (right).

For Rho framework, RHO structure was modeled by means of a cubic unit cell (Im-3m) with lattice parameters a = b = c = 14.985 Å, α = β = γ = 90°, containing 48 Si atoms and 96 O atoms. Meanwhile, DNL-6 structure presented a monoclinic unit cell with lattice parameters a = b = c = 15.188 Å, α = β = γ = 90°, containing 24 Al atoms, 24 P atoms and 96 O atoms.

AI.20. RTH

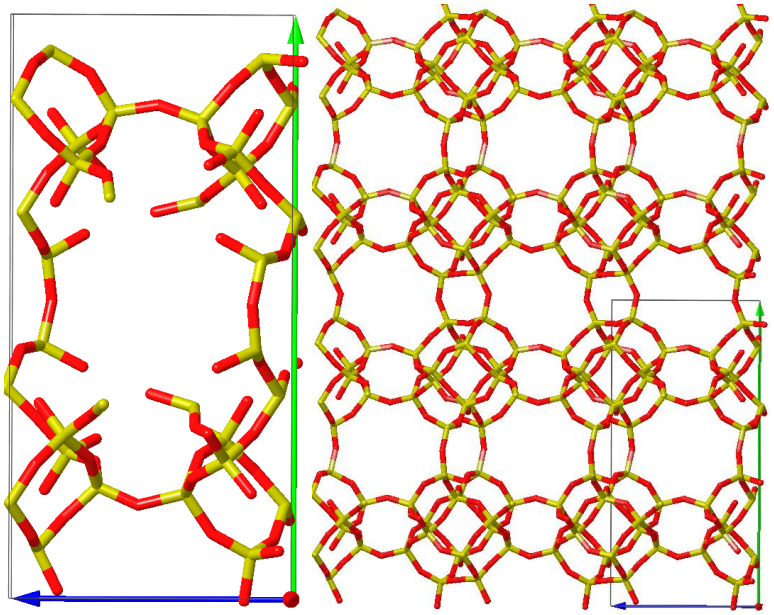

Figure AI.21. RTH unit cell (left). RTH structure expanded (right).

For RTH framework, RUB-13 structure was modeled by means of a monoclinic unit cell (C12/m1) with lattice parameters a = 9.785, b = 20.602 Å, c = 10.018 Å, $\alpha = \gamma = 90°$, $\beta = 97$, containing 32 Si atoms and 64 O atoms.

AI.21. SAV

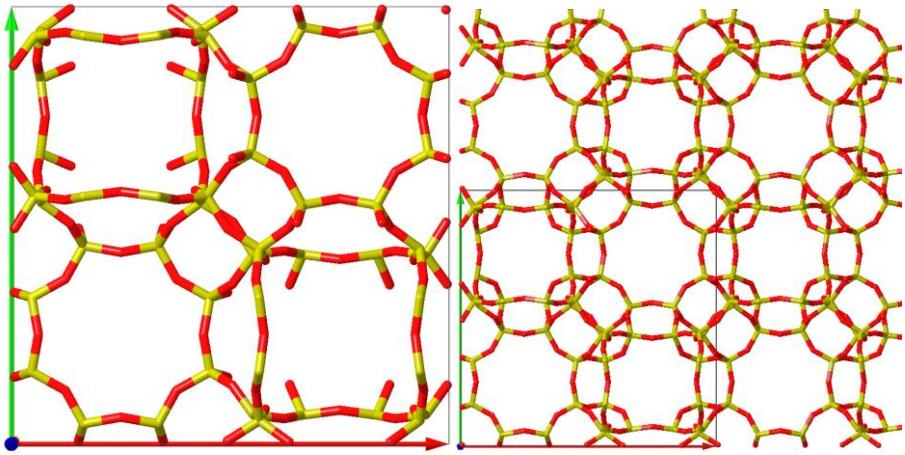

Figure AI.22. SAV unit cell (left). SAV structure expanded (right).

For SAV framework, its hypothetical pure silica structure was modeled by means of a tetragonal unit cell (P4/nmm) with lattice parameters a = b = 18.539, c = 9.385 Å, α = β = γ = 90°, containing 48 Si atoms and 96 O atoms. Meanwhile, STA-7 structure presented a presented a monoclinic unit cell with lattice parameters a = b = 18.612, c = 9.455 Å, α = β = γ = 90°, containing 24 Al atoms, 24 P atoms and 96 O atoms.

AI.22. SEW

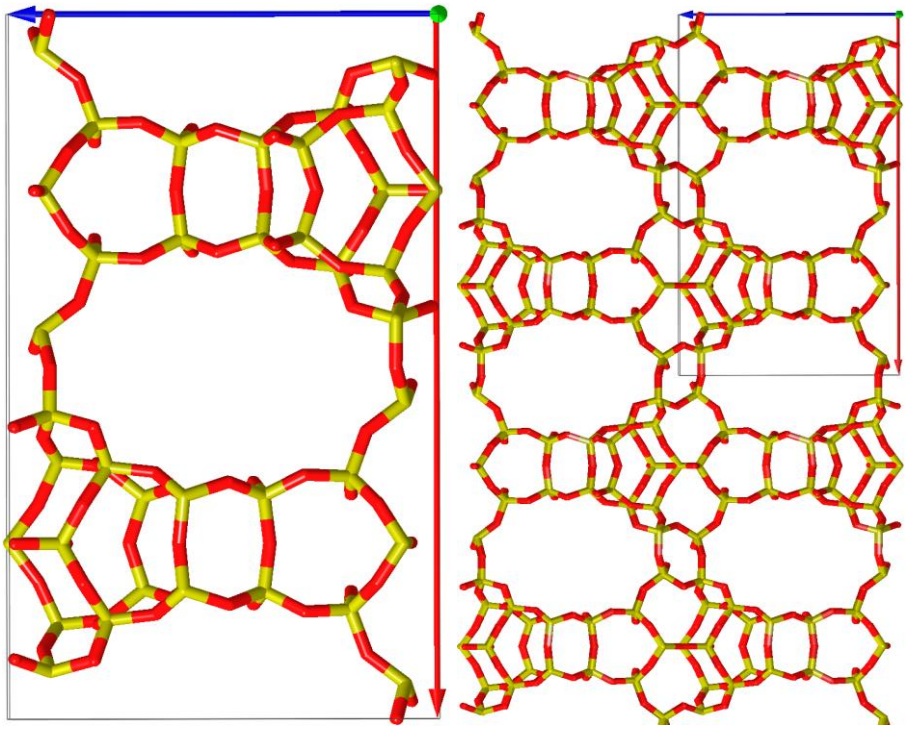

Figure AI.23. SEW unit cell (left). SEW structure expanded (right).

For SEW framework, SSZ-82 structure was modeled by means of an orthorhombic unit cell (Pmmn) with lattice parameters a = 24.217, b = 11.422 Å, c = 14.518 Å, $\alpha = \beta = \gamma = 90°$, containing 132 Si atoms and 264 O atoms.

AI.23. UFI

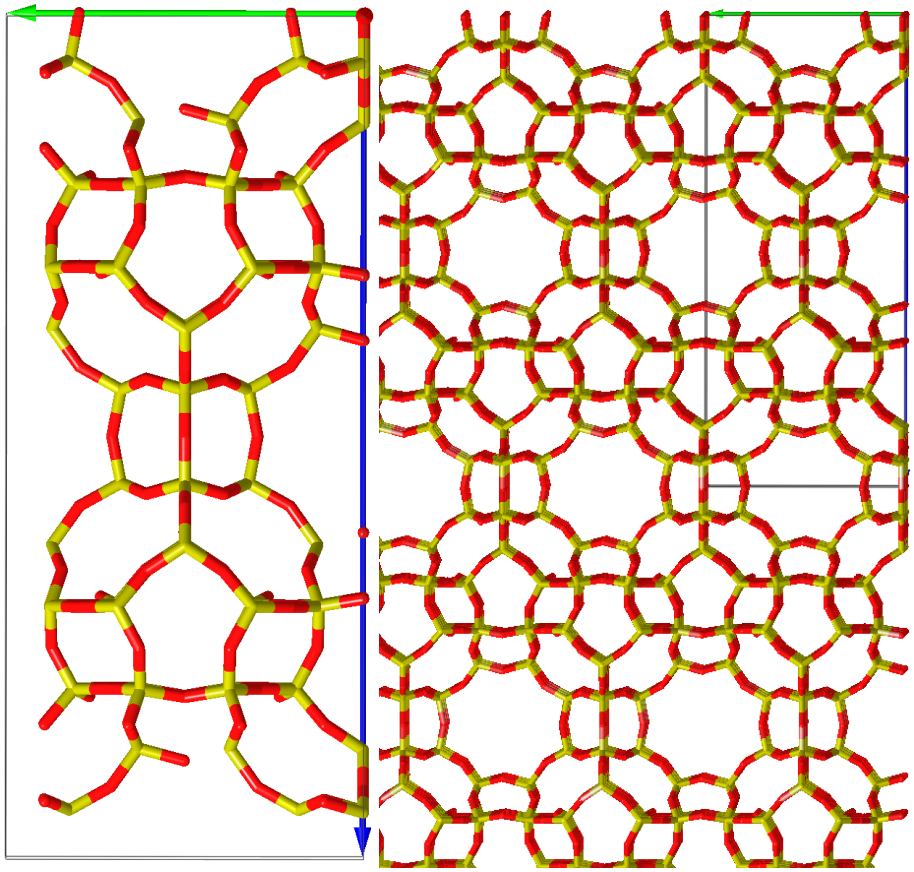

Figure AI.24. UFI unit cell (top). UFI structure expanded (bottom).

For UFI framework, UZM-5 structure was modeled by means of a tetragonal (I4/mmm) unit cell with lattice parameters a = b = 12.631, and c = 27.912 Å, α = β = γ = 90°, and contains 64 Si atoms and 128 O atoms.

AI.24. USI

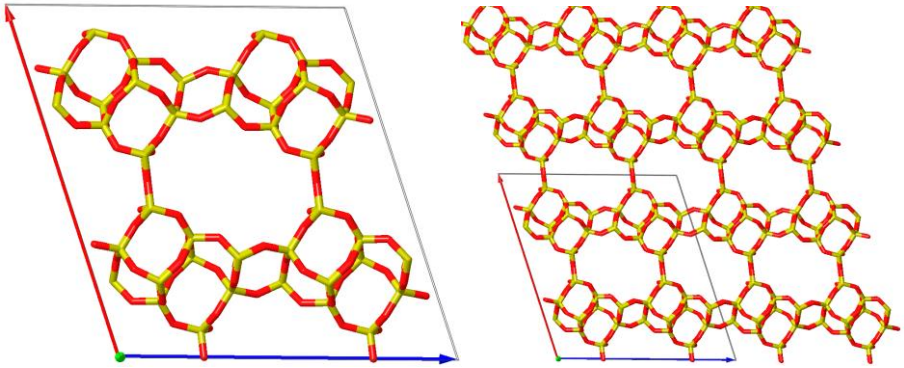

Figure AI.25. USI unit cell (top). USI structure expanded (bottom).

For USI framework, IM-6 structure was modeled by means of a monoclinic unit cell (C12/m1) with lattice parameters a = 21.209, b = 13.001 Å, c = 19.338 Å, $\alpha = \gamma = 90°$, $\beta = 109°$ containing 40 Si atoms and 80 O atoms.

AI.25.1. UTL-Full

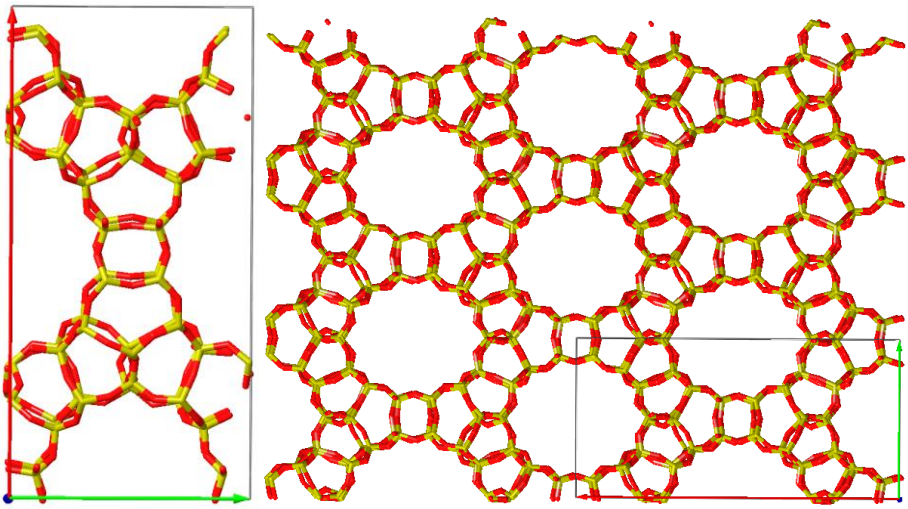

Figure AI.26. UTL unit cell (top). UTL structure expanded (bottom).

For UTL framework, IM-15 structure was modeled by means of a monoclinic (C2/m) unit cell with lattice parameters a = 29.160, b = 14.098, and c = 12.180 Å, $\alpha = \gamma = 90°$, $\beta = 105°$ and contains 76 Si atoms and 152 O atoms.

AI.25.2. UTL-Reduced

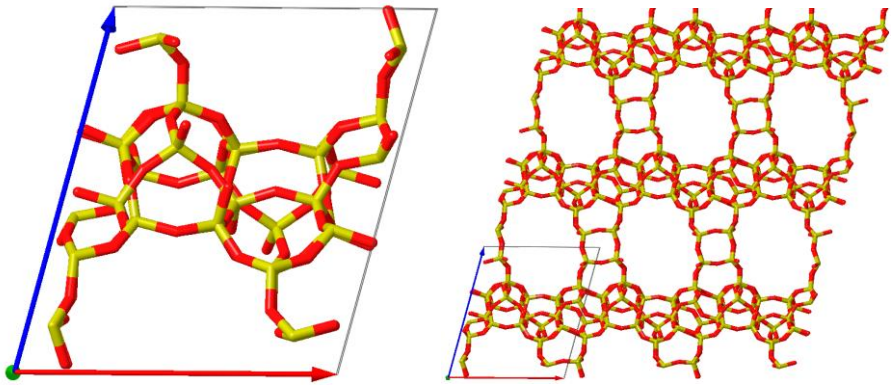

Figure AI.27. UTL primitive reduced unit cell (top). UTL structure expanded (bottom).

For certain simulations of UTL (IM-15) framework in Chapter 4, we used a smaller primitive reduced unit cell obtained through the transformation matrix: c,b,-1/2a+1/2b that has a 2 times smaller volume. This unit cell presents triclinic symmetry (P1) and lattice parameters a = 12.446 Å, b = 13.962 Å, c= 16.199 Å, $\alpha = 65°$, $\beta = 76°$ and $\gamma = 90°$ containing 38 Si atoms and 76 O atoms

Summary Table

Zeolite	Framework	Armstrong (Å)			Degree (°)			Cell Type	T
		a	b	c	α	β	γ		
AEI	SSZ - 39	13.752	12.646	18.482	90	90	90	Ortho	48
	AlPO - 18	13.976	12.715	18.641					
AFX	silica	13.709	13.709	19.809	90	90	120	Hexa	48
	AlPO - 56	13.756	13.756	20.297					
Polymorph A	*BEA	12.593	12.593	26.495	90	90	90	Tetra	64
BEC	FOS - 5	12.935	12.822	12.676	90	90	90	Tetra	32
Boggsite	BOG-F	20.104	23.659	12.799	90	90	90	Ortho	96
	BOG-R	12.812	16.791	16.791	74	68	68	Triclinic	48
CHA	SSZ - 17	13.746	13.746	15.013	90	90	120	Trigonal	36
	AlPO - 34	13.803	13.803	15.075					
CON	CIT - 1	22.459	13.613	12.409	90	70	90	Mono	56
DDR	ZSM - 58	13.882	13.882	15.816	64	64	60	Triclinic	40
ERI	SSZ-16	13.121	13.121	15.230	90	90	120	Hexa	36
	AlPO - 17	13.279	13.279	15.406					
Faujasite	FAU	24.345	24.345	24.345	90	90	90	Cubic	192
ITE	ITQ - 3	20.585	9.757	19.860	90	90	90	Ortho	64
ITT	ITQ - 33	19.039	19.027	11.512	90	90	120	Hexa	46
IWR	ITQ - 24	21.112	13.570	12.608	90	90	90	Ortho	56
IWV	ITQ - 27	14.544	15.784	19.055	48	54	78	Triclinic	38
KFI	ZK - 5	16.153	16.153	16.153	109	109	109	Cubic	48
	STA - 14	16.075	16.075	16.075	110	110	110		
LEV	SSZ - 17	13.202	13.202	22.682	90	90	120	Trigonal	54
	AlPO - 35	13.310	13.310	23.033	90	90	120		
LTA	Zeolite A	11.968	11.968	11.968	90	90	90	Cubic	24
	AlPO - 42	11.984	11.984	11.984					
Mordenite	MOR	18.023	20.042	7.432	90	90	90	Ortho	48
Rho	RHO	14.985	14.985	14.985	90	90	90	Cubic	48
	DNL - 6	15.188	15.188	15.188					
RTH	RUB - 13	9.785	20.602	10.018	90	97	90	Mono	32
SAV	silica	18.539	18.539	9.385	90	90	90	Tetra	48
	STA-7	18.612	18.612	9.455					
SEW	SSZ - 82	24.217	11.422	14.518	90	90	90	Ortho	132
UFI	UZM-5	12.631	12.631	27.912	90	90	90	Tetra	139
USI	IM - 6	21.209	13.001	19.338	90	109	90	Mono	40
UTL-F	IM - 15	29.160	14.098	12.180	90	105	90	Mono	76
UTL-R	IM - 15	12.446	13.962	16.199	65	76	90	Triclinic	38

*Ortho: Orthorhombic, Hexa: Hexagonal, Tetra: Tetragonal, Mono = Monoclinic.

APPENDIX II

Experimental Details for Chapter 4 (pages 178 to 257)

This appendix to the work describes the experimental details corresponding to Chapter 4 "*Design and synthesis of zeolite catalysts for selectively manipulating mechanistic pathways".*

AII.1. Synthesis of zeolites

FAU. The commercially-available CBV720 sample from Zeolyst has been employed.

MOR. 13.4 g of tetraethylammonium bromide (TEABr, Sigma-Aldrich), 8.76 g sodium aluminate (Carlo Erba) and 10.2 g NaOH were dissolved in 344.3 g deionized water. To this solution, 84.8 g fumed silica was added and kept under mechanic stirring until a viscous white gel is obtained. Then, this gel is transferred to a Teflon-lined autoclave and heated under rotation at 150°C for 7 days. The solid product was then separated by filtration, washed with abundant water and then dried in air at 60°C.

In order to prepare the proton form of zeolite for catalysis, the zeolite was first calcined in air in a muffle under 550°C for 6 hours. After cooled to room temperature, the solid was mixed with 1 mol/L ammonium nitrate solution at a liquid/solid mass ratio of 50 without heating for 16 hours. Finally, the solid was separated by filtration and dried in air at 60°C and, then, calcined again in air at 500°C for 3 hours.

ITQ-15 (UTL). A typical synthesis gel was first prepared by dissolving 0.418 g of GeO_2 in 13.38 g of the solution of the ammonium salt derivate from L-Proline in hydroxide form with a concentration of to 0.9 mol OH^-/kg.[1] Then, 3.0 g of Ludox (40 wt.% of colloidal silica suspension in H_2O) was added, and the mixture was maintained under stirring until achieving the following gel molar composition:

$$0.833\ SiO_2 : 0.167\ GeO_2 : 0.5\ OSDA(OH) : 10\ H_2O$$

where OSDA(OH) is the ammonium salt derivate from L-Proline in hydroxide form. Additionally, 0.06 g of ITQ-15 crystals was added as seeds. The synthesis gel was autoclaved at 175°C for 4 days under stirring conditions. The resultant solids were recovered by filtration, washed with distilled water, dried at 100°C for 12 hours and characterized.

The incorporation of aluminum was carried out by a post-synthesis treatment.[1] The as-prepared ITQ-15 was calcined at 580°C for 3 h. Then, 0.5 g of calcined ITQ-15 zeolite was mixed with 7.5 ml of an $Al(NO_3)_3$ solution (5wt. % in H_2O) in an autoclave, which was placed at 150°C for 18 h. The Al-containing ITQ-15 was recovered by filtration, washed with distilled water, dried at 100°C for 12 hours and characterized.

ITQ-24 (IWR). The synthesis of ITQ-24 zeolite was carried out using hexamethonium dihydroxide as OSDA. The gel composition was:

$$SiO_2 : 0.04\ B_2O_3 : 0.25\ OSDA(OH)_2 : 0.5\ NH_4F : 3\ H_2O,$$

where $OSDA(OH)_2$ is hexamethonium dihydroxide. In a typical synthesis, 0.307 g of boric acid (H_3BO_3) was dissolved in 0.94 g of a hexamethonium hydroxide solution (18.84% wt.). Then, 0.458g of Ludox AS-40 and 0.558 g of NH_4F solution (10% wt.) were added. The mixture was stirred to evaporate water until the desired gel composition was reached. Finally, 0.045 g of ITQ-24 zeolite were added as seed and the gel was heated for 14 days at 175°C.

The incorporation of aluminum was done by a post-synthesis treatment.[1] The as-prepared ITQ-24 was calcined at 580°C for 3 h. Then, 0.5 g of calcined ITQ-24 zeolite was mixed with 7.5 ml of an $Al(NO_3)_3$ solution (2wt. % in H_2O) in an autoclave, which was placed at 150°C for 18 h. The Al-containing ITQ-24 was recovered by filtration, washed with distilled water, dried at 100°C for 12 hours and characterized.

ITQ-47 (BOG). This zeolite was synthesized following a procedure reported by Simancas et al. using P1-phosphazene as OSDA.[2] The composition of the synthesis gel was:

$$0.833\ TEOS : 0.167\ GeO_2 : 0.0370\ H_3BO_3 : 0.40\ P1\text{-phosphazene} : 10\ H_2O$$

Where TEOS is tetraethylorthosilicate (TEOS, Sigma-Aldrich, 98%wt). This gel was transferred to Teflon lined stainless-steel autoclaves and heated to 150°C under tumbling for 25 days. The resulting solid was filtered and washed exhaustively with distilled water. The resulting solid was dried at 100°C overnight and, afterwards, calcined in air at 550°C. The calcined material was treated with an 8 wt.% $Al(NO_3)_3$ aqueous solution, and the resulting mixture was transferred to a Teflon lined stainless-steel autoclave and kept heated to 140°C under tumbling for 3 days. The resulting solid was filtered and exhaustively washed with distilled water, dried at 100°C for 12 hours, and, finally, calcined in air at 550°C.

ITQ-17 (BEC). The Al-containing form of the polymorph C of Beta zeolite (Al-BEC) was synthesized following a procedure recently reported by Liang et al. using a dicationic piperidinium derivative OSDA (BPMPOH).[3] The silica source is a colloidal silica suspension (Ludox AS-40), germanium source is germanium oxide (99.999%, Merck), aluminum source is aluminum hydroxide (65% Al_2O_3, Sigma-Aldrich) and fluoride source is hydrofluoric acid (HF, 48%). The composition of the synthesis gel was:

$$0.71\ SiO_2 : 0.29\ GeO_2 : 0.05\ Al(OH)_3 : 0.25\ BPMPOH : 0.5\ HF : 7.5\ H_2O$$

In a typical synthesis, 0.712 g GeO_2 was first mixed with an aqueous solution containing 11.85 wt% of BPMPOH and kept under stirring at room temperature until complete dissolution. Then, 0.184 g of aluminum hydroxide and 2.5 g of Ludox AS-40 were added under stirring. The mixture was kept under stirring at room temperature for 1h until forming a homogeneous gel. The resultant gel was heated at 50°C to allow evaporation to reach the target H_2O content. Finally, 0.465g of the HF solution was added to the gel under stirring with plastic spatula. The solid was transferred to a Teflon-lined stainless autoclave and heated in an oven at 150°C under agitation for crystallization. After 48h, the autoclave was cooled and the solid product was collected by filtration and washed by abundant distilled water. The product was dried in oven at 100°C in air overnight, and, afterwards, calcined in flowing air using a tubular furnace at 550°C for 6h with a heating rate of 1.5°C/min.

ITQ-33 (ITT). ITQ-33 zeolite was synthesized following a previous report using combination of hexamethonium hydroxide (MSPTOH) and hexamethonium bromide (HXMBr) as OSDA.[4] The silica source is TEOS (98%, Merck), germanium source is germanium oxide (99.999%, Merck), aluminum source is aluminum isopropoxide (Sigma-Aldrich) and fluoride source is hydrofluoric acid (HF, 48%). The composition of the synthesis gel was:

$$0.67\ SiO_2 : 0.33\ GeO_2 : 0.05\ Al(OH)_3 : 0.15\ HXM(OH)_2 : 0.1\ HXMBr_2 : 0.3\ HF : 2.5\ H_2O$$

In a typical synthesis, 5.07 g of GeO_2 was first mixed with 66.49 g of an aqueous solution containing 18.8 wt% of $HXM(OH)_2$ and kept stirring at room temperature until complete dissolution. Then, 53.2 g of an aqueous solution of $HXMBr_2$ (20%), 1.51 g of aluminum isopropoxide and 20.56 g of TEOS were added under stirring. The mixture was kept under stirring at room temperature for 16 h to allow full hydrolysis of TEOS. Afterwards, the gel was heated at 50°C to allow evaporation of excessive H_2O and ethanol generated from hydrolysis of TEOS. When H_2O content reached the desired value, 1.84 g HF was added to the gel under stirring with plastic spatula. The solid was transferred to a Teflon-lined stainless autoclave and heated in an oven at 175°C under static conditions for crystallization. After 24 h, the autoclave was cooled and the solid product was collected by filtration and washed by abundant distilled water. Then, the product was dried in oven at 100°C in air. The zeolite product was calcined in flowing air using a tubular furnace at 550°C for 6h with a heating rate of 1.5°C/min.

ITQ-27 (IWV). ITQ-27 zeolite was synthesized following a procedure reported by Li et al. using diphenyldimethylphosphonium $DPDMP^+$ as OSDA.[5] In a typical synthesis, 30.01 g of a hydroxide solution of $DPDMP^+$ (8.12%wt in water) was mixed with 4.37 g of tetraethylorthosilicate (TEOS, Sigma-Aldrich, 98%wt) and 0.12 g of aluminum isopropoxide (IPA, Sigma-Aldrich, 98%wt). The mixture was stirred until the ethanol and isopropanol formed upon hydrolysis of TEOS and IPA were

evaporated by heating at 50°C. The weight of synthesis gel was carefully weighed and the amount of water controlled to $H_2O:SiO_2$ = 3.4 to facilitate further adding of HF. Finally, 0.44 g of HF solution (SigmaAldrich, 48%wt in water) was added and stirred manually with a Teflon spatula, resulting in a thick gel. The final gel composition was SiO_2 / 0.028 Al / 0.5 DPDMP / 0.5 HF / 4 H_2O. This gel was transferred to a Teflon-lined stainless steel autoclave and heated at 150°C in an oven under tumbling conditions. The solid was recovered by filtration, extensively washed with water, and dried at 100°C overnight. The material was calcined at 580°C for 6 hours in air to remove the organic content located within the crystalline material.

AII.2. Characterization

Powder X-ray diffraction (PXRD) measurements were performed with a multisample Philips X'Pert diffractometer equipped with a graphite monochromator, operating at 40 kV and 35 mA, using Cu Kα radiation (λ = 0.1542 nm).

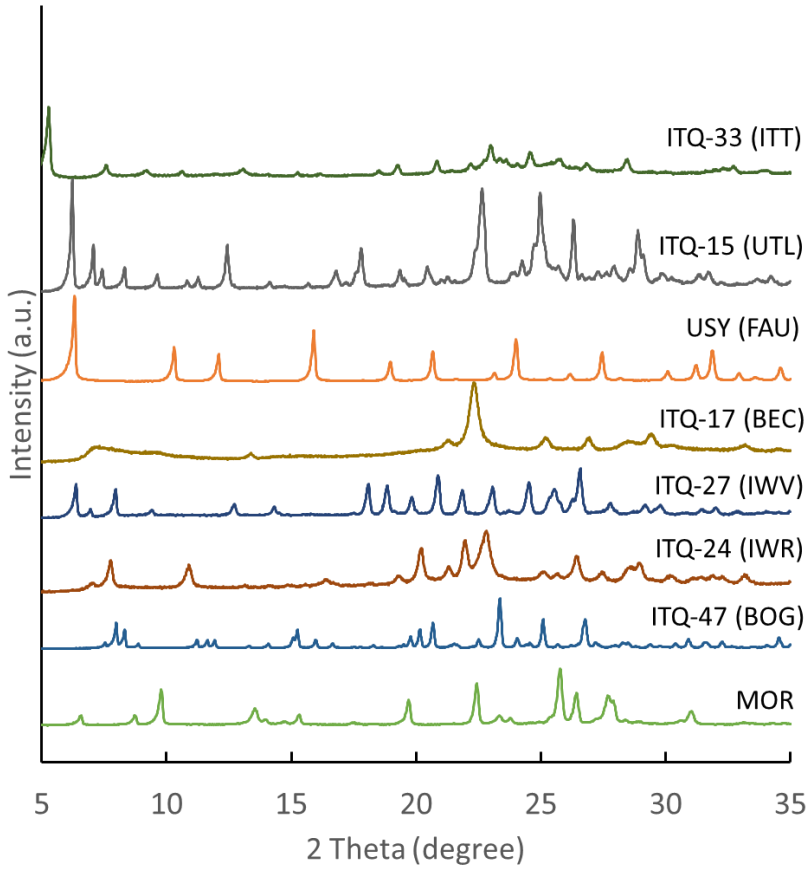

Figure AII.1. PXRD patterns of the zeolites employed in this study.

The chemical analyses were carried out in a Varian 715-ES ICP-Optical Emission spectrometer. The samples were dissolved in HNO_3/HCl/HF aqueous solution before measurement. The organic content of the as-synthesis materials was measured by elemental analysis performed with a SCHN FISONS elemental analyzer.

Textural properties, including BET surface area, micropore volume and external surface area of the samples, were measured by N_2 adsorption/desorption in a Micromeritics ASAP2000. The morphological feature and particle sizes were determined by field emission scanning electron microscope (FESEM, JEOL JSM-6300).

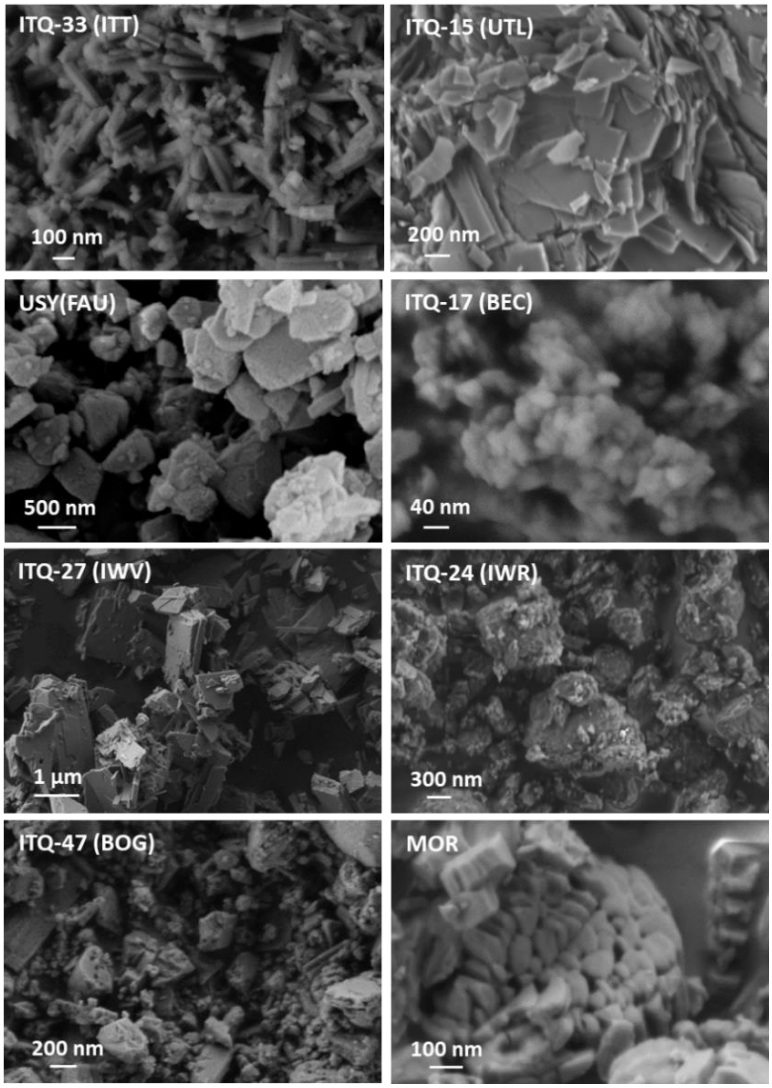

Figure AII.2. FESEM images of zeolite samples employed in this study.

MAS NMR spectra were recorded in a Bruker AVANCE III HD 400 WB. ^{27}Al MAS NMR and ^{27}Al MAS NMR spectra were recorded in a Bruker 3.2mm probe at spinning rate of 20 kHz. ^{27}Al MAS NMR spectra were recorded with $\pi/12$ pulse length of 0.5 μs with a 1s repetition time. ^{27}Al MAS NMR spectra were acquired with selective zero quanto z-filter pulse sequence. 27Al chemical shift was referred to $Al^{3+}(H_2O)_6$.

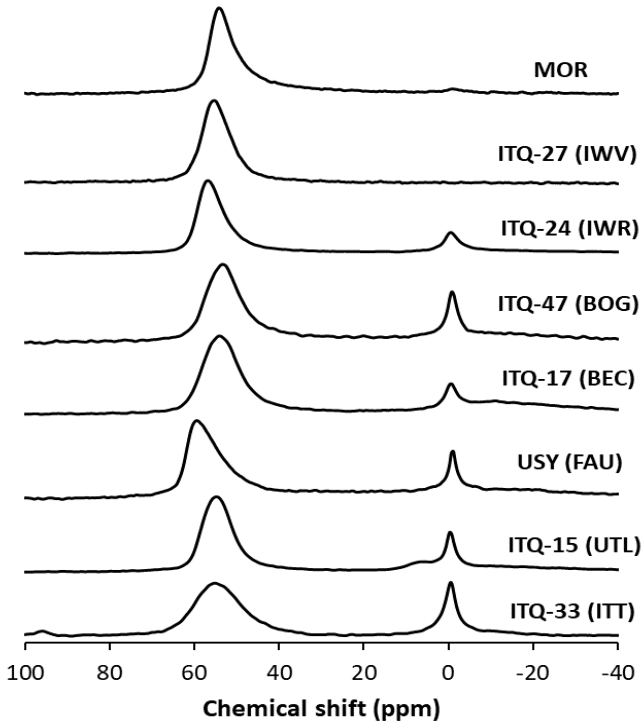

Figure AII.3. ^{27}Al MAS NMR spectra of the zeolite catalysts employed in this study. The acidity of the zeolites was determined by infrared spectroscopy combined with adsorption–desorption of pyridine at different temperatures. Infrared spectra were measured with a Nicolet 710 FT-IR spectrometer. Pyridine adsorption–desorption experiments were carried out on selfsupported wafers (10 mg/cm^2) of original samples previously activated at 400 °C and 10^{-2} Pa for 2 h. After wafer activation, the base spectrum was recorded and pyridine vapor (6.5×10^2 Pa) was admitted into the vacuum IR cell and adsorbed onto the zeolite. Desorption of pyridine was performed under vacuum over 1h periods of heating at 350 °C, followed by IR measurement at room temperature. All the spectra were scaled according to the sample weight. The numbers of Brønsted and Lewis acid sites were determined from the intensities of the bands at ca. 1545 and 1450 cm^{-1}, respectively.

Table AII.1. Physicochemical properties of zeolite materials employed in this study.

zeolite	IZA code	(Si+Ge) /Al	Si/Ge	S_{BET} (m^2/g)	V_{micro} (cm^3/g)	S_{ext} (m^2/g)	Acid amount (μmol/g)	
							150ºC	350ºC
ITQ-33	ITT	19.1	2.3	650	0.28	60	278	150
ITQ-15	UTL	10	49.7	470	0.21	33	434	228
USY	FAU	13.1		723	0.32	75	478	296
ITQ-17	BEC	10.8	3.4	374	0.13	102	348	116
ITQ-27	IWV	23.8		460	0.22	20	309	175
ITQ-24	IWR	13.5		346	0.15	45	389	257
ITQ-47	BOG	24.3	85.5	147	0.18	21	417	147
Mordenite	MOR	12.7		406	0.19	11	733	361

AII.3. Reaction

Prior to catalytic tests, all zeolites were pelletized, crushed and sieved to a particle size of between 0.2 to 0.4 mm. Alternatively, pellets with particle sizes of between 0.1 to 0.2 mm and 0.4 to 0.8 mm were also prepared to investigate to intraparticle diffusion. In all cases, particle sizes of 0.1 to 0.2 mm and 0.2 to 0.4 mm gave same catalytic results while 0.4 to 0.8 mm gave slightly lower activity, indicating that intraparticle diffusion starts to appear when pellet size approximates to 0.8 mm. Then, the pellet size of between 0.2 to 0.4 mm is selected for all catalytic tests.

The gas phase transalkylation of diethylbenzene with benzene was carried out in a fixed bed reactor equipped with a bypass line in parallel with reactor. The feedstock is a liquid mixture of benzene and diethylbenzene (Bz:DEB weight ratio 3:1) containing n-octane as internal standard. Required amount of pelletized catalyst was properly mixed with silicon carbide to reach a total volume of 12.6 ml. The catalyst was activated in dry N_2 flow at 540°C for 3 hours and then the temperature of reactor was cooled down to the reaction temperature. The abovementioned liquid mixture was fed into the bypass together with the desired amount of N_2 as carrier gas. The composition of the feeding gas has a molar ratio of N_2 : DEB : Bz = 30 : 1: 5 and was monitored on-line with a Varian-3800 gas chromatograph equipped with a 30 m 5% phenyl / 95% dimethyl polysiloxane capillary column connected to a flame ionization detector. At this stage, the sample from outlet of the reactor was analyzed every 7 minutes. When the outlet composition according to GC is stable, the feeding was switched to the reactor line and the outlet of the reactor was analyzed by the same gas chromatograph every 9 minutes. The initial activity was measured by precisely sampling at Time On Stream = 0s.

AII.4. Absence of diffusion limited process

Prior to catalytic test, the absence of diffusion limitation was evaluated by testing the reaction under abovementioned procedure changing feeding flow. In gas phase reaction, the N_2 flow was adjusted within the range of 25 ml/min to 1000 ml/min while maintaining the partial pressure of the aromatics. When the flow was above 125 ml/min, the reactions gave identical catalytic results. Then all the gas phase reactions were conducted with a minimum N_2 flow of 250 ml/min to avoid diffusion limitation.

AII.5. Kinetic study

Transalkylation reaction between Bz and DEB is a bimolecular reaction. Since benzene is fed in excessive amount than stoichiometric ratio, the concentration of Bz could be considered constant and the reaction as first order reaction. Then, the first order rate law equation was employed to obtain the rate constant:

$$k = \frac{\ln(1 - Conv.DEB)}{w/F} = \frac{\ln(1 - \frac{1}{2} \cdot Yield.EB.)}{w/F}$$

Where k is the rate constant, and w/F is the contact time.

Activation energy (Ea) was calculated using the Arrhenius equation, by plotting lnk against 1/T:

$$lnk = \frac{-E_a}{\mathrm{R}} \cdot \frac{1}{T} + lnA$$

where k is the reaction rate constant, T is the reaction temperature and A is the pre-exponential factor.

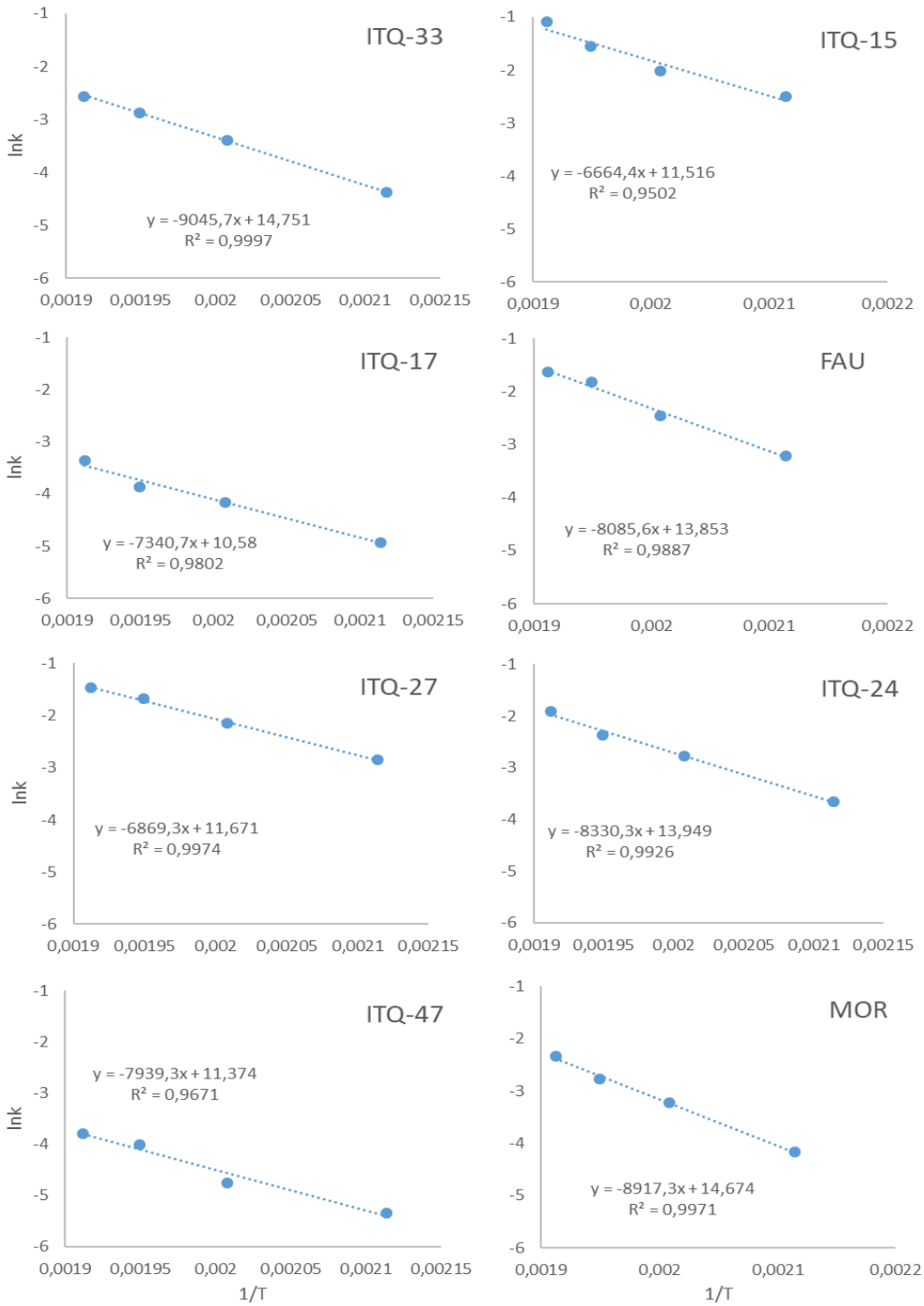

Figure AII.4. Plots of ln*k* versus 1/T for benzene-diethylbenzene transalkylation on different zeolite structures. The reaction rate constants (*k*) and T values are summarized in Table AII.2.

Table AII.2. Reaction rate constant (*k*) of benzene-diethylbenzene transalkylation at EB yield below 20%. Reaction conditions: Pressure: 1 atm, feeding: N_2:DEB:Bz = 30:1:5 (mol).

zeolite	IZA code	T (K)			
		473	498	513	523
ITQ-33	ITT	0.0125	0.0334	0.0565	0.0773
ITQ-15	UTL	0.0829	0.134	0.211	0.338
USY	FAU	0.04	0.0849	0.163	0.194
ITQ-17	BEC	0.0073	0.0157	0.0212	0.0348
ITQ-27	IWV	0.0583	0.1157	0.1861	0.2286
ITQ-24	IWR	0.026	0.0626	0.093	0.1478
ITQ-47	BOG	0.0048	0.0086	0.0182	0.0227
Mordenite	MOR	0.0154	0.04	0.0628	0.0969

AII.6. References

1. Cumplido Comeche, M. P. Síntesis de zeolitas como catalizadores para la optimización de procesos químicos de interés industrial. (Universitat Politècnica de València, 2022). doi:10.4995/Thesis/10251/181697.

2. Simancas, R. *et al.* Modular Organic Structure-Directing Agents for the Synthesis of Zeolites. *Science (80-.).* **330**, 1219–1222 (2010).

3. Liang, J. *et al.* Synthesis of Al-BEC zeolite as an efficient catalyst for the alkylation of benzene with 1-dodecene. *Microporous Mesoporous Mater.* **328**, 111448 (2021).

4. Moliner, M., Diaz-Cabañas, M., Fornes, V., Martínez, C. & Corma, A. Synthesis methodology, stability, acidity, and catalytic behavior of the 18×1018×10 member ring pores ITQ-33 zeolite. *J. Catal.* **254**, 101–109 (2008).

5. Li, C. *et al.* Design and Synthesis of the Active Site Environment in Zeolite Catalysts for Selectively Manipulating Mechanistic Pathways. *J. Am. Chem. Soc.* **143**, 10718–10726 (2021).